Title
Radiochemical Synthesis of 4-[18F]Fluorobenzyl-triphenylphosphonium ([18F]FBnTP) and Ambient Electrophile Modification of Glyceraldehyde-3-Phosphate Dehydrogenase (GAPDH)

Author
Gomez, Adrian Lorenzo

Publication Date
2022

Peer reviewed|Thesis/dissertation

UNIVERSITY OF CALIFORNIA

Los Angeles

Radiochemical Synthesis of 4-[^{18}F]Fluorobenzyl-triphenylphosphonium ([^{18}F]FBnTP) and Ambient Electrophile Modification of Glyceraldehyde-3-Phosphate Dehydrogenase (GAPDH)

A dissertation submitted in partial satisfaction of the requirements for the degree Doctor of Philosophy in Chemistry

by

Adrian Lorenzo Gomez

2022

ABSTRACT OF THE DISSERTATION

Radiochemical Synthesis of 4-[^{18}F]Fluorobenzyl-triphenylphosphonium ([^{18}F]FBnTP) and Ambient Electrophile Modification of Glyceraldehyde-3-Phosphate Dehydrogenase (GAPDH)

by

Adrian Lorenzo Gomez

Doctor of Philosophy in Chemistry

University of California, Los Angeles, 2022

Professor Joseph Ambrose Loo, Chair

Positron emission tomography (PET) is an imaging modality that is capable of 3-dimmensional images where radiolabeled molecules are taken up in the body through absorption, biodistributed *in vivo,* and metabolized. Bioactive molecules with a specific affinity towards pathways or targets of interest can be radiolabeled and visualized. The PET tracer 4-[^{18}F]Fluorobenzyl-triphenylphosphonium ([^{18}F]FBnTP) is capable of targeting the mitochondria membrane potential ($\Delta\Psi_m$) due to its cationic and lipophilic properties. The three pot, four step radiochemical synthesis of [^{18}F]FBnTP was successfully developed using the automated radiosynthesizer ELIXYS, which allowed for a multidose synthesis. The [^{18}F]FBnTP PET tracer was then used for the *in vivo* imaging of non-small cell lung cancer (NSCLC) in disease model mice. This allowed for the profiling of the mitochondrial membrane potential in autochthondous mouse models of lung cancer and find distinct functional mitochondrial heterogeneity for subtypes of lung tumors. The

second area of research included developing a drug analogue containing a 4-(nitrophenylsulfonyl) piperazine backbone, since this class of compounds has been shown to have the ability to decrease murine mortality in hematopoietic acute radiation syndrome (hARS) for the mitigation of radiation damage. The synthesis and characterization, and pharmacokinetics was performed for 52A1, which successfully showed to mitigate radiation damage *in vivo*. The third area of research included the inhibition of glyceraldehyde-3-phosphate dehydrogenase (GAPDH) by ambient electrophiles. GAPDH is an important enzyme for energy metabolism as well as cell proliferation and tumorigenesis. However, upon exposure to ambient pollutants that are produced from incomplete combustion, they can react with the cysteine sites on proteins. The chemical properties of these pollutants make them inherently electrophiles, wherein the cysteine sites are nucleophilic in biological conditions. The cysteine modification then reacts via the Michael Addition, which is an irreversible chemical modification. It was found that when exposed to ambient electrophiles, the Cys 152 and Cys 247 residues of the Human GAPDH were chemically modified, which lead to inhibition and reduced catalytic activity. The quantification and localization of the ambient electrophile modification on GAPDH were determined using intact protein analysis, catalytic activity studies, and bottom-up proteomics approaches.

The dissertation of Adrian Lorenzo Gomez is approved.

Justin Ryan Caram

Ohyun Kwon

Chong Liu

Julian Philip Whitelegge

Joseph Ambrose Loo, Committee Chair

University of California, Los Angeles

2022

Dedicated to my Family, Friends, and Mentors that guided and supported me through this Journey

Table of Contents

Table of Figures

Table of Tables

Table of Appendix Figures

Table of Appendix Tables

Acknowledgments

I would like to thank my family first and foremost including my brothers Adam and Ismael, my sister Tiffany, and my parents Ismael and Ana for always supporting me no matter what. They have all sacrificed so much to help me be where I am today and I am eternally grateful. I would like to thank Alejandra Rios for being by my side for the better part of a decade and for helping me grow into a better person and to appreciate aspects of life that go beyond my comfort zone.

I would like to thank my Professors that helped me along this journey of finding my passion in life. From my days at East Los Angeles College (ELAC) I would like to thank Viken Kiledjian, Veronica Jaramillo, and Armando Rivera-Figueroa. They believed in me when I was still trying to find myself and I am very grateful for them inspiring me to start conducting research.

From my days at Cal State University, Los Angeles (CSULA) I would like to thank my previous lab mates, and mentors Vicki Kubo-Anderson, Maria Manzanares Vargas, Lisa Bautista, Carlos Gutierrez and Krishna Foster. I am immensely grateful for the community that you allowed me to be a part of and for helping me grow into not only the person, but the scientist that I am today.

I would like to thank my lab mates at UCLA that I have had along my journey for allowing me to be apart of your family and for teaching me new lab techniques that have helped me along the way. I would like to thank my committee members Ohyun Kwon, Justin Caram, and Chong Liu for all of their help along these years. I would like to thank Joe Loo for advising and guiding me through all the difficulties that I encountered and for sticking with me after all these years. I would like to give a special thank you to Julian Whitelegge for allowing me into the lab and for giving me a second chance to finish my degree. I have learned so much and am forever grateful for their kindness and generosity.

Chapter 2: An Automated Multidose Synthesis of the Potentiometric PET Probe 4-[^{18}F]Fluorobenzyl-Triphenylphosphonium ([^{18}F]FBnTP) is a modified version of:

> C. Waldmann, A. Gomez, P. Marchis, S. T. Bailey, M. Momcilovic, A. E. Jones, D. B. Shackelford, S. Sadeghi. An Automated Multidose Synthesis of the Potentiometric PET Probe 4-[^{18}F]Fluorobenzyl-Triphenylphosphonium ([^{18}F]FBnTP). *Mol. Imaging Biol.* 2018, *20,* 205—212.

Chapter 3: *In Vivo* Imaging of Mitochondrial Membrane Potential in Non-Small Cell Lung Cancer is a modified version of:

> M. Momcilovic, A. Jones, S. T. Bailey, C. M. Waldmann, R. Li, J. Lee, G. Abdelhady, A. Gomez, T. Holloway, E. Schmid, D. Stout, M. C. Fishbein, L. Stiles, D. V. Dabir, S. M. Dubinett, H. Christofk, O. Shirihai, C. M. Koehler, S. Sadeghi, D. Shackelford. *In Vivo* Imaging of Mitochondrial Membrane Potential in Non-Small Cell Lung Cancer. *Nature,* 2019, *575,* 380—384.

Chapter 4: Classes of Drugs that Mitigate Radiation Syndromes is a modified version of:

> E. D. Micewicz, R. D. Damoiseaux, G. Deng, A. Gomez, K. S. Iwamoto, M. E. Jung, C. Nguyen, A. J. Norris, J. A. Ratikan, P. Ruchala, J. W. Sayre, D. Schaue, J. P. Whitelegge, W. H. McBride. Classes of Drugs that Mitigate Radiation Syndromes. *Front. Pharmacol.* 2021, *12,* 666776.

Appendix Chapter 1: Electrochemical Fluorination and Radiofluorination of Methyl(phenylthiol)acetate Using Tetrabutylammonium Fluoride (TBAF) is a modified version of:

> M. Balandeh, C. Waldmann, D. Shirazi, A. Gomez, A. Rios, N. Allison, A. Khan, S. Sadeghi. Electrochemical Fluorination and Radiofluorination of Methyl(phenylthio)acetate Using Tetrabutylammonium Fluoride (TBAF). *J. Electrochem. Soc.* 2017, *164,* G99—G103.

Appendix Chapter 3: Electrochemical Flash Fluorination and Radiochemicalfluorination is a modified version of:

> M. Balandeh, A. Rios, N. Allison, D. Shirazi, A. Gomez, L. Rambaran, T. Holloway, S. Sadeghi. Electrochemical Flash Fluorination and Radiochemicalfluorination. *ChemElectroChem.* 2018, *5,* 3353—3356.

Appendix Chapter 4: Electrochemical No-Carrier-Added Radiofluorination of Thioethers is a modified version of:

> N. Allison, M. Balandeh, T. Holloway, A. Gomez, A. Rios, C. M. Waldmann, A. Lebedev, S. Sadeghi. Electrochemical no-carrier-added radiofluorination of thioethers. *J. Fluor. Chem.* 2022, *257-258,* 109988.

VITA

Education

09/16-11/18	MS in Chemistry	University of California, Los Angeles (UCLA)
09/14-06/16	MS in Chemistry	California State University, Los Angeles (CSULA)
09/11-06-14	BS in Chemistry	California State University, Los Angeles (CSULA)

Journal Publications

1. N. Allison, M. Balandeh, T. Holloway, **A. Gomez**, A. Rios, C. M. Waldmann, A. Lebedev, S. Sadeghi. Electrochemical no-carrier-added radiofluorination of thioethers. *J. Fluor. Chem.* **2022,** *257-258,* 109988.
2. E. M. Singer, R. M. Chugh, P. Bhanja, **A. Gomez**, L. Gao, J. P. Whitelegge, W. H. McBride, S. Saha, A. J. Norris. BCN057, a Modulator of GSK3ß, Induces KRAS G12D Mutant Pancreatic Cancer Cell Death. *BioRxiv.* **2021**
3. E. D. Micewicz, R. D. Damoiseaux, G. Deng, **A. Gomez**, K. S. Iwamoto, M. E. Jung, C. Nguyen, A. J. Norris, J. A. Ratikan, P. Ruchala, J. W. Sayre, D. Schaue, J. P. Whitelegge, W. H. McBride. Classes of Drugs that Mitigate Radiation Syndromes. *Front. Pharmacol.* **2021,** *12,* 666776.
4. M. Momcilovic, A. Jones, S. T. Bailey, C. M. Waldmann, R. Li, J. Lee, G. Abdelhady, **A. Gomez,** T. Holloway, E. Schmid, D. Stout, M. C. Fishbein, L. Stiles, D. V. Dabir, S. M. Dubinett, H. Christofk, O. Shirihai, C. M. Koehler, S. Sadeghi, D. Shackelford. *In Vivo* Imaging of Mitochondrial Membrane Potential in Non-Small Cell Lung Cancer. *Nature,* **2019,** *575,* 380—384.
5. M. Balandeh, A. Rios, N. Allison, D. Shirazi, **A. Gomez**, L. Rambaran, T. Holloway, S. Sadeghi. Electrochemical Flash Fluorination and Radiochemicalfluorination. *ChemElectroChem.* **2018,** *5,* 3353—3356.
6. C. Waldmann, **A. Gomez**, P. Marchis, S. T. Bailey, M. Momcilovic, A. E. Jones, D. B. Shackelford, S. Sadeghi. An Automated Multidose Synthesis of the Potentiometric PET Probe 4-[^{18}F]Fluorobenzyl-Triphenylphosphonium ([^{18}F]FBnTP). *Mol. Imaging Biol.* **2018,** *20,* 205—212.
7. M. Balandeh, C. Waldmann, D. Shirazi, **A. Gomez**, A. Rios, N. Allison, A. Khan, S. Sadeghi. Electrochemical Fluorination and Radiofluorination of Methyl(phenylthio)acetate Using Tetrabutylammonium Fluoride (TBAF). *J. Electrochem. Soc.* **2017,** *164,* G99—G103.

Selected Conference Presentations

1. A. Gomez, W. Cohn, J. Whitelegge. *Elimination of Formic Acid When Preparing Integral Membrane Proteins for Non-Native Electrospray Ionization Mass Spectrometry.* 70th American Society for Mass Spectrometry Conference, Minneapolis, MN **(2022)**
2. A. Gomez, C. Waldmann, S. Sadeghi. *Automated Three Pot Synthesis of Mitochondrial PET Tracer [^{18}F]FBnTP Using ELIXYS.* UCLA Molecular and Medical Annual Conference **(2017)**
3. M. Balandeh, A. Rios, A. Gomez, A. Khan, S. Sadeghi. *Electrochemical Fluorination of methyl-2-(phenylthio) acetate Using the Cation Pool Method*. UCLA Molecular and Medical Annual Conference (**2016)**

Chapter 1: Introduction

1.1 Positron emission tomography (PET) Tracers

Non-invasive imaging using Positron Emission Tomography (PET), has been a valuable tool for early diagnosis of a variety of diseases.[1] PET works by labelling compounds with radionuclei, which emit positrons that annihilate with nearby electrons to form two gamma rays that travel in opposite directions. These gamma rays are then detected and reconstructed to give a 3-dimmensional image of where the labelled molecules are taken up in the body. Bioactive molecules with a specific affinity towards pathways or targets of interest can be radiolabeled and visualized. One of the more commonly used PET tracers include but are not limited to 2-deoxy-2-[fluorine-18]fluoro-D-glucose ([^{18}F]FDG), an analogue of glucose which is capable of visualizing increased glucose uptake and glycolysis of cancer cells and can depict metabolic abnormalities.[2] Recently, PET tracers have been used for both *in vivo* visualization and treatment, known as Theranostics. Theranostics have been used to treat diseases such as prostate cancer by targeting the prostate specific membrane antigen (PSMA) first with ^{68}Ga-DOTA-PSMA and upon successful imaging, the tumors were treated with ^{177}Lu-DOTAGA-PSMA.[3] Moreover, mitochondrial specific PET tracers, such as [^{18}F]4-fluoro-benzyl-triphenyl-phosphonium ([^{18}F]FBnTP), can be synthesized then visualized using PET for imaging of the mitochondria *in vivo.* Mitochondria key processes involve cellular energy and metabolism and have a major role in growth and survival of cancer cells. Oxidative phosphorylation, which is the process of forming ATP from the electron transport chain (ETC), occurs in the mitochondria.[4] The PET tracer [^{18}F]FBnTP is a cationic lipophilic compound that can target the mitochondrial membrane potential ($\Delta\Psi_m$) due to its negative plasma membrane potential such as in the figure below. This is significant because certain diseases such as diabetes, cardiac failures, neurodegenerative diseases, and cancer

have changes in the mitochondrial membrane potential, which can be detected early and non-invasively.[5–8] These diseases ultimately lead to mitochondrial dysfunction, which causes a

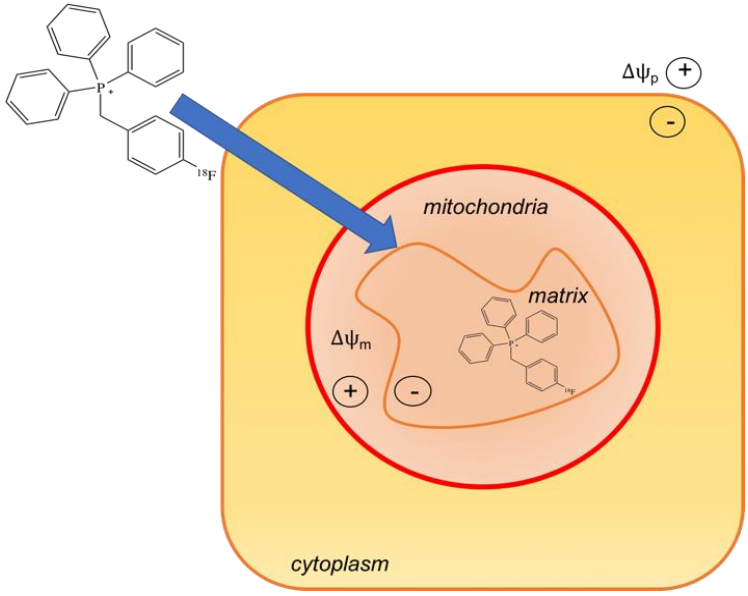

Figure 1. 1. Potentiometic Nature of [18F]FBnTP PET Tracer Uptake in Mitochondria

reduced negative membrane potential among other various harmful downstream cellular processes. Consequently, mitochondrial dysfunction can be monitored via these perturbations in the mitochondria membrane potential (ΔΨ) for non-invasive PET imaging using [^{18}F]FBnTP. In Chapter 3 of this work, [^{18}F]FBnTP was used to visualize mitochondrial dysfunction in non-small cell lung cancer (NSCLC) disease model mice. [^{18}F]FBnTP was able to profile mitochondrial membrane potential in autochthonous mouse models of lung cancer, and ultimately a distinct functional mitochondrial heterogeneity within the subtypes of lung tumors was found. In Chapter 2 of this work, the radiochemical synthesis of [^{18}F]FBnTP PET tracer was be performed using the automated ELIXYS synthesizer in a three pot four step sequence shown below.

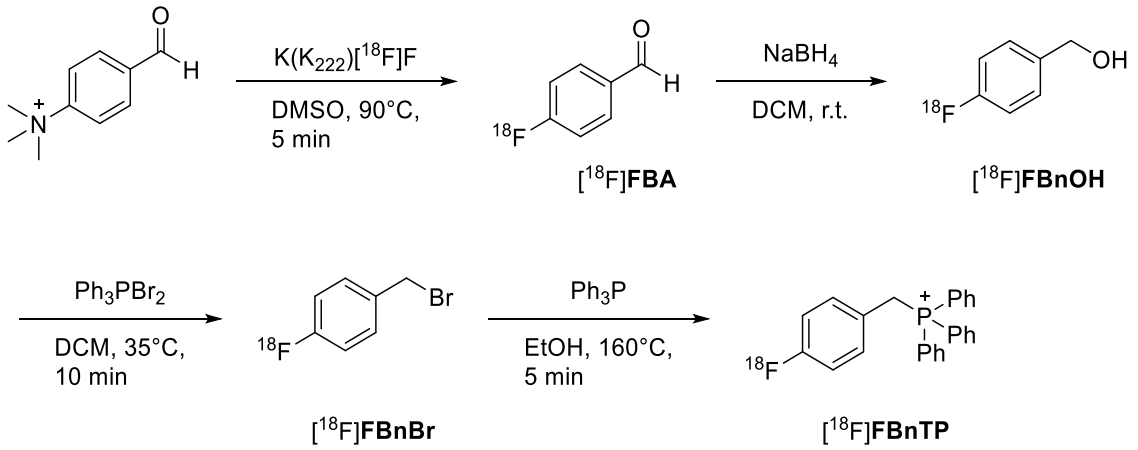

Figure 1. 2. Synthesis schematic of [18F]FBnTP PET tracer

The synthesis of this PET tracer was previously described by Ravert et al. 2004, however the starting radioactivity and activity yields were not disclosed.[9] In this chapter the optimization and successful synthesis of a multidose [^{18}F]FBnTP PET tracer was described.

1.2 Radiation mitigation

The use of ionizing radiation (IR) in medical practice has become increasingly frequent over the years for visualization of tumors and cancers with X-Ray and CT scans, and for treating tumors and cancers with beam therapy.[10] However, IR has deleterious side effects including damage to normal cells and ironically, the initiation of new cancerous growths.[11] Our ability to mitigate cellular damage caused by IR remains limited. Recently, a high throughput screening procedure has shown that compounds containing a 4-(nitrophenylsulfonyl) piperazine backbone have the ability to decrease murine mortality in hematopoietic acute radiation syndrome (hARS).[12] One of the ways the efficacy of a drug can be measured is through pharmacokinetics. Pharmacokinetics allows for the quantification of a drug over time in plasma and tissues. The time course of the study allows for the absorption, distribution, metabolism, and excretion of the drug (ADME). Previously, the compound 512 was synthesized and was shown to uniquely mitigate hARS. However, 512 had challenges in formulation of the compound, which led to the synthesis of 52A1.

The 52A1 analogue was designed to improve the solubility through the addition of a methylamine group to the benzene. The modified synthesis schematic is shown below.

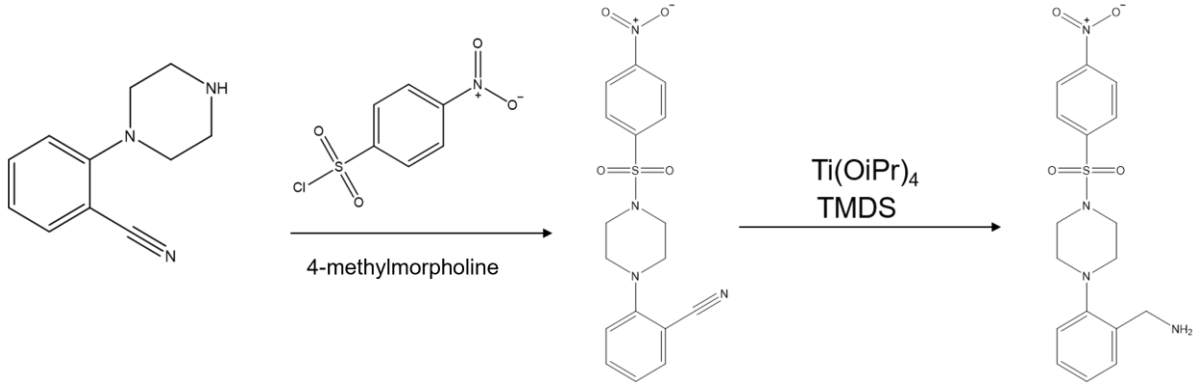

Figure 1. 3. Synthesis schematic of 52A1

In Chapter 4 of this work, 52A1 was synthesized and characterized, and pharmacokinetics were performed on the analogue as well as *in vivo* mice studies.

1.3 Glyceraldehyde-3-phosphate dehydrogenase (GAPDH) Inhibition

Glyceraldehyde-3-phosphate dehydrogenase (GAPDH) is responsible for catalyzing the oxidative phosphorylation of glyceraldehyde 3-phosphate to 1,3-diposphoglycerate, which is a precursor for ATP biosynthesis.[13] The enzyme contains an active site cysteine thiolate (Cys 152 in Human GAPDH, Cys 149 in Rabbit GAPDH), which is located in a pKa-lowering microenvironment (pKa= 6.03).[13,14] The catalytic Cys 152 appears to reside in a pKa-lowering catalytic triad possibly involving Histidine (His179) present in the three-dimensional structure of human GAPDH.[14] The Cys152 is capable of reacting with environmental electrophiles through the irreversible Michael addition. Environmental electrophiles such as acrylamide (ACR) and methyl vinyl ketone (MVK) have been shown to selectively chemically modify the Cys 152 at lower concentrations and at higher concentrations ACR can react with Cys 152 and Cys 247.[14] Additionally, parabenzosemiquinone (p-BSQ), an abundant (100-200 µg/cigarette) long-lived radical quinone is present in cigarette smoke and diesel smoke, which after inhalation is converted to 1,4-benzoquinone (BQ) *in vivo* via the quinone reductases (NQ01).[15–18] Additionally, the inhibition,

chemical modification via electrophile, of the Cys residues in human thioredoxin-1 (Trx1) by 1,4-benzoquinone (BQ) causes reduction of the catalytic activity and activation of apoptosis signal-regulating kinase 1 (ASK1) and p38 mitogen-activated protein kinase (MAPK).[19] Additionally, inhibition of GAPDH by quinones have been observed in gram positive bacterium *Bacillus subtilis*, where a depletion of thiol-containing proteins after quinone exposure was observed.[20] *In vivo,* one of the main processes that GAPDH is responsible for is the conversion of NAD^+ to NADH. A schematic of the biological process is shown below wherein glyceraldehyde-3-phosphate is converted to 1,3-bisphosphoglyceric acid, which is an intermediate in both glycolysis during respiration. Previous studies have investigated the catalytic activity of GAPDH after inhibition via ambient electrophiles, such as quinones, and observed that at concentrations as low as 100 nM inhibition was present.[21]

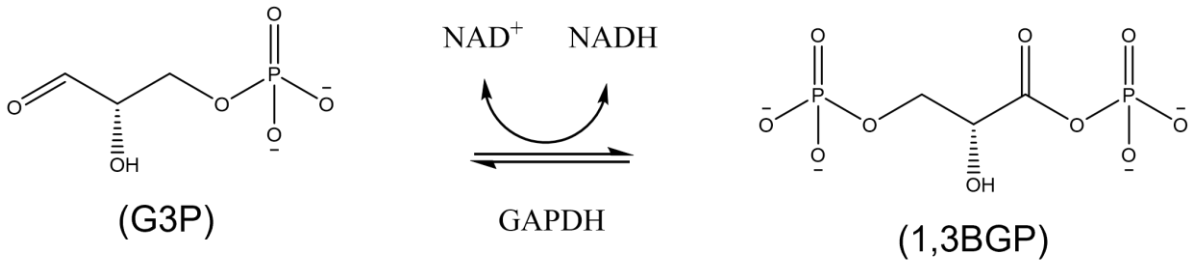

Figure 1. 4. Schematic of GAPDH converting G3P to 1,3 BGP

Previous studies, have utilized bottom-up proteomics for the identification and quantification of the Cys 152 labelled modifications by environmental electrophiles, which include alkenes and quinones.[21,22] A schematic for a typical proteomics flowthrough is shown below.

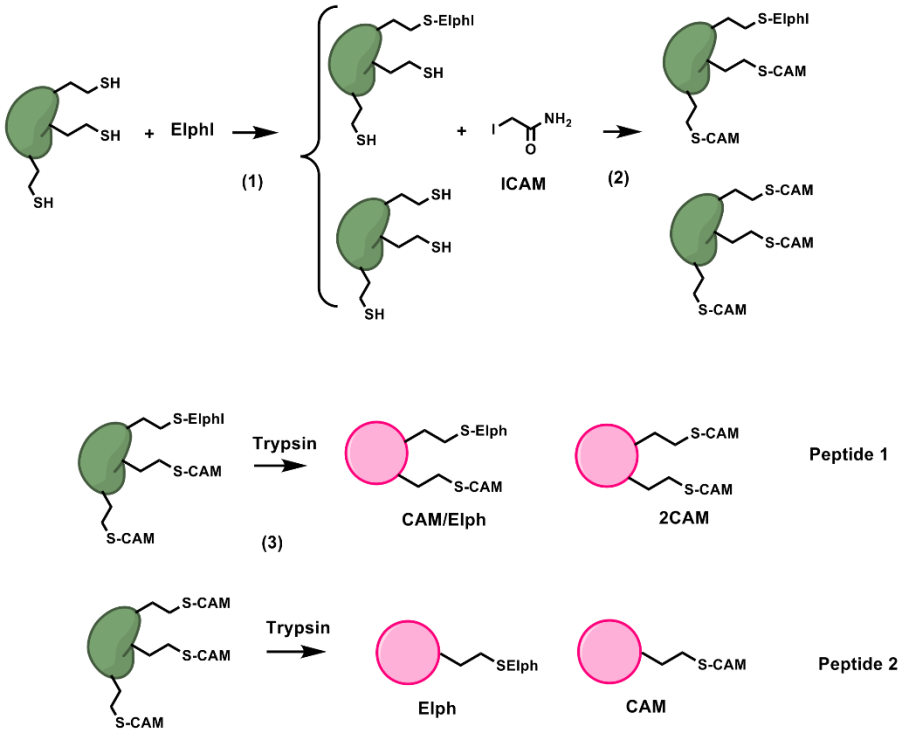

Figure 1. 5. GAPDH proteomics schematic

Here, we describe a mass spectrometry-based approach for the identification and quantification of BQ and MVK at physiologically relevant submicromolar concentrations using intact protein analysis, catalytic activity studies, and bottom-up proteomics.

Chapter 2: An Automated Multidose Synthesis of the Potentiometric PET Probe 4-[^{18}F]Fluorobenzyl-Triphenylphosphonium ([^{18}F]FBnTP)

2.1 Introduction

Mitochondrial metabolism provides adenosine triphosphate (ATP) as the main source of chemical energy in the cell and produces a myriad of other important co-factors as well as metabolites. Mitochondrial dysfunction has been associated with human diseases such as diabetes[5], cardiac failure[6], neurodegenerative diseases[23], and cancer.[24] There have been rapid advances in the development of tools to study mitochondrial metabolism in vitro during the last decades.[25] Among these tools, monitoring mitochondrial membrane potential ($\Delta\Psi_m$) with lipophilic, cationic dyes has emerged as one of the most commonly used techniques.[26] While lipophilic cations have proven good molecular markers of mitochondrial activity, in vivo study of mitochondrial potential requires the development of noninvasive molecular imaging probes.

To harness lipophilic cations for the assessment of $\Delta\Psi_m$-in vivo, carbon-11-labeled phosphonium salts were synthesized[27] and studied as imaging probes[28] for positron emission tomography (PET).[1] The synthesis of 4-[^{18}F]fluorobenzyl- triphenylphosphonium ([^{18}F]FBnTP) was later investigated to take advantage of the superior decay properties of fluorine-18 ($t_{1/2}$ = 109.8 min, maximum β^+ energy = 635 keV).[29] The probe was successfully used in various animal models for imaging of paclitaxel-induced apoptotic activity[30], unstimulated brown adipose tissue[31], ischemic areas after transient coronary occlusion[32], and myocardial perfusion.[33] The original synthesis by Ravert et al.[29] was reported to proceed in four steps, affording the probe in 6 % nondecay corrected (n.d.c.) radiochemical yield (RCY) within 82 min and molar activities (A_m) of 16.7 GBq/ µmol. The synthesis was performed manually and no activity yields (AY) were reported. The same group later reported a microwave-facilitated synthesis using custom hardware delivering the probe in n.d.c. RCY of 8.3 % within 52.4 ± 14 min and A_m of 534.5 ± 371.4 GBq/µmol.[34] Again,

no AY or starting activities were disclosed. Zhang et al. recently described the formation of [^{18}F]FBnTP in one step via copper-mediated ^{18}F-fluorination using a pinacolyl boronate precursor.[35] Formation of the probe was reported in high RCY of 62 ± 1.4 % before purification. The synthesis was performed manually and neither AY nor A_m of the purified product formulation were revealed. Even though metal-mediated ^{18}F- fluorinations will likely be used for the clinical production of PET imaging probes in the future, their compliance with the principles of current good manufacturing practice (cGMP) has not been extensively established to this date.[36]

In this study, we intended to translate the original four-step synthesis into a clinically useful production procedure on a commercially available radiosynthesizer that reliably affords multiple doses ready for injection into patients. Since the three-pot design of the ELIXYS FLEX/CHEM radiosynthesizer allows for complete automation of the sequence, it was chosen for this task.[37]

2.2 Methods and Materials

All commercially available reagents and materials were used as received unless otherwise specified. Acetonitrile (MeCN, extra dry, 99.9%), dimethyl sulfoxide (DMSO, extra dry, 99.7%), and dichloromethane (DCM, extra dry, 99.9%) were obtained from Acros Organics. Ethanol (EtOH, 200 proof, anhydrous) was obtained from Decon. All water used was purified to 18 MΩ and passed through a 0.1-mm filter. 4-Trimethylammoniumbenzaldehyde trifluoromethanesulfonate and 4,7,13,16,21,24-hexaoxa-1,10-diazabicyclo[8.8.8]hexacosane (K_{222}, 98%) were purchased from ABX. Triphenylphosphine dibromide (Ph_3PBr_2, 96%; stored and handled in a glovebox), sodium borohydride on alumina ($NaBH_4 \cdot (Al_2O_3)_X$); stored and handled in a glovebox), and triphenylphosphine (PPh_3, 99 %) were purchased from Sigma-Aldrich. 4-Fluorobenzyl triphenylphosphonium chloride (FBnTP, nonradioactive reference, 98 %) was purchased from Alfa Aesar. L-Ascorbic acid sodium salt (Na-ascorbate, 99 %) was purchased from Acros Organics. Potassium carbonate (K_2CO_3) was purchased from FisherChemical.

Sodium chloride solution (saline, 0.9 %, injection, USP) was purchased from Hospira. Sep- Pak Plus Accell CM cartridges (preconditioned with EtOH (10 mL), followed by deionized water (20 mL)), Oasis WCX Plus cartridges (preconditioned with EtOH (5 mL), followed by deionized water (10 mL)), Sep-Pak Light Plus QMA cartridges (preconditioned with 0.5N $KHCO_3$ (3 mL), followed by deionized water (5 mL)), and Sep-Pak Classic Silica cartridges (wetted with DCM (3 mL)) were purchased from Waters. GraceTM SCX Maxi-Clean cartridges (wetted with deionized water (5 mL)) were purchased from Alltech. Millex-GV (SLGV013SL and SLGV004SL) sterile filters with a 0.22-µm pore size hydrophilic PVDF membrane were purchased from MilliporeSigma. Reactor vials (W986259NG), reagent vial septa (224100-072), and crimp caps (224177-01) were purchased from Wheaton. Reagent vials (62413P-2) were purchased from Voigt. Magnetic stir bars (14-513-65) were purchased from Fisher Scientific. Glass chromatography columns (006SCC-10-10-AA) were purchased from Omnifit Labware.

2.3 Chromatography and Analytical Methods

Radio thin layer chromatography (radio-TLC) was performed on silica plates (TLC Silica gel 60 W F_{254}s, Merck). After spotting a small sample volume (~ 1–5 µL) using a glass capillary, the plate was developed in the mobile phase (MeCN). Chromatograms were obtained using a radio-TLC scanner (miniGita Star, Raytest). Radio high-performance liquid chromatography (radio-HPLC) chromatograms for quality control were registered using a 1200 Series HPLC system (Agilent Technologies) equipped with a GabiStar flow-through gamma detector (Raytest). Data acquisition and processing was performed using OpenLAB CDC ChemStation Edition 2016 (Agilent Technologies). Analytical HPLC was used to estimate the radiochemical purity (RCP), the A_m, and the chemical purity of final formulations of [^{18}F]FBnTP. A radioactive sample (200 µL) was taken from the final formulation and injected for HPLC analysis (5 µL injection volume). HPLC method 1: Alltech Adsorbosphere SCX 5u, 250 × 4.6 mm. Gradient: A = MeCN (+ 0.05 % TFA); B = water (+ 0.05% TFA); flow rate = 1.8 mL/min; 0–12 min 90% B to 5% B, 12–16 min 5 % B,

16–17 min 5% B to 90% B; 254 nm detection wavelength. RCP was calculated by dividing the area under the curve (AUC) for the desired product by the sum of AUC for all peaks. To confirm the structural identity of the synthesized compound, a radioactive sample (195 µL) of the final formulation was diluted with a 10-mM solution of the nonradioactive reference in water (5 µL) and injected for HPLC analysis (5 µL injection volume). Calibration curves of UV absorbance versus molar mass were created in advance for calculating A_m shown below.

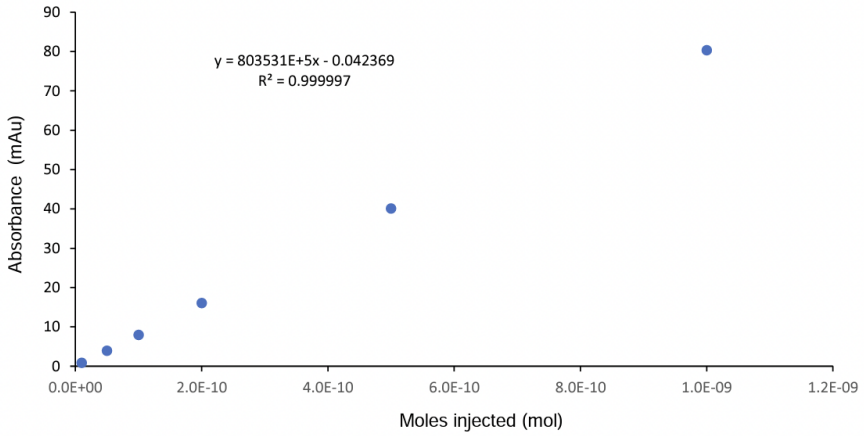

Figure 2. 1. UV absorbance of non-radioactive reference vs. molar mass

Curves were obtained using a linear-least square fit of absorbance versus molar mass for six data points spanning the expected molar mass range. A_m was calculated by dividing the radioactivity of the injected sample by the molar mass (as determined from the AUC for the UV peak and the calibration curve). A_m reported are decay corrected at the end of the synthesis. For measurement of RCY (expressed as the percentage of the starting activity and corrected for decay) or AY (not corrected for decay), final formulations were measured in a dose calibrator (Capintec). Analytical HPLC was used to analyze radioactive samples of intermediate steps of the sequence in low-activity runs. HPLC method 2: Phenomenex Luna 5µ C18 (2) 100 A, 250 × 4.6 mm, 5 µm. Gradient: A = MeCN (+ 0.05 % trifluoroacetic acid (TFA)); B = water (+ 0.05 % TFA); flow rate =

1.8 mL/min; 0–12 min 90 % B to 5 % B, 12–16 min 5 % B, 16–17 min 5 % B to 90 % B; 254 nm detection wavelength.

2.4 Radiosynthesizer Setup

Dedicated cassettes for [^{18}F]FBnTP synthesis were reused, and liquid pathways cleaned with MeCN before each experiment using an automated sequence. The cleaned cassettes were loaded into the synthesizer and locked into position. Clean reactor vials with a magnetic stir bar were placed in the reactor positions. Shortly before the start of the synthesis, reagent vials were filled with the appropriate reagents and then sealed with a septum and crimp cap. Once sealed, the reagent vials were inverted and loaded into the appropriate cassette reagent positions. Preconditioned cartridges and the glass column for the reduction step were installed on the cassettes using Luer fittings in the positions indicated in Fig. 2.2 Interconnections were made as indicated in Fig. 2.2. Finally, a mixture of EtOH (~ 50 mL) and ice was added to the vacuum trap Dewar.

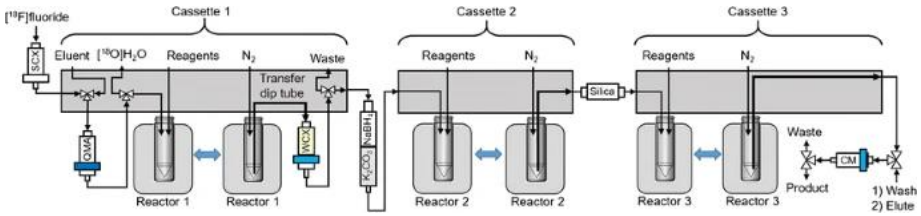

Figure 2. 2. Cassette fluid path diagram showing connections to cartridges, connections between cassettes, and connections of the SPE purification system.

2.5 Synthesis Protocol

No-carrier-added [^{18}F]fluoride was produced by the (p,n) reaction of [^{18}O]H_2O (~ 97 % isotopic purity, Medical Isotopes) in a RDS-112 cyclotron (Siemens) at 11 MeV using a 1- mL tantalum target with Havar foil. The activity was unloaded from the target and pushed through a strong cation exchange (SCX) cartridge (if applicable) before entering the QMA cartridge. Trapped

[^{18}F]fluoride was subsequently eluted with a solution of K_{222} (10 mg, 27 µmol) and K_2CO_3 (1 mg, 7 µmol) in acetonitrile/water (3:5, 0.8 mL) into the first reaction vessel (1.5 min, 7 psig nitrogen pressure). Contents were partially evaporated while applying vacuum and a stream of nitrogen (10 psig) at 110 °C for 3.5 min with stirring. Acetonitrile (1.2 mL) was added through the QMA cartridge to wash residual activity into the vessel, and the combined contents evaporated for 3.0 min at 110 °C (7 psig nitrogen pressure). Acetonitrile (1.2 mL) was directly added to the reactor, and the contents were fully evaporated for 2.5 min at 110 °C (7 psig nitrogen pressure). The reactor was cooled to 35 °C, and a solution of 4-trimethylammoniumbenzaldehyde trifluoromethanesulfonate (5 mg) in DMSO (0.8 mL) was added. Contents were reacted at 90 °C for 5 min with stirring. A 1% (w/v) Na-ascorbate solution (3 mL followed by 2 mL) was added to the reactor under stirring, and the resulting mixture was passed through an Oasis WCX cartridge over a period of 1.5 min (6 psig nitrogen pressure). Another batch of 1% (w/v) Na-ascorbate solution (3 mL followed by 2 mL) was added to the reactor and passed through the cartridge. The cartridge was blow-dried for 1 min (20 psig nitrogen pressure) and eluted with DCM (3 mL). The mixture was passed through a glass chromatography column, containing $NaBH_4 \cdot (Al_2O_3)_X$ (350 mg) followed by K_2CO_3 (2 g) and directed into the second reaction vessel (3 psig nitrogen pressure). Cartridge and column were rinsed with DCM (1 mL, containing 0.2%(v/v) of water) (3 psig nitrogen pressure). A solution of Ph_3PBr_2 (100 mg) in DCM (1.1 mL) was added to the second reaction vessel and the mixture was reacted at 35 °C for 10 min. All contents of the second reaction vessel were passed through a silica cartridge into the third reaction vessel (2 psig nitrogen pressure). A solution of PPh_3 (3 mg) in EtOH (0.6 mL) was added to the third reaction vessel, and all contents were partially evaporated to approximately 2 mL by applying both vacuum and a stream of nitrogen (3 psig) at 45 °C for 3.5 min with stirring. The silica cartridge was rinsed with DCM (1 mL) (1 psig nitrogen pressure), and the contents of the third reaction vessel were partially evaporated to approximately 0.5 mL by applying both vacuum and a stream of nitrogen

(3 psig) at 45 °C for 6.5 min with stirring. EtOH (1 mL) was added and the contents were partially evaporated to approximately 0.5 mL by applying both vacuum and a stream of nitrogen (7 psig) at 80 °C for 2.5 min with stirring. The resulting mixture was reacted in a sealed position at 160 °C for 5 min with stirring. The reaction vessel was cooled to 35 °C and water (3 mL) was added with stirring. The resulting mixture was passed through a Sep-Pak Plus Accell CM cartridge (8 psig nitrogen pressure). The Sep-Pak was immediately washed with EtOH (20 mL) and the product released with 2% EtOH in saline + 0.5% (w/v) Na-ascorbate (10 mL) and directed through a sterile filter into a vented sterile vial.

2.6 Results

The aim of this study was to develop a reliable synthesis protocol for the potentiometric PET-probe [^{18}F]FBnTP on a commercially available radiosynthesizer. For practical clinical translation, the final formulation should be injectable, i.e., pass all applicable quality control tests, and should be obtained in AY that allow for imaging of multiple patients. To achieve these goals, we adapted a four-step, three-pot synthesis[29] by assembling a sequence of “unit operations” (e.g., “trap,” “elute,” “evaporate,” “react”) that are programmed into the synthesizer-software and specifying the parameters for each (e.g., temperature, reaction time, pressure)[38]. A seamLess flow of solvents was tested in abbreviated runs without activity or reagents to ensure its correctness. The sequence was optimized for RCY and RCP during several production runs (n = 24) using activity amounts that averaged around 30.8 GBq. Adjustments to the sequence were made based on careful analysis of the crude product composition as well as the residual activity retrieved from vital parts of the setup (i.a. reactors, SPE-cartridges, and waste containers). We also performed low-activity test runs starting with an average of 300 MBq of [^{18}F]fluoride which allowed for safe withdrawal of samples for radio-HPLC as well as radio-TLC analysis between each step. The reaction vessel was made accessible between steps by using the “Move Reactor” operation. The optimized sequence consists of 33 “unit operations” and runs autonomously without user

interference. The synthesis includes intermediate solid-phase extraction purifications, an on-column reduction, controlled solvent evaporation steps, and reactions in sealed position at temperatures above the boiling points of the respective solvents. An overview of the synthesizer setup as well as the flow of liquids is depicted in Fig. 2.2. The SPE purification with a Sep-Pak Plus Accell CM cartridge is supported by two electrically actuated three-position valves that are controlled by the user from outside the hotcell.

The synthetic steps of the optimized sequence with respective reaction conditions are shown in Figure 2.3.

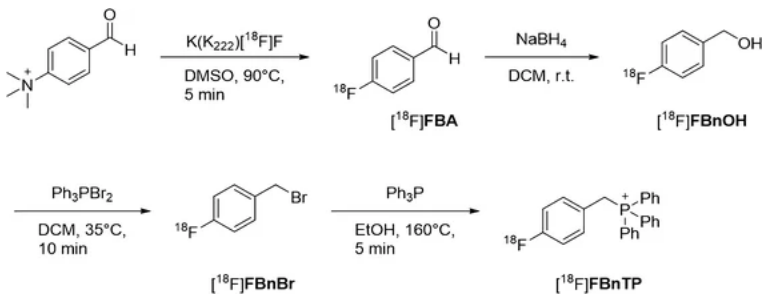

Figure 2. 3. Synthetic sequence showing optimized reaction conditions.

Briefly, the sequence consists of the synthesis of 4-[^{18}F]-fluorobenzaldehyde ([^{18}F]FBA), subsequent reduction of the aldehyde functionality with $NaBH_4 \cdot (Al_2O_3)_X$, conversion of 4-[^{18}F]fluorobenzyl alcohol ([^{18}F]FBnOH) to 4-[^{18}F]fluorobenzyl bromide ([^{18}F]FBnBr) with Ph_3PBr_2, and formation of [^{18}F]FBnTP by nucleophilic substitution with Ph_3P. Following this sequence, the probe was synthesized without the use of HPLC in AY of 1.4–2.2 GBq of [^{18}F]FBnTP from 9.4 to 12.0 GBq [^{18}F]fluoride in 90–92 min (RCY = 28.6 ± 5.1% with n = 3). Molar activities at the end of synthesis ranged from 80 to 99 GBq/µmol and RCP was > 99 % in all cases. The formulated probe in injectable form passed all applicable quality control tests.

2.7 Discussion

Optimization of [^{18}F]FBA Formation

The first synthetic step consists of [^{18}F]FBA formation with subsequent SPE purification using an Oasis WCX cartridge. In our early synthesis attempts, [^{18}F]FBnTP was obtained in poor RCY < 0.6 % with starting activities that averaged around 41.1 GBq. We observed that up to 80% of the starting activity had passed through the Oasis WCX cartridge during SPE purification of [^{18}F]FBA. HPLC analysis of the waste activity showed no evidence of [^{18}F]FBA but of an unknown, polar, impurity alongside unreacted [^{18}F]fluoride. This implies that [^{18}F]FBA was available in RCY < 20% for the subsequent three steps, hampering overall RCY of [^{18}F]FBnTP. Since numerous publications describe the synthesis of [^{18}F]FBA in RCY ranging from 50 to 72%[39,40], we investigated the reason for the low formation of [^{18}F]FBA in our hands. We considered radiolysis of [^{18}F]FBA during SPE purification in the presence of water as a possible reason for low yields from high starting activities[41]. This possibility was explored by synthesizing [^{18}F]FBA with escalating amounts of radioactivity and a negative correlation between starting activities and synthesis yield was indeed observed shown in Table 2.1.

Table 2.1. Synthesis of [^{18}F]FBA with increasing starting activities

Entry	Solvent	Temp. (ºC)	Time (min)	Na-ascorbate (w/v %)	Starting Activity (GBq)	RCY (%)
1	MeCN	100	10	0	0.7	50
2	MeCN	100	10	0	2.8	34
3	MeCN	100	10	0	6.0	23
4	MeCN	100	10	1	5.3	49
5	DMSO	90	5	1	5.0	65

We found that radiolysis during SPE purification was efficiently hindered by replacing water with a 1 % (w/v) Na-ascorbate solution. Analysis of the crude mixture in low-activity test runs showed formation of [^{18}F]FBA in high purity (radio-HPLC = 94–99%, radio-TLC = 92%) shown below in figures 2.4 and 2.5.

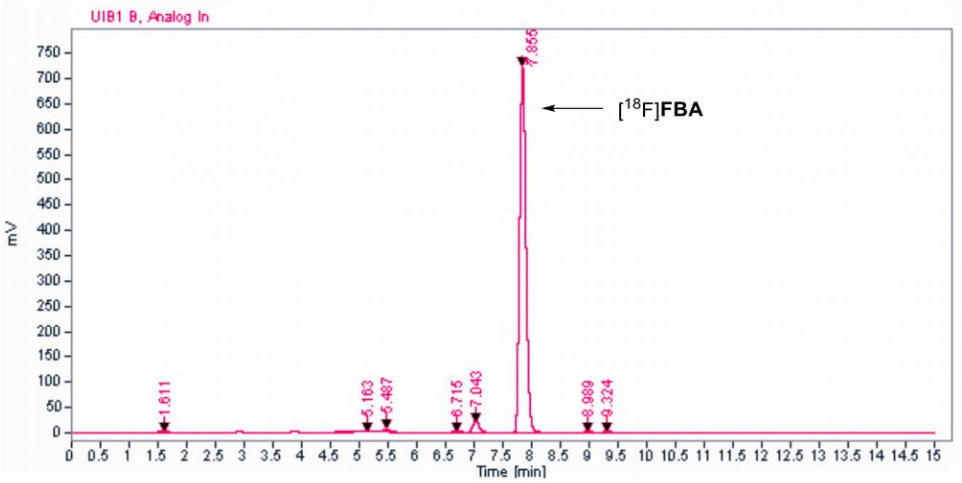

Figure 2. 4. Sample-radio HPLC of crude [18F]FBA

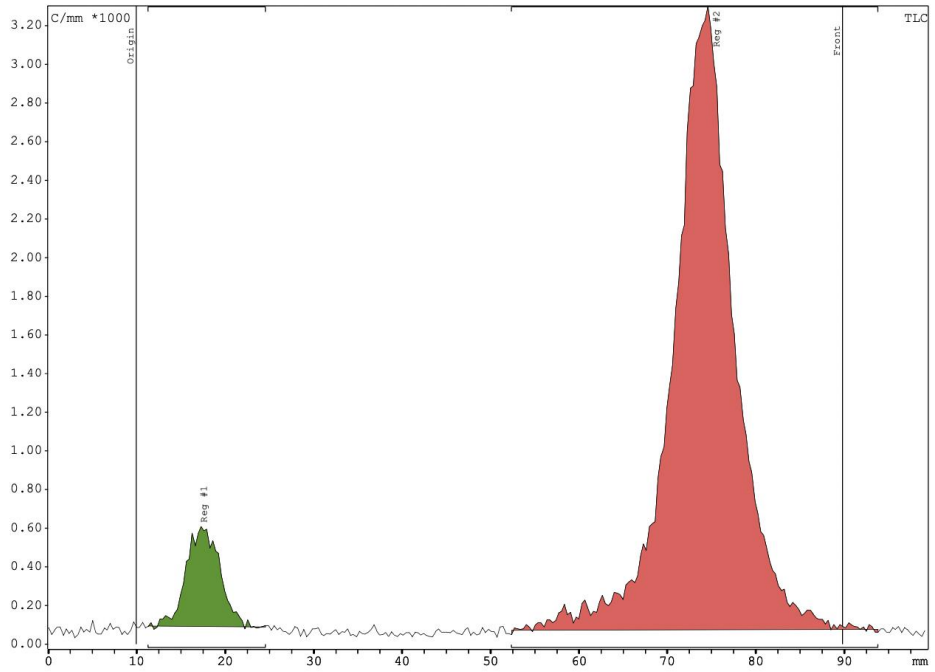

Figure 2. 5. Sample radio-TLC of crude [18F]FBA

After addition of water, 69–79% of the starting activity were trapped on the Oasis WCX cartridge, indicating high yields of [^{18}F]FBA, similar to previously reported results. The waste activities after this step amounted to 20–25% of starting activities. Following the addition of 1% (w/v) Na-ascorbate solution, similar percentages of waste activities were observed in high-activity [^{18}F]FBnTP production runs, leading us to conclude that hindrance of radiolysis was key in enabling the synthesis of [^{18}F]FBA in high AY.

During certain production runs, we observed a considerable decrease of [^{18}F]FBA formation as indicated by SPE waste activities of up to 48 %. This coincided with reports of low 2- deoxy-2-[^{18}F]fluoro-D-glucose ([^{18}F]FDG) yields at the Biomedical Cyclotron facility at our institution. The yield drop was correlated to the release of undesired metal contaminants from the targets, rendering the [^{18}F]fluoride inactive for the nucleophilic attack during [^{18}F]FBA synthesis. With cleaning of the cyclotron target body and replacement of the Havar foil during cyclotron

maintenance, [^{18}F]FBA yield was restored. This led us to place an SCX cartridge in between the [^{18}F]fluoride delivery line and the cassette of the synthesizer as indicated in Fig. 2.1, which equally proved effective in restoring the yield. Between 18 and 27 % of the activity delivered by the cyclotron accumulated in the SCX cartridge. Other strategies that efficiently reduce metal contaminants alongside negligible [^{18}F]fluoride loss have been reported[42].

Optimization of [^{18}F]FBnOH Formation

The formation of [^{18}F]FBnOH proceeds by elution of [^{18}F]FBA from the Oasis WCX cartridge and channeling liquids through a glass column filled with the reducing agent $NaBH_4 \cdot (Al_2O_3)_X$ and subsequent drying with K_2CO_3. In early attempts, diethyl ether (Et_2O) was used as the eluent which efficiently eluted [^{18}F]FBA off the cartridge but turned out to be problematic during the subsequent bromination step (vide infra). Et_2O was successfully replaced with 3 mL of dry DCM, but a second elution with 1 mL of DCM was necessary to sufficiently release [^{18}F]FBA off the Oasis WCX. Since a proton source is necessary to form the OH-functionality from the alcoholate obtained in the reduction of aldehydes with hydride, up to 38 % of the starting activity remained in the $NaBH_4$ bulk when extra dry DCM was used. This was addressed by adding a small amount of water (0.2 % v/v) to the second 1-mL elution with DCM to rinse the column. With this, only 1–3 % of the starting activity remained in the $NaBH_4$ bulk at the end of the synthesis. Efficient reduction of the aldehyde with conversion rates of 83–98 % was confirmed by analytical radio-HPLC in low- activity runs shown below in figure 2.6.

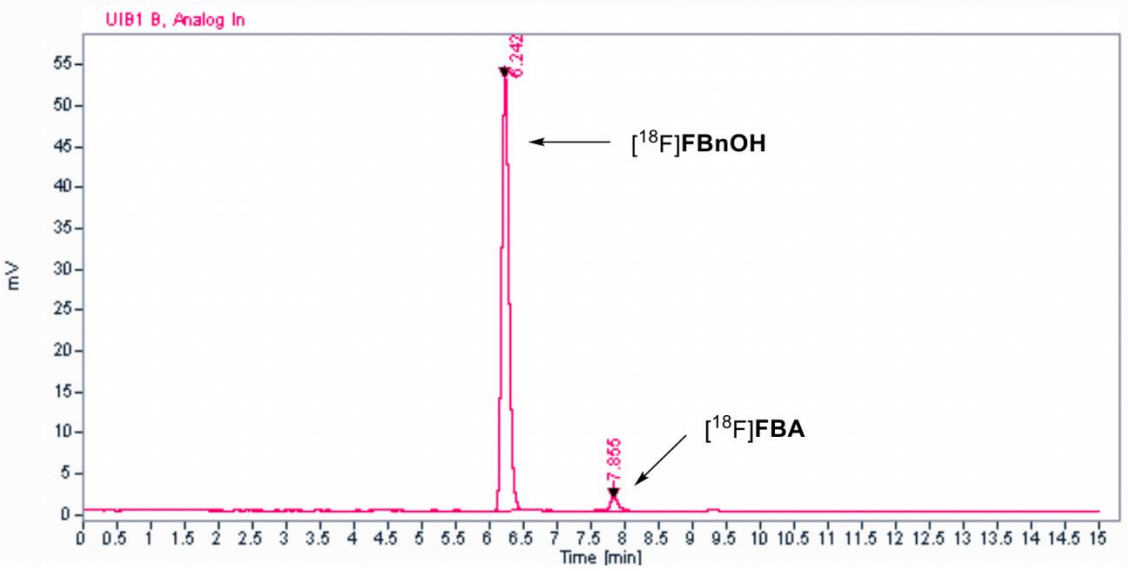

Figure 2. 6. Sample radio-HPLC of crude [18F]FBnOH

Optimization of [^{18}F]FBnBr Formation

Transformation of [^{18}F]FBnOH into [^{18}F]FBnBr is achieved through the use of bromination agent Ph_3PBr_2 with subsequent silica cartridge purification. In early attempts, we added a solution of [^{18}F]FBnOH in Et_2O directly to a solution of Ph_3PBr_2 in DCM, which resulted in unpredictable yields and synthesis failures. Replacing Et_2O with DCM during the on- column reduction avoided the formation of a biphasic system as well as precipitation of by- products derived from Ph_3PBr_2. Moreover, weighing the Ph_3PBr_2 solution in a glovebox, and adding the dry solvent shortly before the start of the sequence to the septum-sealed vial of the reagent resulted in a more reliable bromination efficiency. Dry conditions have been reported to be a crucial requirement for high bromination yields[43] and strong fuming was observed if the brominating reagent was kept in an open vessel. To further increase the dryness of DCM coming from the preceding reduction step, the amount of K_2CO_3 in the column was increased from 0.5 to 2 g. With these measures in place,

up to 88 % bromination of [^{18}F]FBnOH was observed as confirmed by radio-HPLC in low-activity test runs shown below in figure 2.7

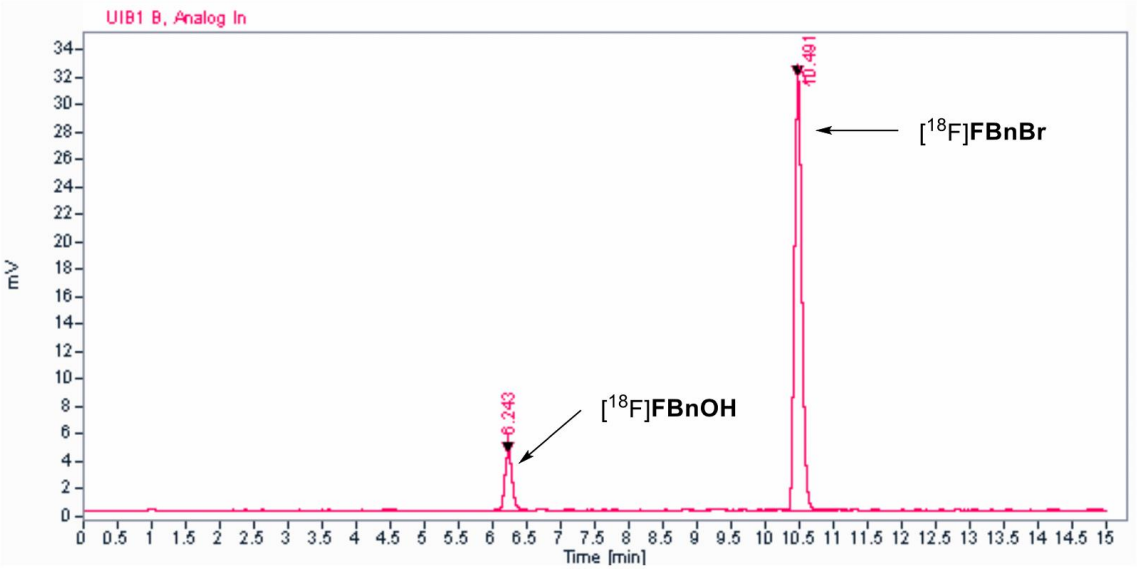

Figure 2. 7. Sample radio-HPLC of crude [18F]FBnBr

Less than 8 % leftover activity on the silica cartridge after purification was an additional indicator of good conversion rates in this step. The leftover activity consisted primarily of unreacted [^{18}F]FBnOH that was predominantly adsorbed on silica whereas [^{18}F]FBnBr passed through efficiently. The more delicate requirements in this step have been the most common cause of inconstant outcomes in our experiments.

Optimization of [^{18}F]FBnTP Formation

The last synthetic step consists of nucleophilic substitution of bromide in [^{18}F]FBnBr with PPh_3. Adapting published procedure[29], we initially added [^{18}F]FBnBr in DCM from the previous step to a 21-mg solution of PPh_3 in toluene followed by removal of most of the DCM under reduced pressure and heating to 110 °C for 5 min. In our hand, [^{18}F]FBnTP formation from [^{18}F]FBnBr

was 28 % using these conditions as confirmed by radio-HPLC. In a nonradioactive condition screening with different solvents and temperatures, we observed almost quantitative FBnTP formation at 160 °C for 5 min in 0.5 mL of either MeCN or EtOH shown in table 2.2.

Table 2. 2. Non-radioactive optimization of FBnTP formation.

Solvent (0.5 mL)	PPh3 (mg)	Temp (°C)	FBnBr consumption (%)	FBnTP formation (%)
Toluene	21	110	3	5
Toluene	21	160	41	43
MeCN	21	110	99	99
MeCN	3	110	30	41
MeCN	3	160	90	79
EtOH	3	160	95	90

EtOH was used as the solvent to hinder radiolysis of [^{18}F]FBnTP during SPE purification (vide infra). The activity fraction associated with [^{18}F]FBnTP in the crude mixture after nucleophilic substitution was 70–81 % in low-activity runs shown below in figure 2.8.

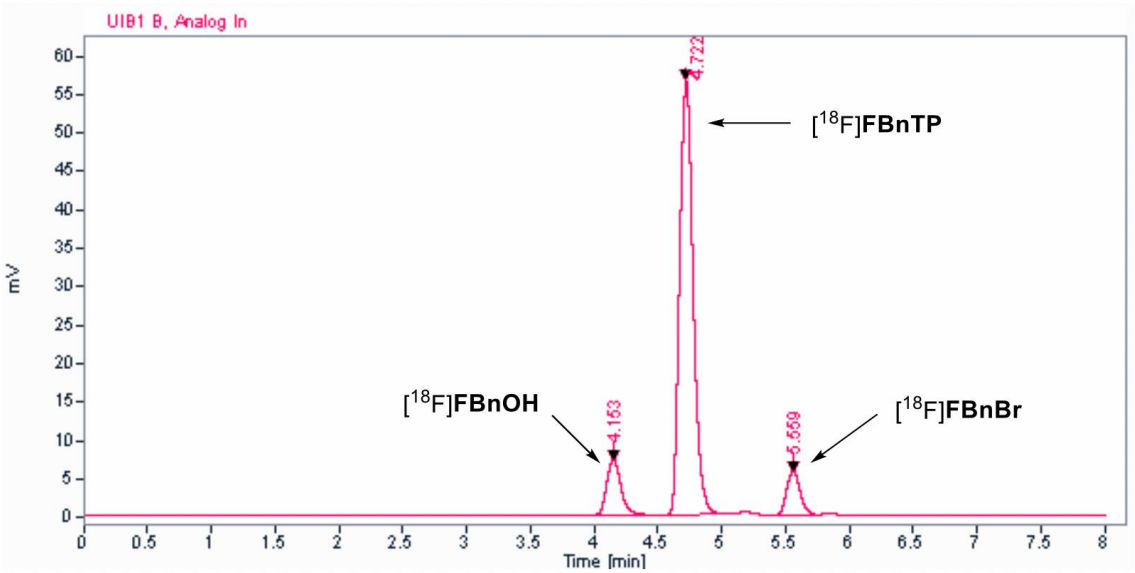

Figure 2. 8. Sample radio-HPLC of crude [18F]FBnTP

Purification and Formulation of [^{18}F]FBnTP

Initially, the crude mixture was purified by semipreparative HPLC. The bulk of unreacted Ph_3PBr_2 and PPh_3 were removed with a Sep-Pak C18 Plus Short cartridge and the resultant mixture was injected into the HPLC system. After collection of fractions containing the desired product and removal of solvent with a rotary evaporator, the probe was reformulated in saline. Problems associated with this approach were loss of product activity to the C18 cartridge, difficulties to remove residual Ph_3PBr_2 that elutes shortly after [^{18}F]FBnTP under reversed phase conditions, and stickiness of the probe to the flask after removal of the HPLC-solvent. Formulations suffered from low chemical purities and low pH, both of which can be attributed to residual Ph_3PBr_2. The cationic nature of [^{18}F]FBnTP led to use an analytical SCX HPLC column for the determination of A_m and resulted in a well separated UV signal of the product. UV and radio-impurities eluted at considerably earlier retention times than the cationic product activity, allowing for an accurate determination of AUC for A_m measurements. This led us to consider using a cation exchange

cartridge for purification instead of HPLC, similar to a previously reported use of SPE purification for a cationic probe with a Sep-Pak Plus Accell CM cartridge[44]. In several radioactive and nonradioactive test runs, we optimized conditions to trap and wash [^{18}F]FBnTP on the Sep- Pak. The probe was efficiently trapped on the Accell CM even in the presence of large amounts of Ph_3PBr_2, PPh_3, and other impurities, making the prepurification requirement obsolete. Trapping was achieved in a nearly quantitative manner by diluting the organic solvent in the last step (MeCN or EtOH) with water (water/solvent > 7). Water can function as an activator of the carboxylic acid functionality on the Accell CM resin to enable binding with the cationic probe. After trapping of [^{18}F]FBnTP, the Sep-Pak was washed with EtOH to remove all noncationic radioactive and nonradioactive impurities without any notable losses shown in figure 2.9. below.

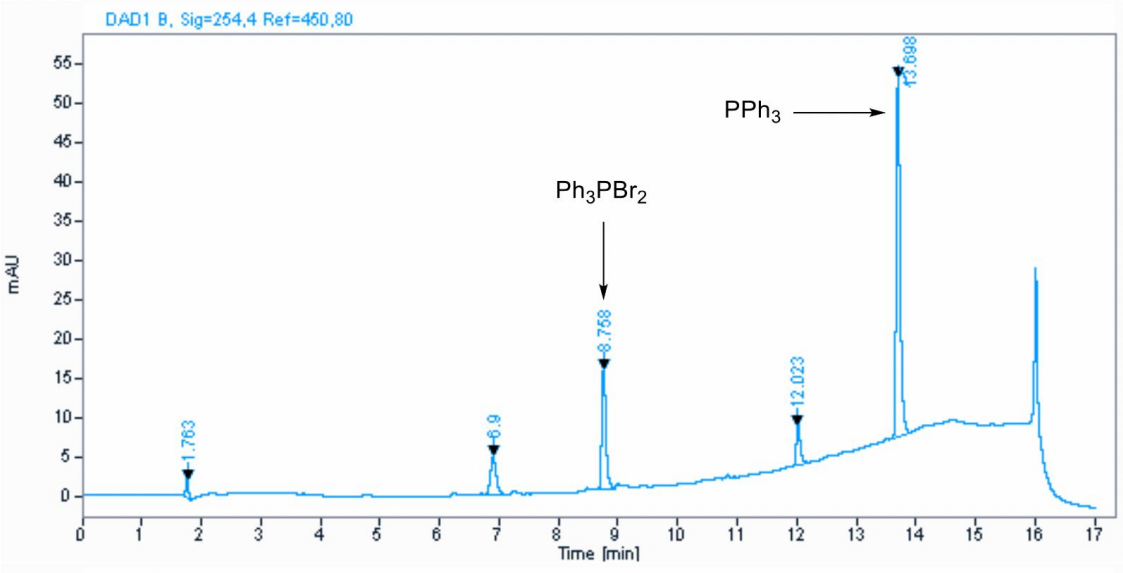

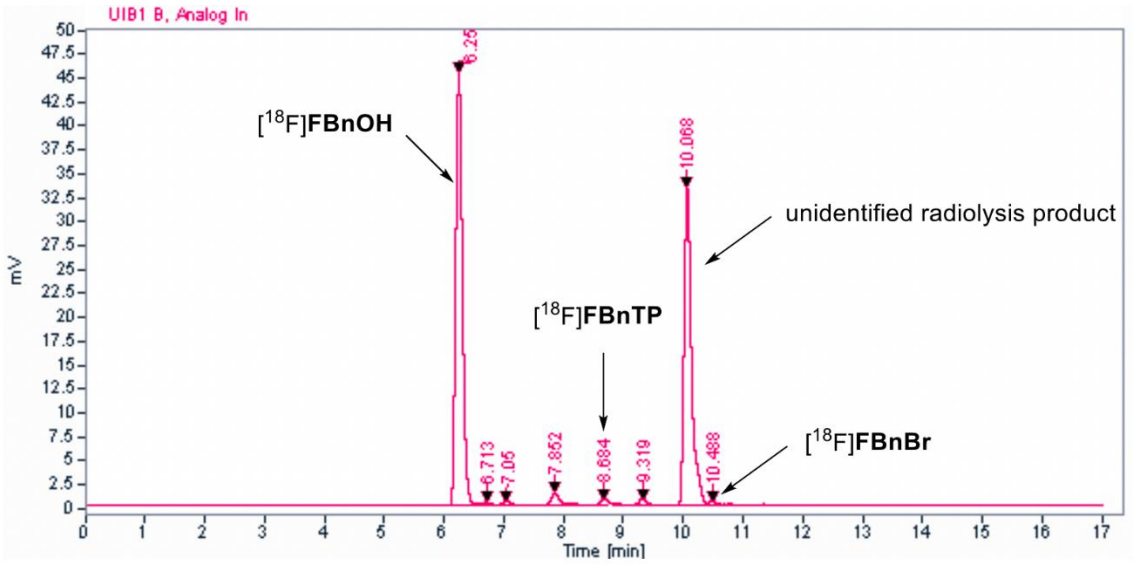

Figure 2. 9. Sample radio-HPLC of waste activity after Accell CM cartridge purification showing negligible losses of product in the waste.

While elution with 0.9 % saline proved inadequate for complete release of [^{18}F]FBnTP, ~ 90 % elution was achieved by increasing the ionic strength of saline with 0.5 % (w/v) Na-ascorbate which also stabilized the final formulation against radiolytic decomposition. The probe was obtained in RCP > 99 % and high chemical purity shown in figure 2.10 below.

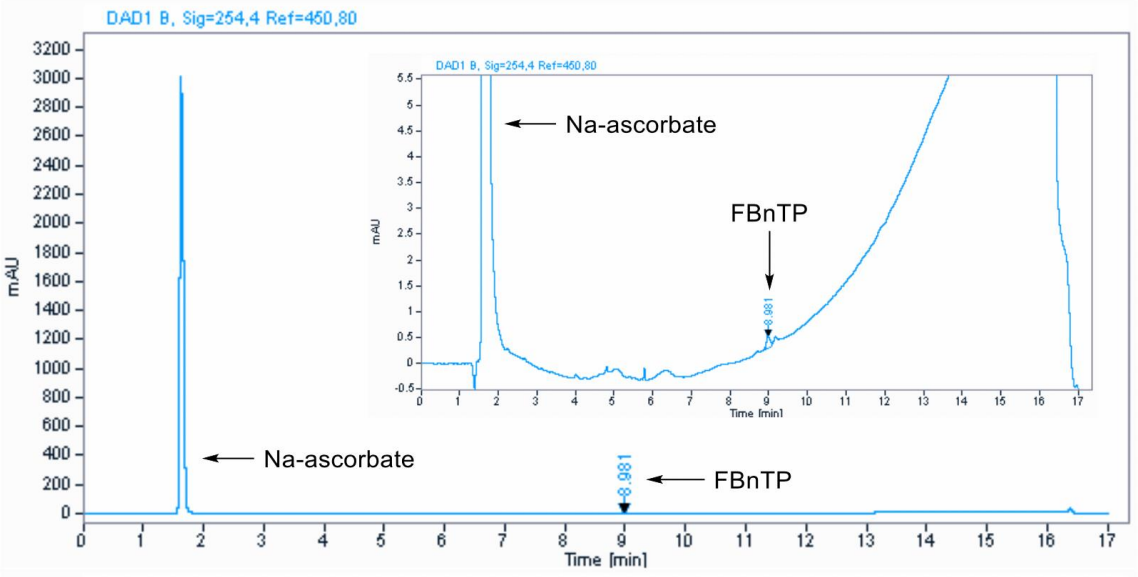

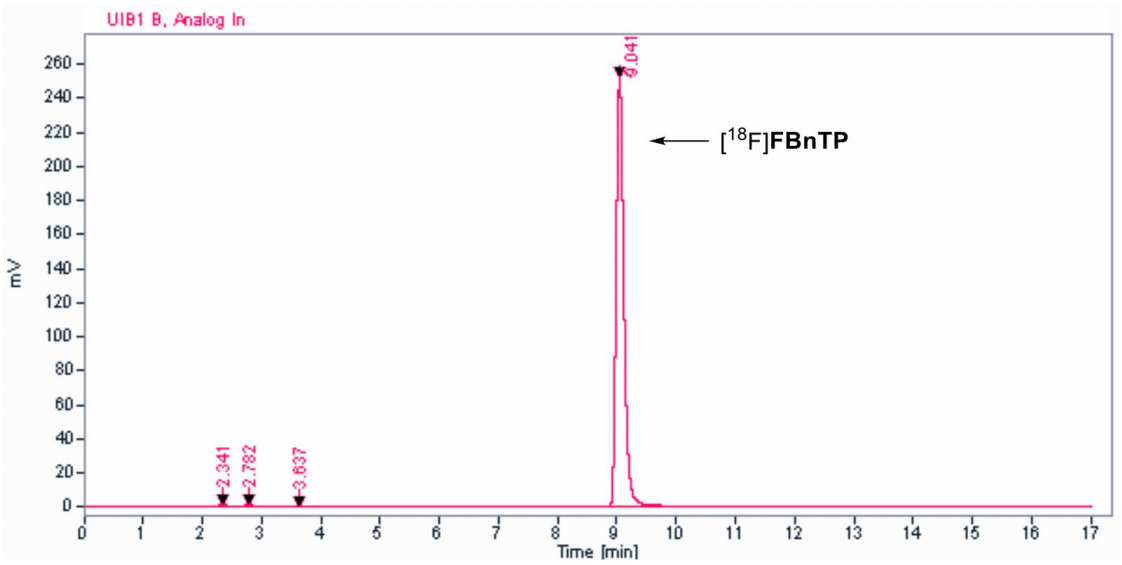

Figure 2. 10. Sample radio-HPLC of [18F]FBnTP formulated in 2% EtOH + 0.5% (w/v) Na-ascorbate. A UV-trace inset with re-scaled Y-axis is shown for better visibility of small signals.

The purification process from the end of the synthetic sequence to the final formulation took less than 4 min. Unfortunately, considerable radiolysis of the probe was observed during Sep-Pak purification when starting with 23.2–33.0 GBq [^{18}F]fluoride. Analysis of the activity that had passed through the Accell CM revealed a radiosignal of an unidentified, nonionic radiolysis product that accounted for up to 87 % of the waste activity and was not observed in low-activity runs. Addition of radical scavengers such as Na- ascorbate, ascorbic acid, and N-tert-butyl-α-phenylnitrone (PBN)[41] or reservatrol-3-β- mono-D-glucoside (polydatin)[45] either prevented trapping of [^{18}F]FBnTP on the Accell CM or did not hinder radiolysis. Trapping efficiencies were low in pure EtOH and water is known to facilitate radiolysis[41]. We therefore considered activation of the Sep-Pak with hydroxide or organic bases prior to purification in the absence of water but the trapping efficiencies remained low. Consequently, RCY of 28.6 ± 5.1 % (n = 3) were observed with starting activities of up to 12.0 GBq, whereas starting activities reaching 33.0 GBq resulted in lower RCY of 16.1 ± 0.4 % (n = 3). Despite the radiolytic decomposition during purification, the highest AY of 3.0 GBq was obtained from 33.0 GBq [^{18}F]fluoride. Considerable higher AY will be

achieved if radiolysis can be prevented in the final step. The probe was used in small animal imaging studies which will be reported elsewhere. Representative maximum intensity projection images of [^{18}F]FBnTP in a wild-type mouse are shown below in figure 2.11.

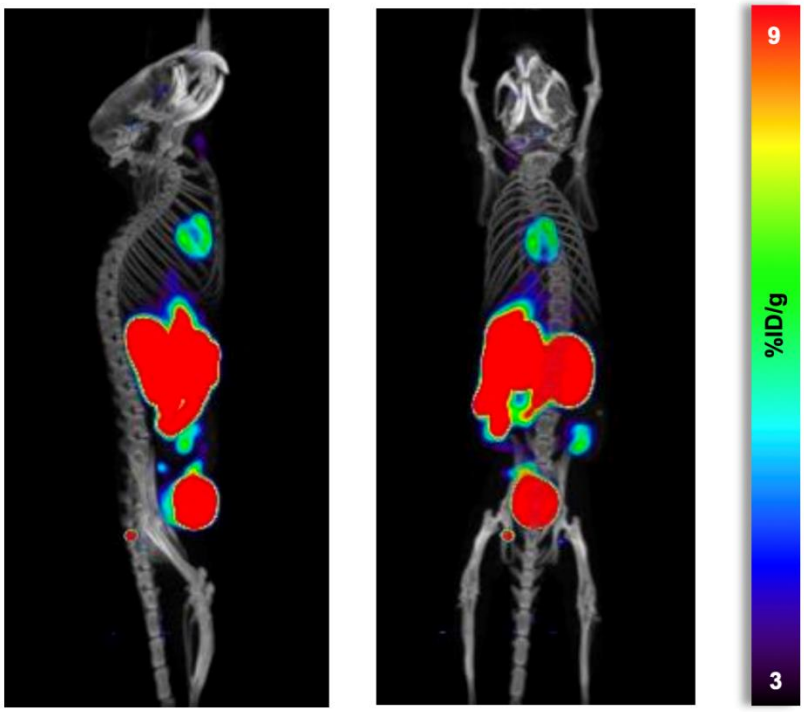

Figure 2. 11. Representative MIP images of [18F]FBnTP in a wild-type mouse at 60 min post-injection

Clinical Quality Control

Formulations of the probe in 2 % (v/v) EtOH in saline + 0.5 % (w/v) Na-ascorbate were subjected to a quality control established at the UCLA Ahmanson Biomedical Cyclotron Facility in accordance with the U.S. Pharmacopeia. RCP at the end of synthesis was > 99 % and remained > 95 % for at least 8 h. Chemical purity was estimated to be high. Doses were clear, colorless, and free of particulate matter with pH ranging from 5.0 to 5.8. Half-life of doses matched that of fluorine-18 (109.8 min) and energy of gamma rays was 511 keV. No kryptofix-222 (K_{222}) levels were observed with the spot test. Since the presence of Na-ascorbate gave false positive results, samples were spotted on a silica plate and developed in a mixture of methanol and 30 %

ammonium hydroxide (9:1) prior to placing the plate in the iodine chamber. Other than the purposely added EtOH, no residual solvents were detected by gas chromatography. Sterile filters were intact after use. Doses contained < 175 endotoxin units (EU) per mL and no growth was observed at days 3, 7, and 14 as required to pass the sterility test.

2.8 Conclusion

A robust synthesis protocol for the production of multiple doses of the potentiometric PET probe [^{18}F]FBnTP was established on the ELYXIS FLEX/CHEM radiosynthesizer. Purification and formulation was achieved in < 4 min with a Sep-Pak Accell CM cartridge. RCY of 28.6 ± 5.1 % (n = 3) were obtained which is a significant improvement to previous reports. Despite our best efforts, radiolysis was not prevented in the final purification step when starting activities exceeded 12.0 GBq [^{18}F]fluoride. Although a possible alternative would be the use of a SCX semipreparative HPLC column and addition of radical scavengers to the mobile phase, this would add additional time and complication. Avoidance of radiolysis with the more elegant Sep-Pak purification can further improve AY in preparing multipatient doses. The reported automated synthesis of clinical grade [^{18}F]FBnTP on a commercially available platform paves the way for the use of the probe in future clinical imaging studies.

Chapter 3: *In Vivo* Imaging of Mitochondrial Membrane Potential in Non-Small Cell Lung Cancer

3.1 Introduction

Mitochondria are essential regulators of cellular energy and metabolism, and have a crucial role in sustaining the growth and survival of cancer cells. A central function of mitochondria is the synthesis of ATP by oxidative phosphorylation, known as mitochondrial bioenergetics. Mitochondria maintain oxidative phosphorylation by creating a membrane potential gradient that is generated by the electron transport chain to drive the synthesis of ATP.[46] Mitochondria are essential for tumor initiation and maintaining tumor cell growth in cell culture and xenografts.[47,48] However, our understanding of oxidative mitochondrial metabolism in cancer is limited because most studies have been performed in vitro in cell culture models. This highlights a need for in vivo studies to better understand how oxidative metabolism supports tumor growth. Here we measure mitochondrial membrane potential in non-small cell lung cancer in vivo using a voltage-sensitive, positron emission tomography (PET) radiotracer known as 4-[18F]fluorobenzyl-triphenylphosphonium (18F-BnTP).[33] By using PET imaging of 18F-BnTP, we profile mitochondrial membrane potential in autochthonous mouse models of lung cancer, and find distinct functional mitochondrial heterogeneity within subtypes of lung tumors. The use of 18F-BnTP PET imaging enabled us to functionally profile mitochondrial membrane potential in live tumors.

3.2 Methods and Materials

Cell Culture

Cells were maintained at 37 °C in a humidified incubator with 5% CO2. A549 cells were obtained from ATCC. The RH2 lung cancer cell line was previously established in our laboratories. All cell lines were routinely tested and confirmed to be free of mycoplasma using the LookOut

Mycoplasma PCR Detection Kit (Sigma). Cells were grown in DMEM plus 5% fetal bovine serum (FBS; Hyclone/Gemini) and 1% penicillin/ streptomycin (Gibco).

Studies in genetically engineered mouse models

We performed studies with the genetically engineered mouse model of lung cancer, in which KrasLSL-G12D mice (which carry a loxP-Stop-loxP sequence followed by the KrasG12D point mutation allele) were crossed with Lkb1-deficient (Lkb1lox/lox) and R26-LuciferaseLSL (which carry a loxP-Stop-loxP sequence followed by luciferase at the Rosa26 locus) mice, to generate KrasG12D;Lkb1−/−;R26LSL-Luc (KL) mice, as previously described.[49] In brief, lung tumors were induced by intranasal administration of 5 × 105 transduction units of Lenti-PGK-Cre (FCT071, Kerafast) and developed nearly 100% lung adenocarcinomas, as previously described.[49,50] KL mice that inhaled Lenti-PGK-Cre were used in studies with phenformin treatment. For studies in which mice were imaged with both 18F-BnTP and 18F-FDG probes, KL mice inhaled Cre-expressing adenovirus (Adeno-Cre), which leads to development of both ADC and SCC tumors. For all treatments, KL mice were imaged with 18F-BnTP and sorted into two groups based on the tumor maximum percentage injected dose per gram (%ID/g) values. Then, the values were normalized to the maximum %ID/g uptake of the heart, so that two groups would have similar matched maximum %ID/g values, as described in ‘PET–CT imaging studies’. Treatment was initiated on the same day or the next day after 18F-BnTP imaging. Mice were treated with 125 mg kg−1 day−1 phenformin for 5 days or 15 mg kg−1 day−1 IACS-010759 for 12 days. The drugs were delivered by oral gavage. All experimental procedures that were performed on mice were approved by the UCLA Animal Research Committee (ARC). Mice were euthanized before the ARC-approved end points were reached; none of the tumors exceeded maximum ARC-defined volumes. Both male and female mice were used in all experiments and no preference in mouse gender was given for any of the studies.

Studies in syngeneic mice

We established the L3161C mouse cell line from a lung tumor dissected from a KrasG12D;p53−/−;Lkb1−/− (KPL) mouse. After resection, the tumor was minced and incubated in collagenase/dispase (10269638001, Sigma) for 3 h. Cells were filtered using a 70-μm strainer, centrifuged, resuspended in DMEM with 5% FBS and plated in a 6-cm dish. The next day, medium was changed and cells that attached were cultured. We confirmed that the L3161C cell line was ADC by implanting cells into syngeneic mice, detecting lung tumors and staining with H&E and CK5 and TTF1. For some experiments, L3161C cells expressed pBabe or pBabe-NDI (from Addgene plasmid 72876,) as previously described.[51] For imaging studies, 1 × 105 L3161C cells suspended in 20 μL PBS were implanted into the left lung lobe via transthoracic injection. Two weeks after injection, mice were imaged by computed tomography. Mice with similar sized tumors were used for 18F-BnTP imaging. For treatment studies, syngeneic mice were imaged with 18F-BnTP, and split into two groups (three groups for Fig. 3.3b) based on tumor maximum %ID/g, such that maximum %ID/g values of tumors in both groups would be similar, as described in 'PET–CT imaging studies'. Treatment was then initiated for the specified time. Mice were treated with a single dose of 0.25 mg kg−1 oligomycin or 0.5 mg kg−1 rotenone; both drugs were delivered by intraperitoneal injection. For other studies, mice were treated with 125 mg kg−1 day−1 phenformin or 500 mg kg−1 day−1 metformin for 5 days; both drugs were delivered by oral gavage

[^{18}F]FBnTP synthesis

The radiotracer 18F-BnTP was synthesized as previously described.[52] The three-pot, four-step synthesis of 18F-BnTP was performed using the automated radiochemical synthesizer ELIXYS FLEX/CHEM (Sofie Biosciences). The no-carrier-added [18F]fluoride was produced from the (p, n) reaction of [18O]H2O with an RDS-112 11 MeV cyclotron (Siemens) in a 1-mL tantalum target with Havar foil. [18F]Fluoride in water was pushed through a strong cation-exchange (SCX) cartridge and trapped on a QMA cartridge. [18F]Fluoride was then eluted with a solution of Kryptofix 222 (10 mg, 27 μmol) and K2CO3 (1 mg, 7 μmol) in an acetonitrile:water (3:5, 0.8 mL)

mixture. Azeotropic evaporation was performed at 110 °C under a stream of nitrogen (7 p.s.i.) to remove excess water using acetonitrile. The 4-trimethylammoniumbenzaldehyde trifluoromethansulfonate (5 mg) precursor was solvated in DMSO (0.8 mL), added to the reactor vial containing the dried [18F]fluoride and allowed to react at 90 °C for 5 min with stirring. The resulting 4-[18F]fluorobenzaldehyde (18F-FBA) mixture was diluted with water containing 1% (w/v) Na-ascorbate solution (5 mL total) and passed through an Oasis WCX cartridge (41 kPa) for 1.5 min. The WCX cartridge was dried with nitrogen (138 kPa) for 1 min and eluted with DCM (3 mL). The mixture was passed through a glass column containing NaBH4·(Al2O3)x (350 mg) on the top half portion and K2CO3 (2 g) on the bottom half portion for a flow-through reduction of 18F-FBA to 4-[18F]fluorobenzyl alcohol (18F-FBnOH), which was directed to the second reactor vial (21 kPa). A subsequent elution and rinsing of the column was performed using DCM (1 mL, containing 0.2% (v/v) of water; 21 kPa). The mixture containing 18F-FBnOH was reacted with Ph3PBr2 (100 mg) in DCM (1.1 mL) at 35 °C for 10 min resulting in the formation of 4-[18F] fluorobenzyl bromide (18F-FBnBr). The resulting mixture was passed through a silica cartridge and directed towards the third reactor vial (14 kPa). A solution of PPh3 (3 mg) in ethanol (0.6 mL) was added, followed by removal of most of the DCM under vacuum and a stream of nitrogen (21 kPa) at 45 °C for 6.5 min while stirring. Ethanol (1 mL) was added and the mixture was evaporated to approximately 0.5 mL under vacuum and a stream of nitrogen (48 kPa) at 80 °C for 2.5 min while stirring. The mixture was reacted at 160 °C for 5 min in a sealed position, which converted the 18F-FBnBr to the desired 18F-FBnTP. The reaction vial was cooled to 35 °C and diluted with water (3 mL) while stirring. The mixture was passed through a Sep-Pak Plus Accell CM cartridge (55 kPa) and the cartridge was washed with ethanol (20 mL). The product was released with 2% ethanol in saline plus 0.5% (w/v) Na-ascorbate (10 mL) and passed through a sterile filter into a vented sterile vial. Under optimized conditions, the resulting 18F-FBnTP PET tracer was obtained in AY of 1.4–2.2 GBq starting from 9.4 to 12.0 GBq [18F]fluoride in 90–92 min (radiochemical

yield = 28.6 ± 5.1% with n = 3). Molar activities ranged from 80 to 99 GBq μmol−1 (end of synthesis) and radiochemical purity was >99%.

PET-CT imaging studies

All PET–CT imaging was performed on KL mice or syngeneic mice transthoracically implanted with L3161C using either single tracer imaging with 18F-BnTP or dual radiotracer imaging with 18F-BnTP and 18F-FDG, as previously described[49,53]. To reduce variability between mice imaged with 18F-BnTP, the maximum %ID/g for each tumor was normalized to maximum %ID/g of heart, as indicated in the figures. For waterfall plots in Figs. 3.2g, 3.3b, d, e and Extended Data Fig. 2.4c, d, we calculated the percentage change in the uptake of the 18F-BnTP probe after treatment relative to before treatment, using maximum %ID/g of the tumor that was normalized to maximum %ID/g of the heart for each mouse.

Respirometry analysis

Experiments were conducted on a Seahorse XF96 Extracellular Flux Analyzer (Agilent Technologies) to measure oxygen consumption rate (OCR) and extracellular acidification rate. L3161C, A549 or RH2 cells were seeded into an XF96 microplate at density of 12,000–15,000 cells per well. Cells were plated in growth medium and maintained overnight in a tissue culture incubator (37 °C, 5% CO2). On the day of the experiment, assay medium (Seahorse XF Base Medium supplemented with 2 mM l-glutamine, 1 mM pyruvate and 10 mM glucose) was freshly prepared. The cells were washed twice with assay medium and brought to a final volume of 175 μl per well. The XF96 plate was placed in a 37 °C incubator without CO2 for 30 min before loading the plate into the instrument. Injection of compounds during the assay included: the mitochondrial ATP synthase inhibitor oligomycin (final concentration 2 μM); the chemical uncoupler FCCP (final concentration 1 μM); and the complex I inhibitors rotenone (final concentration 2 μM) and phenformin (final concentration 1 mM); and the complex III inhibitor antimycin A (final concentration 2 μM). At the conclusion of the assay, the cells were fixed with 4%

paraformaldehyde, stained with Hoechst, and cell number per well was determine based on nuclei number using an Operetta High-Content Imaging System (PerkinElmer). OCRs were normalized to cell number per well. Activity of complex I was measured in permeabilized cells using XF PMP assay where complex I dependent OCR was measured by determining OCR in the presence of pyruvate and malate (as substrates for complex I) before and after addition of rotenone (complex I inhibitor).

Measurement of mitochondrial ΔΨ

Experiments were conducted by analysing TMRE fluorescence using flow cytometry. A549 and L3161C cells were collected on the day of the assay and 500,000 cells were aliquoted into a microcentrifuge tube. Cells were resuspended in 0.5 ml DMEM and 5% FBS with different concentrations of phenformin, oligomycin or FCCP as indicated. Cells were incubated in a tissue culture incubator (37 °C, 5% CO2) for 2 h. After 2 h incubation, medium with TMRE was added to tubes, such that final concentration of TMRE was 7 nM and concentrations of phenformin, oligomycin and FCCP were constant. Cells were incubated for an additional 1 h in a tissue culture incubator (37 °C, 5% CO2). Cells were washed twice in phenol-red-free DMEM and cellular fluorescence was acquired with a BD LSRII analyser at UCLA Flow Cytometry Core. Data were analysed with Flowing Software.

In vitro [^{18}F]FBnTP uptake assay

On the day of the assay, cells were trypsinized, collected in DMEM plus 5% FBS and counted. Then, 1,000,000 cells were aliquoted into a microcentrifuge tube, resuspended in 0.5 ml medium containing DMEM and 5% FBS plus vehicle, 1 mM phenformin, 8 μM oligomycin or 8 μM oligomycin with 4 μM FCCP. Cells were incubated in a tissue culture incubator (37 °C, 5% CO2) for 2 h. After 2 h incubation, 0.5 ml of media with 18F-BnTP was added to tubes, such that final concentration of 18F-BnTP was 10 μCi ml−1 and concentrations of phenformin, oligomycin and FCCP were constant. Cells were incubated for a further 1 h in a tissue culture incubator (37 °C,

5% CO2). The uptake was terminated by centrifugation at 4 °C (134g, 5 min). Cells were washed twice with cold media. After the final wash, cell pellet was resuspended in 500 µL of media, and 300 µL was used in a gamma counter, while 100 µL was used to count viable cells using ViCell counter (Beckman). Counts per minute were normalized to viable cells.

Immunohistochemistry

After the fixation step in 10% neutral buffered formalin overnight, lungs were transferred to 70% ethanol and further processing and embedding was done by the Translational Pathology Core Laboratory at UCLA. The following antibodies were used: anti-CK5 (EP1601Y) (Abcam, ab52635 1:100), anti-TTF1 (8G7G3/1) (DAKO, 1:1,000), anti-Ki67 (SP6) (ThermoScientific, RM-9106-S1, 1:200), anti-GLUT1 (Alpha Diagnostic, GT11-A, 1:400), anti-cleaved caspase 3 (CST, 9664, 1:1,000). Slides were scanned onto a ScanScope AT (Aperio Technologies). Digital slides were analysed with Definiens and QuPath software.

Western blot analysis

Whole-cell lysates from lung tumors isolated from mice were prepared as previously described.[50] In brief, tumors were homogenized in buffer containing phosphatase and protease inhibitors (20 mM Tris pH 7.5, 150 mM NaCl, 1% Triton X-100, 50 mM sodium fluoride, 1 mM EDTA, 1 mM EGTA, 2.5 mM pyrophosphate, 1 mM sodium orthovanadate, protease inhibitor tablet), centrifuged and the supernatant was normalized, aliquoted and stored in −80 °C freezer. Lysates were separated on 4–12% Bis-Tris protein gels (Thermo), transferred to PVDF membrane and probed with the following antibodies: SP-C (1:5,000, AB3786 Milipore); GLUT1 (1:2,000, GT11-A, Alpha Diagnostic); NDUFS1 (1:2,000, ab169540, Abcam); NDUFS1 (1:2,000, sc-271510, Santa Cruz); NDUSV1 (1:500, sc-100566, Santa Cruz), NDUFV2 (1:2,000, sc-271620, Santa Cruz), TOM20 (1:10,000, FL-145, Santa Cruz), TOM40 (1:2,000, 18409-1-AP, Proteintech); TOM70 (1:2,000, 14528-1-AP, Proteintech); TIM23 (1:2,000, 11123-1-AP, Proteintech); actin

(1:8,000, 4970 and 3700, Cell Signaling Technology). Intensity of bands was quantified using Image 3.J.

Blue native gel

Blue native (BN)–PAGE was performed as previously described[54] with minor modifications. In brief, mitochondria (100 µg protein) were solubilized for 15 min with digitonin using a 6 g:1 g digitonin:protein ratio. Insoluble material was removed by centrifugation at 21,000g for 30 min at 4 °C, the soluble component was combined with BN– PAGE loading dye and separated on a 3–13% acrylamide–bisacrylamide precast BN–PAGE gel. For separation, cathode buffer (15 mM Bis-Tris, pH 7.0, and 50 mM tricine) containing 0.02% (w/v) Coomassie blue G was used until the dye front had reached approximately one-third of the way through the gel before exchange with cathode buffer lacking Coomassie blue G. Anode buffer contained 50 mM Bis-Tris (pH 7.0). Native complexes were separated at 4 °C at 110 V for 1 h, followed by 12 mA constant current. Thyroglobulin (669 kDa), ferritin (440 kDa), catalase (232 kDa), lactate dehydrogenase (140 kDa), and bovine serum albumin (BSA 67 kDa) were used as markers (GE Healthcare).

Liquid chromatography-mass spectrometry

Tumors were homogenized with a Tissue Master (Omni international) in 1 ml chilled 80% methanol. Tumor suspensions were spun down at 4 °C for 5 min at 17,000g, and the top layer taken as extracted metabolites. The volume equivalent of 1 mg of tumor was transferred into glass vials and the samples were dried with a EZ2-Elite lyophilizer (Genevac). Dried metabolites were resuspended in 100 µL of 50%:50% acetonitrile:dH2O solution; 10 µL of these suspensions were injected per analysis. Samples were run on a Vanquish (Thermo Scientific) UHPLC system with mobile phase A (5 mM ammonium acetate, pH 9.9) and mobile phase B (acetonitrile). Separation was achieved at a 200 µL min−1 flow rate on a Luna 3mm NH2 100A (150 × 2.0 mm) at 40 °C with a gradient going from 15% A to 95% A in 18 min followed by an 11 min isocratic step. The UHPLC was coupled to a Q-Exactive (Thermo Scientific) mass analyser running in positive mode

at 3.5 kV with an MS1 resolution of 70,000. Metabolites were identified using exact mass (MS1), retention time, and fragmentation patterns (MS2) at normalized collision energy 35. Quantification was performed via area under the curve (AUC) integration of MS1 ion chromatograms with the MZmine 2 software package. For the quantification of absolute moles of phenformin, one tumor from the vehicle group was selected to provide a representative tumor small molecular matrix. The volume equivalent of 1 mg of this tumor was distributed into several glass vials and 10 µL of pure aqueous phenformin standards (0.1–0.5 mM) was added to these samples to span the possible range of phenformin concentrations. From this point on, samples were treated as described above. AUC values from the phenformin standards were used to fit a linear regression model that related MS1 AUC to the moles of phenformin present. The linear regression equation was used to convert MS1 AUC to moles of phenformin in all tumor samples and expressed relative to the tissue mass of each tumor.

Statistical analysis

The in vivo experiments were analysed using analysis of variance (ANOVA) models to evaluate the main effects of the two treatment types on the various quantitative outcome measures. Categorical outcomes were compared between groups with Fisher's exact test. The sample size of 7–10 KL mice per group provided a 99% power to detect differences in the outcomes of percentage CC3, Ki67 and 18F-BnTP %ID/g positivity, based on the observed results previously described[50], assuming a two-sample t-test (a simplification of the ANOVA analysis plan) with a two-sided 0.05 significance level. Mouse experiments involving imaging of KL mice with 18F-BnTP were repeated with three separate cohorts several months apart. For imaging studies with both genetically engineered mouse models and syngeneic mice, after basal 18F-BnTP imaging, mice were split into two groups (three cohorts for Fig. 3b) based on maximum %ID/g values, such that maximum %ID/g values of tumors in both groups would be similar after normalization to the maximum probe uptake in the heart. Variation is indicated using standard deviation or standard

error of the mean as described. Differences between groups were determined using unpaired two-tailed t-test or one-way ANOVA if more than two groups were compared. Western blot analysis of mitochondrial markers was completed on lung nodules isolated from three separate cohorts of mice. Investigators were not blinded to the allocations for treatment groups. This is because allocations to the groups were done on the basis of the maximum uptake of the 18F-BnTP probe, which was calculated using AMIDE computer software. Maximum uptake values were based on the percentage injected doses of the 18F-BnTP probe, which were calculated independently of the investigators. Regions of interest were defined for tumor and heart by investigators, and were used to calculate the maximal uptake value. Regions of interest were independently reviewed by two authors and verified in a blinded manner. For the histological analysis, quantification of the Ki67 and CC3 staining was done using automated morphometric Definiens software that defines positive and negative staining regions using established algorithms before analysis. Histological analysis was verified in a blinded review.

3.3 Results and Discussion

Mitochondria are required for lung tumorigenesis as was shown in a KrasG12D-driven genetically engineered mouse model of lung cancer.[55] We therefore used KrasG12D mutant, Lkb1 (also known as Stk11)-deficient (KrasG12D;Lkb1−/−; hereafter referred to as KL) genetically engineered mouse models to perform 18F-BnTP PET imaging on lung tumors in vivo.[50,56] 18F-BnTP is a positively charged lipophilic cation that localizes to the negatively charged mitochondrial inner membrane in a voltage-dependent manner.[57,58] 18F-BnTP has been studied in rodent and canine myocardium to detect myocardial infarction[33,59] and in tumor xenografts as a surrogate marker of apoptosis after chemotherapy treatment.[30] Although mass spectroscopy-based approaches have been used to study mitochondrial membrane potential ($\Delta\Psi$)[60], to our knowledge, no study has used 18F-BnTP PET to measure mitochondrial $\Delta\Psi$ using autochthonous mouse models of lung cancer. We first synthesized 18F-BnTP as previously described[52] and performed

PET imaging on lung tumors in KL mice ten weeks after tumor induction. We identified both 18F-BnTP-positive lung tumors and heart (Fig. 3.1a).

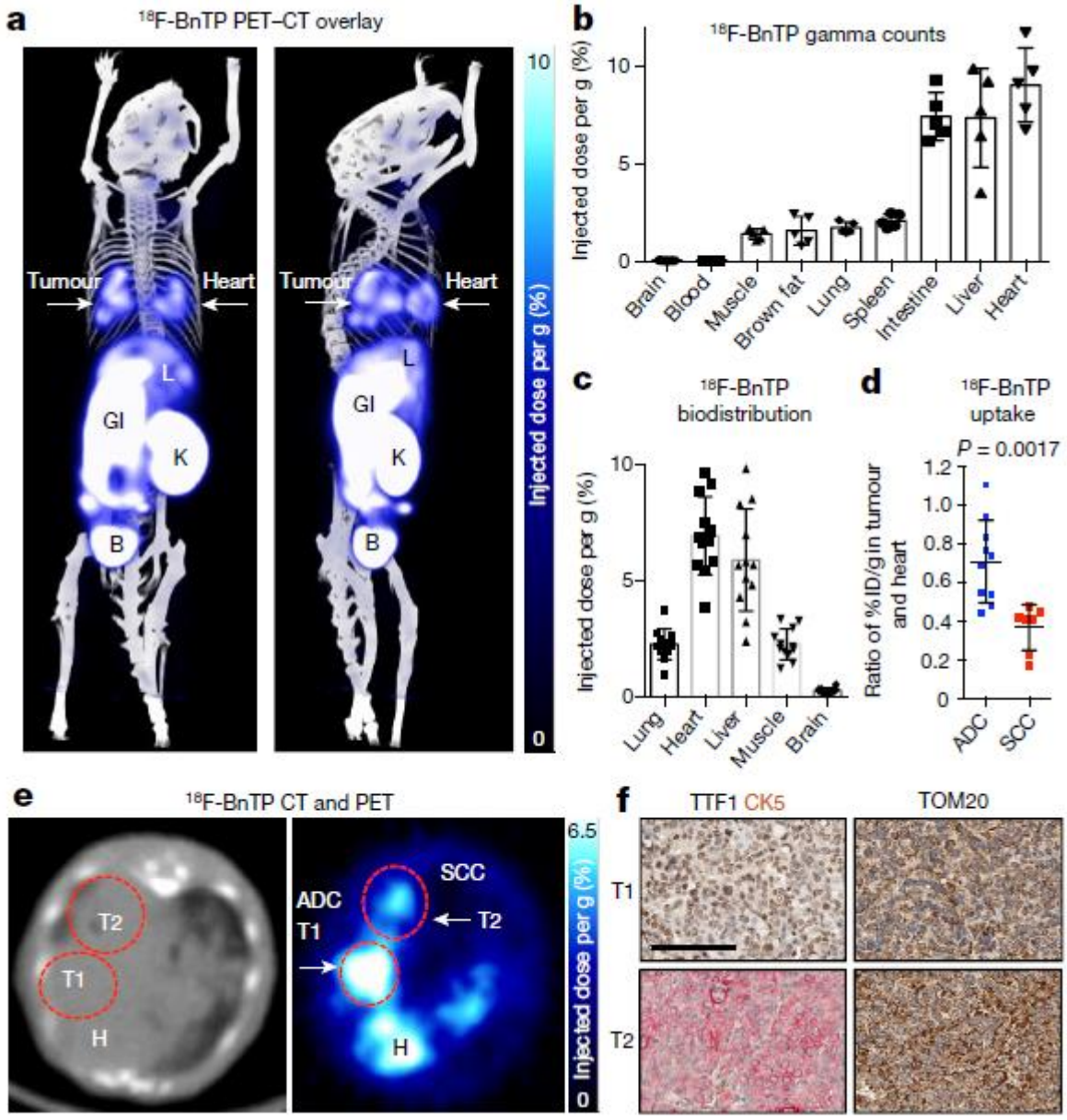

Figure 3. 1. PET imaging of 18F-BnTP and biodistribution analysis of KL lung tumors identified differential uptake between lung ADC and SCC.

a, Overlay of PET and computed tomography (PET–CT) scanning of a *KL* mouse with lung tumors, imaged with 18F-BnTP. Right panel is rotated 90° compared to the left. Heart and tumor are indicated. B, bladder; GI, gastrointestinal tract; K, kidney; L, liver. **b**, Biodistribution of 18F-BnTP probe in tissue from wildtype FVB strain[49] mice measured by gamma counter ex vivo after 1 h uptake (*n* = 5 mice). **c**, Biodistribution of the 18F-BnTP probe in normal tissue of *KL* mice measured by the maximum percentage injected dose per gram after 1 h uptake (*n* = 12 mice). **d**, 18F-BnTP uptake in lung ADC and SCC from *KL* mice, measured as the ratio of the maximum

percentage injected dose per gram (%ID/g) in tumors and heart (*n* = 5 mice, *n* = 10 ADC tumors, *n* = 7 SCC tumors). **e**, Representative transverse image of the heart (H) and lungs of a *KL* mouse imaged by computed tomography (CT; left) and 18F-BnTP PET (right). T1, ADC; T2, SCC. **f**, Immunohistochemistry staining of T1 and T2 tumors from **e**. Scale bar, 100 μm. Data are mean ±} s.d. *P* value determined by unpaired two-tailed *t*-test. Experiments in **b** and **c** were performed once. Data in **a**, **d**–**f** are representative of experiments repeated three times, with similar results.

We performed biodistribution analysis of tissues by measuring either gamma counts or the percentage of injected dose per gram, and confirmed high uptake of the tracer in the heart, liver and intestine as well as low uptake in normal lung, skeletal muscle and brain (Fig. 3.1b, c). Analysis of 18F-BnTP PET imaging in KL mice identified two distinct populations of lung tumors distinguished by either high or low uptake of 18F-BnTP (Fig. 3.1d, e). Notably, we confirmed that tumors with high 18F-BnTP avidity segregated with lung adenocarcinoma (ADC), whereas tumors from lung squamous cell carcinoma (SCC) had uniformly lower avidity for 18F-BnTP (Fig. 3.1d). We confirmed lung tumor histology by staining tumors for cytokeratin 5 (CK5) to mark SCC, and thyroid transcription factor 1 (TTF1) or surfactant protein C (SP-C) to identify ADC (Fig. 3.1f, Extended Data Fig. 2.1). We suspected low mitochondrial content in lung SCC may have explained the reduced mitochondrial ΔΨ and 18F-BnTP uptake. Therefore, we stained tumors for the pan-mitochondrial marker TOM20 and confirmed similar staining intensities for both lung ADC and SCC (Fig. 1f). We performed additional analysis of the mitochondrial membrane proteins TOM20, TOM40, TOM70 and TIM23 in lung ADC and SCC from KL mice and showed that ADC (SP-C:actin ratio > 0.5) had no discernible difference in expression of these proteins compared to SCC (SP-C:actin ratio < 0.5) (Extended Data Fig. 2.1). These results demonstrate that both tumor subtypes have similar mitochondrial content but a twofold difference in 18F-BnTP affinity (Fig. 3.1d). We next sought to validate 18F-BnTP as a voltage-sensitive marker of both ΔΨ and oxidative phosphorylation (OXPHOS) by treating cells with the mitochondrial complex I inhibitor phenformin, which dissipates ΔΨ and inhibits OXPHOS[61] (Fig. 3.2a). Short-term treatment with phenformin of the human lung ADC cell line A549 or the mouse lung ADC line L3161C (derived from a *KrasG12D;p53−/−;Lkb1−/−* (*KPL*) mouse; *p53* is also known as *Trp53*) significantly

reduced ΔΨ in a dose-dependent manner but did not affect cell viability (Extended Data Fig. 2.2a–e). Similarly, acute treatment of A549 cells with phenformin significantly reduced the uptake of 18F-BnTP, similar to results with TMRE staining (Extended Data Fig. 2.2f). Phenformin also resulted in a marked reduction in cellular OXPHOS in both A549 and L3161C cells, as measured by respirometry (Extended Data Fig. 2.2g, h). Furthermore, we treated L3161C cells with oligomycin, a complex V ATPase inhibitor, which induces increased ΔΨ. We detected a significant increase in TMRE and 18F-BnTP uptake after treatment with oligomycin, and ΔΨ was significantly reduced after the addition of the mitochondrial uncoupler FCCP (Extended Data Fig. 2.2i, j), consistent with the response to the MitoClick probe.[60] Oligomycin with or without FCCP did not significantly affect cell viability (Extended Data Fig. 2.2k). We next measured uptake of 18F-BnTP in lung tumors from KL mice before and after treatment with phenformin or vehicle (saline) (Fig. 3.2b). Representative PET images show reduced uptake of 18F-BnTP in lung tumors treated with phenformin (Fig. 3.2c). Treatment groups showed no significant difference in 18F-BnTP uptake values before the start of the treatment (Fig. 3.2d), but showed a significant reduction in 18F-BnTP uptake in the mice that received phenformin (Fig. 3.2e). Three independent experiments performed in KL mice demonstrated a significant reduction in 18F-BnTP uptake in lung tumors after treatment with phenformin compared with vehicle (Fig. 3.2f). We further quantified the percentage change in 18F-BnTP uptake after treatment and showed that phenformin induced a significant drop in tracer uptake compared with mice treated with vehicle (Fig. 3.2g). Lung ADCs from KL mice are sensitive to phenformin[50], and it was therefore possible that the reduced 18F-BnTP uptake was due to phenformin-induced cell death. Staining of cleaved caspase 3 (CC3) and Ki67 showed no evidence of phenformin-induced apoptosis or reduced cell viability (Appendix Extended Data Fig. 2.3a–d), consistent with previously published studies that showed that a longer duration of phenformin treatment induced cellular apoptosis.[50,62] Mass spectrometry analysis of KL lung tumors treated with phenformin showed a significant increase in intra-tumoral phenformin compared with tumors treated with vehicle (Extended Data Fig. 2.3e). Collectively,

results in Fig. 3.2 demonstrate that 18FBnTP is a voltage-sensitive probe that detected changes in mitochondrial ΔΨ and OXPHOS in vitro and in vivo in lung tumor cells. We then investigated whether 18F-BnTP could selectively measure changes in mitochondrial ΔΨ and OXPHOS in vivo after treatment with a broader panel of inhibitors of the electron transport chain. The complex I inhibitors included metformin, phenformin and rotenone, which all reduce ΔΨ and suppress OXPHOS[50,61,63] as well as the complex V inhibitor oligomycin, which induces an increase in ΔΨ. We used an orthotopic mouse model in which we transthoracically implanted L3161C lung tumor cells into the left lobe of syngeneic recipient mice (Fig. 3.3a) to profile mitochondrial ΔΨ in lung tumors. Notably, this enabled us to spatially localize a single lung tumor in the left lobe of the mouse and perform PET imaging of 18F-BnTP in mouse lung ADC tumors (Extended Data Fig. 2.3f–h). We measured 18F-BnTP uptake in these orthotopically implanted mice after acute treatment for 4 h with either oligomycin or rotenone(Fig. 3.3a).[64] We used a safely tolerated dose of rotenone (0.5 mg kg−1) or oligomycin (0.25 mg kg−1) below the toxic dose range.[65] Uptake of 18F-BnTP in lung tumors was significantly increased after the delivery of oligomycin, whereas rotenone treatment significantly reduced 18F-BnTP uptake (Fig. 3.3b). Our results demonstrate that 18F-BnTP PET detected acute changes in mitochondrial ΔΨ in lung tumors after inhibition of respiratory complexes I or V. At a cellular level, metformin, like phenformin, inhibits mitochondrial complex I, resulting in reduced OXPHOS[66–68], and is broadly used worldwide to clinically manage type 2 diabetes.[69] We therefore sought to determine whether PET imaging of 18F-BnTP could measure direct changes in the ΔΨ and complex I activity of lung tumors in vivo after systemic treatment of mice with metformin (Fig. 3.3c). Our results show that uptake of 18F-BnTP in lung tumors was significantly reduced in the mice that received metformin compared with the vehicle-treated mice (Fig. 3.3d). As expected, metformin resulted in less inhibition of 18F-BnTP uptake than its more potent analogue phenformin (Fig. 3.3d, e). Similar to phenformin, metformin did not induce apoptosis and cell death or alter tumor growth, as measured by CC3 or Ki67 staining,

respectively (Extended Data Fig. 2.3j). These results confirm that 18F-BnTP imaging can accurately detect a loss of ΔΨ after delivery of metformin.

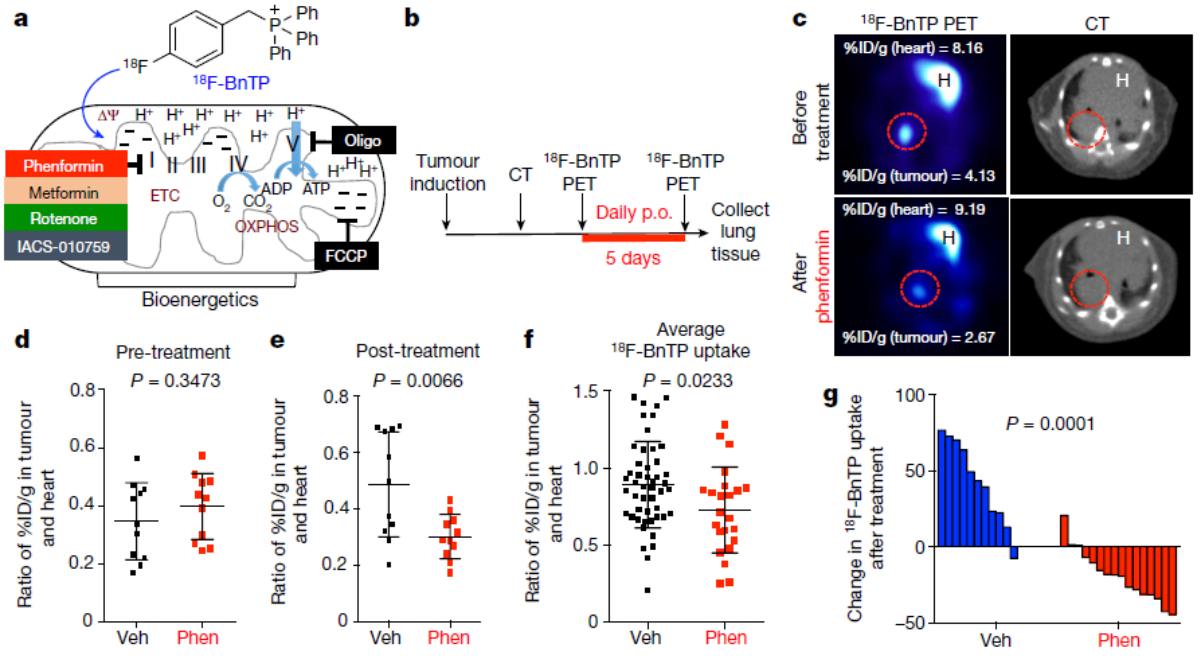

Figure 3. 2. Treatment of KL mice with the complex I inhibitor phenformin suppresses 18F-BnTP uptake in lung tumors.

a, Schematic drawing representing voltage-dependent uptake of 18F-BnTP into the mitochondria. Bioenergetics driven by the electron transport chain (ETC) and OXPHOS are shown. **b**, Schematic drawing of imaging and treatment regiments for *KL* mice treated with 125 mg kg−1 day−1 phenformin. p.o., per os (orally). **c**, Representative images from a *KL* mouse before (top) and after (bottom) treatment for 5 days with 125 mg kg−1 day−1 phenformin. Values for maximum percentage injected dose for the heart and tumor are indicated. **d**, Quantification of maximum percentage injected dose for tumors in vehicle (Veh) and phenformin (Phen) groups before treatment. Each dot represents an individual tumor (*n* = 11 tumors for vehicle and phenformin groups). **e**, Quantification of maximum 18F-BnTP uptake in tumors after treatment with 125 mg kg−1 day−1 phenformin or vehicle for 5 days. Each dot represents an individual tumor (*n* = 11 tumors for vehicle and phenformin groups). **f**, Average 18F-BnTP uptake in *KL* mice after 5 days of treatment with vehicle (*n* = 48 tumors; 10 mice) or phenformin (*n* = 23 tumors; 10 mice). Each dot represents an individual tumor. **g**, Waterfall plot of the percentage change in probe uptake after treatment of mice with vehicle or phenformin for 5 days. Each bar represents an individual tumor. Data are mean ±} s.d. *P* values determined by unpaired two-tailed *t*-test. Data in **d**–**f** are from two separate mouse experiments. Data in **g** are from three individual mouse experiments.

We next tested whether expression of the Saccharomyces cerevisiae NADH dehydrogenase (ND1), which oxidizes NADH in a similar manner to mammalian mitochondrial complex I, would render lung tumor cells insensitive to biguanides and prevent the loss of 18F-BnTP uptake after

inhibition of complex I.[51,68] Expression of ND1 in L3161C lung tumor cells (L3161C-ND1) conferred resistance to phenformin as L3161C-ND1 cells maintained higher OXPHOS after phenformin treatment than cells expressing the vector alone (Extended Data Fig. 2.4a, b). 18F-BnTP PET imaging demonstrated that L3161C-ND1 tumors were resistant to phenformin and showed no loss of 18F-BnTP uptake compared to vector-expressing L3161C tumors (Extended Data Fig. 2.4c), whereas vehicle-treated L3161C-ND1 and vector tumors were both positive for 18F-BnTP uptake (Extended Data Fig. 2.4d). Our results demonstrate that 18F-BnTP imaging is sensitive to functional changes in complex I activity.

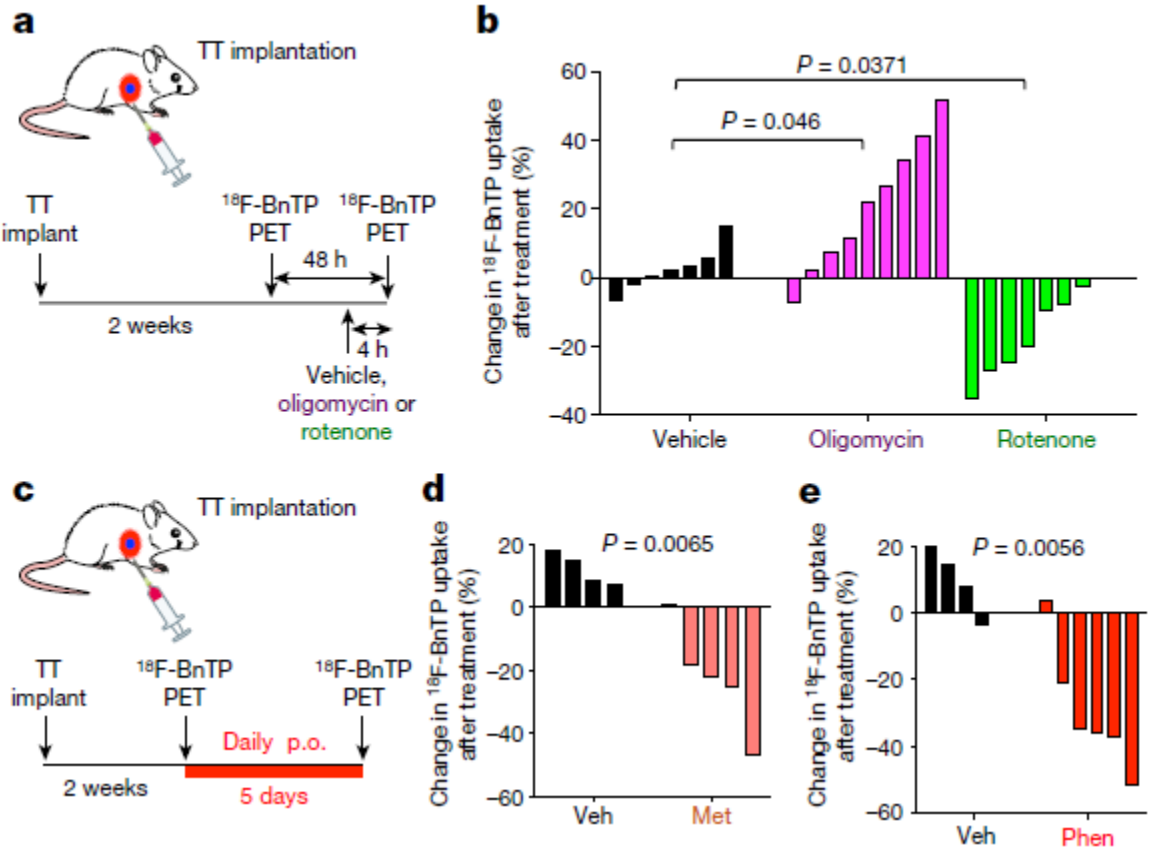

Figure 3. 3. 18F-BnTP detects mitochondrial complex I inhibition in vivo.

a, Schematic drawing of the transthoracic (TT) implantation of *KPL* (bearing mutated *Kras* and deficient in *p53* and *Lkb1*) lung ADC cells into syngeneic recipient mouse, imaging and treatment regiments. **b**, Waterfall plot of the percentage change in 18F-BnTP uptake after treatment of mice with a single dose of vehicle (*n* = 7 mice), 0.25 mg kg−1 oligomycin (*n* = 9 mice) or 0.5 mg kg−1 rotenone (*n* = 7 mice). *P* values determined by one-way ANOVA. **c**, Schematic drawing of the treatment and imaging regiment for syngeneic mice implanted transthoracically with lung ADC

cells from *KPL* mice, and treated with vehicle or complex I inhibitor for the indicated time. **d**, Waterfall plot of the percentage change in 18F-BnTP uptake after treatment of mice with vehicle (*n* = 4 mice) or 500 mg kg−1 metformin (*n* = 5 mice) for 5 days. **e**, Waterfall plot of the percentage change in 18F-BnTP uptake after treatment of mice with vehicle (*n* = 4 mice) or 125 mg kg−1 phenformin (*n* = 6 mice) for 5 days. Experiments in **b**, **d** and **e** were performed once. Statistical significance for **d** and **e** was calculated using unpaired two-tailed *t*-test.

NSCLC is marked by genetic, metabolic and histological heterogeneity in tumors.[53,70,71] We next sought to perform multi-tracer PET imaging in KL mice using the 18F-BnTP and [18F]fluoro-2-deoxyglucose (18F-FDG) PET tracers to non-invasively profile mitochondrial ΔΨ and glucose metabolism, respectively. Multi-tracer PET imaging of KL lung tumors revealed distinct metabolic heterogeneity between lung tumors in which we identified three distinct tumor populations: (1) glycolytic 18F-FDG-positive and 18F-BnTP-negative tumors; (2) oxidative 18F-BnTPpositive and 18F-FDG-negative tumors; and (3) tumors with increased uptake of both tracers (Extended Data Fig. 2.5a). Histological analysis of lung tumors imaged by PET revealed that 18F-FDG-positive, 18F-BnTPnegative tumors were SCC as confirmed by positive staining for CK5 and TTF1, whereas 18F-BnTP-positive, 18F-FDG-negative tumors were positive for TTF1 and negative for CK5 staining, confirming ADC histology (Extended Data Fig. 2.5b, c). Both lung ADCs and SCCs showed distinct 18F-BnTP and 18F-FDG profiles, which suggests that these tumor subtypes may have distinct bioenergetic profiles.

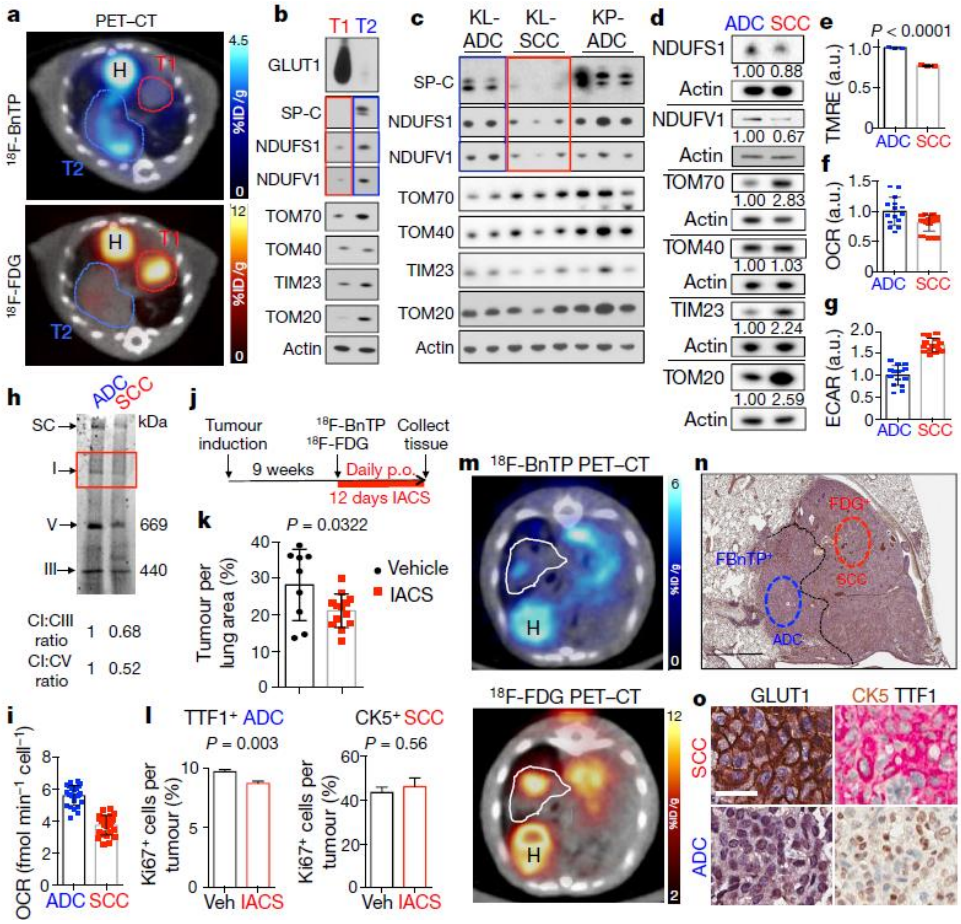

Figure 3. 4. Multi-tracer PET imaging of KL lung tumors with 18F-BnTP and 18F-FDG.

a, PET–CT images of a *KL* mouse with two tumors, T1 and T2. Top, 18F-BnTP/CT overlay; bottom, 18F-FDG/CT overlay. **b**, Western blot of T1 and T2 tumors isolated from mouse in **a** and probed with the indicated antibodies. **c**, Western blot of tumors isolated from *KL* or *KP* (*KrasG12D;p53−/−*) mice and probed with the indicated antibodies. **d**–**i**, Experiments performed on human A549 (ADC) and RH2 (SCC) cell lines. **d**, Western blot probed with the indicated antibodies. Loading control (β-actin) is shown for each blot; intensity of bands relative to actin is indicated. **e**, Quantification of TMRE fluorescence (*n* = 3 biological replicates). **f**, Basal oxygen consumption rate (OCR) (*n* = 15 technical replicates). **g**, Extracellular acidification rate (ECAR) (*n* = 15 technical replicates). **h**, Coomassie staining of mitochondria isolated from A549 and RH2 cells separated on blue native gel. I, II and III, complex I, II and III, respectively; SC, supercomplex. Densitometry quantification of the ratio of complex I (CI) to complex V (CV) or complex III (CIII) is indicated. **i**, Complex I activity in human A549 and RH2 cells (*n* = 25 technical replicates). **j**, Schematic of the treatment regimen for *KL* mice. **k**, Percentage of lung area occupied by tumors in *KL* mice treated with vehicle or 15 mg kg−1 IACS-010759 (*n* = 9 mice (vehicle), *n* = 13 mice (IACS)). **l**, Percentage of Ki67-positive cells per tumor area quantified for TTF1- positive (TTF1+) tumors for *KL* mice treated as indicated in **j** (left; *n* = 861 (vehicle); *n* = 1,068 (IACS)) and CK5-positive (CK5+) tumors (right; *n* = 31 (vehicle); *n* = 26 (IACS)). Data are mean ±} s.e.m. **m**, Transverse view of a *KL* mouse imaged with 18F-BnTP PET–CT (top) and 18F-FDG PET–CT (bottom). Tumor is outlined. **n**, Haematoxylin and eosin (H&E) staining of the PET imaged tumor. Tumor histology is indicated. Scale bar, 1.0 mm. **o**, Representative images of tumors stained with

GLUT1 (left) and CK5 plus TTF1 (right). Scale bar, 25 μm. Data are mean ±} s.d. *P* value determined by unpaired two-tailed *t*-test. Experiments in **a**–**h** were performed twice with similar results. Experiments in **i**, **k** and **l** were performed once. Data in **m**–**o** are representative of three independent mouse experiments. a.u., arbitrary units.

Previous studies have shown that lung SCC tumors from KL mice are refractory to phenformin, which suggests that lung SCC tumors may contain intrinsic defects in complex I that modulate response to complex I inhibition.[49,62] Supporting this, a study of mitochondrial proteins in human NSCLC showed that late-stage lung carcinomas have reduced expression of NDUFS1 and NDUFV1[72], which are complex I subunits involved in the transfer of electrons from NADH (Extended Data Fig. 2.6a). We performed a PET-guided biochemical analysis of NDUFS1 and NDUFV1 in lung ADCs and SCCs in KL mice. We found that 18F-BnTP-negative, 18F-FDG-positive SCC tumors (shown in red) had a marked reduction in NDFUS1 and NDUFV1 proteins compared with 18F-BnTP-positive, 18F-FDG-negative ADC tumors (shown in blue) (Fig. 3.4a, b, Extended Data Fig. 2.6b–d). We analysed NDFUS1 and NDUFV1 proteins in lung ADC and SCC tumors from KL mice across three independent experiments and discovered that SCCs (red boxes) had a consistent reduction in NDFUS1 compared to ADCs (blue boxes) (Fig. 3.4c, Extended Data Figs. 2.6e, 7). Lung ADCs and SCCs were distinguished by the levels of SP-C protein. In addition, immunoblots for TOM20, TOM40, TOM70 or TIM23 showed similar distribution of mitochondrial content between SCC and ADC tumors (Fig. 2.4b, c, Extended Data Fig. 2.1). We then examined the NDUFS1 and NDUFV1 proteins in the human lung ADC cell line A549 and the human lung SCC line RH2. Identical to mouse lung tumors, we identified a decrease in the levels of both NDUFS1 and NDUFV1 proteins in RH2 cells compared with A549 cells (Fig. 3.4d). Functional analysis of mitochondrial ΔΨ in human and mouse ADC and SCC cell lines demonstrated that the SCC tumor cells had a significantly reduced ΔΨ compared with ADC cells (Fig. 3.4e, Extended Data Fig. 2.8a). RH2 cells had a reduced oxygen consumption rate and an increased extracellular acidification rate compared with A549 cells (Fig. 3.4f, g). Analysis of mitochondrial complexes in Coomassie-stained gels showed that RH2 cells had lower levels of

complex I than A549 cells (Fig. 3.4h). In addition, RH2 cells had reduced complex I activity compared with A549 cells (Fig. 3.4i). These results suggest that ΔΨ and complex I activity may be predictive of responses to complex I inhibitors in which 18F-BnTP-positive lung ADCs are predicted to have increased sensitivity compared with 18F-BnTP-negative lung SCCs.

We next demonstrated that both human and mouse lung ADC cell lines were more sensitive than lung SCC cell lines to low doses of the complex I inhibitors phenformin and IACS-010759(Extended Data Fig. 2.8b–d).[73] We tested IACS-010759 in vivo in KL mice and determined that 18F-BnTP-positive tumors were sensitive to complex I inhibition. KL mice were imaged by 18F-BnTP and 18F-FDG PET before treatment to confirm the presence of 18F-BnTP-positive tumors and binned into equal groups based on tumor uptake of 18F-BnTP (Fig. 3.4j, Extended Data Fig. 2.9a). Mice receiving IACS-010759 showed a significant reduction in tumor burden compared to those that received vehicle control (Fig. 3.4k, Extended Data Fig. 2.9b, c). Our data predicted that 18F-BnTPpositive ADCs would show increased sensitivity to IACS-010759 compared with 18F-BnTP-negative SCCs. Analysis of tumor cell proliferation showed a significant reduction in Ki67+ cells in TTF1+ ADCs treated with IACS-010759, whereas CK5+ SCCs were refractory to IACS-010759 (Fig. 3.4l). We next asked whether PET imaging of 18F-BnTP and 18F-FDG could detect metabolic heterogeneity within individual lung tumors. We identified heterogeneous uptake of both 18F-BnTP and 18F-FDG within single lung nodules from KL mice (Fig. 3.4m). Histological analysis revealed squamous cell differentiation in the 18F-FDG-positive, 18F-BnTPnegative region marked by positive staining for CK5 and GLUT1. By contrast, the 18F-BnTP-positive, 18F-FDG-negative tumor region was marked by positive staining for TTF1 and low expression of GLUT1, confirming ADC histology (Fig. 3.4m–o, Extended Data Fig. 2.10). These results demonstrate that multi-tracer PET imaging with 18F-BnTP and 18F-FDG could identify distinct mitochondrial and metabolic heterogeneity within individual lung tumors. Our study represents a new and non-invasive approach to using 18F-BnTP PET imaging to profile mitochondrial ΔΨ and functional mitochondrial heterogeneity within NSCLC. We detected distinct

mitochondrial ΔΨ and complex I activity profiles in lung SCC and ADC tumors that were predictive of responses to complex I inhibitors. Our results suggest that 18F-BnTP may function as a non-invasive biomarker to guide the delivery of complex I inhibitors in cancer. PET imaging of 18F-BnTP represents a valuable resource not only to the field of cancer metabolism but also to other fields that are actively investigating mitochondrial activity in ageing, physiology and disease.

Chapter 4: Classes of Drugs that Mitigate Radiation Syndromes

4.1 Introduction

Historically, tissue damage after exposure to low density ionizing radiation (IR) such as X-rays and γ-rays was ascribed to cell death resulting in large part from the generation of short-lived free radicals and their destructive effects on DNA, events that were widely considered to be determined within minutes to hours after exposure. The finding by the Walter Reed Army Drug Development Program in the 1950s that thiol-based free radical scavengers, from which WR2721 (Amifostine) emerged as the lead compound, non-selectively radioprotect normal tissues if given close to the time of radiation exposure, support this contention (Murray and McBride, 1996).[74] Unfortunately, such radioprotectors are far less effective if given after exposure, which is an essential requirement for radiation mitigation in the context of radiological accidents or terrorist action. Government agencies have outlined a general framework for the development of such mitigators in animal models; agents must be efficacious when administered at least 1 d after IR exposure by a route suitable for mass administration. Despite these tight restrictions, promising mitigators have emerged that are active against potentially lethal, acute radiation syndromes (ARS) in animal models that closely mimic the human situation (Bond et al., 1965; Kim et al., 2009; Burdelya et al., 2012; Medhora et al., 2012; Himburg et al., 2014; Jiang et al., 2014; Cohen et al., 2016; Micewicz et al., 2017; Steinman et al., 2018)[12,75–82], and in many ways they challenge historical radiobiological concepts that DNA damage and repair, and rapid apoptosis, is essentially complete within 24 h since mitigation of radiation-induced syndromes only start at this time point. ARS were first characterized in radiobiological studies performed largely in inbred mice shortly after WWII. As whole-body irradiation (WBI) doses were increased, the dose causing 50% mortality (LD50) of mice plotted against mean/ median survival time (MST) was found to be discontinuous with mortality being expressed within several dose-time windows, each with a characteristic pathogenesis (Quastler, 1945a; Quastler, 1945b; Quastler, 1945c; Austin et al.,

1956; Sacher and Grahn, 1964; Bond et al., 1965).[83–87,75] Lethality in the lowest dose range occurs between 10 and 30 d and can generally be ascribed to hematopoietic failure (H-ARS). An increase in dose precipitates an earlier phase of mortality at around 5–9 d due to gastrointestinal damage (GI-ARS). H-ARS and GI-ARS are primarily due to depletion of highly proliferative stem/ progenitor compartments and failure of these tissues to maintain their functional compartment (Schaue and McBride, 2019; McBride and Schaue, 2020).[88,89] The MST therefore reflects the tissue turnover time. A third, cerebrovascular/central nervous system syndrome (CVS/CNSARS) was identified 1–2 d after very high doses of WBI that is mechanistically different in being marked by brain edema, hemorrhage, and inflammation. Many variables may influence these morbidity and mortality patterns after WBI, including infection, immunosuppression, coincidental trauma, burns, and other exigent circumstances. In addition, individuals who survive ARS often develop delayed effects of acute radiation exposure (DEARE) that are largely associated with chronic inflammation and may display a multi-organ disease syndrome (MODS) with a shortened life span (Williams and McBride, 2011; Micewicz et al., 2019).[90,91] Although colony stimulating factors such as Neupogen (G-CSF), Neulasta (pegylated G-CSF), and Leukine (GMCSF) have been approved by the FDA for H-ARS mitigation in humans (Singh and Seed, 2020)[92], their efficacy may be limited with respect to other ARS and DEARE syndromes (Farese et al., 2019).[93] They may even exacerbate radiobiological damage in some tissues (van Os et al., 2000; Li et al., 2015).[94,95] Since WBI causes multi-organ damage, mitigators should be agnostic with respect to tissue type, which might require that they act through shared highly conserved pathways. Rebalancing all damaged tissue systems might prevent a later downward spiral into MODS. Additional advantageous properties might be selectivity for radiation tissue damage without other normal tissue effects, and formulation in effective doses that are easily administered and not highly dependent on time and route of administration. We have used high throughput screening (HTS) and structure-activity relationship (SAR) analyses to identify classes of novel mitigators with at least some of these attributes when tested in vivo (Micewicz et al., 2017).[12] Remarkably, the HTS platform employed

simple radiationinduced apoptotic death of a CD4+ CD8+ T lymphocyte line (Kim et al., 2009; Kim et al., 2011; Micewicz et al., 2017)[76,96,12], suggesting that common core pathways are being targeted (Lant and Derry, 2014; Contreras et al., 2018).[97,98] We initially reported on results of a screen of 65,000 bioactive compounds that identified several classes of agents that could mitigate both radiation-induced lymphocyte apoptosis in vitro and H-ARS in vivo. These included purine nucleosides and multiple tetracyclines and fluoroquinolones, but not other antibiotics (Kim et al., 2009; Kim and McBride, 2010).[76,99] For the antibiotics, mitigation was unrelated to anti-microbial activity and SAR analysis identified them all as belonging to a class possessing a common ring structure. We then interrogated small chemical libraries of 85,000 compounds using the same screening platform and reported on a class of novel 4- nitrophenylsulfonamide compounds (NPS), in particular piperazine derivatives (NPSP), with a lead compound NPSP512 that uniquely mitigated multiple ARS and late DEARE (Micewicz et al., 2017; Micewicz et al., 2019)[12,91] including H-ARS, GI-ARS, radiation-induced pneumonitis and pulmonary fibrosis, neurological motor, sensory and memory deficits, and DEARE (Micewicz et al., 2017; Micewicz et al., 2019; Bhat et al., 2020; Duhachek-Muggy et al., 2020)[12,91,100,101], as well as radioprotecting mice against H-ARS when given prior to WBI and displaying anti-tumor activity (Micewicz et al., 2017; Bhat et al., 2020; Duhachek-Muggy et al., 2020).[12,100,101] Here, we describe other classes of mitigators from the HTS chemical screen and other sources. Over 20 H-ARS mitigators are described and their properties compared and discussed. We also describe the challenge in formulating the NPSP512 compound that led to analog synthesis designed to improve its pharmacological properties.

4.2 Materials and Methods

HTS Assay

The HTS assay has been described previously (Kim et al., 2009; Micewicz et al., 2017).[12,76] In brief, TIL1 CD4+ CD8+ lymphocytic cells of C3H murine lineage (McBride et al., 1992)[102] were grown in MEM medium with 10% fetal calf serum and irradiated with 2 Gy. One hour later, 85,000 compounds were individually added from the ChemBridge DIVERSet (San Diego, CA, United States) or the Asinex (ASN) or Asinex Targeted (AST) libraries (Moscow, Russia). The AST library is configured around inhibitors of GPCRs (14 groups), kinases (six groups), ion channels (four ligand dependent groups), and proteases, while the others cover a broader pharmacophore space. Compounds were added at 10 μM final concentration in 1% DMSO. Mitigation of radiation-induced apoptosis was assessed at 24 h by measuring ATP release (ATPlite, PerkinElmer, MA, United States). Based on the 99% confidence limits compounds that increased viability to above 130% of the irradiated (diluent) controls (100%) were retested over a range of concentrations using both ATPlite and Annexin/P.I. (Fisher, Carlsbad, CA, United States) for apoptosis. For in vivo assays, compounds were obtained from ChemBridge (San Diego, CA, United States) or synthesized in house (MJ, PR). Purity and stability were assessed by LC/MS and NMR. All chemicals were stored in 15 μL DMSO or freshly suspended in 1 ml of 2 % Cremophor EL in water, and injected s. c. in the flank in 0.2 ml volumes, unless otherwise stated. All control mice received the same diluent as the experimental groups. Other vehicle formulations are noted in the text. The HTS data are archived in The Collaborative Drug Discovery Vault (https:// app.collaborativedrug.com/vaults/425/searches/new) and freely available.

Similarity and Substructure Analyses

Data were compared for similarity and chemical features on a Collaborative Drug Discovery vault platform (CDD™, Burlingame, CA, United States). The entire library was ranked by structural similarity to a referenced hit based upon the Tanimoto coefficient, excluding coefficients

In Vivo Testing

C3Hf/Sed//Kam and C57Bl/6 gnotobiotic male and female mice were bred at UCLA in our Radiation Oncology AAALACaccredited facility. Where indicated, Foxp3DTR/EGFP and Nrf2−/− , both on the C57Bl/6 background were used with the goal to monitor ARS under conditions of limited immune suppression and/or limited anti-oxidant defense, respectively. Foxp3DTR/EGFP transgenic mice (a gift from Dr Chatila) have the Diphtheria toxin receptor under the control of the Foxp3 promoter (a master regulator of regulatory T cells, i.e., Tregs) that allows the conditional depletion of Tregs upon exposure to Diphtheria toxin (DT). In order to deplete Tregs mice were i.p., injected with DT at 1 µg/mouse (Sigma-Aldrich) every 3 days starting 2 days prior to WBI for a total of three injections while on maintenance antibiotics: Sulfatrim, 1 g/L Kanamycin and 1 g/L Ampicillin in drinking water (Haribhai et al., 2011)[103]. Nrf2−/− came from the Jackson Labs (Bar Harbor, ME, United States). All mice were housed at four per cage and randomized to experimental groups of n 8 at around 9–12 weeks of age, restricting the weight to match groups, e.g. males were 28–30 g when used. All IACUC-approved protocols and NIH guidelines were adhered to and defined criteria for premature humane euthanasia were strictly followed. WBI was performed on unanesthetized and unrestrained mice using an AEC Gamma Cell 40 cesium irradiator (Cs-137) at a dose rate of around 60 cGy/min or a Gulmay Medical RS320 Irradiation System X-ray unit operated at 300 kV (Gulmay Medical Ltd., Surrey, UK) with a permanent 4 mm Be filter and 1.5 mm Cu and 3 mm Al giving a HVL of 3 mm Cu. Institutional probit analyses were used to determine the dose that would cause lethality of 70% of mice within 30 d (LD70/30). Dosimetry used a Capintec ionization chamber calibrated to NIST standards and film (GAFCHROMIC EBT2, International Specialty Products, Wayne, NJ, United States) to check that deviations in the field uniformity is <5%. Partial body irradiations used 300 kV X-rays (Gulmay, Surrey, UK) with anesthesia and Cerrobend (1 cm) to prevent exposure to unirradiated body parts. Mice were anaesthetized with an i.p. injection of 80 mg/kg Ketamine (Putney, NADA#200–073)

and 4 mg/kg Xylazine (AnaSed, NADA# 139–236; Lloyd labs #4811). We have outlined the radiation syndromes our mice experience in considerable detail (Micewicz et al., 2017; Bhat et al., 2020; Duhachek-Muggy et al., 2020).[12,100,101] In brief, H-ARS mortality occurred during the "classic" time frame between days 10–30 after exposure. Hematological damage is confirmed by Hemavet CBC observations made on blood from a separate group of identically treated mice so as not to influence survival data. To rule out infection as a cause of death, plasma is cultured for aerobes and anaerobes, which is facilitated by the use of gnotobiotic mice, which have a limited flora that does not change over the experimental period. Active mitigators allowed for CBC recovery around day 10–14, especially for lymphocytes and neutrophils. GI-ARS occurs 5–9 days after abdominal exposure and is accompanied by epithelial denudation that is prevented by mitigators. Lethality after lung irradiation in C3H mice is due to pneumonitis and occurs 80–140 days after exposure, while C57Bl/6 mice present with fibrotic death after 150–200 days. We followed both lung pathologies by CT scans and all syndromes by histology.

Chemical Synthesis of the NPSP512 Derivatives QS1 and 52A1

QS1: The synthetic approach was adapted from Laval et al. (2009).[104] 40 mmol (6.49 g) of 1-phenylpiperazine was placed in a 250 ml Erlenmeyer flask equipped with a magnetic stirrer. Subsequently, 45 ml of anhydrous tetrahydrofuran (THF), 80 mmol (8.8 ml) of 4-methylmorpholine and 50 ml of anhydrous dimethyl sulfoxide (DMSO) were added, and the solution was cooled in an ice bath for 10 min with vigorous mixing. Then, 44 mmol of appropriate sulfonyl chloride was dissolved in 25 ml of anhydrous THF, and the resultant solution added in 2.5 ml portions to the reaction mixture over a period of 10 min with mixing. The flask was covered and mixing continued overnight (~18 h) after which the reaction mixture was transferred to a 500 ml round-bottom flask, and the THF evaporated using a rotary evaporator (bath temp 35° C). The remaining residue was diluted with water and formed precipitate was collected by filtration. Dried crude compounds were crystalized from either ethyl alcohol or acetonitrile giving corresponding compounds with overall

yield of 72–98%. 52A1 (4-(4-[2(aminomethyl)phenyl]piperazine1sulfonyl) phenyl)(hydroxy)oxoammonium): In brief, 3.73 g (10 mmol) of sulfonamide was placed in a 250 ml one-neck round-bottom flask equipped with a magnetic stirrer. Subsequently, 100 ml of anhydrous benzene, 2.97 ml (10 mmol) of titanium (IV) isopropoxide (Ti(OiPr)4), and 8.86 ml (50 mmol) of 1,1,3,3- tetramethyldisiloxane (TMDS) was added to a glass stopper capped bottle and all mixed for 24 h (60° C). The dark brown solution was then acidified with 4N HCl in 1,4-dioxane and evaporated on rotary evaporator. Crude compound was precipitated by addition of dry diethyl ether, separated by centrifugation, and dried under the vacuum. Subsequently, solid residue was extracted with hot water (3 × 50 ml), and combined extracts lyophilized, purified crystallization and a hydrochloride salt made. The formula weight was 377.44.

Pharmacokinetics Analysis

Pharmacokinetic data were obtained from blood plasma samples taken at indicated times after a single s.c., injection of NPSP mitigators at 5 or 10 mg/kg into C3H male mice. Plasma samples (20 µL) and an internal standard (1 µL; F512, 50 pmol) were added to methanol (79 µL, Fisher Scientific Optima® LC/MS) for a total volume of 100 µL, as well as 52A1 standards (1 µL of 10, 50, 100, 250 pmol) similarly prepared. These were vortexed for 2 s and centrifuged for 5 min at 16,000 rcf to obtain supernatants that were run on a 100 × 2.1 mm C18 column (Phenomenex Kinetex) using the 1290 Infinity LC system (Agilent 6460). The mobile phase was 0.1% formic acid in Milli-Q water, and 0.1% formic acid in acetonitrile. After elution, the NPSP was characterized on a triple quadrupole LC/MS system with an electrospray ionization source (Agilent 6460). Data acquisition was made in the positive ion mode for multiple reactions monitoring (MRM). The analyte signal was normalized to the internal standard and concentrations were determined by comparison to the calibration curves for plasma using linear regression analysis. PK values were obtained using SummitPk software to calculate Cmax and T1/2.

Statistics

Kaplan-Meier plots with log rank statistics were used to test for significant survival differences. Probit analyses were performed using SPSS v20 software and NCSS PASS 13 Power Analysis and Sample Size Software, Kaysville, Utah for power analysis. Analyses of variance were performed on all other data with a Brown-Forsythe test where homogeneity of variance assumptions were not met. Multiple comparisons procedures using Sidak were also performed. The Kruskal-Wallis non-parametric test was performed for some data distributions with less stringent assumptions. Significance was assessed at the 5% level using SPSS v20 software (IBM SPSS Statistics, Armonk, NY, United States).

4.3 Results

In Vitro Screening

Primary HTS of the chemical libraries identified 220 potential “hits” that enhanced lymphocytic cell survival to >130% which was outside the 99% confidence limits of the control. Maximal common substructure analysis classified most of these hits to fall within 11 clusters, each with a common core pharmacophore and containing at least three active compounds (Figure 4.1–shaded).

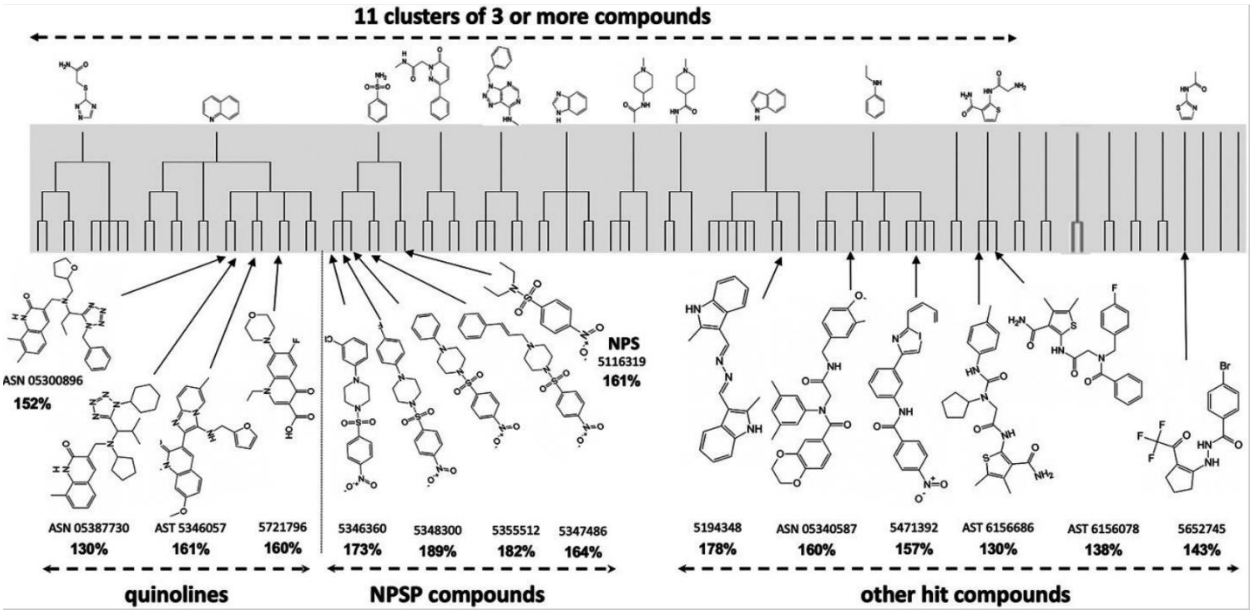

Figure 4. 1. Maximal Common Substructure analysis of in vitro HTS "hits"

Maximal Common Substructure analysis of *in vitro* HTS "hits" (shaded) showing clusters of at least three active compounds. The 15 validated hits cherry-picked for *in vivo* testing are shown along with the extent to which they mitigated 2 Gy *in vitro* radiation cytotoxicity (in bold) compared to controls treated with 2 Gy alone (100%).

Secondary screening validated 23 compounds, of which 15 were cherry-picked for in vivo testing for mitigation of H-ARS in mice; the others being difficult to obtain. Four had a quinoline scaffold and came from the largest cluster (a total of 14 compounds at four levels of similarity). Five bore a 4-nitrophenylsulfonamide motif. All compounds had very little activity on non-irradiated cells suggesting some selectivity for radiation damage.

In Vivo Screening

H-ARS was induced in C3H or C57Bl/6 male or female mice by WBI with LD70/30 doses estimated from institutional probit curves. Unless otherwise stated, all drugs were tested using the same schedule of five daily s. c. injections starting 1 d after LD70/30 doses of WBI, most at three different doses unless limited by availability. All 15 compounds shown in Figure 1 mitigated H-ARS at least one dose regimen without observed toxicity.

4-(Nitrophenylsulfonyl)-4-Phenylpiperazine Compounds

We previously reported on a novel and unique class of 4- nitrophenylsulfonamide (NPS) H-ARS mitigators, four of which were 4-(nitrophenylsulfonyl)-4-phenylpiperazines (NPSP) (Micewicz et al., 2017).[12] Lead NPS and NPSP compounds effectively mitigated H-ARS in both strains of mice and both sexes. The lead NPSP compound 5355512 [a.k.a. 512 or #5 (Bhat et al., 2019)][105] mitigated multiple radiation syndromes. The shared nitrophenylsulphonamide moiety obviously is the active warhead for this class of drugs, but we chose a piperazine derivative as the lead compound because of its more favorable PK properties (Micewicz et al., 2017).[12] We hypothesize that this enabled activity at 5mg/kg, which is easier to deliver to humans than the 75 mg/kg required for activity of simpler NPS compounds (Micewicz et al., 2017).[12] In keeping with this hypothesis, analogs of NPSP512 that we synthesized without piperazine lost low dose (5 mg/kg) efficacy (Figure 2). Although the piperazine group could be modified with retained activity, not all NPSPs in our HTS dataset with >70% similarity were active mitigators and this appeared to be due to subtle chemical features associated with the piperazine group (Micewicz et al., 2017).[12]

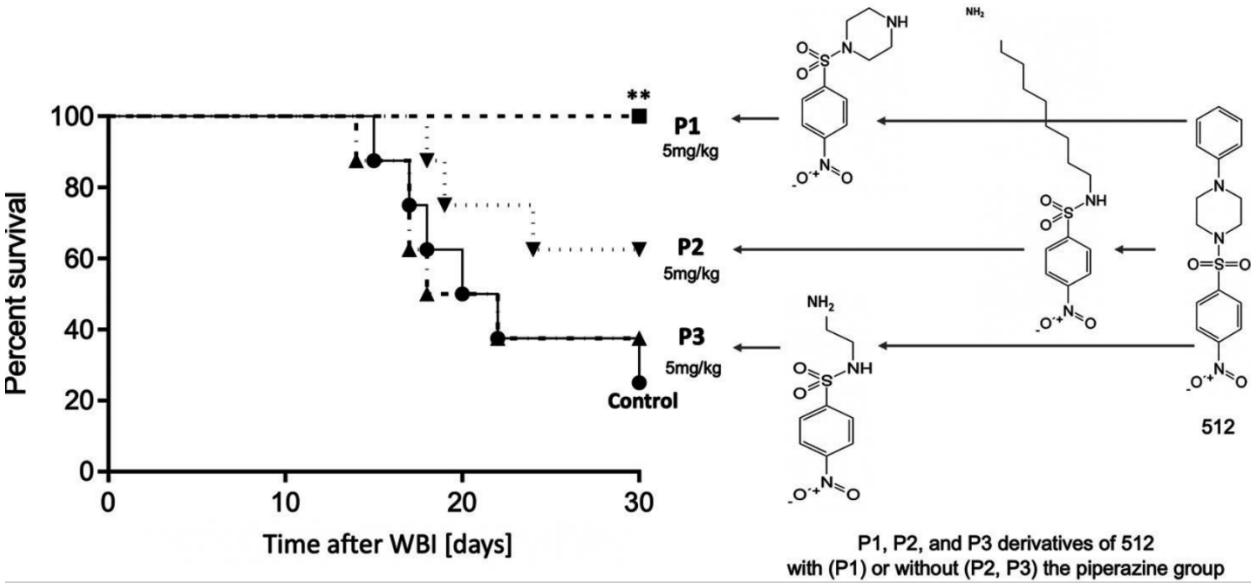

Figure 4. 2. Efficacy of Piperazine Group

The piperazine group is essential for efficacy of 512 at 5 mg/kg, but can be modified without loss of activity, P1 being able to fully mitigate H-ARS (p = 0.0085) whereas P2 and P3 analogs without piperazine lost activity.

Formulation, Quarternization, and Derivatization of 512

For preliminary in vivo studies, drugs were dissolved in DMSO and formulated in Cremophor EL to minimize inter-drug differences in solubility. However, high concentrations of Cremophor have been reported to be associated with occasional hypersensitivity reactions in patients (Gelderblom et al., 2001)[106], and the FDA now consider it an undesirable excipient. NPSP512 needed to be formulated for further advancement. Dozens of FDA-approved excipients were tested without much success. By analogy with x-ray crystallography of N-(4-nitrophenyl)-N-phenylsulfonamide (Gomes et al., 1993)[107], it seems that NPSPs can "stack" head to tail in alternate hydrophobic and hydrophilic layers to form large intermolecular complexes that "crash out" over time in aqueous solution. This was not a problem in our preliminary studies because solutions for injection were made fresh before use. Since we could find no excipient that could overcome this problem, we resorted to synthesis of chemically modified analogs. Guided by the extensive SAR studies, we knew that the groups attached to piperazine most likely affected solubility and chose this as the target for modification. NPSP512 was quaternized as shown in Figure 3A and designated QS1. QS1 was 50 times more soluble in water than NPSP512 reaching 2.4 mg/ml. Although not shown here, like the parent molecule, QS1 mitigated radiation-induced apoptosis and enhanced mobilization of $CD11b^{+}Ly6G^{+}Ly6C^{+}$ myeloid cells (Micewicz et al., 2017).[12] The optimal dose of QS1 needed for mitigating H-ARS lethality in C3H mice was determined using 1, 5, 10, or 20 mg/kg injected s. c., 5× daily starting 1 d after an $LD_{70/30}$ WBI dose and found to be 5 mg/kg (not shown)—identical to that for the parent compound (Micewicz et al., 2017).[12] In several different H-ARS experiments, 5 mg/kg s.c., (5x) increased survival from 30% to 90–100%, a regime that was also effective for gavage delivery (Figure 4.3B). A single injection of QS1 24 h after WBI was also effective if given s. c., but not by gavage. Like the parent 512, the standard

5 d schedule of 5 mg/kg s. c. mitigated GI-ARS lethality in mice receiving 20 Gy to the abdomen (Figure 4.3C) and radiation pneumonitis after 16 Gy to the thorax (Figure 4.4D). PK studies (Figure 4.3E) showed that the C_{max} for QS1 was almost 100-fold higher than for NPSP512 but that it had a very short half-life and could not be detected in plasma for longer than 3–4 h after injection, likely due to its metabolism. For comparison, the C_{max} for NPSP512 occurs after 2 h and drug is detectable for up to 24 h (Micewicz et al., 2017).[12] The PK characteristics were very similar in non-irradiated and WBI mice when drug was injected 24 h after WBI, but when injected 72 h post-WBI the C_{max} was lower indicating radiation changes the plasma fluid volume over time.

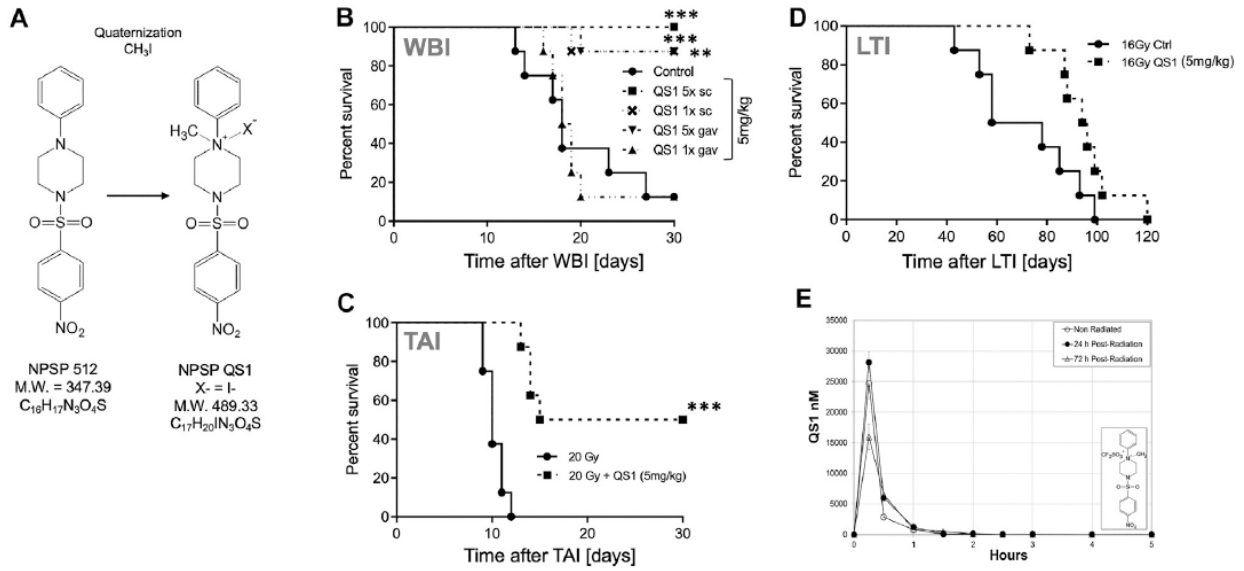

Figure 4. 3. Quaternization of NPSP512 to Yield QS1

(A) Quaternization of NPSP512 to yield QS1. **(B)** QS1 at 5 mg/kg mitigates H-ARS lethality in C3H male mice after LD70/30 WBI ($p < 0.0001$; Cs source; 7.725 Gy) if given 5× daily by s.c., or gavage, or 1× if given s.c., ($p = 0.0023$), but not by gavage. **(C)** QS1 at 5 mg/kg, 5X daily s.c., mitigates GI-ARS after 20 Gy total abdominal irradiation in C57BL/6 male mice and **(D)** radiation pneumonitis in C3H mice after 16 Gy local thoracic irradiation. **(E)** PK parameters for 10 mg/kg QS1 injected s.c., assessed when drug is given 24 or 72 h after WBI showing a decrease in plasma concentration if given at 72 h. * = $p < 0.05$, ** $p < 0.01$, *** $p < 0.001$.

Although QS1 solubility was improved 50 fold by quaternization, its bioavailability became suboptimal compared to the parent molecule. Over 90 derivatives of NPSP512 were therefore synthesized in attempts to optimize its pharmacology with respect to a) viable substituents for the

-NO_2 group, b) solubility in water, and c) enhanced oral bioavailability using lipidation to improve intestinal absorption (Madsen et al., 2007; Bellmann-Sickert et al., 2011).[108,109] All were screened for anti-apoptotic activity *in vitro* and seven of the most promising were tested for ability to mitigate H-ARS *in vivo* (Figure 4.4). The water-soluble 2-(aminomethyl)-derivative of NPSP512, 52A1, emerged with greatly improved pharmacology while still being highly effective at mitigating lethality from H-ARS in C3H mice (Figure 4.4B). 52A1's ability to mitigate GI-ARS in C57Bl/6 mice was also robust albeit just below reaching statistical significance (Figure 4.4C, $p = 0.09$) with the new FDA-preferred GI-ARS model, which is WBI with one leg shielded (2.5% bone marrow shielding) (Farese et al., 2019).[93] Note that the MST for GI-ARS is delayed in gnotobiotic over more conventional mice (Wilson, 1963; Matsuzawa, 1965)[110,111], and that 18.5 Gy is a high dose GI-ARS model that is not bone marrow-dependent, unlike lower dose models (Mason et al., 1989)[112]. The PK of 52A1 was very similar to NPSP512, but with an almost 40-fold higher C_{max} (Figure 4.4D). Lipidation of NPSP512 yielded a water insoluble hydrophobic compound that was suspended in Kollipher for oral delivery. The length of the fatty acid chain is an important parameter for improving bioavailability (Madsen et al., 2007).[108] Derivatives with chains of up to 20-carbon fatty acids were synthesized and tested by the oral route (not shown). The 12-carbon molecule, 52L12 was the most effective ($p < 0.001$; Figure 4.4B).

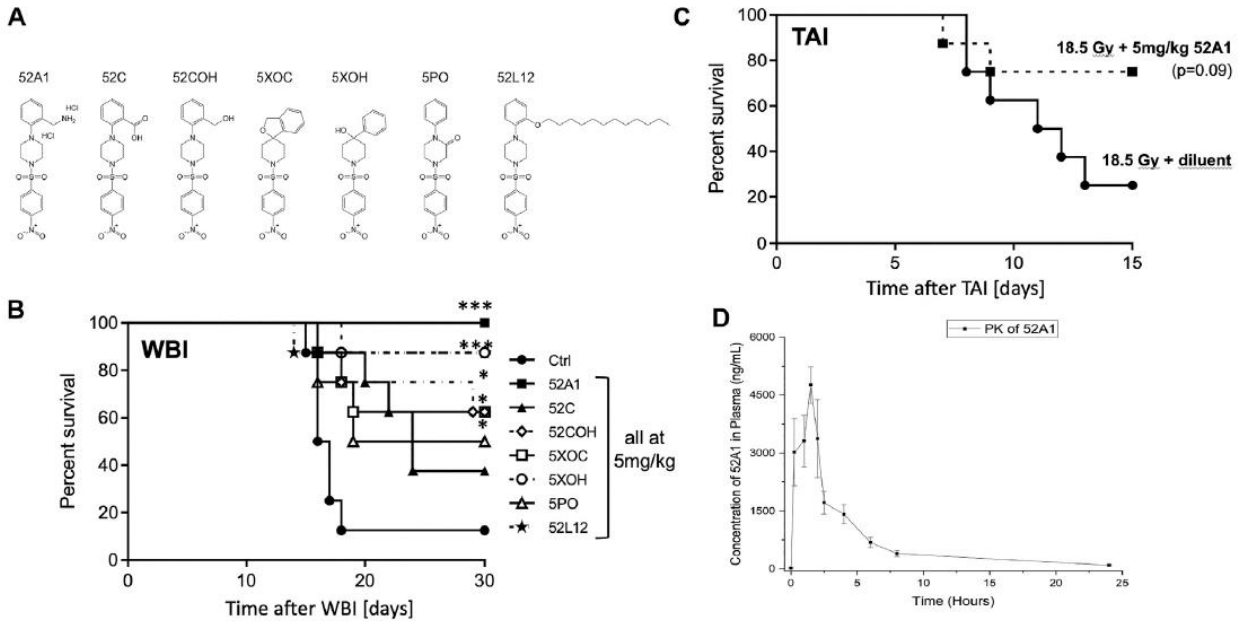

Figure 4. 4. 512 Derivatives synthesized and tested in H-ARS models

(A) 512 derivatives synthesized and tested in **(B)** a model of H-ARS using LD70/30 doses (X-rays) in C3H mice. Drugs were given 5× s.c., except for the lipidated 52L12, which was given by gavage in Kollopher EL. The water soluble 2-(aminomethyl)-derivative of 512, 52A1, was most effective. **(C)** 52A1 also mitigated GI-ARS in C57Bl/6 mice given 18.5 Gy WBI with 2.5% body shielding. **(D)** PK of 52A1 is similar in shape to 512 but the Cmax is almost 40 times higher. * = $p < 0.05$, ** $p < 0.01$, *** $p < 0.001$.

Quinoline Compounds

The quinoline class detected by maximal common subclustering had four compounds that stood out after secondary screening. Their ability to inhibit radiation killing *in vitro* is shown in bold in Figure 4.1 and their ability to mitigate H-ARS is shown in Figure 4.5. Although drug availability and therefore dose response data was limited for three compounds, at least three of the four had significant *in vivo* activity at 75 mg/kg and lower doses seemed less effective, where tested. One of the compounds in Figure 4.5, 5346057 (a.k.a. 057, BCN057, or YEL002), was of interest because it was identified as active in another HTS yeast screen, performed in parallel based on the DEL assay that measures mitigation of radiation cytotoxicity and genotoxity in the diploid yeast *S. cerevisiae* strain RS112 (Hafer et al., 2010; Kim et al., 2011)[113,96] indicating that a

conserved pathway is involved in mitigation. 057 had a dose modification factor for H-ARS of 1.15 when given s. c. in a daily 5 day course starting 24 h after WBI (Drs. Y. Revina, R. Schiestl pers. comm.). These drugs are very hydrophobic, which may be why high doses are needed for bioavailability. We had previously formulated 057 in 30% Captisol and shown that 90 mg/kg BCN057 given daily s.c., for 8 d starting on day +1 after 14, 15, and 16 Gy total abdominal irradiation mitigated GI-ARS in C57Bl/6 mice by enhancing regeneration of Lgr5+ intestinal stem cells *in vivo* and in organoid culture (Bhanja et al., 2018).[114] The same compound, as YEL002, also decreased $^{(131)}$I-induced DNA double strand breaks in thyroid cells (Hershman et al., 2011)[115] and prevented radiation-induced carcinogenesis in mice (RS, pers. comm.). The lead quinoline therefore seems active in more than one model of radiation damage and this is likely true for the whole class given their structural similarity.

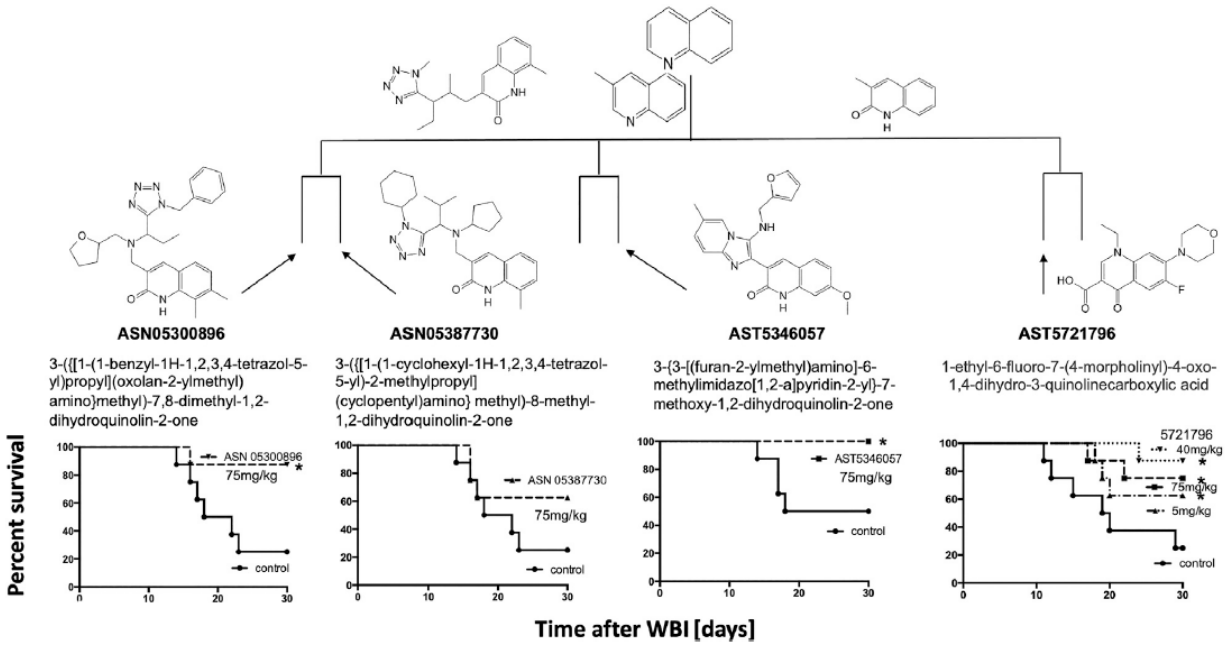

Figure 4. 5. Activity of Quinoline Class of Radiomitigators

Activity of the quinoline class of radiomitigators of H-ARS in C3H male mice with drugs given s.c., at the stated doses (5× daily) starting 1 d after LD70/30 doses of radiation (Cs-137). *$p < 0.05$, ***$p < 0.001$.

Other HTS Compounds

Since the two major groups of the most promising compounds in the HTS showed mitigator activity *in vivo*, "hit" compounds from the other groups (n = 6) with diverse structures shown in Figure 4.1 were also synthesized and tested for their ability to mitigate H-ARS *in vivo* after LD70/30 radiation doses (Figure 4.6). Although studies were limited by compound availability to five of these, all had some mitigating ability, and all but one reached statistical significance.

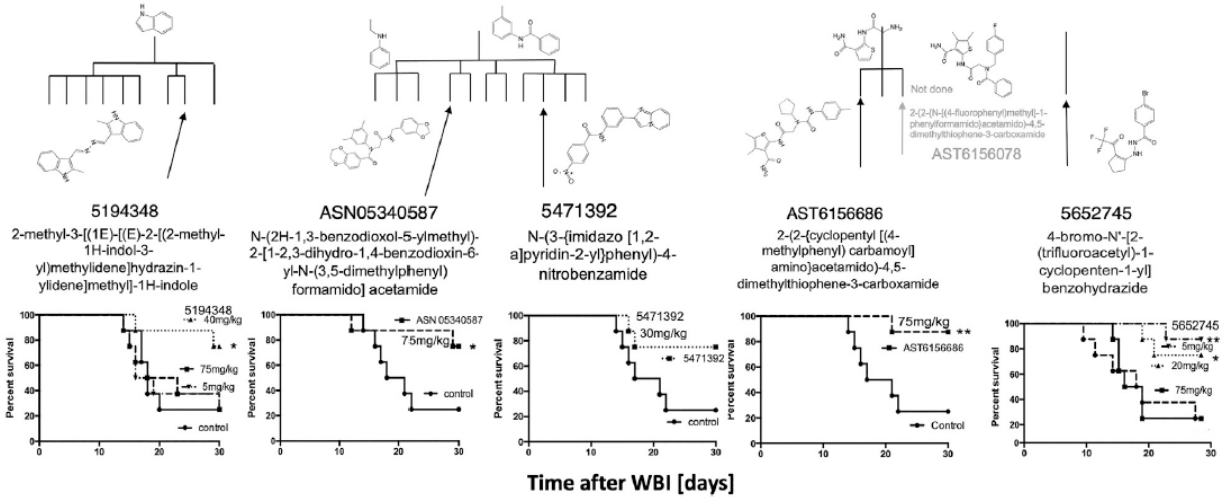

Figure 4. 6. Five other HTS in vitro "hits"

Five other HTS *in vitro* "hits" mitigated H-ARS in C3H mice given once daily for 5 d starting 24 h after LD70/30 doses of WBI (Cs). * $p < 0.05$, ** $p < 0.01$, *** $p < 0.001$.

To determine if compounds that were suboptimal during the initial *in vitro* screen (and below the potency of the 15 prime candidates), could still be active against H-ARS, we picked and tested four based on the fact that these four had increased *in vitro* cell survival to 135–145% and fell within the 122 compounds initially identified by HTS. The *in vitro* data are shown in bold in Figure 4.7. There was some efficacy, but only one was statistically significant and only at one concentration (Figure 4.7), which validated our selection process.

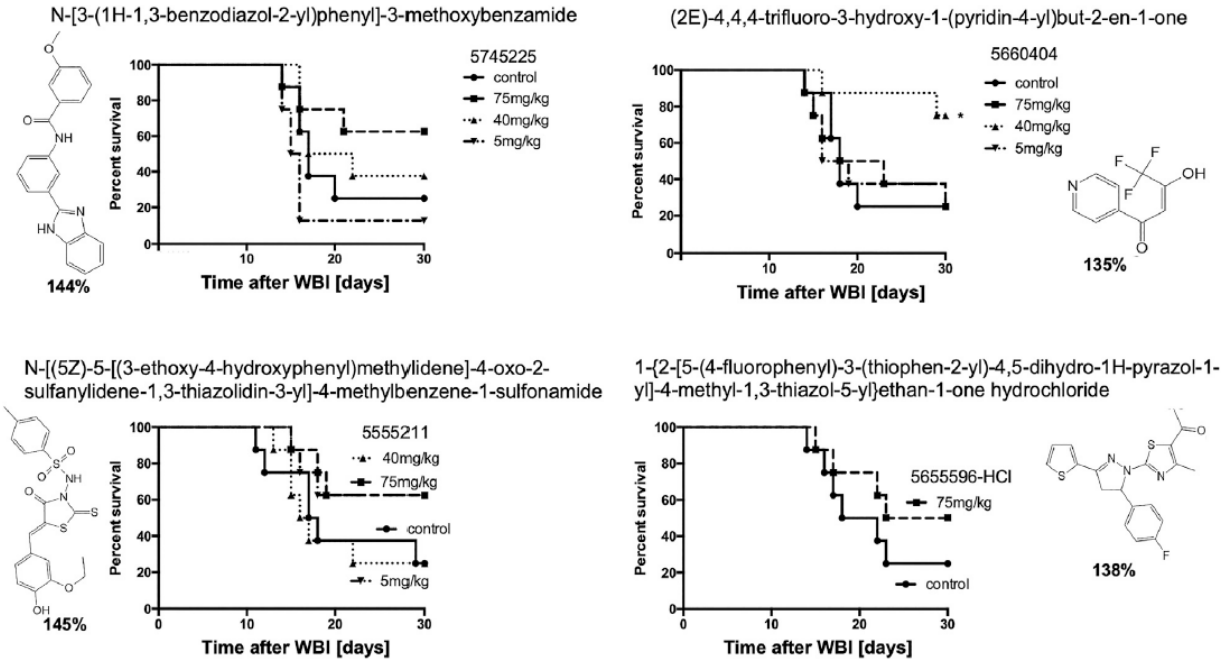

Figure 4. 7. Other lesser HTS "hits" tested

Other, lesser HTS “hits” tested in C3H mice with 5X daily drug doses, as stated, starting 24 h after WBI at LD70/30 doses. *$p < 0.05$.

Other Classes of Mitigators

Purine Nucleosides

We previously reported that the nucleoside adenosine, its derivative deoxyadenosine, and its analog vidarabine, which are 97% similar, were hits in our earlier bioactive HTS screen and showed some ability to mitigate H-ARS in mice (Kim et al., 2011).[96] Nucleotides have a very short half-life *in vivo* but agonists and antagonists specific for one or more of the four known adenosine receptors, A1, A2a, A2b, and A3, have been generated with effects ranging from pro-to-anti-inflammatory and aiding-to-limiting bone marrow recovery. We have investigated whether they might have better properties as H-ARS mitigators. The A1 and A2 receptor agonist 5′-(N-ethylcarboxamido)adenosine (NECA) at 0.1 mg/kg s.c., (5x) in our standard H-ARS model increased survival of C3H male mice after 8 Gy WBI from 0 to 50%. The A2 agonist CGS21680 at 2 mg/kg s. c. (5x) increased survival of C57Bl/6 mice after 9 Gy WBI from 20 to 80% and of C3H

mice after 8 Gy WBI from 0 to 25% (not shown). However, the A3 agonist 2-Cl-IB-MECA, the A2 agonist CV1808 at 1 mg/kg, and IB-MECA at 1 mg/kg, were ineffective. Although these studies were limited, there was little evidence that these compounds were sufficiently superior to warrant further development as sole mitigators.

Natural Disaccharides

Natural disaccharides, in particular D-(+)-trehalose, have been shown to protect DNA, cells, and organisms against UVB (Cejková et al., 2010; Cejková et al., 2012; Emanuele et al., 2014)[116–118] and ionizing (Ledney et al., 1992; Yoshinaga et al., 1997; Webb and DiRuggiero, 2012; Liu et al., 2017; Paithankar et al., 2018)[119–123] radiation damage, although few studies have been performed in mammalian systems. Trehalose is a multifunctional molecule that can act as an antioxidant (Elbein et al., 2003; Cejková et al., 2010)[124,116] and anti-inflammatory agent (Ledney et al., 1992; Cejková et al., 2011)[119,125], reducing stress in multiple models. We had included it in excipient testing for NPSP512, only to find that alone it mitigated H-ARS lethality. Animal survival was increased by both single and five daily doses of 400 mg/kg trehalose/mouse administered 24 h after WBI by the s. c. route, and to a lesser extent orally (Figure 4.8). Comparison with several other saccharides (sucrose, raffinose, maltose, lactose) and carnosine, suggested that trehalose is superior at mitigation. Although the administered dose was high (~12 mg/mouse), its solubility (68.9 g/100 g in H_2O) (Higashiyama, 2002)[126], ready availability, high thermostability, and established lack of toxicity—it being a component of various pharmaceutical formulations and a frequent food additive—makes it a particularly intriguing candidate for clinical development.

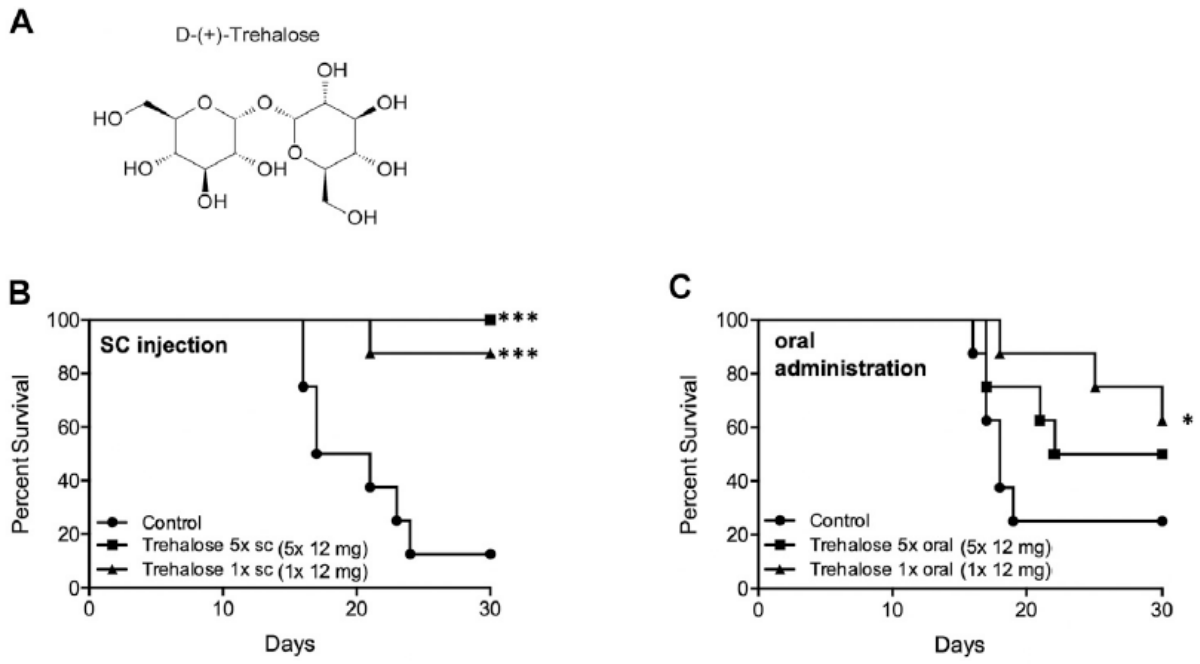

Figure 4. 8. Trehalose Class of Radiomitigators

Trehalose **(A)** and mitigation of radiation damage by **(B)** Trehalose (s.c., LD70/30), **(C)** Trehalose (oral, LD70/30). Each dose was 12 mg/animal in water. *$p < 0.05$, ***$p < 0.001$.

4.4 Discussion

We have used maximal common substructure analysis to classify 220 drugs capable of increasing lymphocytic survival *in vitro* 24 h after exposure to 2 Gy ionizing radiation. Remarkably, almost all of these could be attributed to 11 clusters of three or more compounds. Further screening to select for the most active compounds resulted in 15 drugs to test *in vivo*, and in spite of their diverse structures, almost all of these mitigated against H-ARS *in vivo*. Five had a 4-nitrophenylsulfonamide (NPS) group in common that is likely the active moiety. Here we showed that a piperazine moiety in 4-nitrophenylsulfonamidepiperazines (NPSP) improved the pharmacokinetics making the drug active at lower concentrations. Our lead NPSP, and all active agents in this class, act broadly by mitigating multiple acute and late radiation syndromes (Micewicz et al., 2017; Bhat et al., 2020; Duhachek-Muggy et al., 2020)[12,100,101] at doses

convenient for human administration. This is important because all tissues suffer radiation damage after WBI.

Unfortunately, these studies were performed with the drug formulated in Cremophor, which the FDA considers an undesirable excipient. The sulfonamide pharmacophore has been used as a drug since the 1930s and is a current component of well over 100 approved drugs with anti-bacterial, anti-cancer, anti-carbonic anhydrase, anti-diabetic, anti-protease, anti-inflammatory, and many other activities (Supuran, 2017)[127]; to which radiation mitigation can now be added. Given their popularity, the lack of literature on their solubility and lipophilicity, which are key parameters for drug development and utilization, is puzzling (Perlovich et al., 2014)[128]. Formulation attempts to find suitable excipients for NPSPs unexpectedly failed and can be explained by the tendency for these structures to “stack” and crash out of solution over time, but we were able to overcome these limitations by synthesizing alternative structures QS1 and 52A1 that retained their mitigation properties while having markedly improved water solubility and bioavailability.

Four of the 15 chemicals selected for further study were quinolines, which is another versatile scaffold for drug development forming a broad spectrum of drugs with anti-microbial, anti-inflammatory, anti-diabetic, anti-cancer, anti-malarial, anti-kinase, and other activities (Hussaini, 2016)[129]. Three of the four quinolines are shown here to have significant activity as H-ARS mitigators. These compounds are even more hydrophobic than NPSP512 but the lead compound 057 could be formulated in Captisol™ and has been shown to also mitigate H-ARS (Bhanja et al., 2018)[114] and other radiation-induced conditions (R. Schiestl, pers. comm.). Another 4 of the 15 selected compounds, which were of diverse structures, were also active against H-ARS, as was Trehalose, which we tested as a possible excipient rather than a mitigator.

This study raises the question as to why a 24 h HTS screen using apoptosis by lymphocytic cells after 2 Gy irradiation should yield multiple mitigators of H-ARS that can be classified and grouped

by common chemical moieties, and why at least some of these compounds can, additionally to being effective against hematopoietic death can also mitigate damage to epithelial structures in multiple tissues, where the critical cellular target for lethality is quite different. For H-ARS, in most species, damage to the myeloerythroid-restricted common progenitor cell compartment, and not the lymphocyte, is most likely to result in H-ARS, and transfer of these cells is sufficient to prevent H-ARS, bridging the developmental gap until more pluripotential stem cells develop (Na Nakorn et al., 2002).[130] The FDA-approved mitigator, G-CSF is thought to act against H-ARS by acting as a survival and proliferative signal for this population (Williams et al., 1990)[131], although it can also decrease reactive oxygen species (ROS) and prevent apoptosis through activating the anti-oxidant, anti-inflammatory Nrf2 pathway (Yamaguchi et al., 2020).[132] For GI-ARS, $Lgr5^+$ epithelial cells in the base of the crypt appear to be the weak link (Hua et al., 2012).[133] In this case, a quiescent, Bmi1+ “reserve” stem cell population (Tian et al., 2011; Yan et al., 2012)[134,135] may repopulate empty stem cell niches after injury, reprograming themselves as $Lgr5^+$ cells (Tetteh et al., 2015; Wabik and Jones, 2015; Beumer and Clevers, 2016; Jones and Dempsey, 2016; Gehart and Clevers, 2019).[136–140]

Our HTS discovery of multiple classes of ARS mitigators using radiation-induced cell death of lymphocytic cells as targets might implicate a role for apoptosis in ARS. However, mitigators are given 24 h after IR *in vivo*, when most rapid p53-dependent apoptosis is over. A second wave of radiation-induced, p53-independent apoptosis does occur as do later waves of ROS production and inflammation and those are the much more likely mitigator targets (Schaue and McBride, 2010; Schaue et al., 2015).[141,142] Pro-inflammatory cytokines are generated through radiation-activated NF-κB and MAPK pathways, the classic DSB-initiated DNA damage response, and nucleic acid sensing pathways downstream of micronuclei and cytoplasmic nucleic acids that are increased after IR (Maelfait et al., 2020).[143] From an evolutionary perspective, inflammatory

programs enacted in immune and non-immune cells aim to remove potential pathogens, but after WBI they come at a risk of exacerbating radiation damage.

This simple view must be tempered by the fact that pro-oxidant, pro-inflammatory milieus provoke an anti-inflammatory antagonistic response, often involving the anti-oxidant Nrf2 pathway. Mechanistically it is still not entirely known how tissues transition to an anti-inflammatory state that can support cell proliferation and restore tissue function, but it is clear that healing is compromised by RT and that radiation disease evolves over time with cyclical changes in inflammatory/anti-inflammatory pathways and in redox and metabolic status (Schaue et al., 2015).[142] The contribution of Nrf2 can be judged by the fact that mice with the Nrf2 pathway deleted are about 15% more radiosensitive to WBI than wild type C57Bl/6 mice (Figure 4.9), which is in keeping with the finding that NRF2-mediated Notch signaling improves hematopoietic stem/progenitor function after IR (Kim et al., 2014).[144] Similarly, depletion of anti-inflammatory Tregs increases the pro-inflammatory response to IR (Schaue et al., 2012)[145] and radiosensitizes C57Bl/6 mice to WBI (Figure 4.9). In fact, when studied, all of the mitigators mentioned in this paper, and others like G-CSF (Yamaguchi et al., 2020)[132], quench radiation-induced inflammation and ROS production (Kim et al., 2009; Micewicz et al., 2017; Bhat et al., 2020)[12,76,100] and it is reasonable to speculate that this is a requirement for effective mitigation. However, this is not the complete story, as can be seen from the other properties of the mitigator classes we discovered. Tissue recovery after injury engages many complex, interactive, highly conserved pathways within an entire responsive biological network which offers many possible points of intervention.

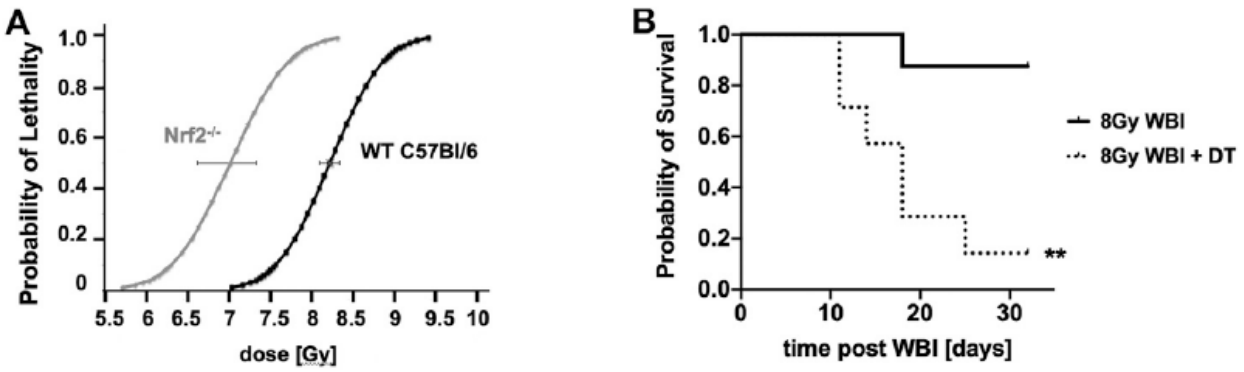

Figure 4. 9. Impact of Nrf2 and Treg depletion on responses to WBI

The impact of Nrf2 depletion **(A)** and Treg depletion in Diphtheria toxin (DT)-treated Foxp3DTR/EGFP transgenic mice **(B)** (***p* = 0.0037) on responses to WBI compared to aged-matched controls. ***p* < 0.01.

Both lead compounds from these two major classes of mitigators, the NPSPs and quinolones, where found to stimulate proliferation in stem cell organoid cultures of intestine, brain, lung and bone marrow (Micewicz et al., 2017; Bhanja et al., 2018; Bhat et al., 2019; Bhat et al., 2020; Duhachek-Muggy et al., 2020).[12,100,114,105,101] This includes Lgr5+ stem cells present in steady state and during post-injury tissue regeneration in the intestinal crypts, and other tissues. The balance between self-renewal and differentiation in these stem/progenitor cells is tightly controlled by a complex interplay of evolutionary conserved signaling pathways, including Wnt, Notch, bone morphogenetic protein, and Hedgehog (Clevers, 2019).[146] Smoothened, a key component of the sonic hedgehog (SHH) signaling pathway is activated in the gut by NPSP 512 leading to nuclear translocation of the GLI1 transcriptional activator to mitigate GI-ARS (Duhachek-Muggy et al., 2020).[101] Further, the quinoline 057 activates canonical Wnt-β-catenin signaling to mitigate GI-ARS (Bhanja et al., 2018)[114] and extracellular vesicular delivery of Wnt rescues intestinal stem cells from radiation toxicity (Saha et al., 2016).[147] It is reasonable to suggest that these agents may work through the same integrated signaling network. The SHH and Wnt signaling pathways are closely linked and, with Bmi-1, are involved in regulating

embryonic and post-natal development, and stem cell proliferation (Ouspenskaia et al., 2016)[148] to affect tissue repair and regeneration (Singh et al., 2018; Cao et al., 2020).[149,150] We speculate that these developmental signaling pathways are reactivated in many tissues to promote tissue recovery and that mitigators can promote this process. Our colleagues (Himburg et al., 2017)[151] have shown that, while IR activated canonical Wnt signaling, the Wnt antagonist Dickkopf-1 (Dkk1) mitigated H-ARS and promoted recovery of both long-term repopulating hematopoietic stem and progenitor cells, both directly and through niche interactions perhaps illustrating the complexity inherent in these pathways.

Others have reported that inhibition of the Wnt activator GSK-3β by SB21676324 mitigated H-ARS in C57Bl/6 male, but not female C57Bl/6 or C3H mice, indicating sex and strain differences (Daniel et al., 2020).[152] The only sex difference we found was that NPSP512 stimulated neural progenitor populations in female, but not male mice (Bhat et al., 2020).[100] Investigation of these pathways with a view to reconciling divergent results will need to take into account differences between tissues and sexes, comparison of varying radiation doses and administration schedules, and the degree of canonical activation of the Wnt pathway, which substantially impacts stem cell proliferation and differentiation (Luis et al., 2011).[153] It is worth noting that Wnt signaling also provides crucial proliferative and survival signals to immature T cells (Ma et al., 2012)[154], and our use of such cells for mitigator screening may have inadvertently biased our HTS towards agents that increase cell survival through activating these signaling pathways.

We suggest that the mitigators described here have, in addition to anti-inflammatory properties, the ability to enhance stem cell signaling through elements of the Hedgehog/Patch/Smoothened/Gli, BMP/TGF-β, FGF, WNT and Notch networks that govern embryogenesis, homeostasis and repair of adult tissues (Katoh and Katoh, 2006; Amankulor et al., 2009; Pitter et al., 2014; Caradu et al., 2018; Guo et al., 2018; Moparthi and Koch, 2019; Zhou et al., 2019).[155–161] As far as mitigation of radiation damage is concerned, the enormous

complexity inherent in these networks and the importance of context indicate a need for much further consideration as to mechanism. However, it should be pointed out that there is a close relationship between pathways controlling tissue repair and regeneration and inflammation, which may account for why these two aspects appear to be linked as common properties shared by classes of mitigators (Omenetti and Diehl, 2008; Amankulor et al., 2009; de la Roche et al., 2013; Braune et al., 2017; Shen et al., 2017; Caradu et al., 2018; Guo et al., 2018; Razumilava et al., 2018).[162,156,163–165,158,159,166]

Chapter 5: Environmental Electrophilic Inhibition of GAPDH at Submicromolar Concentrations

5.1 Introduction

Glyceraldehyde-3-phosphate dehydrogenase (GAPDH) is an enzyme that is abundant in the cell and is responsible for catalyzing the oxidative phosphorylation of glyceraldehyde 3-phosphate to 1,3-diphosphoglycerate, which is an intermediate for glycolytic adenosine triphosphate (ATP) synthesis.[13] Inhibition of GAPDH has been observed to interrupt aerobic glycolysis in activated immune cells, and overall a reduction in the inflammation process.[167] GAPDH contains an active site cysteine thiolate (Cys 152 in Human GAPDH, Cys 149 in Rabbit GAPDH), which is located in a pKa-lowering microenvironment (pKa= 6.03).[13,14] The catalytic Cys 152 appears to reside in a pKa-lowering catalytic triad possibly involving Histidine (His179) present in the three-dimensional structure of human GAPDH.[14] The Cys152 of the enzyme is capable of reacting with environmental electrophiles through the irreversible Michael addition, which has been shown to irreversibly inhibit the enzyme activity of GAPDH in a dose and time dependent manner.[14] Environmental electrophiles such as acrylamide (ACR) and methyl vinyl ketone (MVK) have been shown to selectively chemically modify the Cys 152 at lower concentrations, and at higher concentrations ACR can react with Cys 152 and Cys 247.[14] Additionally, parabenzosemiquinone (p-BSQ), an abundant (100-200 µg/cigarette) long-lived radical quinone is present in cigarette smoke and diesel smoke, which after inhalation is converted to 1,4-benzoquinone (BQ) *in vivo* via the quinone reductases (NQ01).[15–18] Previous studies have utilized bottom-up proteomics for the identification and quantification of the Cys 152 labelled modifications by environmental electrophiles, which include alkenes and quinones.[21,22] Here, we describe a mass spectrometry based approach for the identification and quantification of BQ and MVK at physiologically relevant submicromolar concentrations using intact protein analysis, catalytic activity studies, and bottom-up proteomics.

5.2 Methods and Materials

Intact protein methods

10 µg of Human or Rabbit GAPDH was aliquoted into 1.5 mL micro centrifuge tubes with 100 mM HEPES buffer. The reaction was performed at 24 ºC for 2 hours with varying concentrations of electrophile ranging from 0.5 µM to 10 µM. The experiments were performed using size-exclusion chromatography on the LTQ XL linear ion trap, with an Agilent LC running Methanol: Chloroform: 0.1% Aqueous Formic Acid (4:4:1).

Proteomics methods

10 µg of Rabbit GAPDH, and 500 nM to 10 µM 1,4-parabenzoquinone (BQ) were added to the reaction vial with a total volume of 15 µL for 2 hrs in the dark. 10 mM Iodoacetamide (IAM) and 6 mM tris(2-carboxyethyl)phosphine (TCEP) were added to a total volume of 25 µL for 30 mins in the dark. 6 µL of Trypsin was added to the total volume of 30 µL and placed on the oscillating rack for 2 hrs. 100 µL of HEPES buffer (100 mM) was added to the trypsinized mixture. Stage tips with C-18 resin were activated with 40 µL of MeOH, 40 µL of elution buffer (80% MeCN, 0.1% TFA), 80 µL of loading buffer (2% MeCN, 0.1% TFA), and the 130 µL trypsinized sample was loaded into the stage tip and desalted. The sample was centrifuged for 2 mins at 1000 RPM to desalt, then 40 µL of elution buffer was added and centrifuged again for 2 mins at 1000 RPM to elute the peptides. The sample was then dried in the speed vac to dryness for 20 mins. The samples were then reconstituted in 10 µL of 0.1% TFA and 5 µL was injected for HPLC analysis on the Q-Exactive Plus using DDA analysis. The mobile phase consisted of A [0.1% formic acid in DI water] and B [0.1% formic acid in acetonitrile], and the gradient elution employed was: 0% B for 4 min, 5% B to 25 % B to 54 min, 25 % B to 45% B to 69 min, 45% B to 95% B at 74 min and held for 3 min, 95% B to 0% B at 80 min and held for 10 min with a total time of 90 min, with a flow rate of 500 nL/min. The Mascot software search engine was used for peptide fragment and

chemical modification identification, wherein BQ-induced modification and S-carbomidomethylation at Cys were set as dynamic modifications. Xcalibar was used for data processing and quantification of peptide abundances.

Catalytic activity methods

30 µg (2.5 units/mL) of Rabbit GAPDH, and 100 nM to 10 µM 1,4-parabenzoquinone (BQ) were added to the reaction vial with a total volume of 250 µL for 2 hrs in the dark. 2 mM 1,4-dithiothreitol (DTT) was added to quench the reaction with a total volume of 300 µL for 30 mins in the dark. 10x PBS buffer (50 µL), 8 mM DTT (10 µL), 15 mM of glyceraldehyde-3-phosphate (G3P) (10 µL) was added to the reaction mixture and the reaction proceeded once G3P was added to the reaction. The assay was conducted at 24 ˚C and was incubated for 2 mins, then analyzed using a 96 well plate reader at 340 nm for 40 seconds of monitoring.

5.3 Results and discussion

Intact protein analysis

In figure 5.1 below, intact protein mass spectrometry was performed for the Human GAPDH has a corresponding mass at 35,916 Da and the protein appears to be somewhat homogenous.

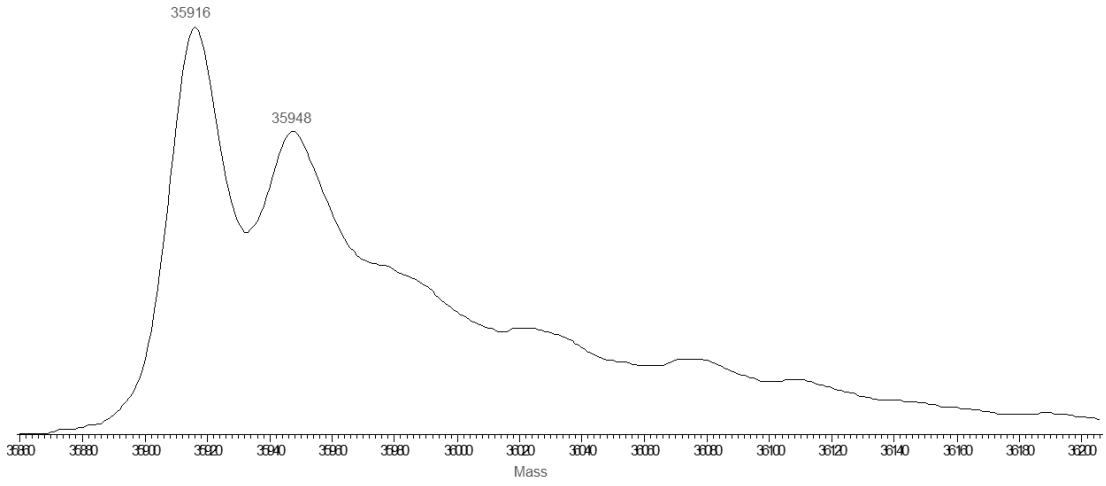

Figure 5. 1. Human GAPDH protein intact protein mass spectrum

In figure 5.2 below, the intact protein mass spectrum of Human GAPDH is treated with varying concentrations of BQ ranging from 500 nM to 10 µM. The compound at A corresponds to the intact mass for Human GAPDH, the compound at B corresponds to one addition of BQ to the catalytic cysteine, and the compound at C corresponds to two BQs reacting with two cysteines of the intact protein. The mono modified protein appears to dominate as the concentration of BQ is increased from 500 nM to 10 µM.

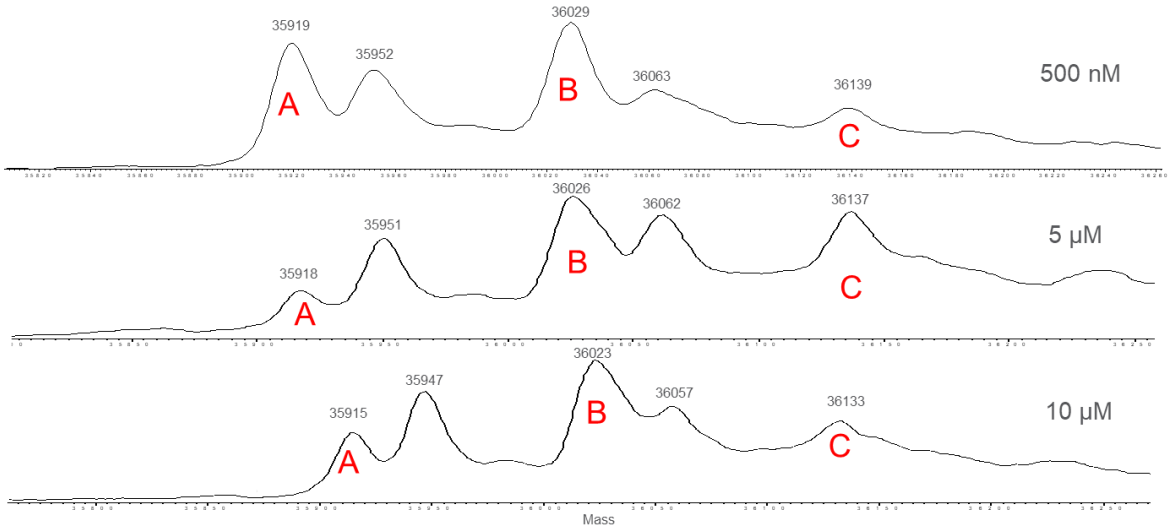

Figure 5. 2. Human GAPDH treated with 500 nM BQ Pane 1, 5 µM BQ Pane 2, 10 µM BQ Pane 3

In figure 5.3 below, the intact protein mass spectrum for the Rabbit GAPDH has a corresponding mass at 35,696 Da and the protein appears to be somewhat heterogenous.

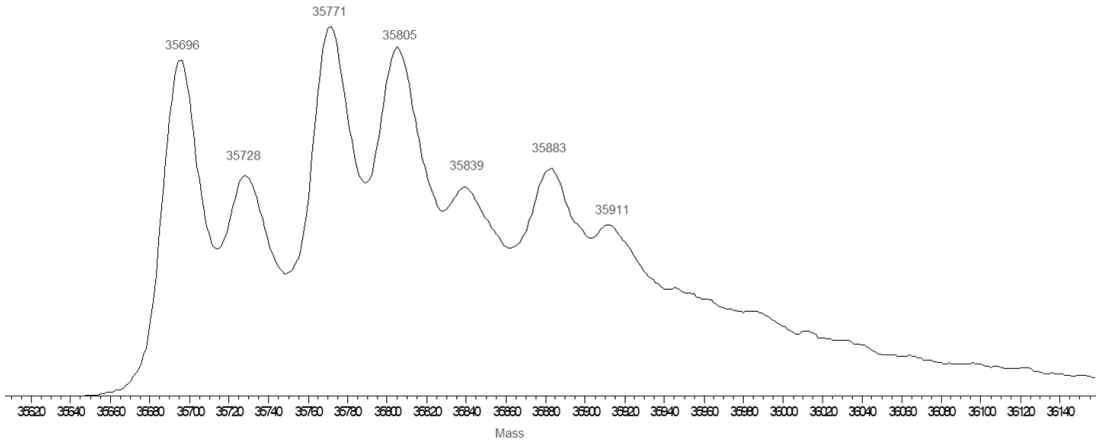

Figure 5. 3. Rabbit GAPDH protein intact protein mass spectrum

In figure 5.4 below, the intact protein mass spectrum of Rabbit GAPDH is treated with varying concentrations of BQ ranging from 500 nM to 10 µM. The compound at A corresponds to the intact mass for Human GAPDH, the compound at B corresponds to one addition of BQ to the catalytic cysteine, and the compound at C corresponds to two BQs reacting with two cysteines of the intact protein. The doubly modified protein appears to dominate as the concentration of BQ is increased from 500 nM to 10 µM and the intact protein appears to be fully modified at the 10 µM concentration.

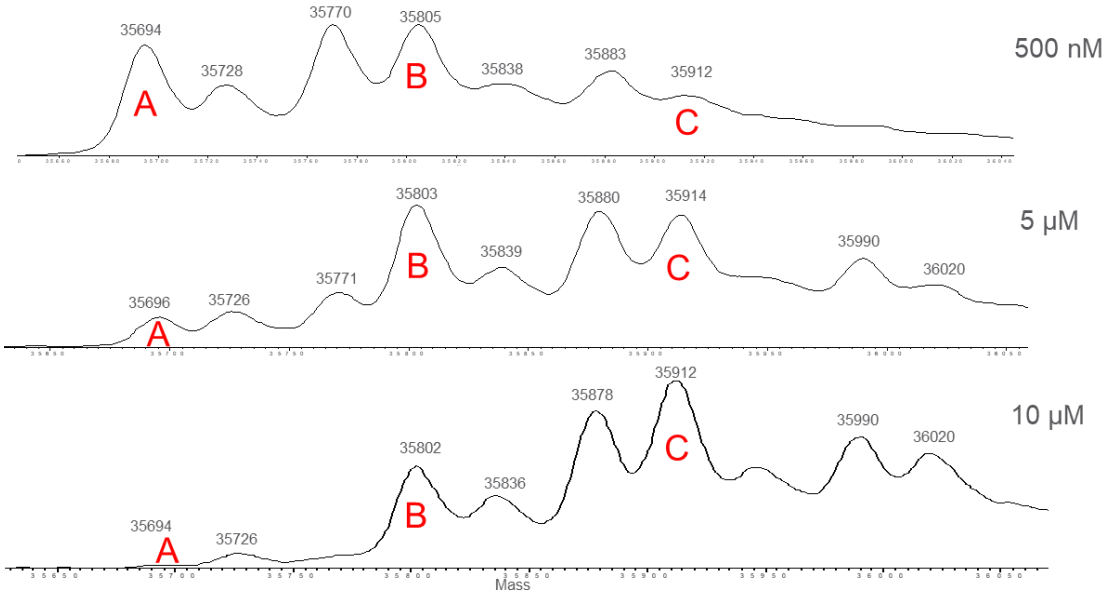

Figure 5. 4. Rabbit GAPDH treated with 500 nM BQ Pane 1, 5 µM BQ Pane 2, 10 µM BQ Pane 3

Catalytic activity analysis

In figure 5.5 below, catalytic activity studies were performed on Human GAPDH at 24 ˚C after an initial 2 hour exposure to BQ at varying concentrations ranging from 100 nM to 10 µM. The control sample without BQ appeared to have the largest slope, which is indicative of the highest conversion of NAD^+ to NADH. Whereas, with increasing amount of BQ concentration the rate of NAD^+ conversion decreased initially by 20% at 100 nM and had almost complete inhibition at 10 µM.

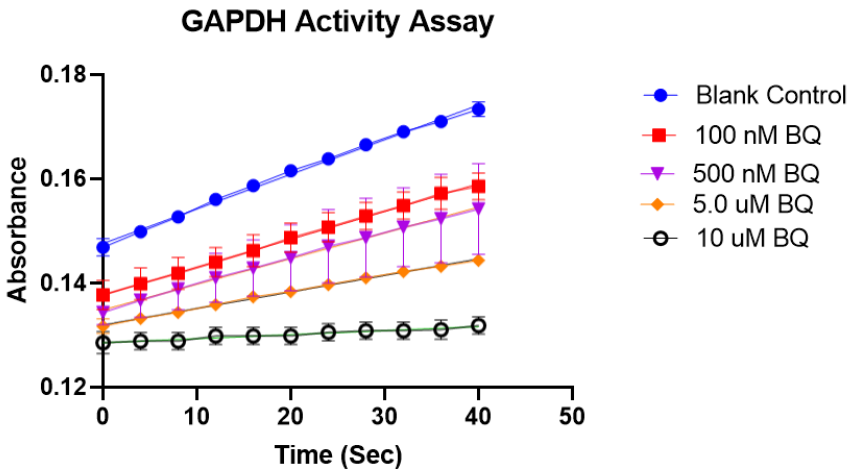

Figure 5. 5. Rabbit GAPDH Activity Assay with BQ treatment at varying concentrations

Bottom-up proteomics analysis

In Table 5.1 below, peptide location, peptide sequence, theoretical masses and observed masses, and position of cysteine modification for each species of GAPDH and electrophile are tabulated and listed. The asterisk (*) is indicative of the cysteine modification site.

Table 5. 1. GAPDH location of modification and mass observed

Protein	Peptide #	Position	Peptide Sequence	Theoretical MS	Observed MS	Cys
GAPDH+ BQ (Human)	1	146-162	IISNASC*TTNCLAPLAK	1881.8988	1881.8964	152
GAPDH+ BQ (Rabbit)	1	144-160	IVSNASC*TTNCLAPLAK	1867.8782	1867.8808	149
	2	233-246	VPTPNVSVVDLTC*R	1604.7841	1604.7869	245
GAPDH + MVK (Rabbit)	1	144-160	IVSNASC*TTNCLAPLAK	1831.9146	1831.9172	149
	2	233-246	VPTPNVSVVDLTC*R	1568.8207	1568.8233	245

In Figure 5.6 below, a representative chromatogram of the trypsinized Rabbit GAPDH control is shown. The sample was monitored using the mass spectrometer for the various peptide masses containing the carbomidomethylation (CAM) modification and reference peptide. The abundances of these modified peptides were used for quantification of the modification.

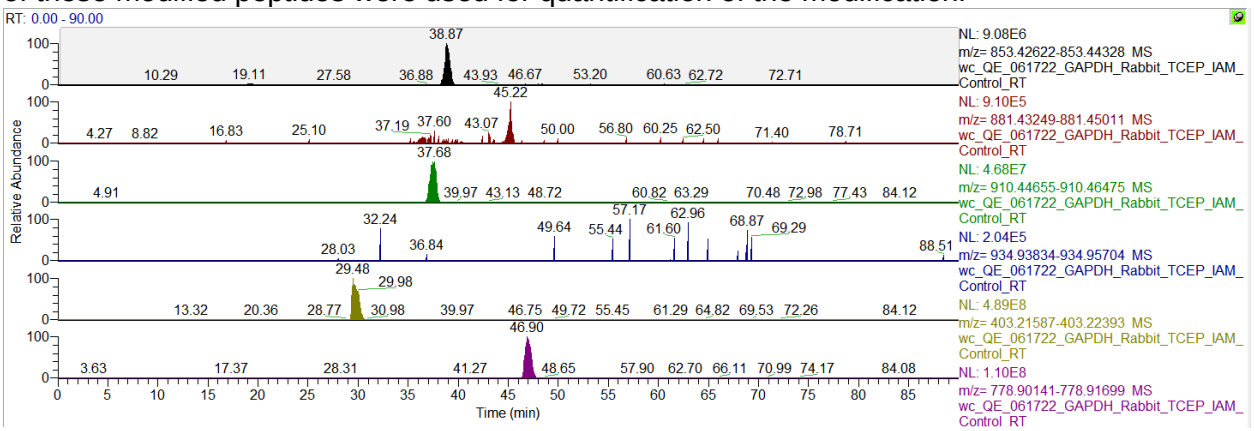

Figure 5. 6. Representative chromatogram of Rabbit GAPDH peptide 144-160 control sample

In Figure 5.7 below, a representative chromatogram of the trypsinized Rabbit GAPDH treated with BQ at 10 µM is shown. The sample was monitored using the mass spectrometer for the various peptide masses containing CAM and BQ modifications. Prominent abundance peaks were formed indicative of the BQ + CAM labelled peptide 1 and the BQ labelled peptide 2. The abundances of these modified peptides were used for quantification of the modification.

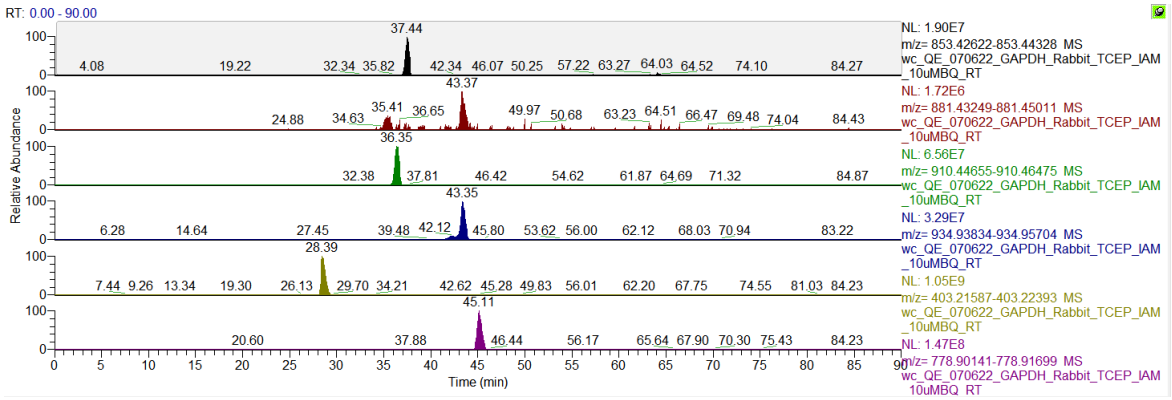

Figure 5. 7. Representative chromatogram of Rabbit GAPDH peptide 144-160 exposed to 10 µM BQ

Figure 5.8 below, a representative chromatogram of the trypsinized Rabbit GAPDH control. The sample was monitored using the mass spectrometer for the various peptide masses containing the CAM modification and reference peptide. The abundances of these modified peptides were used for quantification of the modification.

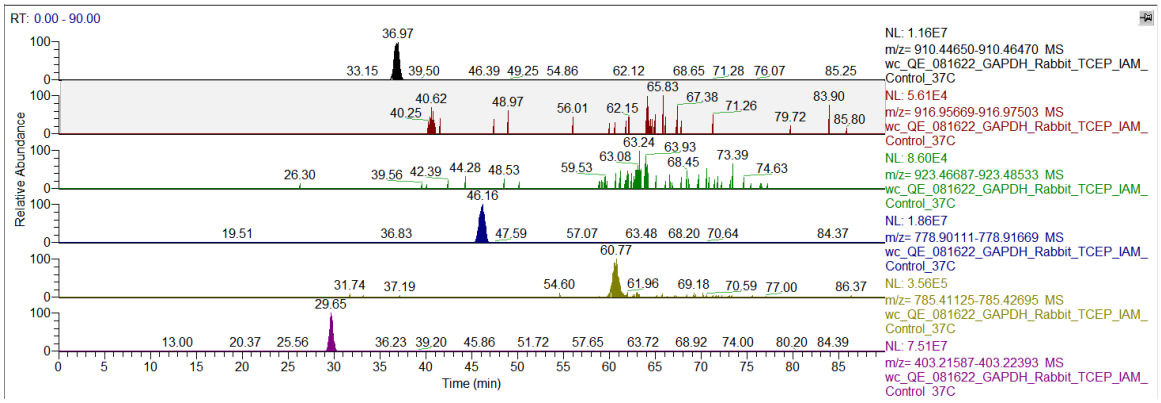

Figure 5. 8. Representative chromatogram of Rabbit GAPDH peptide 144-160 control sample

In Figure 5.9 below, a representative chromatogram of the trypsinized Rabbit GAPDH treated with MVK at 1 µM is shown. The sample was monitored using the mass spectrometer for the various peptide masses containing CAM and MVK modifications. Prominent abundance peaks were formed indicative of the MVK + CAM labelled peptide 1 and the MVK labelled peptide 2. The abundances of these modified peptides were used for quantification of the modification.

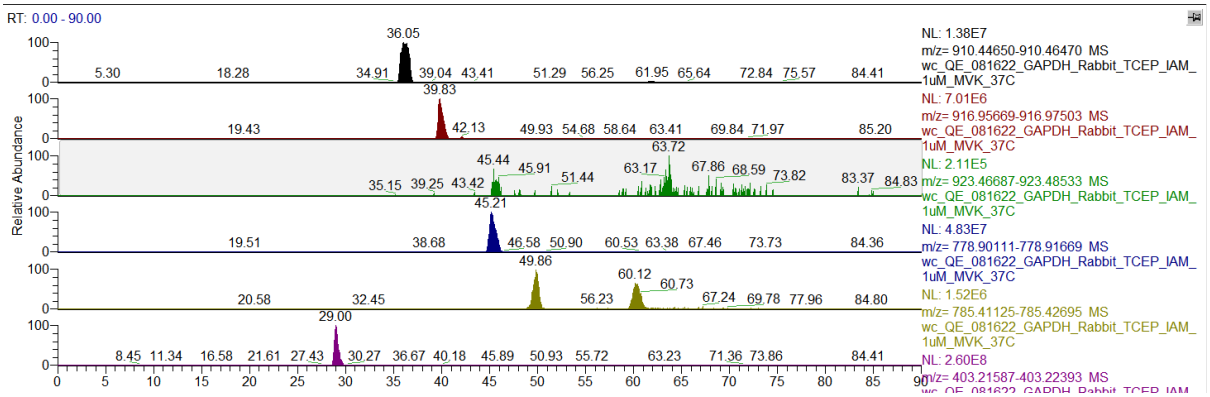

Figure 5. 9. Representative chromatogram of Rabbit GAPDH peptide 144-160 exposed to 1 µM MVK

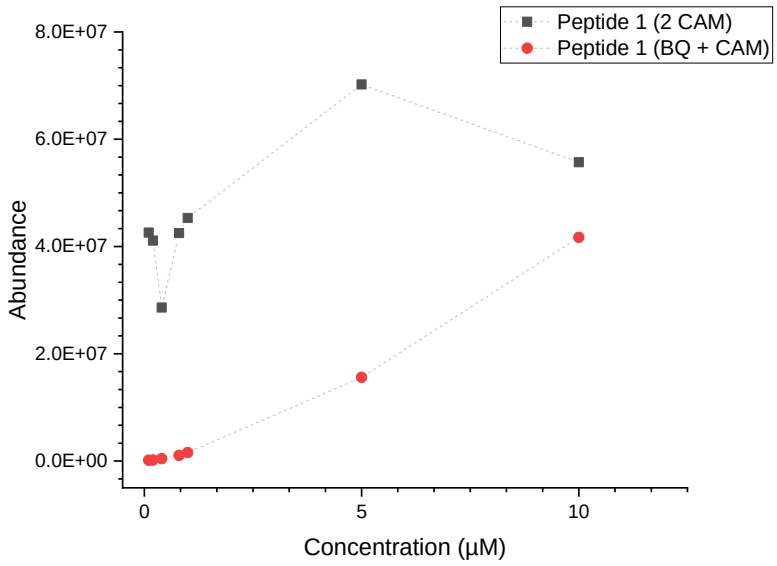

Figure 5. 10. Abundance versus concentration of peptide 1 treated with BQ

Figure 5. 10 (above) shows the abundance versus concentration dependence of peptide 1 labelled with 2 CAM and peptide 1 labelled with BQ + CAM over the concentration range from 100 nM to 10 µM. The abundance of BQ + CAM steadily increased with increasing BQ concentration exposure, whereas 2 CAM started to decrease at higher BQ concentrations.

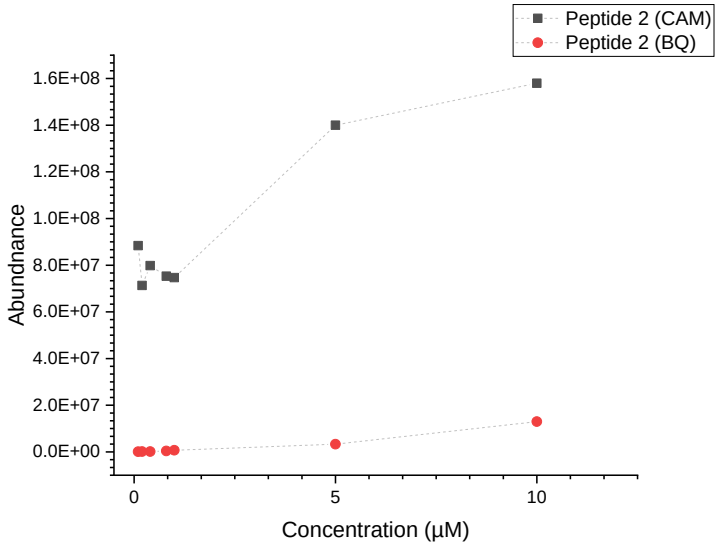

Figure 5. 11. Abundance versus concentration of peptide 2 treated with BQ

Figure 5. 11 (above) shows the abundance versus concentration dependence of peptide 2 labelled with CAM and peptide 1 labelled with BQ over the concentration range from 100 nM to 10 µM. The CAM labelled peptide 2 did not appear to be consumed over the concentration range due to the lower reactivity of peptide 2 towards BQ.

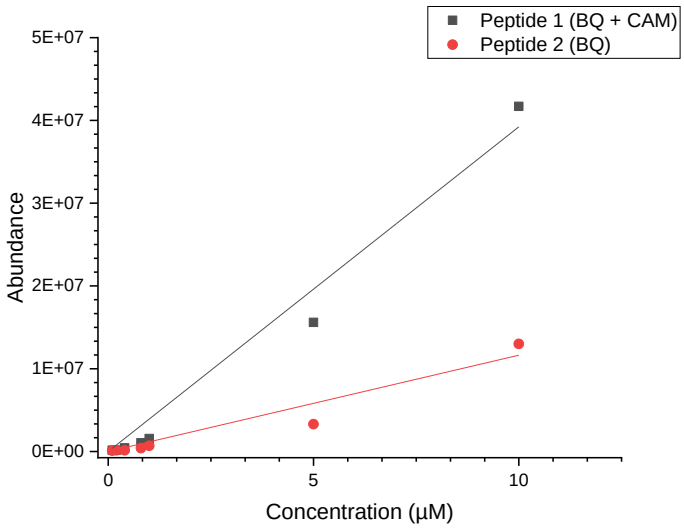

Figure 5. 12. BQ dose dependent response for peptide 1 versus peptide 2

Figure 5. 12 (above) shows the abundance versus concentration dependence of peptide 1 versus peptide 2 labelled with BQ over the concentration range from 100 nM to 10 µM. There appeared to be a dose dependent response of BQ towards both peptide 1 and peptide 2, with peptide 1 having a faster reactivity rate and peptide 2 have a slower reactivity rate towards BQ.

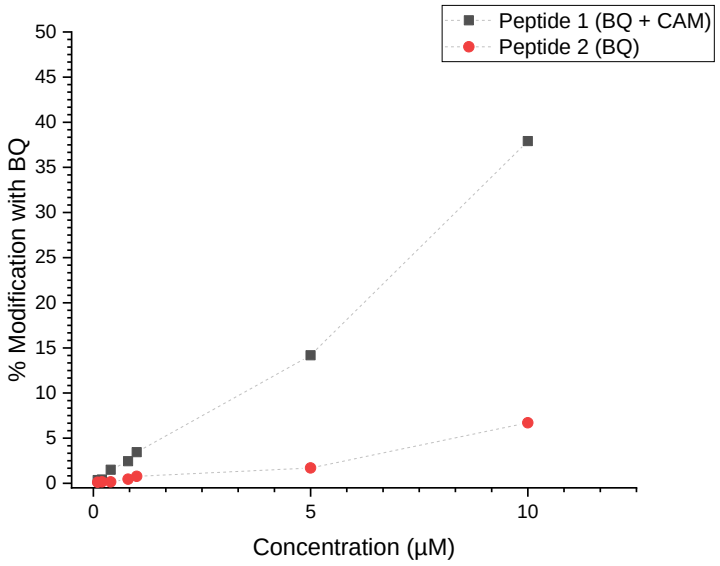

Figure 5. 13. Modification of peptide 1 versus peptide 2 exposed to BQ

Figure 5. 13 (above) shows the percent modification of peptide 1 versus peptide 2 exposed to BQ over the concentration range 100 nM to 10 µM. Peptide 1 appeared to be readily modified by BQ and at 10 µM BQ exposure, roughly 37% of the peptide was modified with respect to the unmodified control peptide. Peptide 2 appeared to have a slower reactivity rate than peptide 1 towards BQ and at 10 µM BQ exposure there was roughly 8% of the peptide that was modified. The theoretical maximum of modification is 50% since 20 µM of protein is being used and 10 µM of electrophile is the maximum amount that was used.

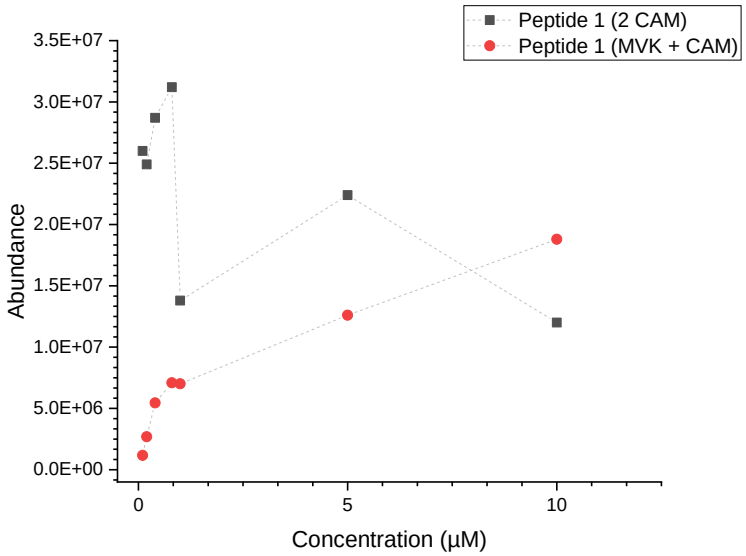

Figure 5. 14. Abundance versus concentration of peptide 1 treated with MVK

Figure 5. 14 (above) shows the abundance versus concentration dependence of peptide 1 labelled with 2 CAM and peptide 1 labelled with MVK + CAM over the concentration range from 100 nM to 10 µM. The abundance of MVK + CAM steadily increased with increasing MVK concentration exposure, whereas 2 CAM started to decrease at higher MVK concentrations.

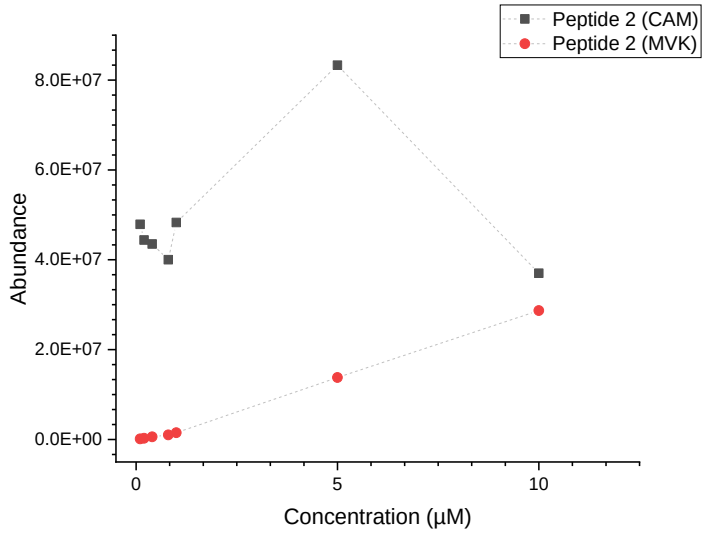

Figure 5. 15. Abundance versus concentration of peptide 2 treated with MVK

Figure 5. 15 (above) shows the abundance versus concentration dependence of peptide 2 labelled with CAM and peptide 1 labelled with MVK over the concentration range from 100 nM to 10 µM. The CAM labelled peptide 2 abundance started to decrease at the higher MVK concentrations, whereas the MVK labelled peptide 2 abundance was steadily increasing over the concentration range.

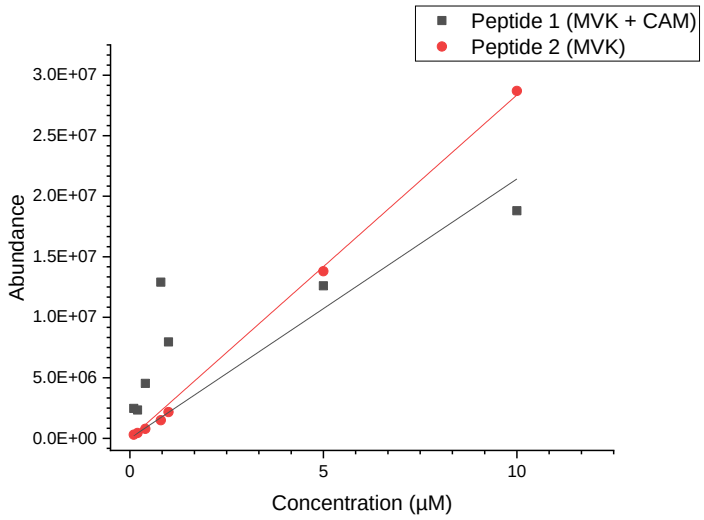

Figure 5. 16. MVK dose dependent response for peptide 1 versus peptide 2

Figure 5. 16 (above) shows the abundance versus concentration dependence of peptide 1 versus peptide 2 labelled with MVK over the concentration range from 100 nM to 10 µM. There appeared to be a dose dependent response of MVK towards both peptide 1 and peptide 2, with peptide 1 and peptide 2 having similar reactivity towards MVK.

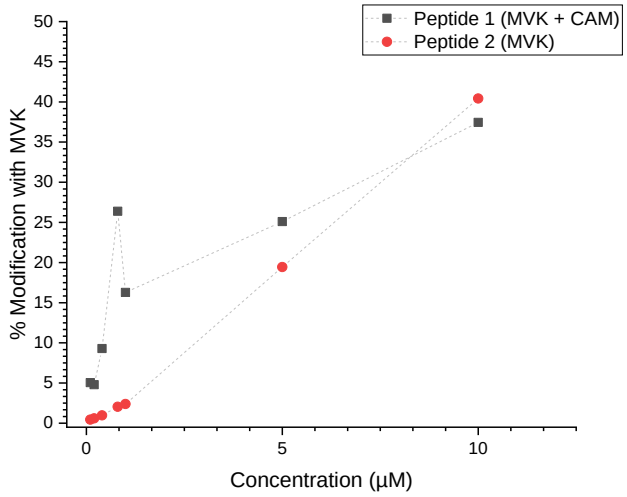

Figure 5. 17. Modification of peptide 1 versus peptide 2 exposed to MVK

Figure 5. 17 (above) shows the percent modification of peptide 1 versus peptide 2 exposed to MVK over the concentration range 100 nM to 10 µM. Peptide 1 appeared to be readily modified by MVK and at 10 µM MVK exposure, roughly 37% of the peptide was modified with respect to the unmodified control peptide. Peptide 2 appeared to have an equally high reactivity rate towards MVK and at 10 µM MVK exposure since there was roughly 34% of peptide 2 that was modified. The theoretical maximum of modification is 50% since 20 µM of protein is being used and 10 µM of electrophile is the maximum amount that was used.

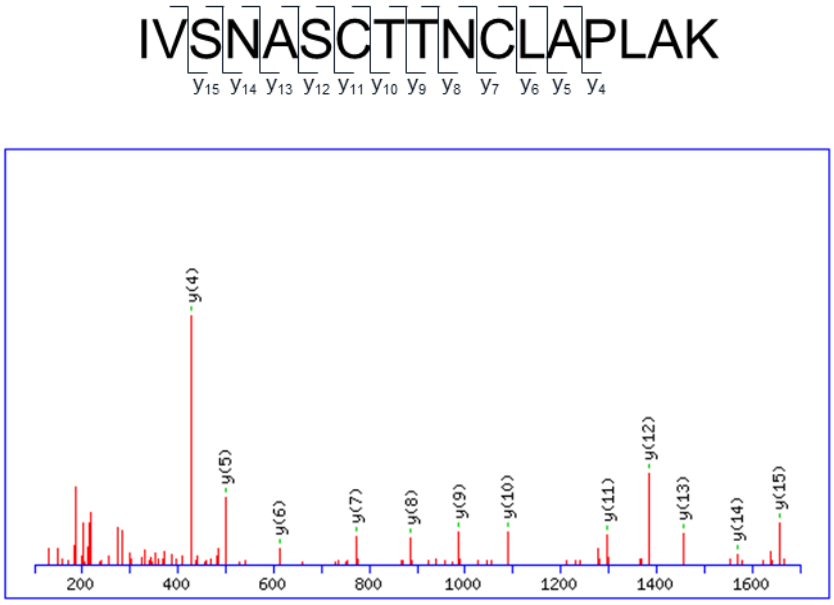

Figure 5. 18. Representative peptide fragment mass spectrum of peptide 1 treated with BQ (Rabbit)

Figure 5. 18 (above) is a representative peptide fragment mass spectrum of peptide 1 that was treated with 10 µM of BQ in the Rabbit species. The y-ion peptide ladder is used to confirm the mass and location of the cysteine labelled modification.

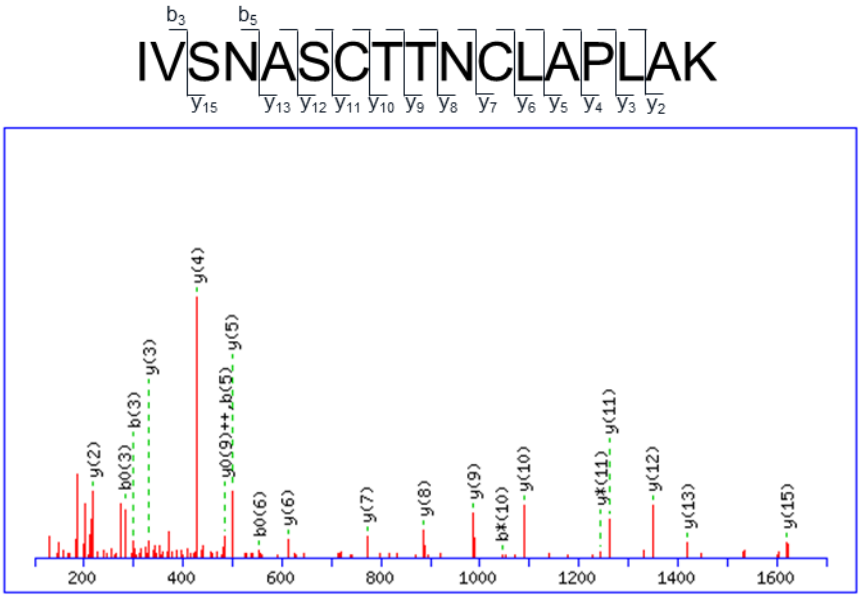

Figure 5. 19. Representative peptide fragment mass spectrum of peptide 1 treated with MVK (Rabbit)

Figure 5. 19 (above) is a representative peptide fragment mass spectrum of peptide 1 that was treated with 1 µM of MVK in the Rabbit species. The y-ion peptide ladder is used to confirm the mass and location of the cysteine labelled modification

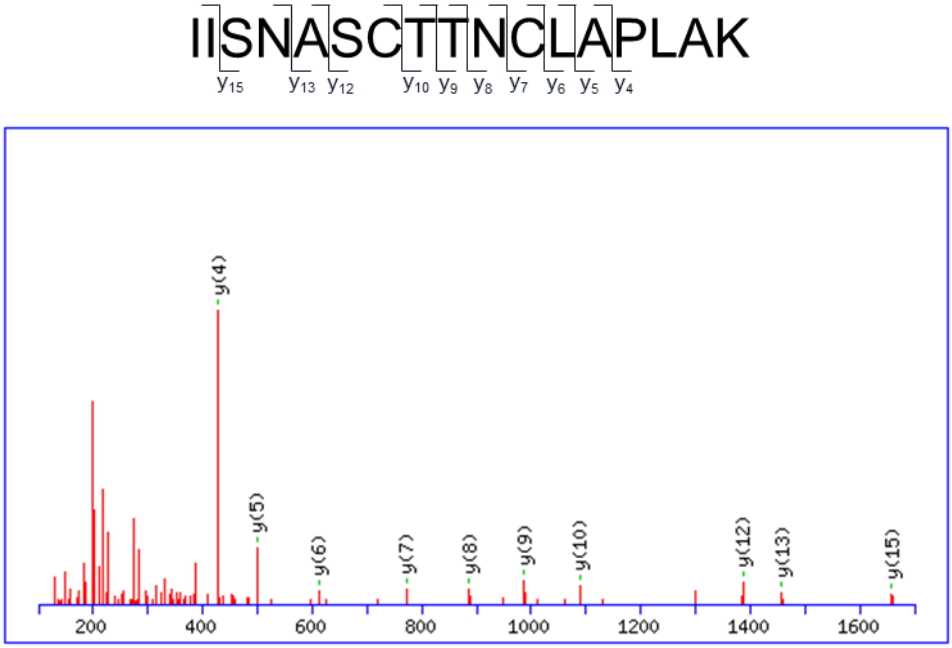

Figure 5. 20. Representative peptide fragment mass spectrum of peptide 1 treated with BQ (Human)

Figure 5. 20 (above) is a representative peptide fragment mass spectrum of peptide 1 that was treated with 10 µM of BQ in the Human species. The y-ion peptide ladder is used to confirm the mass and location of the cysteine labelled modification.

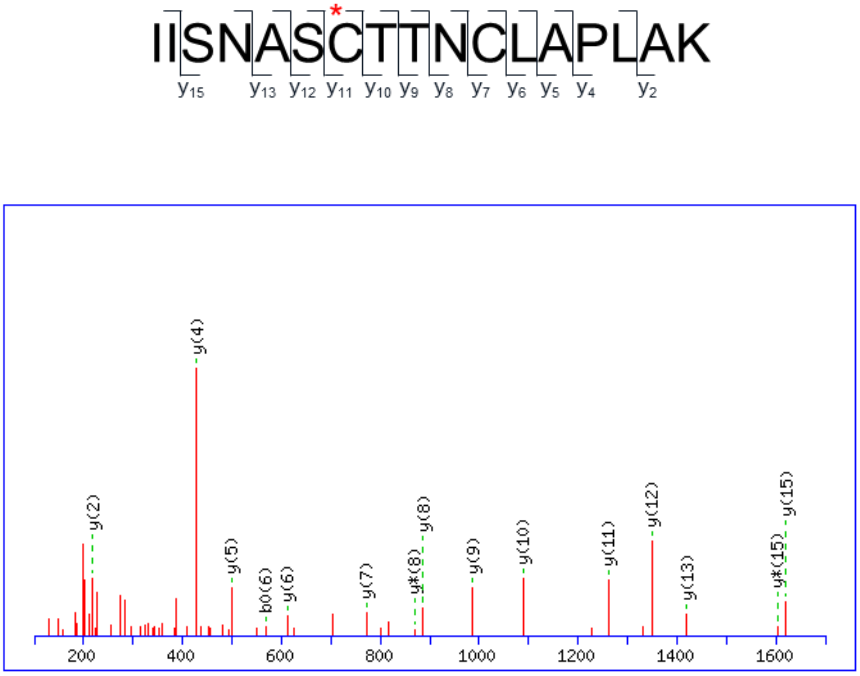

Figure 5. 21. Representative peptide fragment mass spectrum of peptide 1 treated with MVK (Human)

Figure 5. 21 (above) is a representative peptide fragment mass spectrum of peptide 1 that was treated with 10 µM of MVK in the Human species. The y-ion peptide ladder is used to confirm the mass and location of the cysteine labelled modification.

5.4 Conclusion

The intact protein analysis showed that GAPDH modification at the varying concentrations ranging from 500 nM to 10 µM of BQ was successful for both the Human and the Rabbit. The human and Rabbit GAPDH were modified at sub-micromolar concentrations, which is in good agreement with previous studies. The submicromolar inhibition was apparent in the catalytic activity assay studies, which showed about a 20% decrease in turnover at 100 µM concentrations. In addition, the Rabbit GAPDH enzyme was almost completed inhibited at 10 µM BQ exposure, which was demonstrated by the unchanged slope which is indicated of no conversion from NAD^+ to NADH. These results supported the intact protein results that showed that the modification of

GAPDH occurred with BQ, which started near 500 nM on the intact protein studies. Moreover, bottom-up proteomics confirmed the peptides mass fragments containing both the BQ and MVK modifications that were localized to the Cys 152 and Cys 247 on the Human protein and Cys 149 and Cys 245 on the Rabbit protein. The modification of peptide 1 by BQ appeared to have a dose dependent response as the concentration increased from 100 nM to 10 µM, wherein peptide 1 with 2 CAM appeared to decrease along the concentration range as expected. The modification of peptide 1 by MVK appears to have a somewhat log curvature, which is indicative of a saturation process. An unexpected result appeared that yielded a third species for peptide 1 when exposed to higher concentrations of MVK. The 2 MVK peptide 1 appears to begin to form at concentrations near 800 nM, which may account for the decrease in peptide 1 modification as the concentration increases due to a competing species now forming at a faster rate. Peptide 1 was modified faster with respect to BQ and MVK. Additionally, the modification of peptide 2 by BQ and MVK appeared to have a dose dependent response as the concentration increased from 100 nM to 10 µM, wherein the CAM modified peptide decreased minimally with BQ and drastically with MVK. This shows that MVK appeared to favor peptide 2 much greater than BQ favored peptide 2. Peptide 2 was modified equally as fast with respect to MVK and slower with respect to BQ. Peptide 1 was observed to be modified about 37% for BQ and as well as MVK exposure. This is in good agreement with what is expected to be the theoretical limit of 50% modification given that 20 µM of GAPDH and 10 µM of electrophile were the max concentration used. Overall, a mass spectrometry-based approach for the identification and quantification of BQ and MVK at physiologically relevant submicromolar concentrations using intact protein analysis, catalytic activity studies, and bottom-up proteomics was successfully performed.

Chapter 6: Future Outlook

6.1 [^{18}F]FBnTP PET Analogues

In chapter 2 and 3 of the PET probe [^{18}F]FBnTP synthesized using an automated synthesizer and was a useful imaging agent for imaging the *in vivo* mitochondrial potential in NSCLC, however due to its lipophilicity it was not able to cross the blood brain barrier (BBB). Currently, [^{18}F]FBnTP contains a phosphonium group with three aryl groups that are lipophilic and bulky, which also is recognized by the p-glycoprotein (P-gp) receptor and is removed as a xenobiotic.[168] A benefit of crossing the BBB is that various neurological diseases may stem from mitochondrial dysfunction in the brain such as parkinsons and alzheimers disease.[169] In order to address this limitation of [^{18}F]FBnTP, hydrophilic analogues can be synthesized with the goal and capability of penetrating the BBB. One route to increase the hydrophilicity is to modify the phosphonium group on [^{18}F]FBnTP, replacing the aryl rings for smaller or more polar functional groups. Groups that contain methyl or hydroxyethyl moieties can increase the hydrophilicity of the phosphonium groups and at the same time help retain the functionality of the PET probe of interest.

6.2 52A1 Stability

The 512 compound used for the radiation mitigation studies initially encountered a formulation issue, which required the synthesis of a novel analogue. 52A1 was then synthesized to alleviate this solubility issue that had arose from having a low lattice energy, which caused crystallization to form. 52A1 is a much better analogue than 512, however, there appears to be an additional formulation issue. Wherein the NO_2 moiety on the benzene ring appears to be a labile group, which can readily reduce the NO_2 to the NH_2 group during the last step of the synthesis. An alternative route could be to possibly protect this nitrous group during the reaction since that appears to labile step of this synthesis. Alternatively, a different class of the radiation mitigation

compounds found in the High Throughput Screening (HTS) could be explored further if this issue is not resolved.

6.3 GAPDH *in vitro* exposure

Future studies can include performing catalytic activity studies at 37˚C with the Human and Rabbit GAPDH since there could be drastic differences in reactivity towards these electrophiles between species at a biologically relevant temperature. Additionally, kinetic studies can be performed in order to assess the rate at which BQ and MVK modify each peptide containing the reactive cysteines. This can be achieved by conducting a catalytic activity study with a quicker scanning speed of the well plate reader to measure smaller intervals of time. In addition, a time course study can be performed by exposing BQ and MVK to quicker exposure times in order to measure the time dependent uptake of these electrophiles. Additionally, there is evidence that electrophiles such as 1,2 napthoquinone (NQ) and 2,3-dibutadione may not be cleared by the cell due to their off-target abilities to react with additional amino acids such as Arginine. Another area of exploration can be to perform proteomics studies on environmental samples as well as include cell studies with exposure to BQ, MVK. These environmental samples can include those exposed to biomass burning or E-cigarette smoke, which contain higher concentrations of MVK and BQ respectively. These samples can be analyzed using catalytic studies and proteomics can be performed right after with the same samples to get a comparable study for both methods.

Appendix

Electrochemical Fluorination and Radiofluorination of Methyl(phenylthiol)acetate Using Tetrabutylammonium Fluoride (TBAF)

A1.1 Introduction

Incorporation of fluorine into a lead molecule can have a positive impact on metabolic stability, pKa, intrinsic potency, membrane permeability and pharmacokinetic of bioactive molecules.[170–175] Organofluorine molecules can rarely be found in nature and hence the introduction of a fluorine atom into a naturally occurring organic molecule requires the development of appropriate synthetic methods developed in the lab. Fluorine gas and fluorinating agents derived from it have widely been used as the source of fluorine atom for fluorination of organic compounds.[176–179] However, fluorination of organic substances using fluorine gas is difficult because fluorine gas is highly toxic and reactive. Furthermore, the ^{18}F isotope of fluorine, which has been established as the most promising isotope for Positron Emission Tomography (PET), is most accessible and practical for PET tracer development in 18F-fluoride form produced via a $^{18}O\text{-}H_2O(p,n)^{18}F$ nuclear reaction in a cyclotron.[180] PET has extensive clinical applications in early disease diagnosis, treatment progression monitoring as well as in drug discovery and development.[1] Despite the synthesis of a wide variety of ^{18}F labeled PET probes, their clinical translation is often hindered due to a lack of viable late-stage synthesis methods with ^{18}F-fluoride and the 110-minute half-life of the isotope.[181] The biggest roadblock in making a wider scope of fluorinated molecules easily accessible, is that precursors with no positive charge at the site of fluorine labeling are not readily amenable to nucleophilic substitution reactions with fluoride.[182] Development of PET tracers and availability of fluorinated bioactive molecules synthesized by nucleophilic fluoride would benefit from a convenient late stage fluorination method.[183] Electrochemical nucleophilic fluorination of organic molecules has been reported as a powerful

method for introduction of the fluorine atom into organic compounds.[184–186] Electrochemical fluorination has commonly been performed in solutions containing an excess of poly HF salts such as $Et_3N.3HF$ and $Et_3N.4HF$ as a fluoride source.[187–190] However, HF salts are expensive, toxic and corrosive. Tetrabutylammonium fluoride (TBAF) is a source of fluoride which is less toxic, easier to handle and also inexpensive compared to HF salts, making it a suitable alternative for electrochemical fluorination. A further advantage of using TBAF, instead of HF salts as a source of fluoride, is the traditional use of ^{18}F-TBAF in radiofluorination.[191] Previous attempts at electrochemical radiofluorination with ^{18}F-poly-HF salts, which severely limits specific activity and places a theoretical limit on radiochemical yield, have been reported.[192,193] However, previous reports on the use TBAF for electrochemical fluorination of phenyl(2,2,2-trifluoroethyl)sulfane, have not been successful.[184] [^{18}F]fluoride in form of ^{18}F-TBAF in this report was obtained by first trapping [^{18}F]fluoride anion on an anion exchange resin in order to remove the water, and subsequent elution of [^{18}F]fluoride from the cartridge using tetrabutylammonium fluoride.

Electrochemical fluorination using TBAF was only made possible with the addition of trifluoromethanesulfonic (triflic) acid during electrolysis. Triflic acid is a known super acid whose conjugate base is a very weak nucleophile.[194] The addition of triflic acid may form HF molecules that can participate in electrochemical fluorination, while the very weak conjugate base of triflic acid will not react with the intermediate carbocations formed during electrochemical oxidation.

The successful electrochemical fluorination of methyl(phenylthio)acetate using TBAF as a source of fluorine will be shown. Furthermore, ^{18}F-methyl 2- fluoro-2-(phenylthio)acetate was radiosynthesized using ^{18}F-TBAF as a source of fluorine. The products were detected and analyzed using HPLC, GC-MS and NMR. Effect of several parameters such as electrolysis potential, time, temperature, triflic acid concentration and TBAF concentration were investigated and optimized.

A1.2 Experimental Methods and Materials

High-resolution mass spectra and chromatograms were obtained with an Agilent 5975C TAD inert MSD mass spectrometer coupled with an Agilent 7890A gas chromatograph. Cyclic voltammeteric (CV) and electrosynthesis experiments were performed using the Metrohm PGSTAT128N electrochemical workstation. All CVs were performed at room temperature using a 200 mV/s scan rate.

Radiofluorination conversion was measured using Radio-thin-layer-chromatography (radio- TLC). Radio-TLC was performed on silica plates (TLC Silica gel 60 W F_{254}s, Merck). After dropping a sample volume (~1–5 µL) using a glass capillary, the plate was developed in the mobile phase (ACN). Chromatograms were obtained using a radio-TLC scanner (miniGita Star, Raytest).

Analytical High Performance Liquid Chromatography (HPLC), equipped with a UV and gamma detector was used to determine radiochemical purity (RCP) of the radio-fluorinated product. HPLC was performed using a 1200 Series HPLC system (Agilent Technologies) equipped with a GabiStar flow-through gamma detector (Raytest). Data acquisition and processing was performed using GINA Star Software version 5.9 Service Pack 17 (Raytest). Typically, 20 µL of radioactive sample was diluted with 180 µL of ACN and 5–20 µL of this solution was injected for HPLC analysis. Column: Phenomenex Luna 5u C18 (2) 100 A, 250 × 4.6 mm, 5 micron. Gradient: A = ACN; B = water; flow rate = 1.8 mL/min; 0–12 min 90% B to 5% B, 12–13 min 5% B, 13–14 min 5% B to 90% B.

Radio-TLC chromatograms were used to measure radiochemical conversions (RCC). RCP and RCC were measured by dividing the area under the curve (AUC) for the desired product by the sum of AUC for all peaks. The TLC purity accounts for unreacted ^{18}F-fluoride while the HPLC

purity corrects for radiochemical side-products. The radiochemical fluorination efficiency (RCFE) was determined by the equation: RCFE = TLC RCC × HPLC RCP.

The GC-MS, TLC and HPLC analysis were performed on crude samples, and the reported yields in optimization studies are based on the quantification of GCMS results. The reaction products were HPLC purified and isolated for purposes of proton and fluorine NMR analysis for further identification.

The electrochemical fluorination and CVs were carried out using a conventional undivided 3-electrode cell with two platinum wires (length = 200 mm, diameter = 0.33 mm) as working and counter electrode and Ag/Ag^+ reference electrode in a 13.2 mL solution containing dry ACN (11 mL), 2 mL of 1 M TBAF solution in tetrahydrofuran (THF) (154 mM TBAF final concentration), 120 µL of triflic acid (104.6 mM final concentration) and 50.8 µL of methyl(phenylthio)acetate (25 mM final concentration). The reference electrode solution was 10 mM $AgNO_3$ plus 100 mM tetrabutylammonium perchlorate in dry ACN. The reference electrode solution was separated from the reaction mixture by porous glass frit.

The counter electrode and working electrode were cleaned before each experiment using potential cycling in 1 M sulfuric acid solution in water. The electrodes were cycled between −2 V and 2 V (2 electrode configuration) 10 times before each experiment.

Trifluoromethanesulfonic acid (triflic acid, CF_3SO_3H, 99%) and methyl(phenylthio)acetate ($C_9H_{10}O_2S$, 99%) were purchased from Oakwood Chemical. Acetonitrile (ACN, anhydrous, 98%), tetrabutylammonium fluoride solution 1.0 M in THF (TBAF solution, ~5 wt% water) and platinum wire (99.9%) were purchased from Sigma-Aldrich.

Electrolysis was performed using a constant potential technique while the solution was stirred at 300 rpm. In order to prevent formation of polymerized products on the working electrode, the polarity of the electrode was alternated every 60 s between the chosen fluorination potential and −0.6 V; electrode was kept at −0.6 V for 5 s.

No-carrier-added ^{18}F-fluoride was produced by the (p,n) reaction of $^{18}O–H_2O$ (84% isotopic purity, Medical Isotopes) in a RDS-112 cyclotron (Siemens) at 11 MeV using a 1 mL tantalum target with havar foil.[195] The radioactive isotope was trapped on an anion exchange resin by passing through the 1mL of bombarded $^{18}O–H_2O$. Most of the water on the resin was removed by washing with 10 mL of anhydrous ACN and drying with ultra-pure N_2 for 10 min. [^{18}F]fluoride was subsequently eluted out from the cartridge with a 2 mL solution containing 0.5 mmol TBAF in THF + ACN solution (1:1). In a typical experiment, approximately 5 mCi was eluted from the anion exchange cartridge in ^{18}F-TBAF form in dry ACN.

A1.3 Results and Discussion

Figure A1.1 shows CVs of different combination of chemicals used in the electrochemical fluorination experiments. It can be seen that the CV of ACN + precursor shows a very small cathodic or anodic current between −1 V to 2 V. While CVs of ACN + triflic acid and ACN + triflic acid + THF also shows very small anodic current at potentials higher than 0 V vs Ag/Ag^+, a high cathodic current can be observed at potentials below 0 V vs Ag/Ag^+, which can be attributed to the hydrogen evolution on the working electrode. Although ACN + precursor and ACN + triflic acid don’t show any anodic current at positive potentials, a combination of these (ACN + triflic acid + precursor) displays an anodic current at potentials higher than 1 V vs Ag/Ag^+.

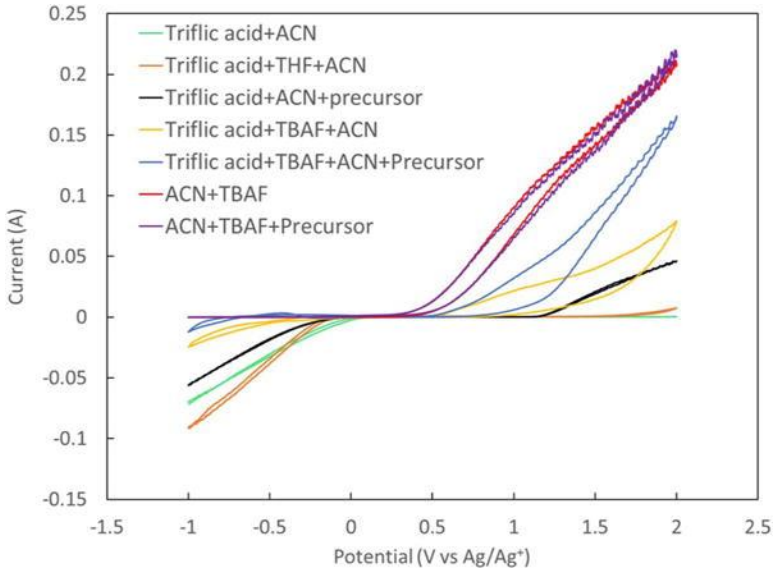

Figure A1. 1. CVs of different combination of materials were used in the electrochemical fluorination of methyl(phenylthio)acetate. The CVs were run using 200 mv.s−1 at room temperature (21°C)

This can be due to the oxidation of the precursor, promoted by the addition of triflic acid. Furthermore, CVs of ACN + TBAF and ACN + TBAF + precursor are very similar, in the way that they don't show any cathodic current, while at potentials higher than 0.5 V vs Ag/Ag^+ an increase in anodic current can be observed. Similarity in anodic current is due to the high oxidation current from the TBAF solution which has a lower onset potential and occurs at much higher rate compared to the oxidation of the precursor and masks any additional negligible current contribution from the oxidation of the precursor. The addition of triflic acid to these solutions causes a sharp decrease in the anodic current, which is in line with the proposed reaction of triflic acid with TBAF, with hydrogen fluoride as a possible product of this reaction.

The anodic fluorination of methyl(phenylthio)acetate was carried out at constant potential in an undivided cell. The products were analyzed using GC-MS. Figure A1.2 shows a representative GC-MS chromatogram of the solution before and after electrolysis at 1.4 V for 30 min at room temperature. The chromatogram of the solution before electrolysis shows only one peak for the

precursor with the m/z equal to 182. Figure A1.2 shows that after electrolysis the precursor peak area has decreased and the product peak is observed at 11 min with the m/z of 200.

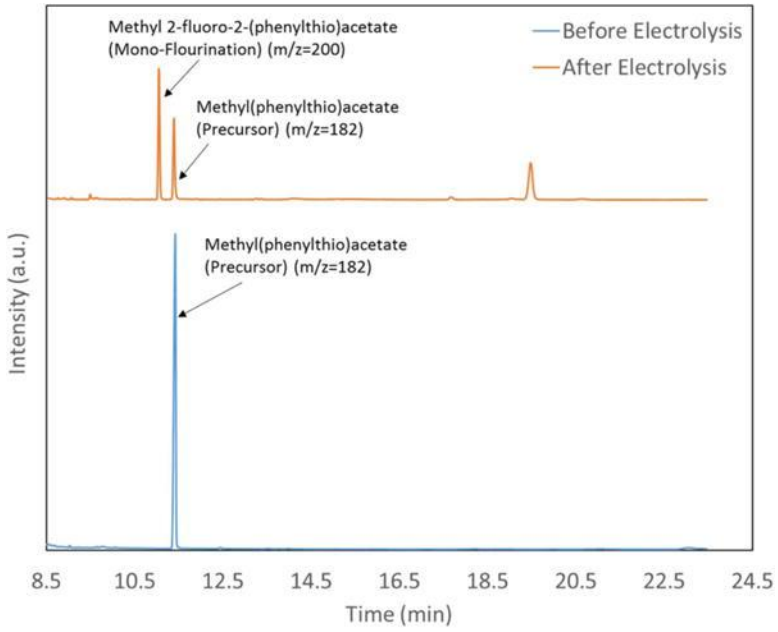

Figure A1. 2. GC-MS chromatogram of the solution before and after electrochemical fluorination. The solution contains 25 mM of 1, 154 mM TBAF and 104.6 mM of triflic acid in acetonitrile.

The 11 min product is attributed to methyl 2-fluoro-2- (phenylthio)acetate (**2**) (monofluorination). The schematic for the electrochemical fluorination of methyl(phenylthio)acetate (**1**) has been shown in the Figure A1.3.

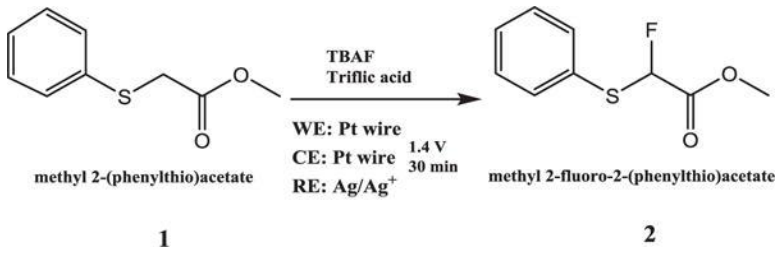

Figure A1. 3. Schematic of the electrochemical fluorination of methyl-2(phenylthio)acetate 1 using TBAF

Product yields and precursor conversion of the electrofluorinated samples are presented in Figure A1.4 with different oxidation potentials and in Figure A1.5 with different electrolysis times.

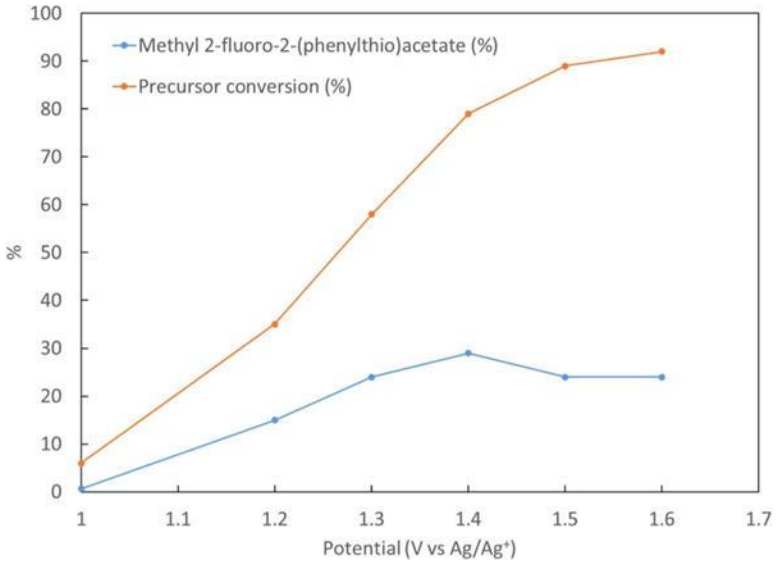

Figure A1. 4. Effect of electrolysis potential on the yield of product and precursor conversion. Synthesis has been performed at the constant time of 30 min, using ACN solution containing 154 mM of TBAF, 25 mM of precursor 1 and 104.6 of triflic acid

Experiments were performed in triplicates. It can be seen that by increasing the potential from 1 V to 1.4 V vs Ag/Ag^{+} both the yields and precursor conversion increase. However, further increase in the potential reduces yields.

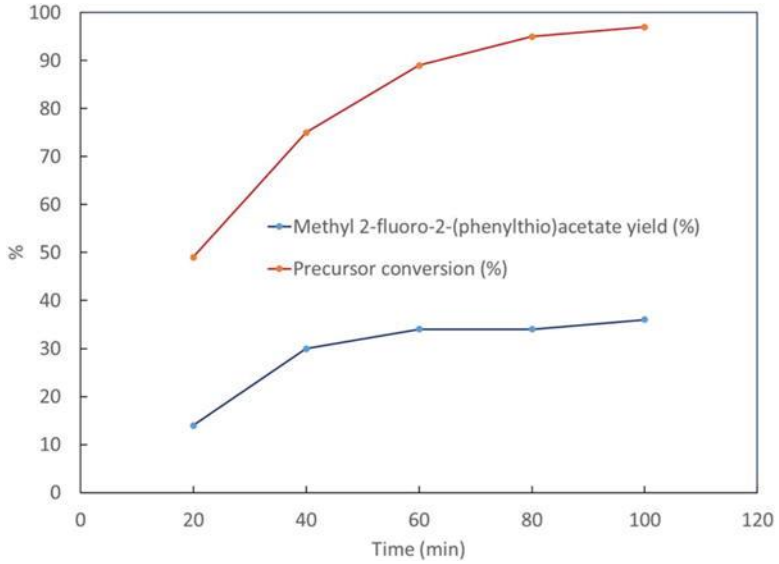

Figure A1. 5 Effect of time on the yield of product and precursor conversion. Synthesis has been performed at constant potential of 1.4 V vs Ag/Ag+, using ACN solution containing 154 mM of TBAF, 25.1 mM of 1 and 104.56 of triflic acid

This may be due to enhanced product oxidation and decomposition at potentials higher than 1.4 V vs Ag/Ag^{+}. It can also be seen from Table A1.2 that by increasing electrolysis time, the yield increases with time until a saturation is reached at 36% yield for **2** at 100 min when most of the precursor has been consumed.

Table A1. 1. Effect of acid type on the product yield and precursor conversion. Synthesis was performed at constant time and potential of 30 min and 1.4 V vs Ag/Ag+, using ACN solution containing 154 mM of TBAF, 25 mM of 1 and 104.6 mM acid

Type of Acid	**Methyl 2-fluoro-2-(phenylthio) acetate yield (%)**	**Precursor conversion (%)**
Trifluoromethanesulfonic Acid	29 ± 2	74 ± 14
Sulfuric Acid	3.0 ± 0.2	11 ± 2
Acetic Acid	0.3 ± 0.1	42 ± 8

A shorter electrolysis time of 30 min with a comparable yield of 29% was selected for further optimization. This was selected in preparation for radiochemical fluorination with ^{18}F-fluoride, which has a 110 min half-life, and benefits from increased non-decay-corrected radiochemical yield with shorter synthesis times.

The effect of triflic acid concentration was also examined. The results are shown in Figure A6. When acid concentration increases from 0 to 104.6 mM yield of **2** increases from 0.7% to 29%. Further increase in acid concentration beyond 104.6 mM results in a decrease in yield of **2** until a yield of 0.03% is reached using 208 mM triflic acid.

Electrofluorination was performed using triflic acid, acetic acid and sulfuric acid to study the effect of acid type on product yield. The results are shown in the Table A1.1, with triflic acid providing the highest precursor conversion and yield for **2**.

Table A1. 2. shows the results of the electrofluorination experiments performed at three different temperatures. It was observed that elevating the temperature has a positive effect on the electrofluorination yield

Temperature (°C)	**Methyl 2-fluoro-2-(phenylthio)acetate (%)**	**Precursor conversion (%)**
0	7.6 ± 0.5	65 ± 12
21	29 ± 2	74 ± 14
60	44 ± 3	63 ± 12

For instance, the yield of the **2** could be increased from 8% to 44% by increasing temperature from 0 °C to 60°C. Elevating the temperature can enhance the diffusion of the molecules in the solution leading to increased yields. The solution was also sonicated in order to confirm if promoting convection in the solution could enhance the yield. Sonication at room temperature increased the yield of **2** from 29% to 42%, a similar gain in yield as was observed with the increase in temperature.

It was also observed that triflic acid to TBAF concentration ratio has a crucial effect on the electrofluorination yield. As the TBAF concentration was decreased and triflic acid concentration was maintained constant, much lower yield of **2** was observed as compared to when TBAF and triflic acid concentrations were proportionally decreased together to maintain a constant ratio. The triflic acid to TBAF ratio, with 154 mM of TBAF, was optimized at 0.68 from the data in Figure A1.6.

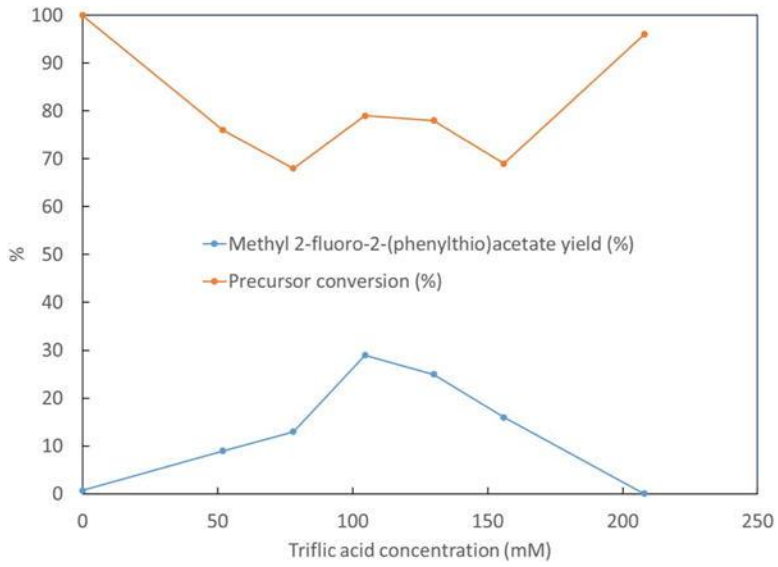

Figure A1. 6. Effect of triflic acid concentration on the product yield and precursor conversion. Synthesis has been performed at constant time and potential of 30 min and 1.4 V vs Ag/Ag+, using ACN solution containing triflic acid, 154 mM of TBAF and 25 mM of 1

To study the effect of acid to TBAF concentration ratio, two sets of experiments were performed. In the first set the concentration of TBAF was changed and the triflic acid concentration was kept constant, in the second set the TBAF concentration was changed and the triflic acid concentration also was changed in order to keep the triflic acid to TBAF concentration ratio constant at 0.68. The results are compared and presented in the Table A1.3 for TBAF concentration ranging from 154 mM to 10 mM.

Synthesis was performed at constant time and potential of 30 min and 1.4 V vs Ag/Ag+, using ACN solution containing triflic acid, TBAF, and 25 mM of 1.

Table A1. 3. Effect of triflic acid to TBAF concentration ratio on the product yield and precursor conversion

TBAF Concentration (mM)	**Acid Concentration (mM)/TBAF concentration (mM)**	**Methyl 2-fluoro-2-(phenylthio)acetate yield (%)**	**Precursor conversion (%)**
154	0.68	29 ± 2	74 ± 14

	1.36	0.03 ± 0.01	95 ± 3
100	0.68	21 ± 2	68 ± 12
	1.04	5.0 ± 0.3	69 ± 13
25	0.68	6.0 ± 0.4	37 ± 7
	4.16	0	94 ± 3
10	0.68	3.0 ± 0.2	24 ± 4
	10.40	0	74 ± 13

One of the advantages of using TBAF as a fluoride source in electrochemical fluorination is its compatibility and traditional use in radiofluorination with ^{18}F-fluoride. Compared with poly-HF salts, TBAF introduces fewer carrier ^{19}F-fluoride molecules, increasing specific activity and radiochemical yield, which is measured with respect to ^{18}F-fluoride incorporation into the desired product. Since the concentration of ^{18}F-fluoride used in radiochemistry is negligibly small, we studied the effect of decreasing TBAF concentration on electrofluorination yield. The results are shown in Table A1.4, indicating that lowering the fluoride concentration from 308 mM to 154 mM does not significantly change the yield of **2**, however a further decrease in fluoride concentration below 154 mM decreases yield of **2**.

Synthesis was performed at constant time and potential of 30 min and 1.4 V vs Ag/Ag+, using ACN solution containing 154 mM of TBAF, 25 mM of 1 and the ratio of triflic acid to TBAF concentration was kept constant at 0.68.

Table A1. 4. Effect of TBAF concentration on the product yield and precursor conversion

TBAF Concentration (mM)	Methyl 2-fluoro-2-(phenylthio)acetate yield (%)	Precursor conversion (%)	Methyl 2-fluoro-2-(phenylthio)acetate yield (%)[a]
308	29 ± 2	76 ± 14	2.5 ± 0.2
154	29 ± 2	74 ± 14	5.0 ± 0.3
100	21 ± 2	68 ± 12	5.0 ±0.3
25	6.0 ± 0.4	37 ± 7	5.5 ± 0.4
10	3.0 ±0.2	24 ± 4	7.5 ± 0.5
5	0.15 ± 0.01	10 ± 2	0.75 ± 0.05

While lowering fluorine concentration below the concentration of precursor would limit the theoretical chemical yield, the decrease in yield at higher concentrations may be attributed to the limited lifetime of carbocations formed at the surface of the working electrode. At lower concentrations of TBAF, cationic intermediates created on the anode with no fluoride in close vicinity, will have a diminishing chance to react with the fluoride nucleophile before they undergo side reactions. Table A1.4 also shows the yield of **2** based on the fluoride concentration. It can be seen that by lowering the fluoride concentration from 308 mM to 10 mM the yield of **2** increases, while a further decrease in concentration of fluoride below 10 mM causes a drastic decrease in the yield of **2**.

Electrochemical radiofluorination of the **1** was successfully achieved using the optimized parameters obtained from the cold electrofluorination experiments. (1.4 V, 30 min, 60°C, 154 mM of TBAF, 25 mM of **1** and 104.6 mM of triflic acid). Radiochemical fluorination efficiency obtained by TLC and gamma HPLC was 7 ± 1% (n = 3). The chemical yield (based on the initial precursor concentration) obtained from the decayed samples analyzed by GC-MS showed a yield of 43% ±

3% (n = 3), which would predict a fluorination yield (based on the initial fluorine concentration) of 7 ± 1% (n = 3) for the mono-fluorinated product, in line with the radiochemical yields obtained.

A1.4 Conclusions

For the first time, electrochemical fluorination of methyl(phenylthio)acetate has been achieved using TBAF as a source of fluorine under controlled potentiostatic conditions. It was observed that the use of triflic acid along with TBAF is crucial for successful fluorination and that the TBAF to triflic acid concentration ratio plays a key role in the process. Electrochemical cell parameters such as potential, electrolysis time, and temperature as well concentrations of fluoride source and triflic acid were optimized. CVs guided the selection of oxidation potentials and our understanding of the electrochemical oxidation/reduction response of the system. The optimum oxidation potential of **1** was found to be 1.4 V vs Ag/Ag^+. Potentials higher than 1.4 V vs Ag/Ag^+ resulted in lower yields, likely due to the breakdown of the product. Fluorination at potentials between 1.3 V vs Ag/Ag^+ and 1.1 V vs Ag/Ag^+ required a long time to achieve acceptable yields, which isn't desirable for radioelectrochemical fluorination with ^{18}F-fluoride, which has a 110 min half- life. It was also observed that elevating temperature and sonication could enhance the yield. The highest yield for the mono fluorinated product at 44% was obtained after 30 min of electrolysis at 1.4 V vs ag/Ag^+ using an ACN solution containing 154 mM of TBAF, 25 mM of precursor **1** and 104.6 mM of triflic acid at 60°C.

Electrochemical radiofluorination of methyl 2- [^{18}F]fluoro-2-(phenothio) acetate was confirmed by GC-MS, radio-TLC and HPLC analysis. A radiochemical fluorination efficiency of 7 ± 1% was achieved under the same conditions as the optimized cold reaction for the mono fluorinated product.

A2.1 Extended Figures

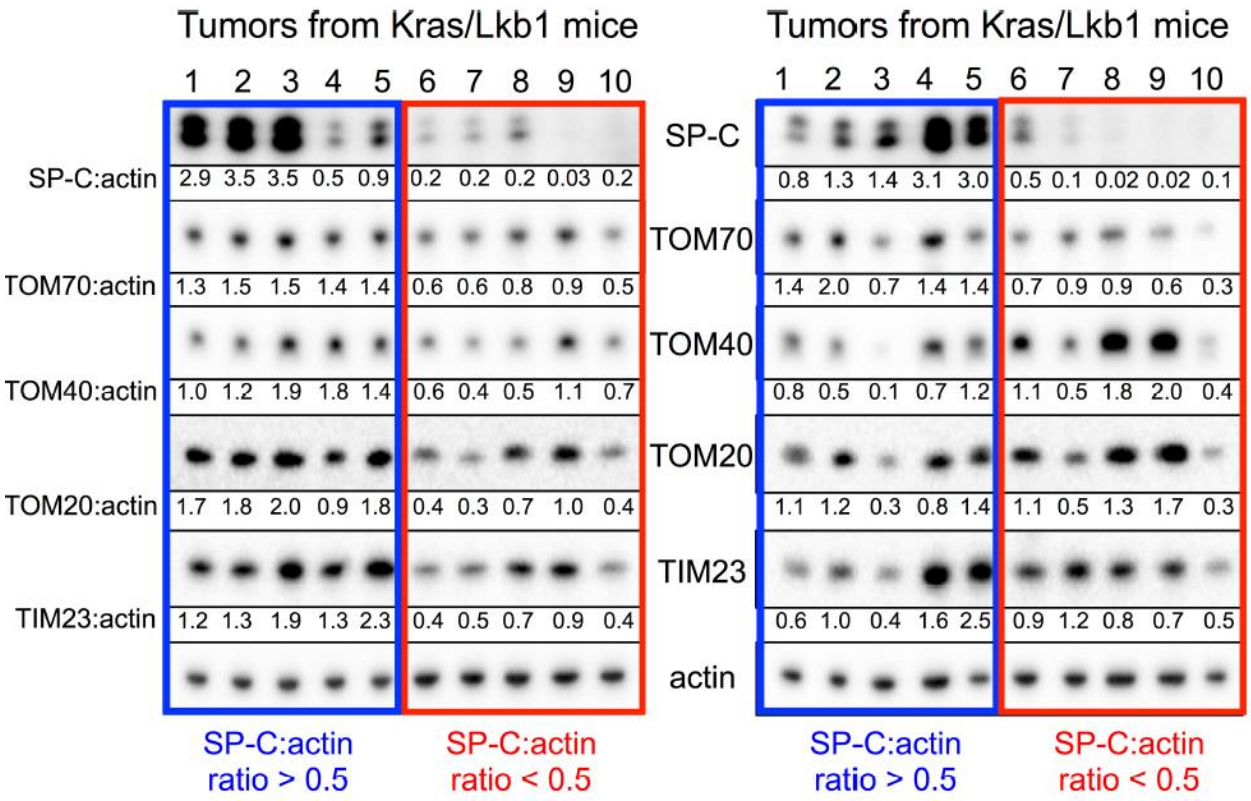

Figure A2. 1. Mitochondrial markers in KL mouse lung tumors

Whole-cell lysates from lung tumors isolated from *KL* mice were immunoblotted with the indicated antibodies. Tumors with high levels of the ratio of SP-C to actin (>0.5) were defined as ADCs (blue box), whereas tumors with low SP-C to actin ratios (<0.5) were defined as SCCs (red box). Each lane represents an individual tumor isolated from *KL* mice. Western blot was done on 20 individual tumors isolated from *KL* mice from three independent experiments.

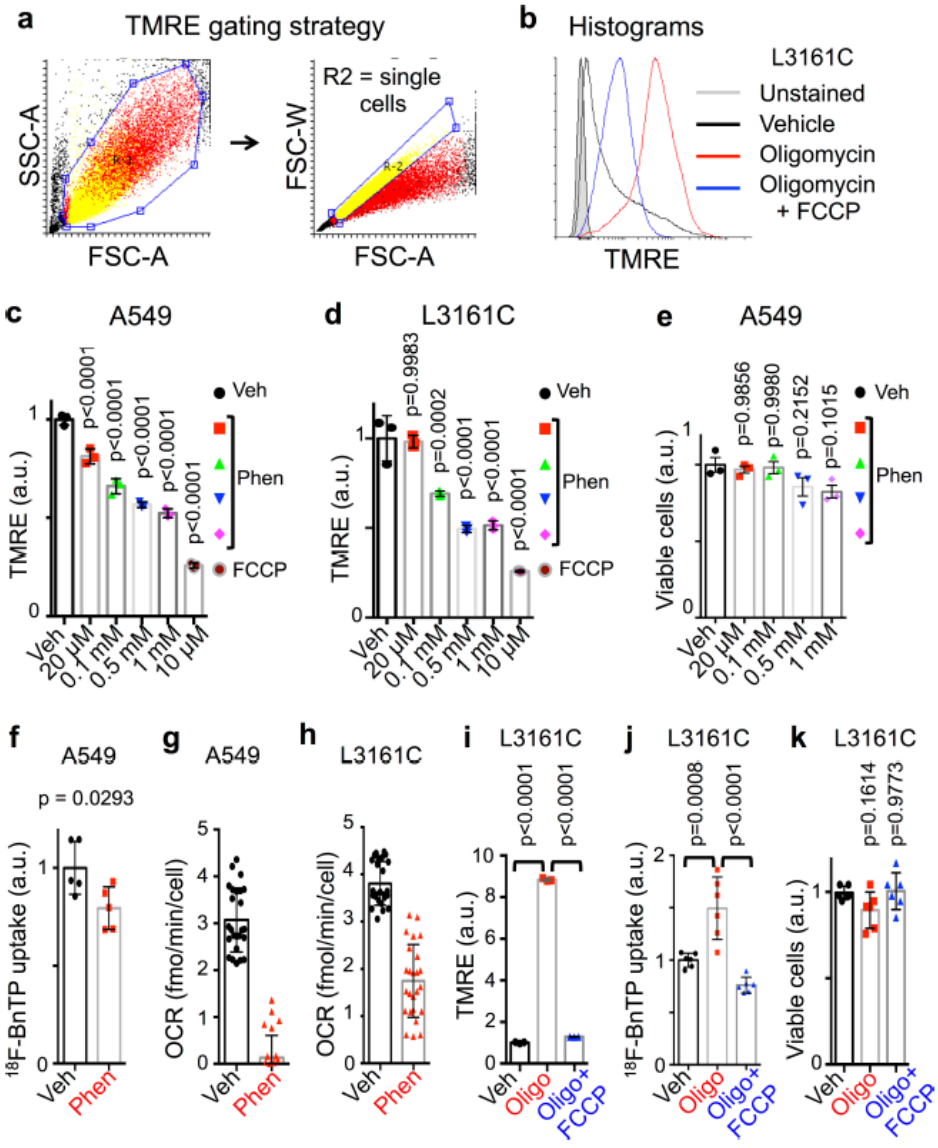

Figure A2. 2. Measuring mitochondrial membrane potential in vitro in A549 and L3161C cells

a, Gating strategy used for the quantification of TMRE signal. The R2 region representing single cells was used for quantification of the TMRE signal. **b**, Overlay histogram showing shifts in TMRE staining in L3161C cells treated with vehicle, 8 µM oligomycin or 8 µM oligomycin plus 4 µM FCCP. **c**, TMRE measurements in A549 cells treated with the indicated concentrations of phenformin or FCCP for 3 h (*n* = 3 biological replicates). **d**, TMRE measurements in mouse cell line L3161C treated with the indicated concentrations of phenformin or FCCP for 3 h (*n* = 3 biological replicates). **e**, Viability of A549 cells treated with the indicated concentrations of phenformin for 3 h (*n* = 3 biological replicates). **f**, Uptake of 18F-BnTP probe measured by gamma counter in A549 cells treated with 1 mM phenformin for 3 h (*n* = 5 biological replicates). **g**, OCR per cell measured in A549 cells treated acutely with 1 mM phenformin (*n* = 25 technical replicates). **h**, OCR per cell measured in mouse cell line L3161C treated acutely with 1 mM phenformin (*n* = 25 technical replicates). **i**, TMRE measurements in mouse cell line L3161C treated with vehicle, 8 µM oligomycin, or 8 µM oligomycin with 4 µM FCCP for 3 h (*n* = 3 biological

replicates). **j**, Uptake of 18F-BnTP probe measured by gamma counter in mouse L3161C cells treated with vehicle, 8 μM oligomycin, or 8 μM oligomycin with 4 μM FCCP for 3 h (*n* = 6 biological replicates). **k**, Viability of L3161C cells treated as in **j** (*n* = 6 biological replicates). Data are mean ±} s.d. Experiments in **c**–**i**, were repeated twice with similar results. Experiments in **j** and **k** were done once.

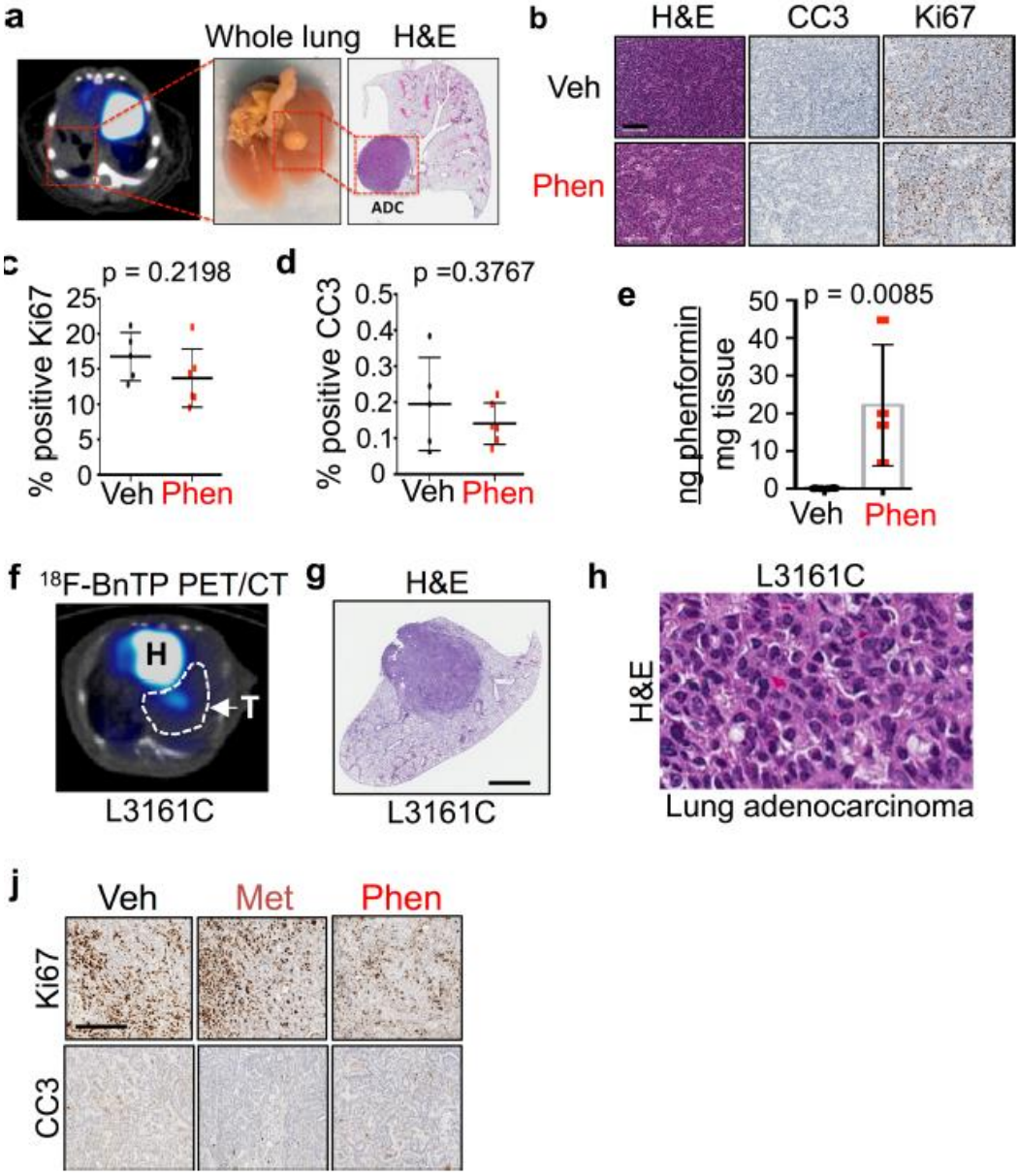

Figure A2. 3. Short-term treatment with phenformin does not lead to changes in proliferation or apoptosis

a, Transverse 18F-BnTP PET–CT overlay (left) of mouse lung (middle) after treatment with phenformin. H&E staining of a lung lobe with an ADC tumor (right). **b**, Representative slides stained with H&E (left), CC3 (middle) and Ki67 (right), from tumors from *KL* mice treated with vehicle (top) or phenformin (bottom). Experiment was performed once on slides from *n* = 5 (vehicle) and *n* = 6 (phenformin) mouse lungs. **c**, **d**, Quantification of staining for Ki67 (**c**) and CC3 (**d**) for tumors from *KL* mice treated with vehicle (*n* = 5 mice) or phenformin (*n* = 6 mice). Experiment was performed once. **e**, Phenformin in lung tumors isolated form *KL* mice was

quantified using liquid chromatography–mass spectroscopy. Tumors were isolated from mice treated with vehicle (*n* = 6) or 100 mg kg−1 (*n* = 2) or 200 mg kg−1 phenformin (*n* = 2) for 5 days. Experiment was performed once. **f**, Representative 18F-BnTP PET–CT overlay of a tumor formed by transthoracically implanted L3161C lung cells into syngeneic recipient mice. This image is representative of at least 20 PET–CT images. **g**, H&E slide of a tumor formed as in **f**. **h**, Higher magnification image of H&E staining of tumor formed by L3161C mouse cell line as in **f**. **j**, Representative slides stained with Ki67 (top), and CC3 (bottom) from tumors formed by transthoracically transplanted L3161C cells that were treated with vehicle, metformin or phenformin. Experiment was performed once on slides from *n* = 8 (vehicle), *n* = 5 (metformin) or *n* = 6 (phenformin) tumors. Data are mean ±} s.d. *P* values determined by unpaired two-tailed *t*-test.

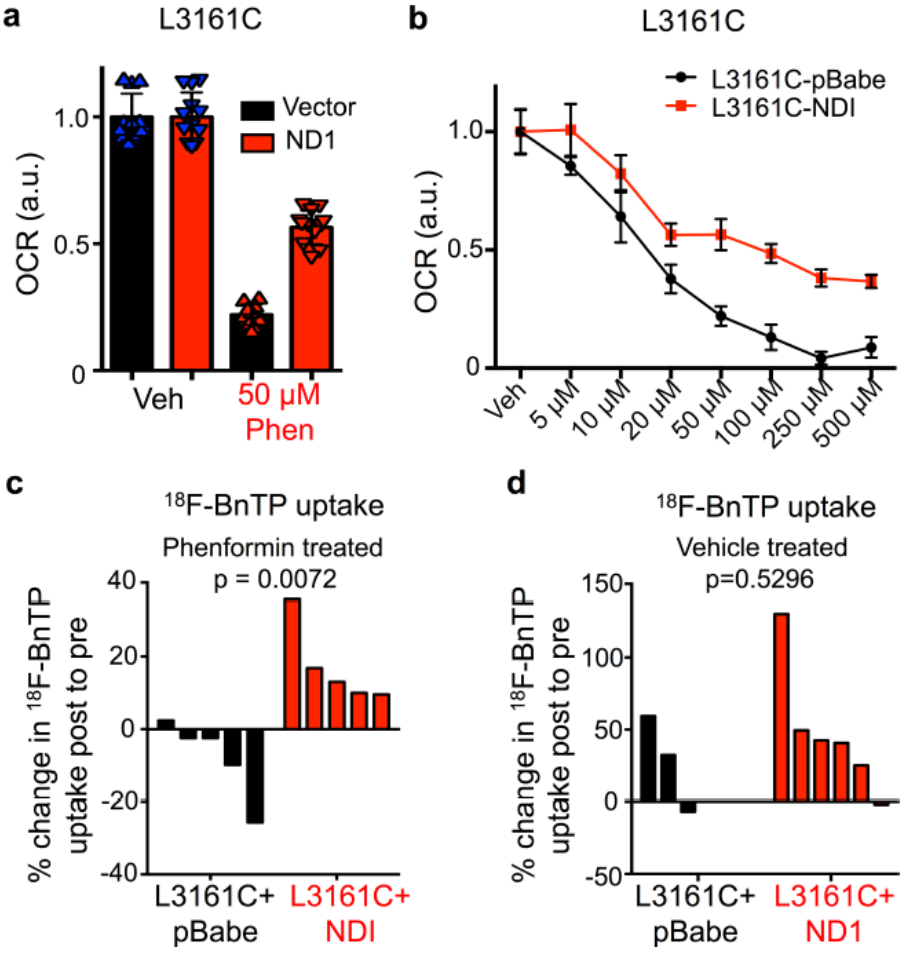

Figure A2. 4. Expressing ND1 in mouse L3161C lung ADC cell line reduces sensitivity of mitochondrial membrane potential to phenformin in vitro and in vivo

a, Basal OCR rate per cell for L3161C cells expressing empty vector (pBabe; black) (*n* = 12 technical replicates) or L3161C cells expressing ND1 (L3161C-ND1; red) (*n* = 12 technical replicates) treated with 50 µM phenformin for 24 h. **b**, Basal OCR rate per cell for L3161C-pBabe (black) (*n* = 12 technical replicates for all conditions, except *n* = 6 for 250 µM and *n* = 9 for 500 µM phenformin) and L3161C-ND1 cells (red) (*n* = 12 technical replicates) treated with the indicated concentrations of phenformin for 24 h. Data are mean ±} s.d. **c**, Waterfall plot of the percentage change in maximum uptake of 18F-BnTP after treatment relative to before treatment

for mice transthoracically implanted with L3161C cells expressing empty vector (pBabe; *n* = 5 mice) or ND1 (*n* = 5 mice) and treated with 125 mg kg−1 phenformin for 5 days. **d**, Waterfall plot of the percentage change in maximum uptake of 18F-BnTP in tumors formed by transthoracically implanted L3161C-pBabe (*n* = 3 mice) or L3161C-ND1 cells (*n* = 5 mice) treated with vehicle for 5 days. Experiments in **a**–**d** were performed once. *P* values determined by unpaired two-tailed *t*-test.

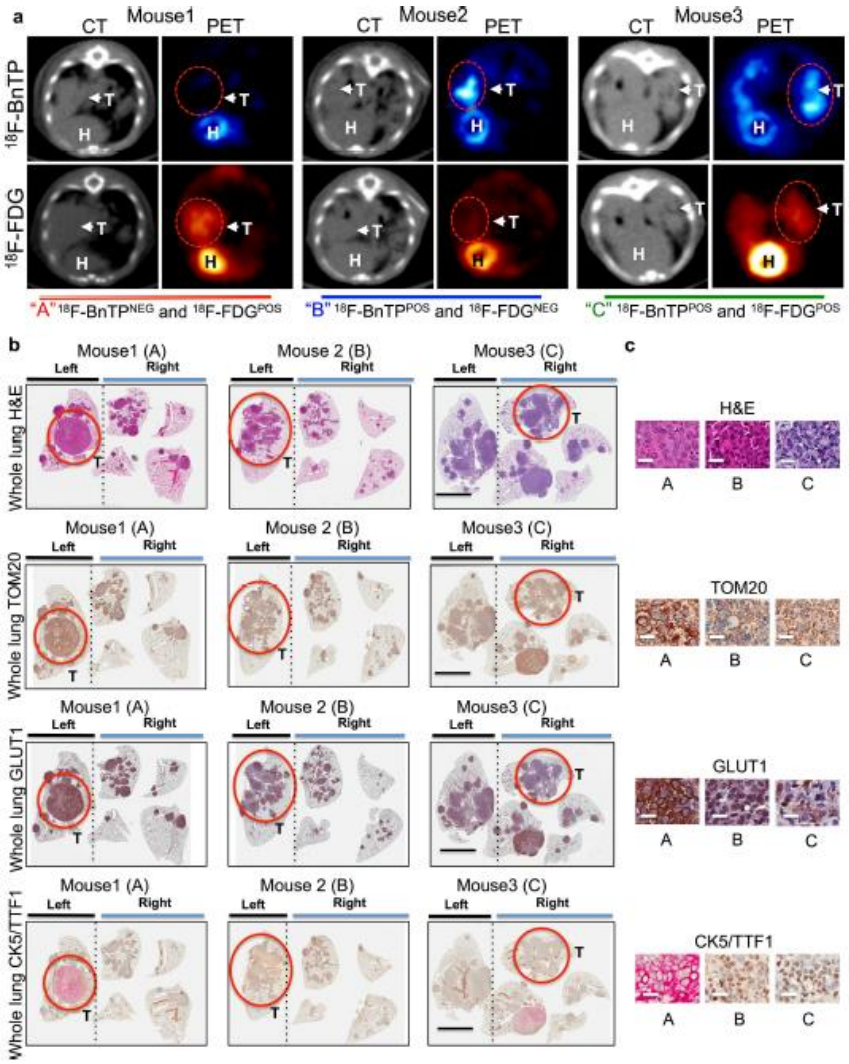

Figure A2. 5. Multi-tracer imaging and immunohistochemistry markers in lung tumors from KL mice

a, Representative PET and computed tomography (CT) images of three *KL* mice imaged with 18F-BnTP (top) and 18F-FDG (bottom) on sequential days. H, heart; T, tumor. Arrows and circles denote tumors. **b**, Whole lung slides stained with H&E, TOM20, GLUT1, or CK5 plus TTF1 from three mice. Scale bars, 5 mm. **c**, Representative higher magnification images of the tumors circled in **b** stained with H&E, TOM20, GLUT1, CK5 plus TTF1 as indicated. Scale bars, 25 μm. Data are representative of three independent mouse experiments.

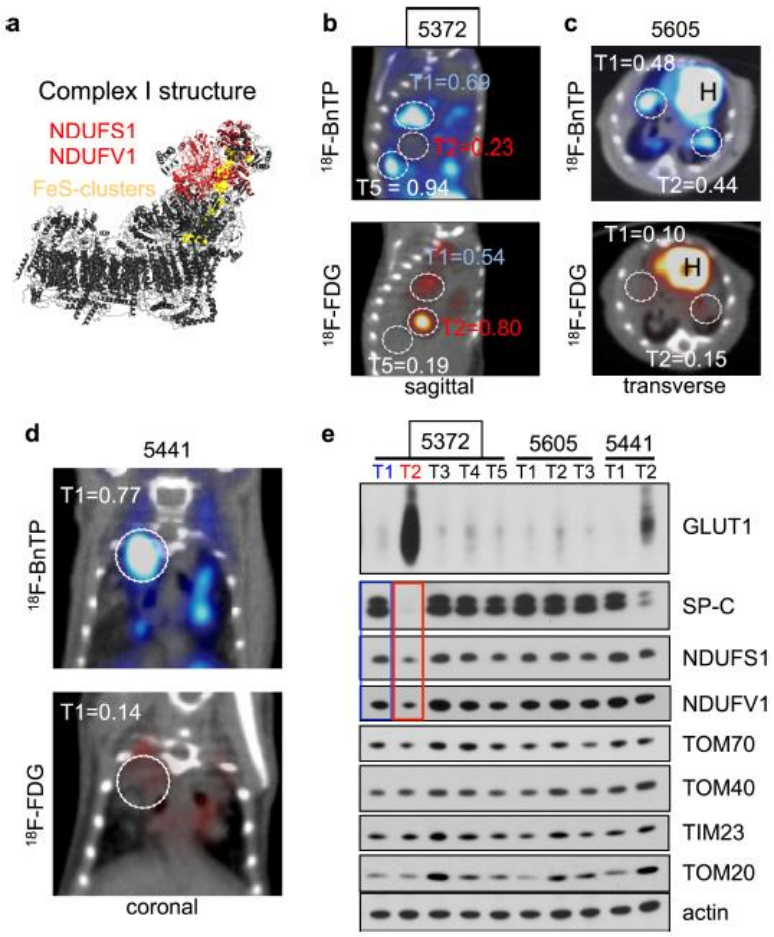

Figure A2. 6. PET–CT and biochemical analysis of KL tumors

a, Crystal structure of complex I (PDB accession 5lc5), with NDUFS1 and NDUFV1 subunits in red, and FeS clusters in yellow.**b**–**d**, PET–CT images from three *KL* mice that were imaged on sequential days with 18F-BnTP (top) and 18F-FDG (bottom). Tumors are circled. Maximum uptake value for each tumorafter normalization to maximum uptake of the heart is indicated. **e**, Western blot analysis from lung nodules that were isolated from mice imaged in **b**–**d**. Two lung tumors from mouse 5372 (imaged in **b**) are shown—T1 in blue (low 18F-FDG and GLUT1 levels; high 18F-BnTP, NDUFS1 and NDUFV1 levels); and T2 in red (high 18F-FDG and GLUT1 levels; low 18F-BnTP, NDUFS1 and NDUFV1 levels). Experiments in **b**–**d** are representative of three independent mouse experiments. Experiment in **e** was performed once.

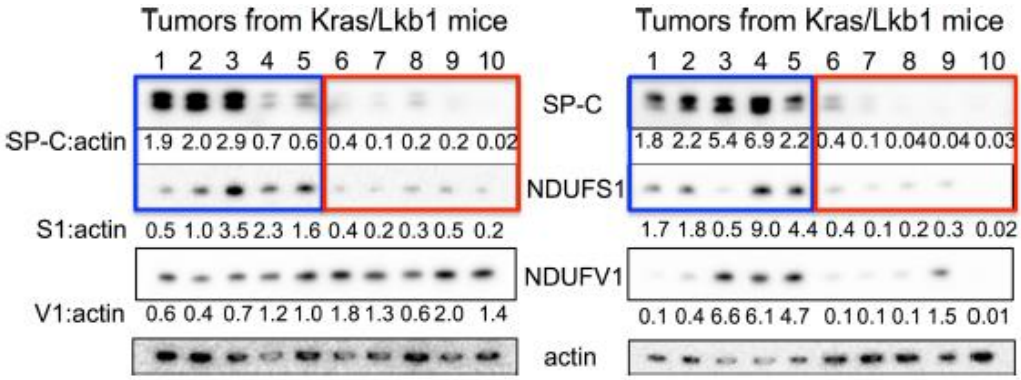

Figure A2. 7. Levels of NDUFS1 and NDUFV1 in KL tumors

Whole-cell lysates from lung tumors isolated from *KL* mice were immunoblotted with the indicated antibodies. This western blot was done on 20 individual tumors isolated from *KL* mice from three independent experiments.

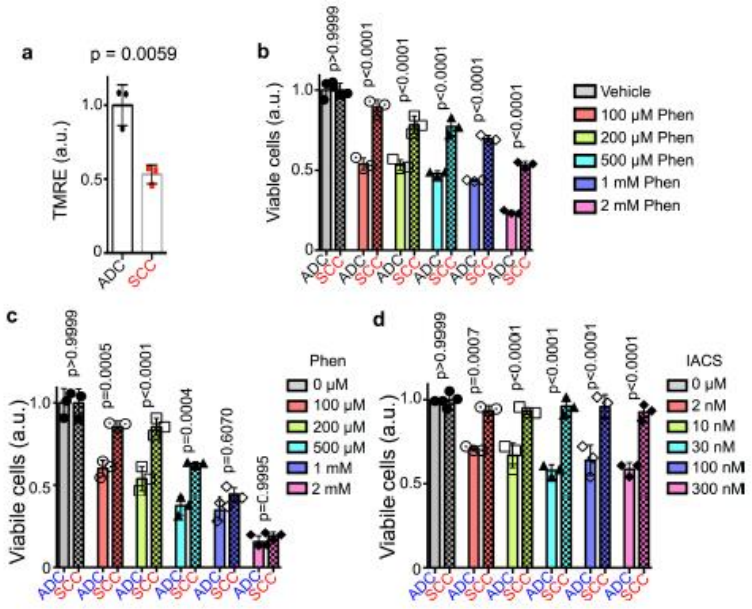

Figure A2. 8. Sensitivity of mouse and human lung cancer cell lines to complex I inhibitors phenformin and IACS-010759

a, TMRE measurement as determined by flow cytometry comparing mouse ADC (*n* = 3 biological replicates) and mouse SCC (*n* = 3 biological replicates) cell lines. **b**, Cell viability of mouse ADC (*n* = 3 biological replicates) and mouse SCC (*n* = 3 biological replicates) cells was measured in the presence of indicated concentrations of phenformin for 48 h. **c**, Cell viability of human ADC (A549; *n* = 3 biological replicates) and human SCC (RH2; *n* = 3 biological replicates) cells was measured in the presence of indicated concentrations of phenformin for 48 h. **d**, Cell viability of human ADC (A549; *n* = 3 biological replicates) and human SCC (RH2; *n* = 3 biological replicates) cells was measured in the presence of indicated concentrations of IACS-010759 for 48 h. Data are mean ±} s.d. *P* values determined by unpaired two-tailed *t*-test or one-way ANOVA (for **b**–**d**).

Experiments were repeated twice with similar results.

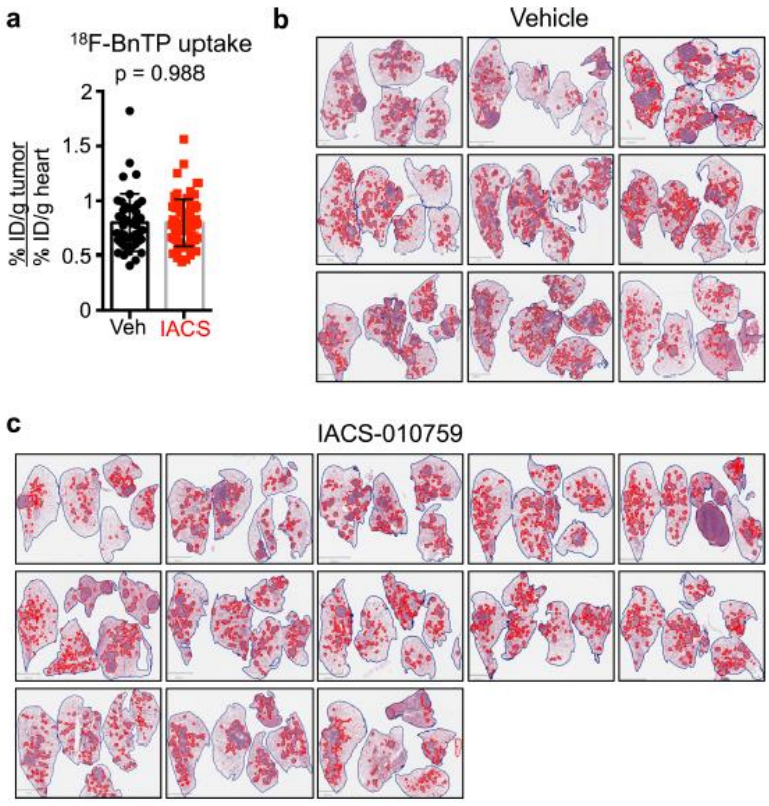

Figure A2. 9. Characteristics of tumors from KL mice treated with vehicle or IACS-010759

a, Uptake of 18F-BnTP in tumors from *KL* mice before the start of treatment with vehicle or 15 mg kg−1 IACS-010759. Each dot represents a tumor; *n* = 44 (vehicle), *n* = 66 (IACS) tumors. **b**, **c**, H&E staining images from lung sections from *KL* mice treated with vehicle (**b**) or 15 mg kg−1 IACS-010759 (**c**) for 12 days, with tumors delineated by red lines. Quantification of these data is shown in Fig. 3.4l. Experiment was performed once.

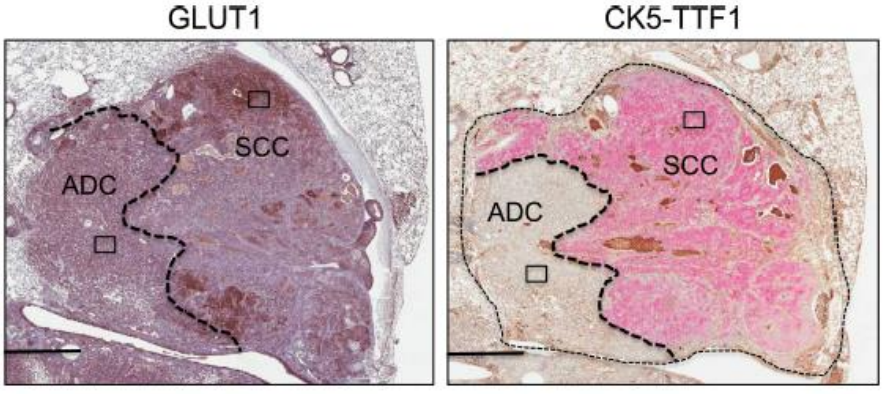

Figure A2. 10. Intra-tumoral heterogeneity in KL mice

Higher magnification images of tumor shown in Fig. 3.4n, o with GLUT1 staining (left) and CK5 and TTF1 staining (right). Areas corresponding to ADC and SCC are indicated, with rectangular boxes corresponding to magnified images shown in Fig. 3.4n. Data are representative of three independent mouse experiments.

Electrochemical Flash Fluorination and Radiochemicalfluorination

A3.1 Introduction

Fluorinated organic compounds have distinguishing physical, biological and chemical properties with a wide range of applications in fields such as agrochemicals, pharmaceuticals and materials science.[196–198] Recently, there has been growing interest in the chemistry and properties of fluorinated organic compounds.[198,172,199] Fluorine gas and anhydrous HF have been broadly used for fluorination of organic compounds.[176,200,173] However, these chemicals are costly, highly reactive, corrosive, hazardous, and difficult to handle. There is a consensus in the community that given the wide-ranging applications of fluorine in design of bioactive molecules and molecular imaging through positron emission tomography (PET), there is still a strong demand for further development of new synthetic methodologies to expand the chemist's toolbox for easier access to a broader scope of fluorinated and radiochemical compounds.[201] There have been significant recent developments in the area of nucleophilic fluorination, a more accessible form of fluorination, and their application to radiochemistry with [18F]fluoride, such as syn-thesis of aryl fluorides directly from the corresponding phenols,[178] hypervalent iodine reagents used as fluorine sources in fluorocyclization reactions,[202,203] radiofluorination of diaryl-iodonium salts and Cu-catalyzed mesityl-aryl-iodonium precursors,[204] metal-catalyzed aryl fluoride bond formation,[205] and recent reviews on these advances and their limitations[206]. Despite the development of modern fluorination techniques, many challenges still exist in terms of limited substrate scope, lack of functional group tolerance, difficulty in synthesizing the precursors and their stability, and the need for strict control of synthesis conditions. No one technique can address all the challenges for site specific fluorination. The electro-chemical approach to fluorination of stabilized cations presents a unique method for direct and very rapid fluorination in one step under mild conditions. The method described here can target moieties such as thioethers not amenable to late-stage fluorination with existing methodologies, allowing their radio-fluorination for PET tracer

development. Electrochemistry is gaining renewed prominence as a versatile tool in organic synthesis.[207,208] Electrochemical fluorination of organic compounds can be a powerful alternative technique for direct fluorination. Electrochemical oxidation can create an electron-poor carbon, potentially without the need for chemical modification, preparing the organic molecules for nucleophilic fluorination.[186,209] Fluorine atoms can be added to organic compounds in one step under mild conditions using electrochemistry, even for electron rich moieties such as aromatic and heteroaromatic rings, without the need to have leaving groups.[210,192] Traditionally, the oxidative formation of a carbocation intermediate in electroorganic synthesis has been performed in the presence of an excess of nucleophile due to the instability of the carbocations. The presence of reactive and low oxidation potential nucleophiles and products in the anodic chamber during electrolysis can limit reaction yields and scope. To overcome this problem Yoshida and co-workers developed the cation pool method, with which they could stabilize the carbocations formed during the electrochemical oxidation of carbamates by performing the electrochemical oxidation at low temperatures (-72˚C) followed by addition of nucleophiles such as allylsilanes post electrolysis.[211] Subsequently, the same group reported thiofluorination of alkenes and alkynes using low-temperature anodic oxidation of ArSSAr in Bu4NBF4/CH_2Cl_2.[212] In their process, the counter anion of the supporting electrolyte (BF_4^-), which was present during the electrolysis was also the source of fluoride. Here, for the first time, the electrochemical fluorination and radiofluorination of organic molecules using the cation pool technique is reported, where the fluoride is added post electrolysis. This approach enables the use of the cation pool method for the widely useful application of rapid and late-stage fluorination and radiochemistry. The cation pool method has tremendous potential especially for radiofluorination experiments. The excess concentration of reactive cations can provide an efficient reaction mechanism for late-stage fluorination under low fluoride concentrations encountered during radio-fluorination.[213] Furthermore, radiochemical yield, which is reduced by decay of the radioisotope, can benefit from a rapid late-stage fluorination reaction. The cation pool can be prepared prior to cyclotron

production of [18F]fluoride isotope, thereby, providing a truly late-stage fluorination reaction, maximizing radiochemical yield by minimizing decay through a flash reaction of the previously prepared cations with[18F]fluoride.

A3.2 Methods

In this study, a divided electrochemical cell was used for electrolysis. The anodic and cathodic chambers were separated by a Nafion membrane. Methyl (phenylthio) acetate (12 mM) was used as substrate and 2,2,2-trifluoroethanol (TFE) as solvent with different supporting electrolytes in the anodic chamber. TFE, tetrabutylammonium perchlorate (TBAP) and triflic acid were used in the cathodic chamber. 1,1,1,3,3,3-Hexafluoroiso-propanol (HFIP) has also recently been reported as a solvent for electroorganic synthesis with a stabilizing effect on carbocation intermediates.[214–217] However, yields were negligible due to instability of fluorinated products reported here in HFIP. Previous reports on electrochemical fluorination of Methyl(phenylthio) acetate guided our choice for the substrate.[214,218] Traditional fluorination of sulfoxides have been based on fluoro-Pummerer rearrangement with DAST, electrophilic fluorination of thioethers and the combinations of chemical oxidants with nucleophilic fluorinating reagents.[219] Previous electro-chemical fluorination of thioethers were performed with excess amounts of HF salts or TBAF present in the cell during electrolysis, resulting in low fluoride conversion yield and preventing no-carrier-added fluorination.[210,220,221]

A3.3 Results and Discussion

Here, electrochemical oxidation was performed for 60 min at a constant potential of 1.6 V vs Ag wire quasi-reference electrode followed by addition of a fluoride nucleophile to the anodic chamber at the end of electrochemical oxidation. The mixture was stirred and allowed to react for 30 min while the temperature was rising to room temperature. With 168 mM of CsF, KF, Et3Nx3HF and tetrabutylammonium fluoride (TBAF) used as fluoride (nucleophile) sources, respective yields of 4.5%,1.4%, 4% and 4.5% of methyl 2-fluoro-2-(phenylthio) acetate were obtained. The yields

were quantified using gas chromatography mass spectrometry (GC-MS). Figure A3.1 shows the schematic of the reaction and representative GC-MS chromatograms can be found in the supporting information.

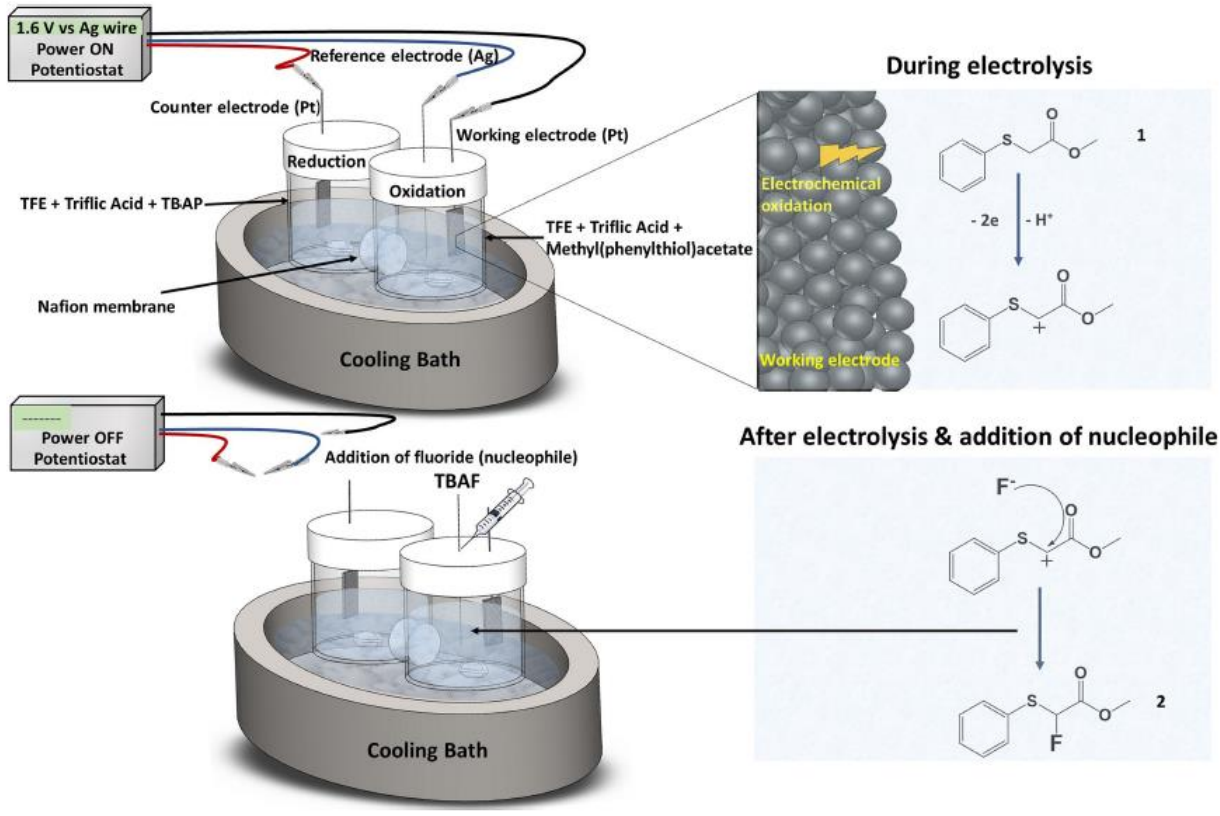

Figure A3. 1 Schematic of the cation pool method for fluorination of methyl-2-(phenylthiol) acetate

Electrolysis was repeated with TBAF at different temperatures of 21˚C, 0˚C, -20˚C and-40˚C and chemical yields of 2.2%, 4%, 6% and 3% were obtained respectively. The drop in the yield from -20˚C to -40˚C is due to the low oxidation current resulting in the slowing of precursor oxidation. 68% of the precursor was consumed when oxidation was performed at -20˚C, while only 12% of the precursor was consumed at -40˚C. -20˚C was chosen as the optimum temperature for further optimization. The effect of changes in supporting electrolyte on the chemical yield is shown in Table A3.1.

Table A3. 1. Effect of supporting electrolyte on the chemical yield of 2

Electrolyte (TFE based)	Yield [%]
50 mM NBu_4ClO_4 (TBAP)	0
300 mM NBu_4ClO_4 (TBAP)	0
300 mM NBu_4ClO_4 + 14.2 mM triflic acid	6.0
300 mM NBu_4BF_4 + 14.2 mM triflic acid	1.3
300 mM *p*-toluenesulfonic acid + 14.2 mM triflic acid	2.0
142 mM triflic acid	12.5

Electrolysis was carried out using 12 mM of 1 in TFE for 60 min at 1.6 V vs Ag wire at -20 ˚C followed by addition of 168 mM of TBAF post electrolysis. It can be seen from Table A3.1 that TBAP alone results in negligible product formation, while addition of 14.2 mM of triflic acid increases the yield to 6%. The highest yield of 12.5% was obtained where only 142 mM of triflic acid was used without addition of salts as supporting electrolyte.

Further optimization was performed using only triflic acid as supporting electrolyte and the effect of triflic acid concentration on the yield was examined. Yields of 3.6%, 12.5% and 0% was obtained when 71 mM, 142 mM and 284 mM of triflic acid were used, respectively. The effect of precursor concentration on the product yield is presented in Table A3.2.

Table A3. 2. Effect of precursor 1 concentration on the chemical yield of product 2

Precursor concentration [mM]	Yield [%] (n=3)
0.5	8.5 ± 0.9
1	9.6 ± 1.0
2	11.5 ± 1.2

4	10.6 ± 1.1
6	12.7
12	11.2 ± 1.3
24	9.2 ± 1.0

Electrolysis was carried out using precursor 1, and 142 mM of triflic acid in TFE for 60 min at 1.6 V vs Ag wire at -20 ˚C. 168 mM TBAF was added at the beginning of the electrochemical oxidation. Precursor concentration changes from 0.5 mM to 24 mM resulted in only a moderate change in the yield. Due to the diminishing [18F]TBAF concentration during no-carrier-added radiochemistry experiments, the effect of lowering of TBAF concentration and ratio of TBAF to triflic acid concentration were also investigated and the results are shown in table A3.3.

Table A3. 3. Effect of TBAF concentration and TBAF concentration/triflic acid concentration ratio on the chemical yield of product 2

TBAF Concentration [mM]	TBAF concentration/triflic acid concentration	Yield [%]
21	1.18	1.6
	0.15*	0
42	1.18	3.8
	0.30*	0
84	1.18	4.0
	0.60*	0
168	1.18*	12.5

	0.60	0
	2.36	3.6

Electrolysis was carried out using 12 mM of 1 and triflic acid in TFE for 60 min at 1.6 V vs Ag wire at -20 ˚C. The values marked with an asterisk in the second column reflects experiments where triflic acid concentration was kept constant at 142 mM. It was observed that by lowering the TBAF concentration the product yield decreased to 1.5% when 21 mM of TBAF was used. It was further observed that the ratio of TBAF to triflic acid concentration plays a crucial role with optimum product yield obtained when this ratio is maintained at 1.18. This may be due to the instability of product at low pH where TBAF addition can act as a base to increase the pH of the solution. Using the optimized parameters, radiofluorination of 1 was performed with the cation pool method with 142 mM of triflic acid and 24 mM of 1in TFE in the anodic chamber. Radio-chemical fluorination efficiencies (RCFEs) were calculated based on conversion of [18F]fluoride to product 2. Initially [18F]fluoride in the form of [18F]TBAF was added to the anodic chamber after60 min of electrolysis, however no radio-fluorinated product was observed. Due to the diminishing TBAF concentrations in the radiochemistry experiment, addition of a non-nucleophilic base was necessary to increase the pH to 3, at which point the product was observed to be stable. To address this challenge,5 mCi of [18F]fluoride was mixed with 300 mM of 2,6-di-tert-butyl-4-methylpyridine and the mixture was added to the anodic chamber after electrolysis resulting in RCFE of 5.7±1.0% (n=3) and molar activity of 1.13±0.2 Ci/mM (n=3).Similar to cold experiments with [19F]-TBAF, samples for characterization were taken 30 min after [18F]fluoride addition. Notably, RCFE of 4.8±0.6% (n=3) was obtained after just 5 min post [18F]fluoride addition. Successful radiofluorination of methyl 2-(methylthio) acetate and methyl 2-(ethylthio) acetate were performed using cation pool technique with same condition as above, the RCFE of 20.6±2.0% and 18.2±1.5% were obtained, respectively (Figure A3.2).

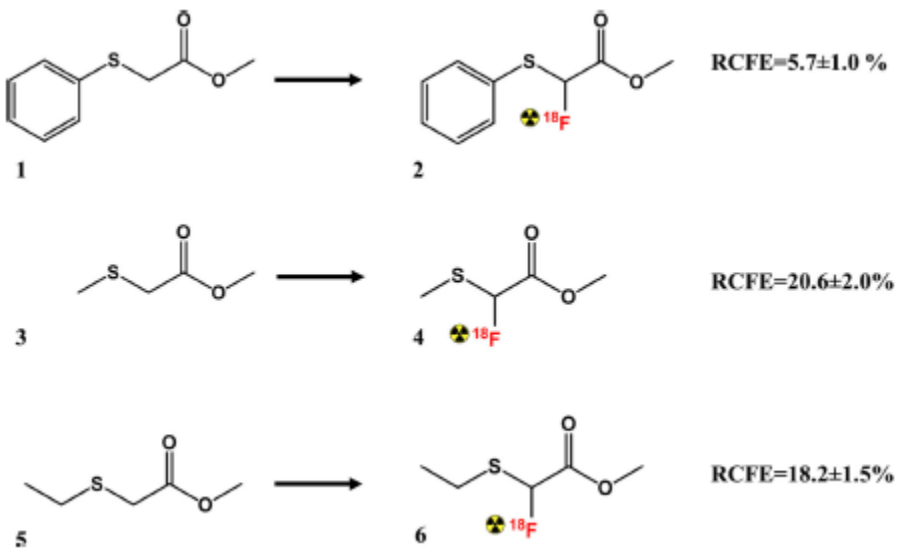

Figure A3. 2. Schematic of the radiofluorination reactions

A3.4 Conclusion

In Summary, this report demonstrates a new tool for rapid late-stage fluorination and radiofluorination using the cation pool method. This is made possible through generation and pooling of stable cations under low temperature using TFE as solvent, and the subsequent fluorination reaction of carbocations with fluoride under non-oxidative conditions. Cation pool fluorination prevents further oxidation of the fluorinated product during the electrolysis and rapid late-stage radio-fluorination can minimize the losses of [18F]fluoride due to radioactive decay. More in-depth studies of scope and the use of microfluidic platforms are currently in progress to increase yields and introduce automation. Flash fluorination and radio-fluorination based on the cation pool method can be used to produce PET radiotracers and fluorinated pharmaceuticals, potentially expanding the library of fluorinated bioactive molecules available for medicinal chemistry and molecular imaging.

A3.5 Extended Information & Figures

Materials

2,2,2-trifluoroethanol (TFE, 99.9%, C2H3F3O), trifluoromethanesulfonic acid (triflic acid, CF3SO3H, 99%), methyl (ethylthio)acetate (99%, C5H10O2S) and methyl(phenylthio)acetate (C9H10O2S, 99%) were purchased from Oakwood Chemical. Acetonitrile (ACN, anhydrous, 98%), tetrabutylammonium fluoride solution 1.0 M in THF (TBAF solution, ~5 wt% water), cesium fluoride (99%, CsF), Potassium fluoride (≥99.9%, KF), triethylamine trihydrofluoride (98%, (C2H5)3N·3HF) and platinum wire (99.9%) were purchased from Sigma-Aldrich. Tetrabutylammonium perchlorate (TBAP, >98.0%, C16H36ClNO4) methyl (methylthio)acetate (>99.0%, C4H8O2S), tetrabutylammonium tetrafluoroborate (>98.0%, C16H36BF4N) and ptoluenesulfonic acid (>98.0%, C7H8O3S·H2O) were purchased from TCI America. 2,6-Di-Tertbutyl-4-methylpyridine (98%, C14H23N) was purchased from Ark Pharm, Inc. Nafion® membrane N117, 7 mils (178 µm thickness) was purchased from Fuel Cell Earth. Analytical grade (AG) MP1M anion exchange resin was purchased from Bio-Rad.

Electrochemical Synthesis

The electrochemical oxidation (the cation pool formation) and cyclic voltammetry (CV) were performed using an H shape divided 3-electrode cell with two platinum wires (length = 200 mm, diameter = 0.33 mm) as working and counter electrodes and Ag wire as quasi-reference electrode. The cathodic chamber and anodic chamber were separated by a nafion membrane. The anodic chamber contained 10 ml of TFE as solvent, methyl(phenylthio)acetate (precursor) and different supporting electrolytes such as triflic acid, tetrabutylammonium perchlorate, tetrabutylammonium tetrafluoroborate and p-toluenesulfonic acid. The cathodic chamber contained 10 ml of TFE as solvent, 300 mM tetrabutylammonium perchlorate and 757 mM of triflic acid. The reference electrode (Ag wire) was immersed in the anodic reaction mixture. The counter electrode and working electrode were cleaned before each experiment using potential cycling in

1 M sulfuric acid solution in water. The electrodes were cycled between −2 V and 2 V (2 electrode configuration) 10 times before each experiment. The electrochemical oxidation of methyl(phenylthio)acetate (carbocations formation) was performed at constant potential of 1.6 V vs Ag wire for 60 min. At the end of electrolysis, the nucleophile (TBAF) was added to the anodic chamber and allowed to react for 30 min while the reaction mixture was stirred using a magnetic stirring bar at 500 RPM and temperature was rising to the room temperature. The CVs and electrochemical oxidation experiments were performed using the Metrohm PGSTAT128N electrochemical workstation. The CVs were performed using a 200 mV/s scan rate and no stirring. Figure A3.5.1 shows the CV of background (TFE + supporting electrolyte in the anodic chamber) and CV of the cation pool reaction mixture (methyl(phenylthio)acetate + TFE + supporting electrolyte in the anodic chamber).

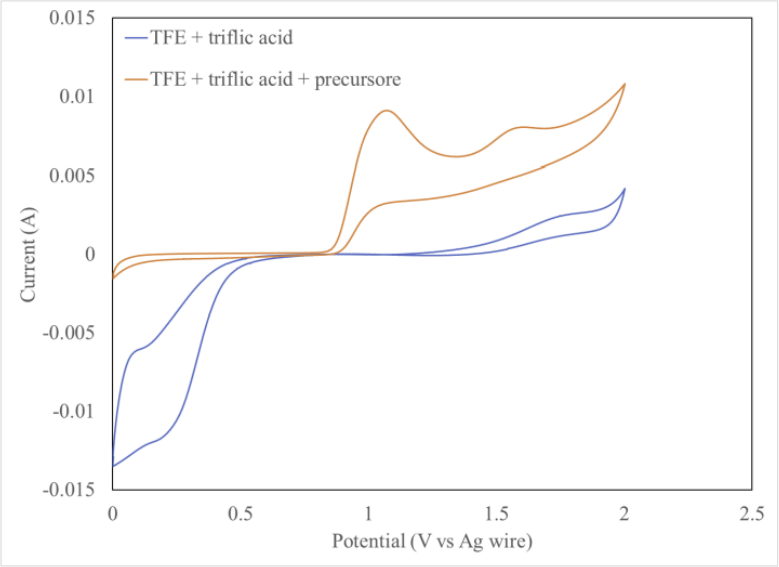

Figure A3. 3. CV using TFE + triflic acid with and without precursor

CVs of TFE and triflic acid with and without precursor (background). The CVs were run with 200 mv.s−1 scan rate at room temperature (21 °C) using a divided cell and no stirring. It can be seen from figure A3.5.1 that the oxidation of precursor starts at 0.9 V vs Ag wire and reaches a peak at 1.08 V vs Ag wire due to the diffusion limit. The CV of the background shows very small anodic currents up to 1.5 V vs Ag wire; by increasing the potential further the background anodic current starts to increase to higher values. It also can be seen that adding the precursor to the solution can suppress the cathodic currents at potentials lower than 0.5 V vs Ag wire.

Gas Chromatography–Mass Spectrometry (GC-MS) Spectra

The product identification and quantification was performed using GC-MS. Mass spectra and chromatograms were carried out using an Agilent 5975C Triple-Axis Detector (TAD) inert MSD mass spectrometer coupled with an Agilent 7890A gas chromatograph. The mass spectrum was set to electron ionization mode with a voltage of 1.9 kV. The mass range was 50-250 (amu). The details of gas chromatograph's column and the method are outlined below: Inlet was set at 120 °C and had 1:10 split ratio. Oven was set to 120 °C and held for 1 min, then increased to 138 °C at a rate of 1 °C/min and held for 15 mins. Column was Agilent 122-5532, maximum operating temperature 325 °C; 30 m length, 250 µm internal diameter and 0.25 µm film thickness. A constant flow of 1 mL/min was delivered to the transfer column. The transfer column Agilent G3185-60062, 450 °C; 0.17 m length, 100 µm internal diameter and 0 µm film thickness delivered a constant flow of 1.5 mL/min to the source. The GC-MS method had a 10 min solvent delay in order to enhance the MS filament lifetime. Figure A.3.5.2 is the GC-MS calibration plot used in the quantification of product 2 yield.

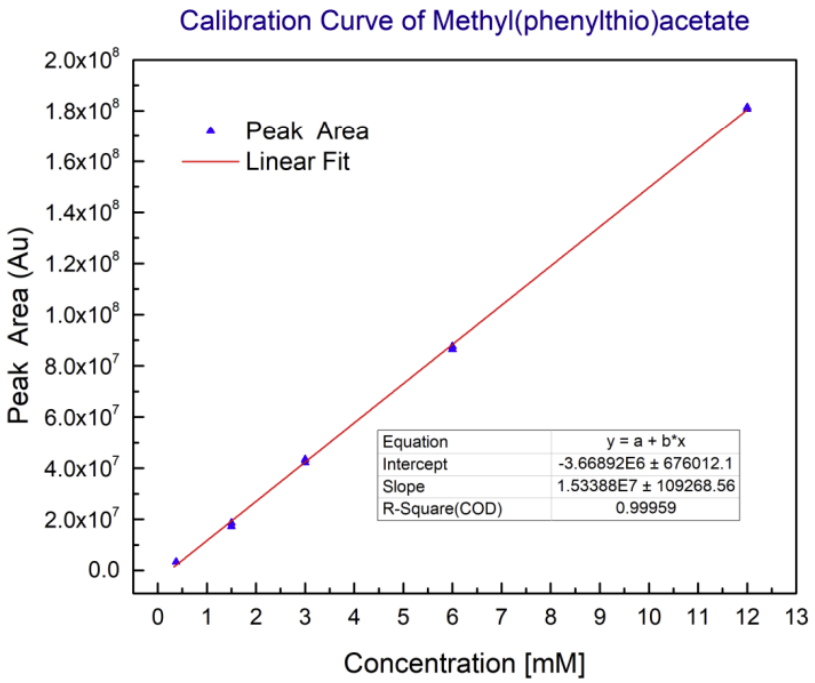

Figure A3. 4. The GC calibration plot used in the quantification of formation of product 2

Figures A3.5.3, A3.5.4 and A3.5.5 show the GC-MS mass spectra of the products 2, 4 and 6, respectively. Figure A3.5.6 shows a representative GC-MS chromatogram of the crude product.

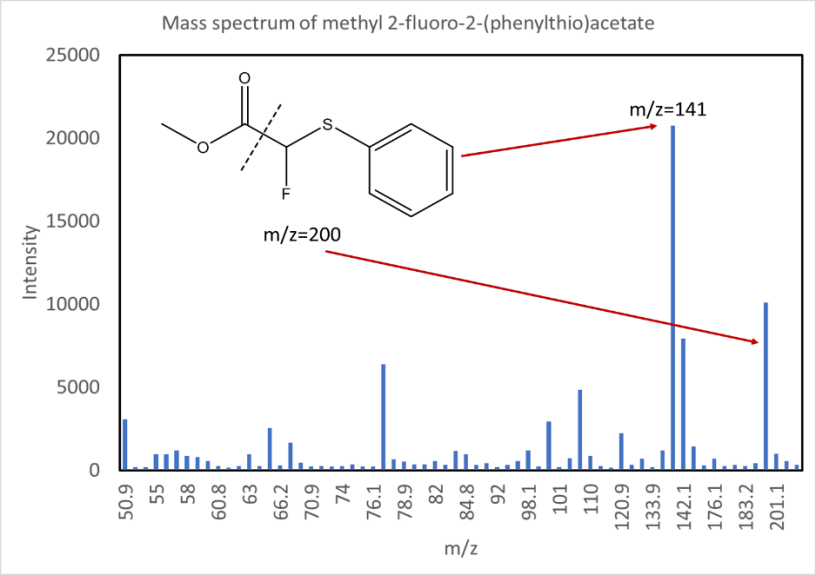

Figure A3. 5. The mass spectrum of the product 2

It can be seen from figure A3.5.6 that after electrolysis, 70% of the precursor has been consumed and no product peak can be observed at 21.7 min. The product is only observed after the injection of TBAF post electrolysis, pointing to the reaction of fluoride anions with stabilized carbocations formed during electrolysis.

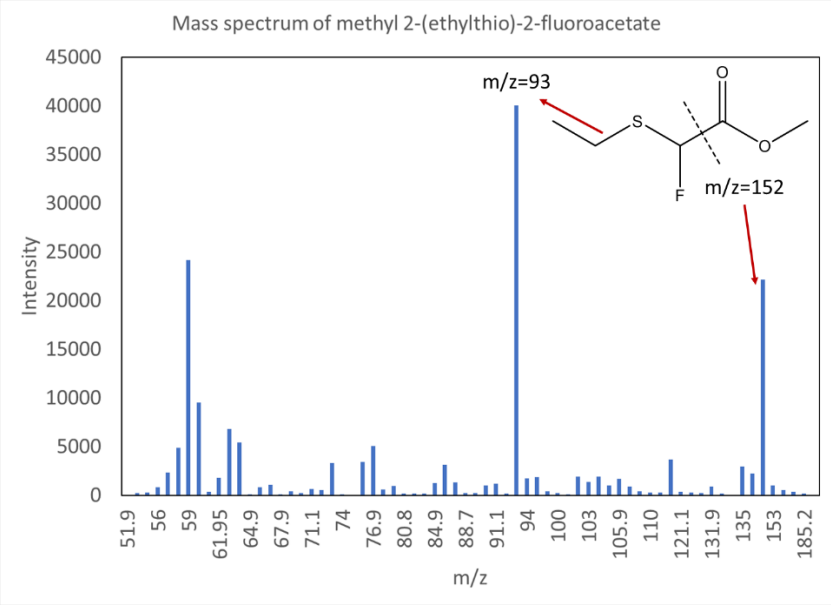

Figure A3. 6. The mass spectrum of the product 4

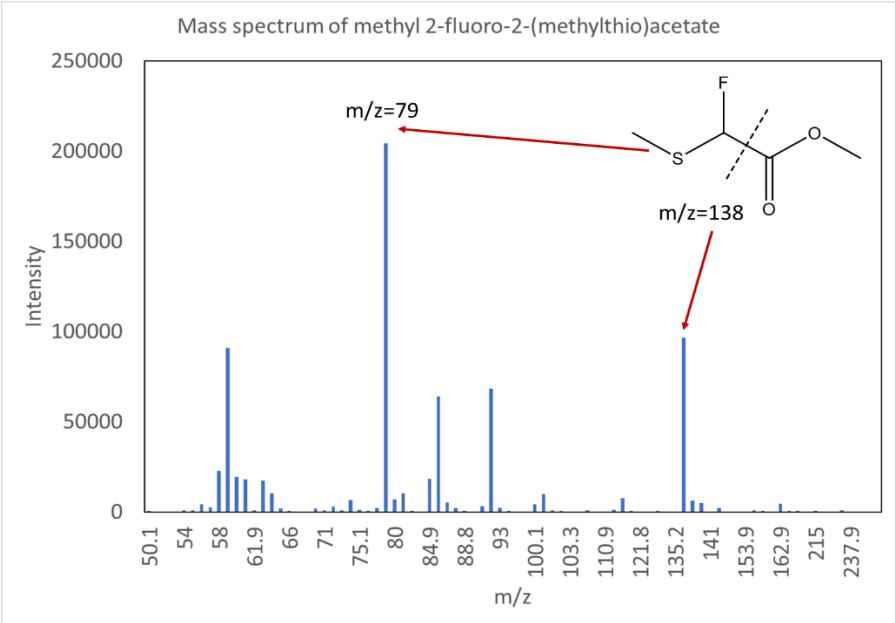

Figure A3. 7. The mass spectrum of the product 6

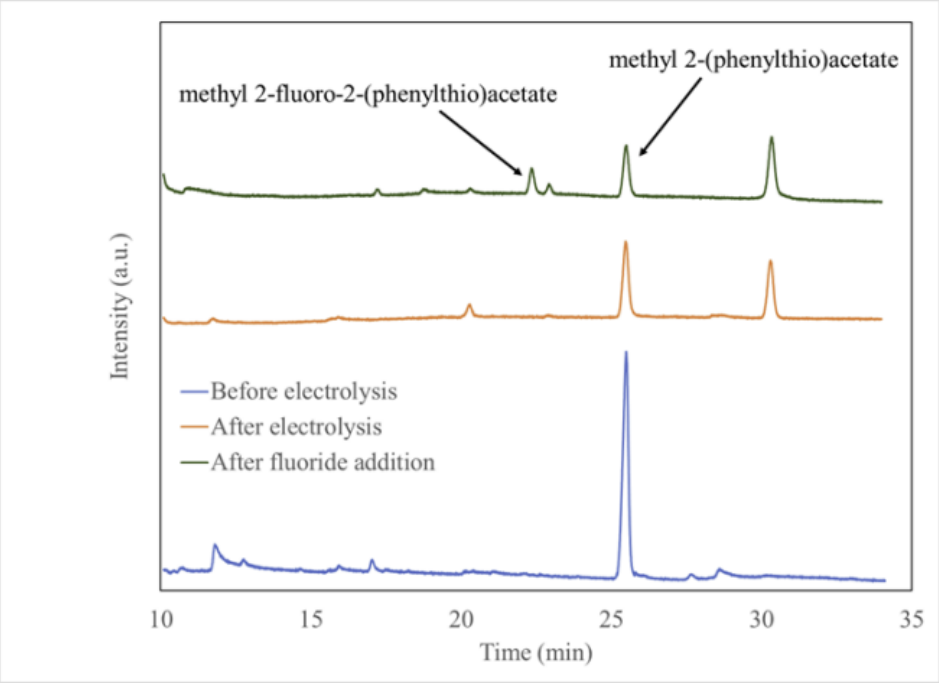

Figure A3. 8. GC-MS chromatograms of the crude reaction mixture before and after electrochemical oxidation and after fluoride addition

Electrolysis was carried out using 12 mM of 1 and 142 mM of triflic acid in TFE for 60 min at 1.6 V vs Ag wire at -20 °C. 168 mM TBAF was added at the end of electrochemical oxidation and allowed to react for 30 min while the reaction mixture was stirring and temperature was rising to the room temperature.

Nuclear Magnetic Resonance (NMR) Spectra

^{19}F-Nuclear-Magnetic-Resonance (^{19}F-NMR) was performed on the ^{19}F-fluorinated thioether reference standards. ^{19}F-NMR spectroscopic data were in agreement with previous reports [1-8]. Nuclear magnetic resonance spectroscopy (NMR) The identity of the product 2 was also further characterized by 19F-NMR. The 19F-NMR spectrum was obtained on a Bruker AV400 (400 MHz). 19F chemical shift is reported in parts per million (ppm) using the trifluoro acetic acid (CF3COOH) as a reference. Figures A3.5.7, A3.5.8 and A3.5.9 show the 19FNMR spectra of the products 2, 4 and 6, respectively. 19F-NMR spectroscopic data for products 2 and 6 were in agreement with previous reports.

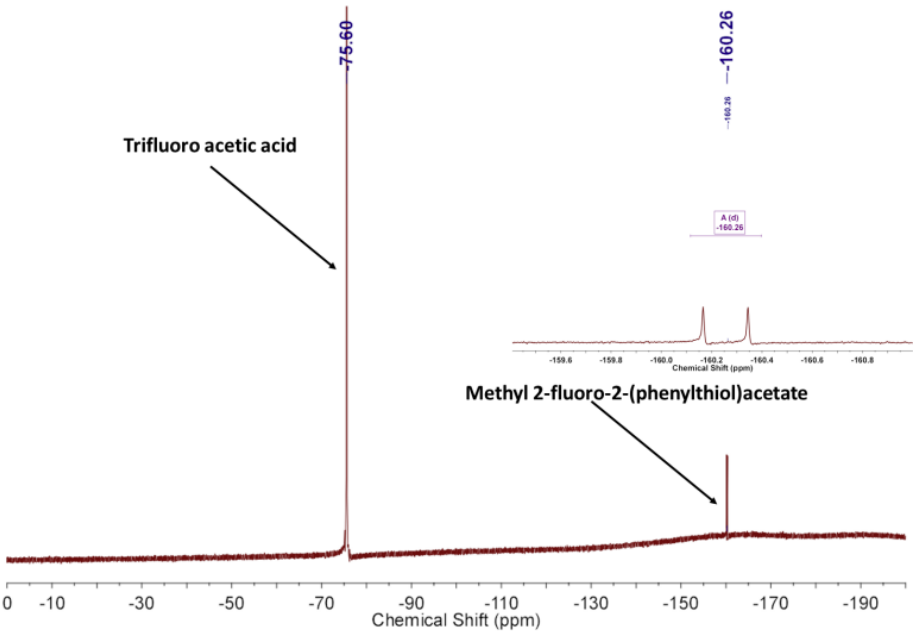

Figure A3. 9. The 19F NMR of the HPLC purified product 2 plus trifluoro acetic acid as standard for further identification of the fluorinated product obtained by cation pool method

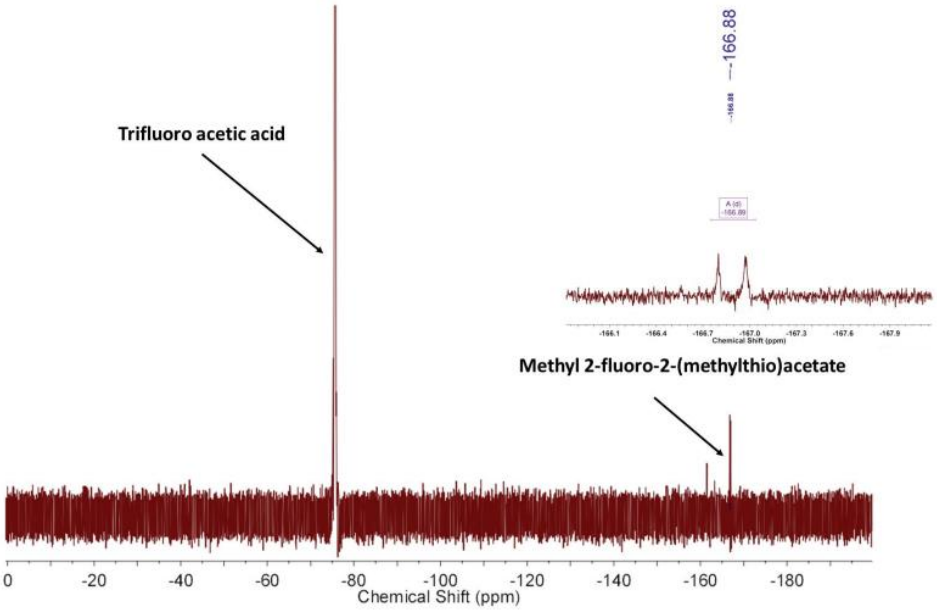

Figure A3. 10. The 19F NMR of the HPLC purified product 4 plus trifluoro acetic acid as standard for further identification of the fluorinated product obtained by cation pool method

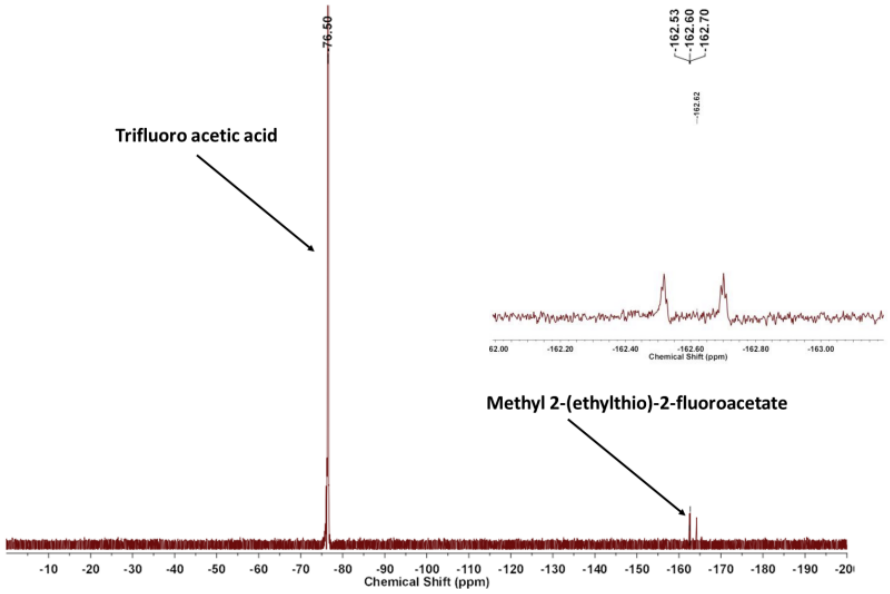

Figure A3. 11. The 19F NMR of the HPLC purified product 6 plus trifluoro acetic acid as standard for further identification of the fluorinated product obtained by cation pool method

Radiochemical characterization

No-carrier-added 18F-fluoride was produced by the (p,n) reaction of 18O–H2O (84% isotopic purity, Medical Isotopes) in a RDS-112 cyclotron (Siemens) at 11 MeV using a 1 mL tantalum target with havar foil.27 The radioactive isotope was trapped on analytical grade (AG) MP-1M anion exchange resin by passing through the 1 ml of bombarded 18O–H2O. Most of the water on the resin was removed by washing with 10 mL of anhydrous ACN and drying with ultra-pure N2 for 10 min. [18F]fluoride was subsequently eluted out from the cartridge with a 2 ml TFE containing 25 mM TBAP salt. In a typical experiment, approximately 5 mCi was eluted from the anion exchange cartridge in 18F-TBAF form in TFE. Radiofluorination conversion was measured using Radio-thinlayer-chromatography (radio-TLC). Radio-TLC was performed on silica plates (TLC Silica gel 60 W F254s, Merck). After dropping a sample volume (~1–5 µL) using a glass capillary, the plate was developed in the mobile phase (ACN). Chromatograms were obtained using a radio-TLC scanner (miniGita Star, Raytest). Analytical High Performance Liquid Chromatography (HPLC), equipped with a UV and gamma detector was used to determine radiochemical purity (RCP) of the radio-fluorinated product. HPLC was performed using a 1200 Series HPLC system

(Agilent Technologies) equipped with a GabiStar flow-through gamma detector (Raytest). Data acquisition and processing was performed using GINA Star Software version 5.9 Service Pack 17 (Raytest). Typically, 20 µL of radioactive sample was diluted with 180 µL of ACN and 5–20 µL of this solution was injected for HPLC analysis. Column: Synergy 4u Polar RP 80 A, 250 × 4.6 mm, 4 micron. Gradient: A = ACN; B = water; flow rate = 1.8 mL/min; 0–28 min 95% B to 45% B, 28–29 min 45% B to 5% B, 29–32 min 5% B, 32–34 min 5% B to 95% B. Radio-TLC chromatograms were used to measure radiochemical conversions (RCC). RCP and RCC were measured by dividing the area under the curve (AUC) for the desired product by the sum of AUC for all peaks. The TLC purity accounts for unreacted 18F-fluoride while the HPLC purity corrects for radiochemical side-products. The radiochemical fluorination efficiency (RCFE) was determined by the equation: RCFE = TLC RCC × HPLC RCP

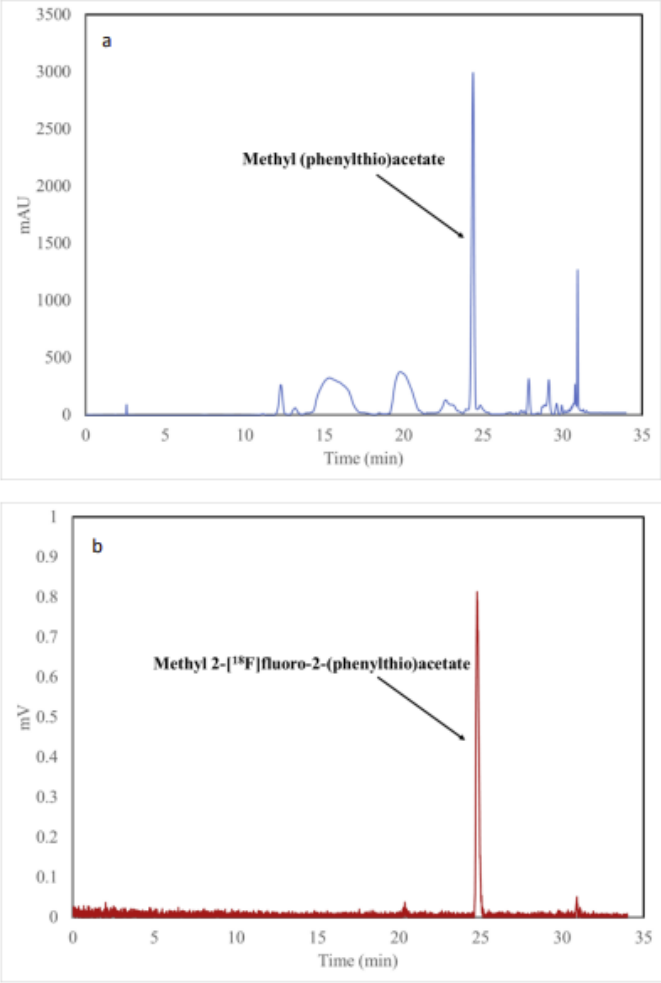

Figure A3. 12. Analytical a) UV HPLC and b) gamma HPLC profiles of the crude sample after electrolysis

Electrolysis was performed for 60 min at 1.6 V vs Ag wire at -20 ºC using TFE solution containing 24 mM of product 1, 142 mM of triflic acid. 2 ml of TFE solution containing 25 mM TBAP and 5 mCi 18F-fluoride was added after electrolysis was finished and the sample was taken for analysis 30 min after 18F-fluoride addition.

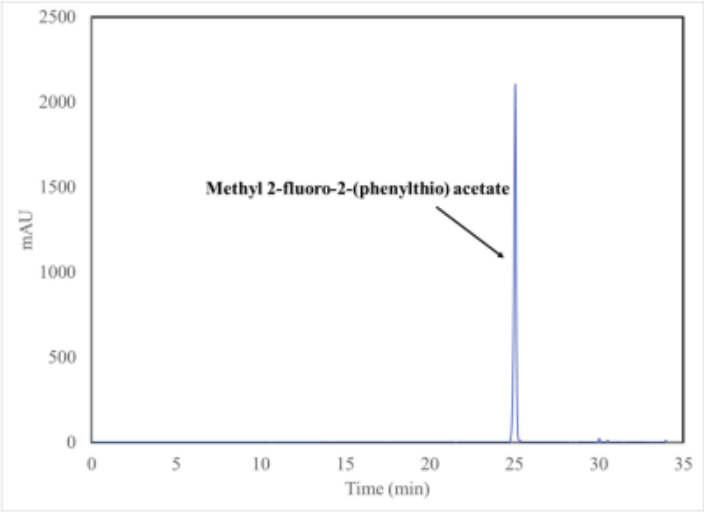

Figure A3. 13. UV HPLC profile of purified product

Electrolysis was performed for 60 min at 1.6 V vs Ag wire at -20 ºC using TFE solution containing 24 mM of product 1, 142 mM of triflic acid. 2 ml of TBAF solution was added after electrolysis was finished and the sample was HPLC purified 30 min after TBAF addition.

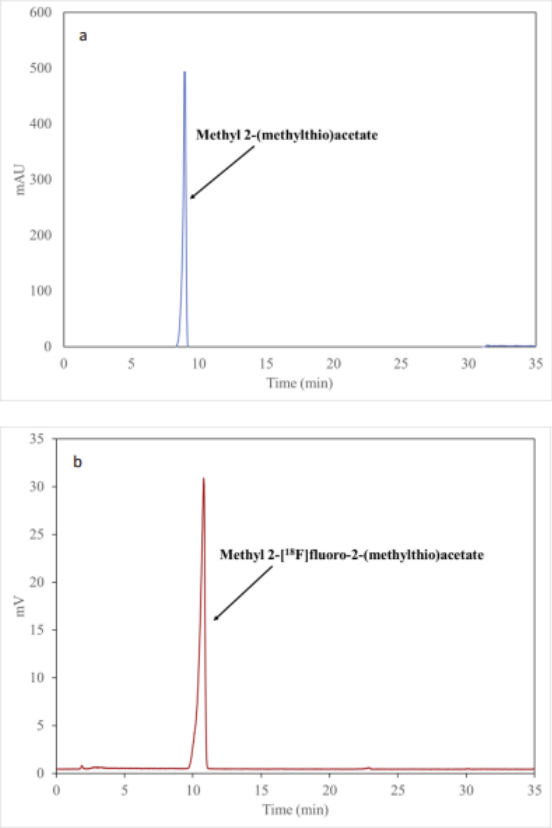

Figure A3. 14. Analytical a) UV HPLC and b) gamma HPLC profiles of the crude sample after electrolysis

Electrolysis was performed for 60 min at 1.6 V vs Ag wire at -20 ºC using TFE solution containing 24 mM of product 3, 142 mM of triflic acid. 2 ml of TFE solution containing 25 mM TBAP and 5

mCi 18F-fluoride was added after electrolysis was finished and the sample was taken for analysis 30 min after 18F-fluoride addition.

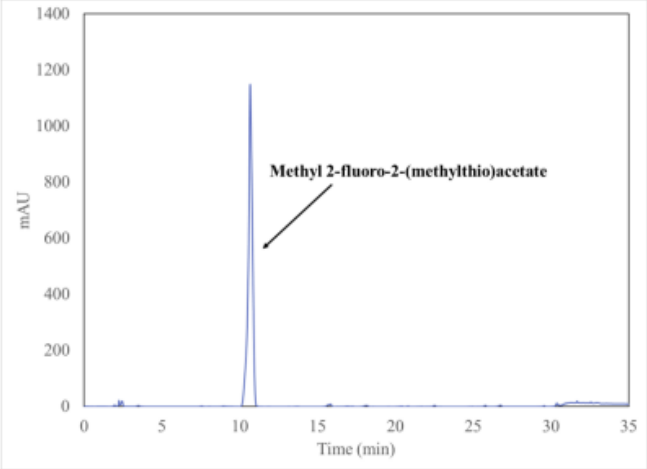

Figure A3. 15. UV HPLC profile of purified product

Electrolysis was performed for 60 min at 1.6 V vs Ag wire at -20 ºC using TFE solution containing 24 mM of product 3, 142 mM of triflic acid. 2 ml of TBAF solution was added after electrolysis was finished and the sample was HPLC purified 30 min after TBAF addition.

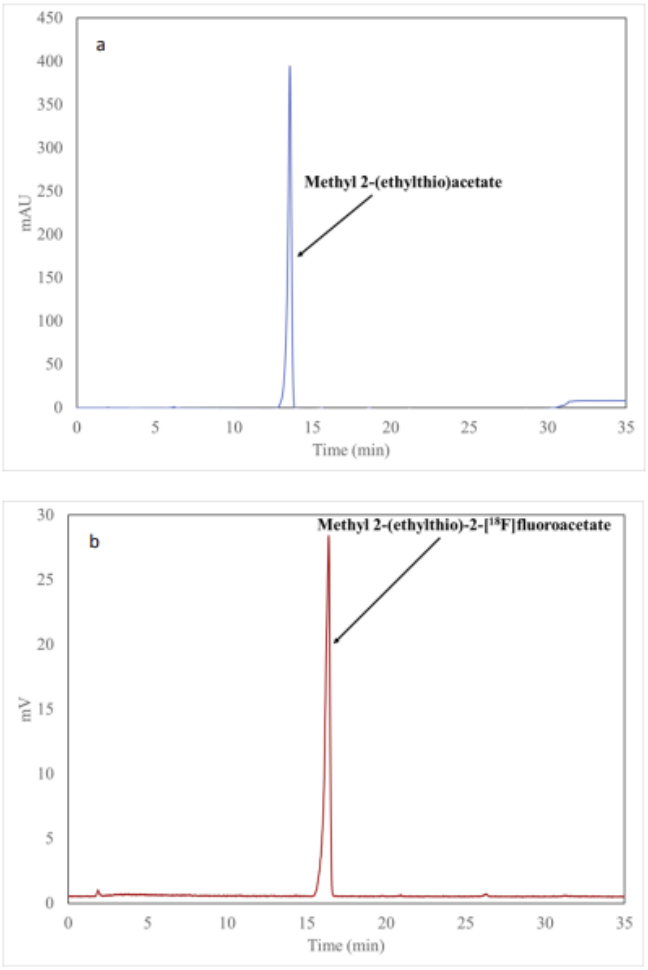

Figure A3. 16. Analytical a) UV HPLC and b) gamma HPLC profiles of the crude sample after electrolysis

Electrolysis was performed for 60 min at 1.6 V vs Ag wire at -20 ºC using TFE solution containing 24 mM of product 5, 142 mM of triflic acid. 2 ml of TFE solution containing 25 mM TBAP and 5 mCi 18F-fluoride was added after electrolysis was finished and the sample was taken for analysis 30 min after 18F-fluoride addition.

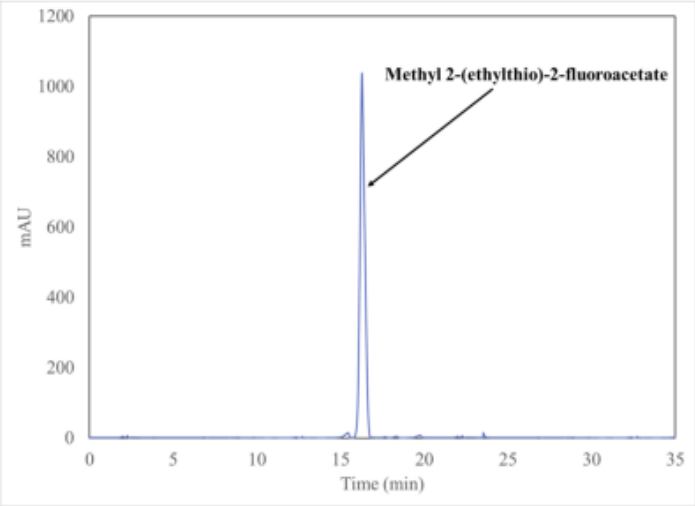

Figure A3. 17. UV HPLC profile of purified product

Electrolysis was performed for 60 min at 1.6 V vs Ag wire at -20 ºC using TFE solution containing 24 mM of product 5, 142 mM of triflic acid. 2 ml of TBAF solution was added after electrolysis was finished and the sample was HPLC purified 30 min after TBAF addition.

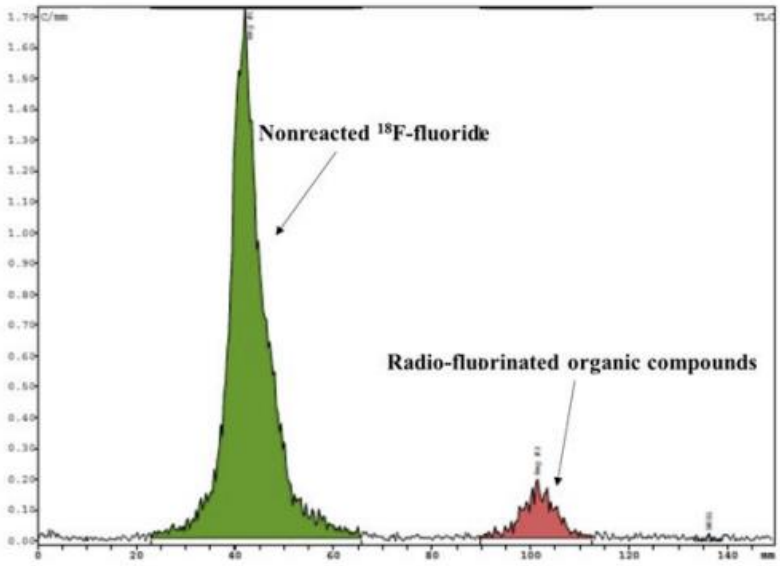

Figure A3. 18. Gamma TLC of the crude sample post radio-electrochemical synthesis

Electrolysis was performed for 60 min at 1.6 V vs Ag wire at -20 ºC using TFE solution containing 24 mM of product 1, 142 mM of triflic acid. 2 ml of TFE solution containing 25 mM TBAP and 5 mCi 18F-fluoride was added after electrolysis was finished and the sample was taken for analysis 30 min after 18Ffluoride addition

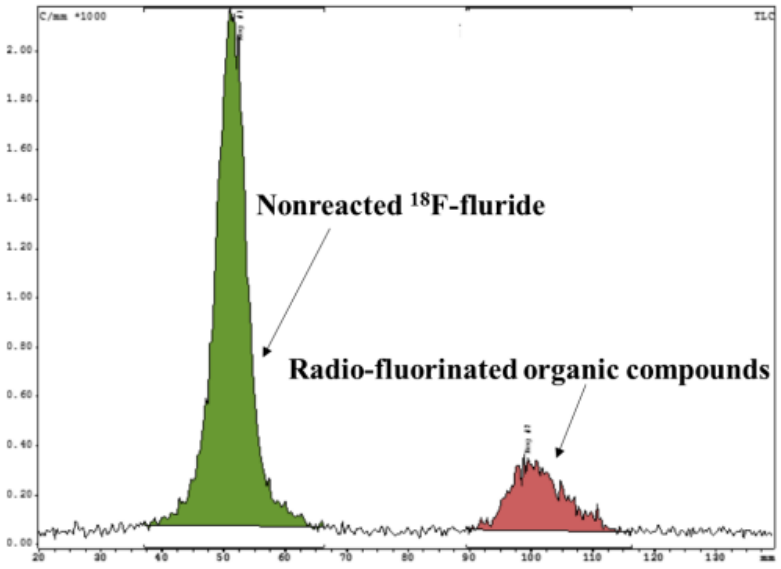

Figure A3. 19. Gamma TLC of the crude sample post radio-electrochemical synthesis

Electrolysis was performed for 60 min at 1.6 V vs Ag wire at -20 ºC using TFE solution containing 24 mM of product 3, 142 mM of triflic acid. 2 ml of TFE solution containing 25 mM TBAP and 5 mCi 18F-fluoride was added after electrolysis was finished and the sample was taken for analysis 30 min after 18F-fluoride addition

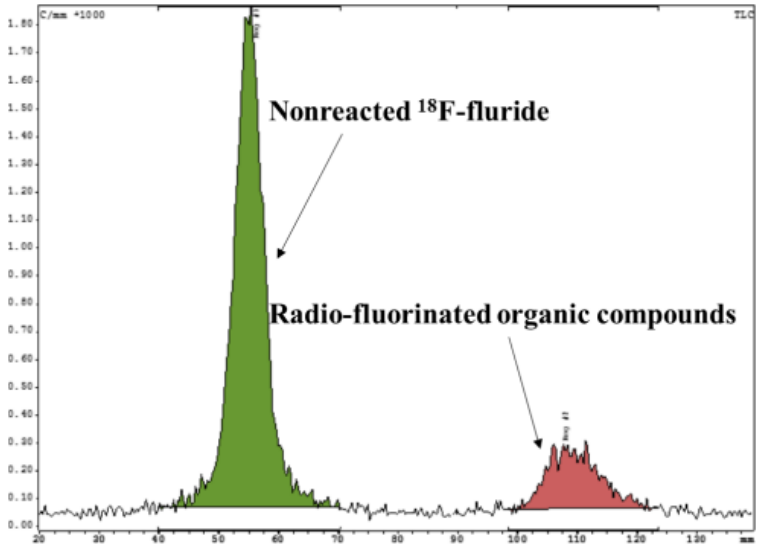

Figure A3. 20. Gamma TLC of the crude sample post radio-electrochemical synthesis

Electrolysis was performed for 60 min at 1.6 V vs Ag wire at -20 ºC using TFE solution containing 24 mM of product 5, 142 mM of triflic acid. 2 ml of TFE solution containing 25 mM TBAP and 5 mCi 18F-fluoride was added after electrolysis was finished and the sample was taken for analysis 30 min after 18Ffluoride addition.

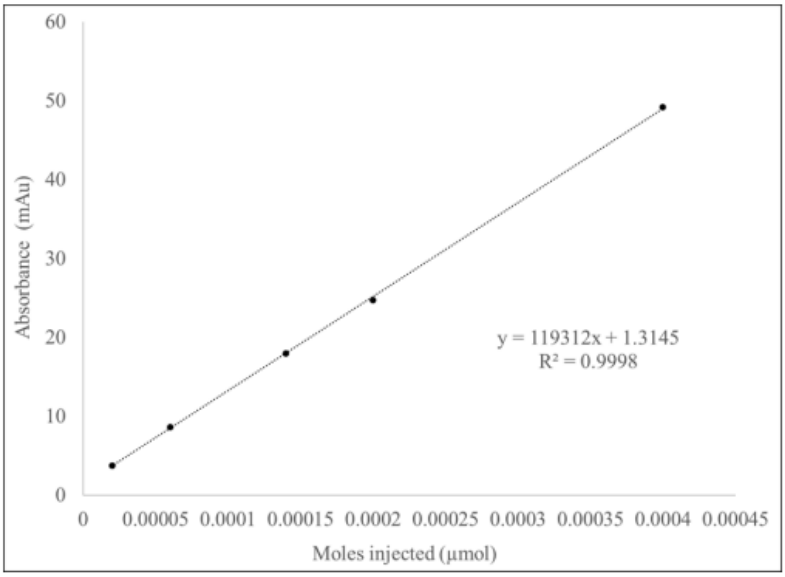

Figure A3. 21. Calibration curve of UV absorbance vs. molar mass

Calibration curves of UV absorbance versus molar mass were created in advance for calculating A_m.

Electrochemical No-Carrier-Added Radiofluorination of Thioethers

A4.1 Introduction

Positron Emission Tomography (PET) is an established molecular imaging technology widely used for the visualization of biological processes in clinical and research settings.[1] This technology relies on radioactively labeled molecules, called tracers. Fluorine-18 is the most frequently used radionuclide in PET due to its wide availability, physical half-life (t1/2 = 109.8 min), which closely matches biological half-life of many small molecules, and its favorable decay characteristics for imaging. Importantly, [^{18}F]fluoride is routinely produced in a no-carrier-added (NCA) form, that is, without added stable ^{19}F-species. Tracer formulations prepared from NCA [^{18}F]fluoride[222] contain only nanomolar quantities of the physiologically active molecule. This low amount allows for imaging without perturbing the biochemical process under investigation. If ^{19}F-carrier is added for production purposes, product molar activity (Am – amount of radioactivity per mole of product) is decreased and total amount of physiologically active tracer in the final formulation is increased. Low Am formulations can lead to saturation of the biological target under investigation and is suitable for only a handful of applications. Thioethers are attractive scaffolds for PET tracer development, yet approaches for their radiolabeling are limited. Examples of biologically relevant thioethers include radiolabeled methionine and cysteine, which are important in elucidating amino acid metabolism in multiple diseases.[223–225] The strongly nucleophilic sulfur atom hinders the use of weakly nucleophilic [^{18}F]fluoride in labeling reactions. Due to this interference, methionine radiolabeling mostly relies on electrophilic agents based on [^{11}C]carbon, a suboptimal choice due to 20 min half-life of this isotope. Despite these limitations, [^{11}C]-methionine has demonstrated significant clinical utility[226], urging further development in this area[227]. Several pharmaceuticals in clinical use contain thioether scaffolds and can be potentially radiolabeled by electrochemical radiofluorination if appropriately protected precursors are

synthesized.[226,228] Among them are nucleotide receptor antagonist Ticagrelor[229], antiretroviral Nelfinavir[230], and a urate transporter inhibitor Lesinurad[231]. Using [^{18}F] fluoride for radiolabeling of thioethers remains an important but elusive target.

A4.2 Experimental

In brief, electrolysis was performed in a 1.5 mL electrochemical cell that included a silver wire pseudo reference electrode with platinum anode and cathode electrodes. Cyclic Voltammetry was used to determine the onset oxidation potential of the precursor allowing for tailored voltage selection for the process of electrochemical fluorination.

A4. 3 Results and Discussion

In this paper we report no-carrier-added electrochemical fluorination (NCA-ECF) of a range of thioethers (Figure A4.1).

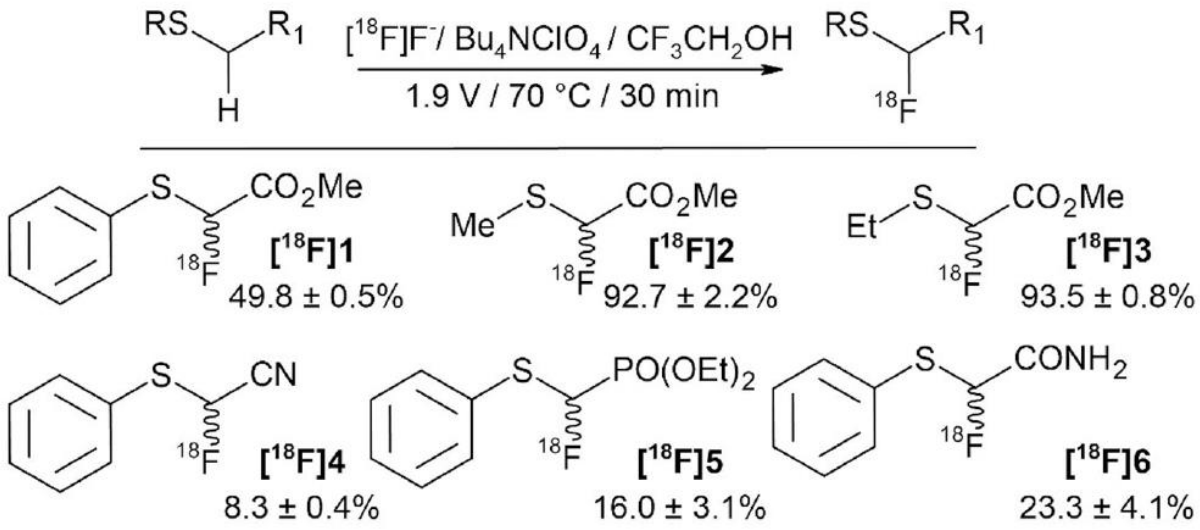

Figure 4A. 1. Scope of the NCA-ECF. Radiofluorination was performed on platinum electrodes under potentiostatic conditions

This success is enabled by electrochemical methodology, which to the best of our knowledge, is the first report of electrochemical production of NCA radiotracers in quantities typically used in clinical settings. Outside of radiochemistry, electrochemical methods offer a unique approach to

the fluorination of thioethers.[186,232–235] Unfortunately, it relies on excess of (HF)n salts and thus cannot yield NCA products. Fuchigami et al. first proposed a mechanism for the electrochemical fluorination (ECF) of thioethers[190,236] (Figure A4.2).

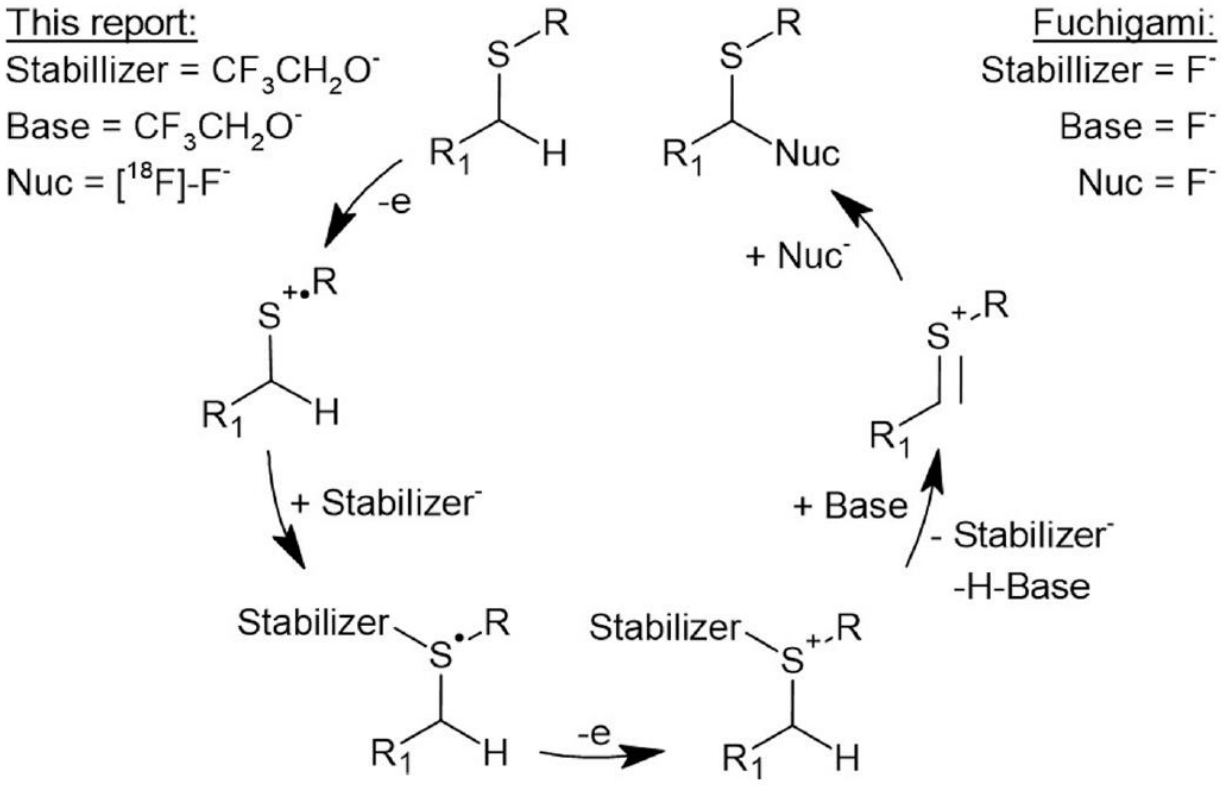

Figure 4A. 2. Proposed mechanism for the NCA-ECF compared to Fuchigami mechanism

In this mechanism, fluoride plays a 3-fold role: it stabilizes the radical cation intermediate after first oxidative step, acts as a base in the elimination step and as a nucleophile to produce the α-fluorinated sulfide.[237] There is a clear need for an excess of fluoride for this reaction to proceed in good yields.[238] The use of fluorinating agents that are not HF-based is still very rare.[239] In previous reports, we applied the Fuchigami methodology for the electrochemical 18F-fluorination of a model compound, methyl-2-(phenylthio)acetate.[215,217] Predictably, only low Am product was produced and lowering HF concentration reduced Radiochemical Yield (RCY) without significant gain in Am. We hypothesized that an auxiliary reagent could be used to replace fluoride in two roles that it plays in the Fuchigami mechanism: to stabilize the radical

intermediate and to act as Lewis base. This study reports the successful search for a Brønsted acid that plays a role of this auxiliary reagent and facilitates no-carrier-added electrochemical radiofluorination (NCA-ECF). Table A4.1. summarizes RCY, [^{18}F]fluoride conversion (Radiochemical Conversion, RCC; assessed with radio-TLC) and radiochemical purity (RCP; assessed with radio-HPLC) in a series of experiments exploring radiolabelling conditions of methyl(phenylthiol) acetate.

Table 4A. 1. NCA-ECF of Precursor 1 Using Potential Auxillary Groups (average of 3 experiments). PPTS= Pyridinium p-Toluenesulfonate; TBA-OTf= Bu4N+ CF3SO3-; TfOH= CF3SO3H; TBAP= Bu4NClO4.

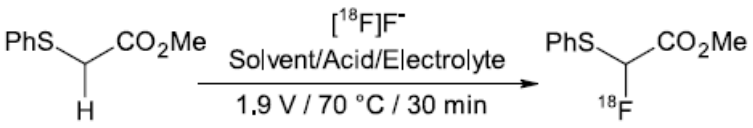

#	Solvent	Acid (mM)	Electrolyte (50 mM)	RCC,%	RCP, %	RCY, %
1	MeCN	–	TBAP	18.9 ± 0.8	2.2 ± 0.1	0.5 ± 0.1
2	DME	–	TBAP	0	0	0
3	TFE	–	TBAP	59.3 ± 1.0	84.1 ± 2.1	49.8 ± 0.5
4	HFIP	–	TBAP	58.1 ± 4.4	27.2 ± 0.4	15.8 ± 1.4
5	TFE	–	PPTS	70.5 ± 1.9	21.9 ± 0.6	15.4 ± 1.8
6	MeCN	–	PPTS	62.6 ± 7.7	6.1 ± 1.2	3.9 ± 1.2
7	TFE	–	TBA-OTf	30.9 ± 1.8	79.9 ± 1.3	24.7 ± 1.8
8	MeCN	–	TBA-OTf	0	0	0
9	TFE	2 mM TfOH	TBAP	27.5 ± 1.5	84.2 ± 4.1	23.2 ± 2.1
10	TFE	10 mM TfOH	TBAP	2.4 ± 0.1	13.5 ± 0.8	0.3 ± 0.1
11	MeCN	2 mM TfOH	TBAP	0	0	0
12	MeCN	10 mM TfOH	TBAP	0	0	0
13	TFE	2 mM TsOH	TBAP	35.8 ± 0.4	71.1 ± 1.7	25.5 ± 0.3
14	TFE	10 mM TsOH	TBAP	15.9 ± 0.5	85.8 ± 2.6	13.7 ± 0.8
15	MeCN	2 mM TsOH	TBAP	0	0	0
16	MeCN	10 mM TsOH	TBAP	0	0	0

To establish a baseline yield, NCA-ECF of [^{18}F]**1** in acetonitrile (MeCN) with tetrabutylammonium perchlorate (TBAP) as the electrolyte was investigated. The non-isolated, decay-corrected RCY of the reaction was 0.5 ± 0.2% (*n* = 3; Table A4.1, entry 1). Using dimethoxyethane (DME) as a solvent failed to produce any radioactive products (Table A4.1, entry 2) despite its reported ability to solvate quaternary ammonium cations, thereby increasing the availability of fluoride for ECF.[240,241] We explored the use of relatively weak nucleophilic triflate (OTf) and tosylate (OTs) additives in an attempt to provide stability for the cation-radical without competing with [^{18}F]fluoride nucleophile.[242] TBAP was replaced with either pyridinium tosylate or Bu4N-OTf in the NCA synthesis of [^{18}F]**1**. While the use of OTf yielded no product (Table A4.1 entry 8), a more nucleophilic[243] OTs additive led to an observed RCY of 3.9 ± 1.2% (*n* = 3): an order of magnitude increase from that observed with TBAP. This led us to hypothesize that using triflic or toluenesulfonic acids instead of their salts might have a beneficial effect. In this way, respective conjugate bases would form after cathodic reduction of acidic protons in situ. However, low pH was previously reported to diminish product yields in ECF[215], leading us to examine two concentrations of TfOH and pTSA (2 mM, 10 mM). Unfortunately, these studies did not lead to product formation. In search of additives that would be more nucleophilic than OTs, yet only modestly competitive with [^{18}F]fluoride species, we discovered that Eberson suggested use of trifluoroethanol (TFE) and hexafluoroisopropanol (HFIP) for stabilization of radical cations.[244] These solvents are known to have high dielectric constants, low polarizabilities and propensities to solvate competing anions thereby increasing the cationic intermediate lifetime.[219,220,244–246] Recently, fluorination of thioethers has been successfully demonstrated in these solvents.[247] This data encouraged us to try TFE and HFIP in NCA-ECF. This strategy proved to be fruitful and good conversion of [^{18}F] fluoride in the NCA synthesis of [^{18}F]**2** was observed with TFE and HFIP as the solvent and TBAP as the electrolyte. Whereas in the case of HFIP, considerable amounts of unknown byproducts were formed, with TFE, the vast majority of [^{18}F]fluoride incorporation resulted in

the formation of the desired product [^{18}F]**2**. It is likely that the byproducts are formed through formation of perfluorinated ethers previously described.[248] The observed RCY of 49.8 ± 1.0% with TFE as the solvent marked a breakthrough in the NCA-ECF of thioethers. In a series of follow-up experiments, the previously investigated triflate and tosylate compounds (pTS, TBATF, TfOH and pTSA) were retested as additives to the solvent TFE, resulting in reduced formation of [^{18}F]**2** as compared to the use of neat TFE. The promising results with TFE as the solvent can be explained by the proposed fluoro-Pummerer-type mechanism. Fig. A4.2 presents a combined illustration of commonly accepted fluoro-Pummerer mechanism (Fig. A4.2, right) and its modification that we suggest to explain the no-carrier added reaction reported here (Fig. A4.2, left). Trifluoroethanolate enhanced by reduction of TFE on the cathode in the single chamber cell, acts as a promoting agent in the fluoro-Pummerer-type rearrangement. TFE and HFIP alcoholates stabilize the sulfur carbocation after the first anodic oxidation. Following the second anodic oxidation reaction, fluorinated alcoholate abstracts proton in the α-position to sulfur forming a sulfonium ion. The latter can react with either [^{18}F]fluoride or competing nucleophiles to yield the desired product or an auxiliary-ether, respectively. Indeed, a substantial amount of the auxiliary-ether was observed using GC–MS.[215] HFIP alcoholate seems to have weaker stabilizing effect on the sulfur carbocation as suggested by the increased formation of undesired side products. TFE is likely to extend the cation intermediate lifetime, thereby increasing the probability of the nucleophilic attack at diminishing NCA concentrations of fluoride. In a limited study of the scope of this approach, NCA-ECF of several thioethers in TFE was performed (Fig. A4.1). Excellent RCYs were observed in the formation of [^{18}F]**2** and [^{18}F]**3**. Notably, both respective substrates lack the phenyl group adjacent to sulfur as compared to substrate 1. Poor RCY was observed in the formation of [^{18}F]**4**. The nitrile group potentially exerts a destabilizing effect on the sulfonium/carbenium cation resulting in the formation of unidentified radiochemical side products. A similar trend was seen in case of [^{18}F]**5** with the second lowest RCY within the

scope, likely caused by electron withdrawing properties of the phosphonate group. The NCA-ECF of 2-(phenylthio) acetamide to yield [^{18}F]**6** is notable since the primary amide has an oxidation potential similar to that of sulfur. The fact that this transformation proceeds without the protection of the primary amide illustrates the versatility of this methodology, in that a wider range of thioethers can potentially be fluorinated without prior modification. A complete radiosynthesis of [^{18}F]**2** that includes the HPLC isolation of the final product was performed. Up to 700 MBq of [^{18}F]**2** were synthesized within 90 min from the end of bombardment in 88 ± 3% isolated RCY and RCP of >95%. Am ranged from 4.7 to 5.3 GBq/μmol, representing >100x increase compared to previous reports on electrochemical radiofluorination, and approaching values observed in other NCA techniques.[249]

A4.3 Conclusion

This is the first example of no-carrier added radiofluorination of thioethers. The methodology tolerates a range of functional groups, including unprotected amides. This methodology offers the possibility to produce high Am ^{18}F-fluorinated thioethers as tracers for PET imaging. Further research is underway to increase the yield of NCA-ECF and extending the scope beyond thioethers and to biologically relevant molecules.

References:

(1) Phelps, M. E. Positron Emission Tomography Provides Molecular Imaging of Biological Processes. *PNAS* **2000**, *97* (16), 9226–9233. https://doi.org/10.1073/pnas.97.16.9226.

(2) Almuhaideb, A.; Papathanasiou, N.; Bomanji, J. 18F-FDG PET/CT Imaging In Oncology. *Ann Saudi Med* **2011**, *31* (1), 3–13. https://doi.org/10.4103/0256-4947.75771.

(3) Baum, R. P.; Kulkarni, H. R.; Schuchardt, C.; Singh, A.; Wirtz, M.; Wiessalla, S.; Schottelius, M.; Mueller, D.; Klette, I.; Wester, H.-J. Lutetium-177 PSMA Radioligand Therapy of Metastatic Castration-Resistant Prostate Cancer: Safety and Efficacy. *J Nucl Med* **2016**, jnumed.115.168443. https://doi.org/10.2967/jnumed.115.168443.

(4) Liu, S. Chapter 9 - Cell Metabolism. In *Bioprocess Engineering (Second Edition)*; Liu, S., Ed.; Elsevier, 2017; pp 451–533. https://doi.org/10.1016/B978-0-444-63783-3.00009-5.

(5) Montgomery, M. K.; Turner, N. Mitochondrial Dysfunction and Insulin Resistance: An Update. *Endocr Connect* **2014**, *4* (1), R1–R15. https://doi.org/10.1530/EC-14-0092.

(6) Dorn, G. W.; Vega, R. B.; Kelly, D. P. Mitochondrial Biogenesis and Dynamics in the Developing and Diseased Heart. *Genes Dev.* **2015**, *29* (19), 1981–1991. https://doi.org/10.1101/gad.269894.115.

(7) Johri, A.; Beal, M. F. Mitochondrial Dysfunction in Neurodegenerative Diseases. *J Pharmacol Exp Ther* **2012**, *342* (3), 619–630. https://doi.org/10.1124/jpet.112.192138.

(8) Weinberg, S. E.; Chandel, N. S. Targeting Mitochondria Metabolism for Cancer Therapy. *Nat. Chem. Biol.* **2015**, *11* (1), 9–15. https://doi.org/10.1038/nchembio.1712.

(9) Ravert, H. T.; Madar, I.; Dannals, R. F. Radiosynthesis of 3-[18F]Fluoropropyl and 4-[18F]Fluorobenzyl Triarylphosphonium Ions. *J Label Compd Radiopharm* **2004**, *47* (8), 469–476. https://doi.org/10.1002/jlcr.835.

(10) Commission, I. of M. (US) C. for R. and E. of the M. U. P. of the N. R.; Gottfried, K.-L. D.; Penn, G. *Clinical Applications of Ionizing Radiation*; National Academies Press (US), 1996.

(11) Ma, S.; Kong, B.; Liu, B.; Liu, X. Biological Effects of Low-Dose Radiation from Computed Tomography Scanning. *Int. J. Radiat. Biol.* **2013**, *89* (5), 326–333. https://doi.org/10.3109/09553002.2013.756595.

(12) Micewicz, E. D.; Kim, K.; Iwamoto, K. S.; Ratikan, J. A.; Cheng, G.; Boxx, G. M.; Damoiseaux, R. D.; Whitelegge, J. P.; Ruchala, P.; Nguyen, C.; Purbey, P.; Loo, J.; Deng, G.; Jung, M. E.; Sayre, J. W.; Norris, A. J.; Schaue, D.; McBride, W. H. 4-(Nitrophenylsulfonyl)Piperazines Mitigate Radiation Damage to Multiple Tissues. *PLoS ONE* **2017**, *12* (7), e0181577. https://doi.org/10.1371/journal.pone.0181577.

(13) Rodriguez, C. E.; Fukuto, J. M.; Taguchi, K.; Froines, J.; Cho, A. K. The Interactions of 9,10-Phenanthrenequinone with Glyceraldehyde-3-Phosphate Dehydrogenase (GAPDH), a Potential Site for Toxic Actions. *Chemico-Biological Interactions* **2005**, *155* (1–2), 97–110. https://doi.org/10.1016/j.cbi.2005.05.002.

(14) Martyniuk, C. J.; Fang, B.; Koomen, J. M.; Gavin, T.; Zhang, L.; Barber, D. S.; LoPachin, R. M. MOLECULAR MECHANISM OF GLYCERALDEHYDE-3-PHOSPHATE DEHYDROGENASE (GAPDH) INACTIVATION BY α,β-UNSATURATED CARBONYL DERIVATIVES. *Chem Res Toxicol* **2011**, *24* (12), 2302–2311. https://doi.org/10.1021/tx200437y.

(15) Das, A.; Chakrabarty, S.; Choudhury, D.; Chakrabarti, G. 1,4-Benzoquinone (PBQ) Induced Toxicity in Lung Epithelial Cells Is Mediated by the Disruption of the Microtubule Network and Activation of Caspase-3. *Chem. Res. Toxicol.* **2010**, *23* (6), 1054–1066. https://doi.org/10.1021/tx1000442.

(16) Banerjee, S.; Chattopadhyay, R.; Ghosh, A.; Koley, H.; Panda, K.; Roy, S.; Chattopadhyay, D.; Chatterjee, I. B. Cellular and Molecular Mechanisms of Cigarette Smoke-Induced Lung Damage and Prevention by Vitamin C. *J Inflamm* **2008**, *5* (1), 21. https://doi.org/10.1186/1476-9255-5-21.

(17) Chatterjee, N. S.; Pinkerton, K. E.; Said, H. M. P-Benzoquinone (p-BQ) , a Major Cigarette Smoke-Derived Quinone, Inhibits Vitamin B1 (Thiamin) Uptake by Human Lung Cells. *The FASEB Journal* **2012**, *26* (S1), lb755–lb755. https://doi.org/10.1096/fasebj.26.1_supplement.lb755.

(18) Ross, D.; Siegel, D. Functions of NQO1 in Cellular Protection and CoQ10 Metabolism and Its Potential Role as a Redox Sensitive Molecular Switch. *Frontiers in Physiology* **2017**, *8*.

(19) Shu, N.; Hägglund, P.; Cai, H.; Hawkins, C. L.; Davies, M. J. Modification of Cys Residues in Human Thioredoxin-1 by p-Benzoquinone Causes Inhibition of Its Catalytic Activity and Activation of the ASK1/P38-MAPK Signalling Pathway. *Redox Biol* **2019**, *29*, 101400. https://doi.org/10.1016/j.redox.2019.101400.

(20) Liebeke, M.; Pöther, D.-C.; Van Duy, N.; Albrecht, D.; Becher, D.; Hochgräfe, F.; Lalk, M.; Hecker, M.; Antelmann, H. Depletion of Thiol-Containing Proteins in Response to Quinones in Bacillus Subtilis. *Molecular Microbiology* **2008**, *69* (6), 1513–1529. https://doi.org/10.1111/j.1365-2958.2008.06382.x.

(21) Shu, N.; Lorentzen, L. G.; Davies, M. J. Reaction of Quinones with Proteins: Kinetics of Adduct Formation, Effects on Enzymatic Activity and Protein Structure, and Potential Reversibility of Modifications. *Free Radic Biol Med* **2019**, *137*, 169–180. https://doi.org/10.1016/j.freeradbiomed.2019.04.026.

(22) Miura, T.; Kakehashi, H.; Shinkai, Y.; Egara, Y.; Hirose, R.; Cho, A. K.; Kumagai, Y. GSH-Mediated S-Transarylation of a Quinone Glyceraldehyde-3-Phosphate Dehydrogenase Conjugate. *Chem. Res. Toxicol.* **2011**, *24* (11), 1836–1844. https://doi.org/10.1021/tx200025y.

(23) Johri, A.; Beal, M. F. Mitochondrial Dysfunction in Neurodegenerative Diseases. *J Pharmacol Exp Ther* **2012**, *342* (3), 619–630. https://doi.org/10.1124/jpet.112.192138.

(24) Weinberg, S. E.; Chandel, N. S. Targeting Mitochondria Metabolism for Cancer Therapy. *Nat. Chem. Biol.* **2015**, *11* (1), 9–15. https://doi.org/10.1038/nchembio.1712.

(25) Zhang, Y.; Avalos, J. L. Traditional and Novel Tools to Probe the Mitochondrial Metabolism in Health and Disease. *Wiley Interdiscip Rev Syst Biol Med* **2017**, *9* (2). https://doi.org/10.1002/wsbm.1373.

(26) Ehrenberg, B.; Montana, V.; Wei, M. D.; Wuskell, J. P.; Loew, L. M. Membrane Potential Can Be Determined in Individual Cells from the Nernstian Distribution of Cationic Dyes. *Biophys J* **1988**, *53* (5), 785–794. https://doi.org/10.1016/S0006-3495(88)83158-8.

(27) Fukuda, H.; Syrota, A.; Charbonneau, P.; Vallois, J.; Crouzel, M.; Prenant, C.; Sastre, J.; Crouzel, C. Use of 11C-Triphenylmethylphosphonium for the Evaluation of Membrane Potential in the Heart by Positron-Emission Tomography. *Eur J Nucl Med* **1986**, *11* (12), 478–483. https://doi.org/10.1007/BF00252793.

(28) Madar, I.; Anderson, J. H.; Szabo, Z.; Scheffel, U.; Kao, P. F.; Ravert, H. T.; Dannals, R. F. Enhanced Uptake of [11C]TPMP in Canine Brain Tumor: A PET Study. *J Nucl Med* **1999**, *40* (7), 1180–1185.

(29) Ravert, H. T.; Madar, I.; Dannals, R. F. Radiosynthesis of 3-[18F]Fluoropropyl and 4-[18F]Fluorobenzyl Triarylphosphonium Ions. *J Label Compd Radiopharm* **2004**, *47* (8), 469–476. https://doi.org/10.1002/jlcr.835.

(30) Madar, I.; Huang, Y.; Ravert, H.; Dalrymple, S. L.; Davidson, N. E.; Isaacs, J. T.; Dannals, R. F.; Frost, J. J. Detection and Quantification of the Evolution Dynamics of Apoptosis Using the PET Voltage Sensor 18F-Fluorobenzyl Triphenyl Phosphonium. *J Nucl Med* **2009**, *50* (5), 774–780. https://doi.org/10.2967/jnumed.108.061283.

(31) Madar, I.; Isoda, T.; Finley, P.; Angle, J.; Wahl, R. 18F-Fluorobenzyl Triphenyl Phosphonium: A Noninvasive Sensor of Brown Adipose Tissue Thermogenesis. *J Nucl Med* **2011**, *52* (5), 808–814. https://doi.org/10.2967/jnumed.110.084657.

(32) Higuchi, T.; Fukushima, K.; Rischpler, C.; Isoda, T.; Javadi, M. S.; Ravert, H.; Holt, D. P.; Dannals, R. F.; Madar, I.; Bengel, F. M. Stable Delineation of the Ischemic Area by the PET Perfusion Tracer 18F-Fluorobenzyl Triphenyl Phosphonium After Transient Coronary

Occlusion. *Journal of Nuclear Medicine* **2011**, *52* (6), 965–969. https://doi.org/10.2967/jnumed.110.085993.

(33) Madar, I.; Ravert, H. T.; Du, Y.; Hilton, J.; Volokh, L.; Dannals, R. F.; Frost, J. J.; Hare, J. M. Characterization of Uptake of the New PET Imaging Compound 18F-Fluorobenzyl Triphenyl Phosphonium in Dog Myocardium. *Journal of Nuclear Medicine* **2006**, *47* (8), 1359–1366.

(34) Ravert, H. T.; Holt, D. P.; Dannals, R. F. A Microwave Radiosynthesis of the 4-[18F]-Fluorobenzyltriphenylphosphonium Ion. *J Labelled Comp Radiopharm* **2014**, *57* (12), 695–698. https://doi.org/10.1002/jlcr.3241.

(35) Zhang, Z.; Zhang, C.; Lau, J.; Colpo, N.; Bénard, F.; Lin, K.-S. One-Step Synthesis of 4-[18F]Fluorobenzyltriphenylphosphonium Cation for Imaging with Positron Emission Tomography. *Journal of Labelled Compounds and Radiopharmaceuticals* **2016**, *59* (11), 467–471. https://doi.org/10.1002/jlcr.3436.

(36) Sanford, M. S.; Scott, P. J. H. Moving Metal-Mediated 18F-Fluorination from Concept to Clinic. *ACS Cent. Sci.* **2016**, *2* (3), 128–130. https://doi.org/10.1021/acscentsci.6b00061.

(37) Lazari, M.; Collins, J.; Shen, B.; Farhoud, M.; Yeh, D.; Maraglia, B.; Chin, F. T.; Nathanson, D. A.; Moore, M.; van Dam, R. M. Fully Automated Production of Diverse 18F-Labeled PET Tracers on the ELIXYS Multireactor Radiosynthesizer without Hardware Modification. *J Nucl Med Technol* **2014**, *42* (3), 203–210. https://doi.org/10.2967/jnmt.114.140392.

(38) Claggett, S. B.; Quinn, K. M.; Lazari, M.; Moore, M. D.; van Dam, R. M. Simplified Programming and Control of Automated Radiosynthesizers through Unit Operations. *EJNMMI Research* **2013**, *3* (1), 53. https://doi.org/10.1186/2191-219X-3-53.

(39) Speranza, A.; Ortosecco, G.; Castaldi, E.; Nardelli, A.; Pace, L.; Salvatore, M. Fully Automated Synthesis Procedure of 4-[18F]Fluorobenzaldehyde by Commercial Synthesizer: Amino-Oxi Peptide Labelling Prosthetic Group. *Appl Radiat Isot* **2009**, *67* (9), 1664–1669. https://doi.org/10.1016/j.apradiso.2009.04.008.

(40) Poethko, T.; Schottelius, M.; Thumshirn, G.; Hersel, U.; Herz, M.; Henriksen, G.; Kessler, H.; Schwaiger, M.; Wester, H.-J. Two-Step Methodology for High-Yield Routine Radiohalogenation of Peptides: (18)F-Labeled RGD and Octreotide Analogs. *J Nucl Med* **2004**, *45* (5), 892–902.

(41) Scott, P. J. H.; Hockley, B. G.; Kung, H. F.; Manchanda, R.; Zhang, W.; Kilbourn, M. R. Studies into Radiolytic Decomposition of Fluorine-18 Labeled Radiopharmaceuticals for Positron Emission Tomography. *Appl Radiat Isot* **2009**, *67* (1), 88–94. https://doi.org/10.1016/j.apradiso.2008.08.015.

(42) Schueller, M. J.; Alexoff, D. L.; Schlyer, D. J. Separating Long-Lived Metal Ions from 18F during H218O Recovery. *Nuclear Instruments and Methods in Physics Research Section B: Beam Interactions with Materials and Atoms* **2007**, *261* (1), 795–799. https://doi.org/10.1016/j.nimb.2007.04.193.

(43) Iwata, R.; Pascali, C.; Bogni, A.; Horvath, G.; Kovacs, Z.; Yanai, K.; Ido, T. A New, Convenient Method for the Preparation of 4-[18F]Fluorobenzyl Halides. *Appl Radiat Isot* **2000**, *52* (1), 87–92. https://doi.org/10.1016/s0969-8043(99)00117-7.

(44) Rodnick, M. E.; Brooks, A. F.; Hockley, B. G.; Henderson, B. D.; Scott, P. J. H. A Fully-Automated One-Pot Synthesis of [18F]Fluoromethylcholine with Reduced Dimethylaminoethanol Contamination via [18F]Fluoromethyl Tosylate. *Appl Radiat Isot* **2013**, *78*, 26–32. https://doi.org/10.1016/j.apradiso.2013.04.017.

(45) Su, D.; Cheng, Y.; Liu, M.; Liu, D.; Cui, H.; Zhang, B.; Zhou, S.; Yang, T.; Mei, Q. Comparision of Piceid and Resveratrol in Antioxidation and Antiproliferation Activities In Vitro. *PLoS One* **2013**, *8* (1), e54505. https://doi.org/10.1371/journal.pone.0054505.

(46) Mitchell, P.; Moyle, J. Evidence Discriminating between the Chemical and the Chemiosmotic Mechanisms of Electron Transport Phosphorylation. *Nature* **1965**, *208* (5016), 1205–1206. https://doi.org/10.1038/2081205a0.

(47) Morais, R.; Zinkewich-Péotti, K.; Parent, M.; Wang, H.; Babai, F.; Zollinger, M. Tumor-Forming Ability in Athymic Nude Mice of Human Cell Lines Devoid of Mitochondrial DNA1. *Cancer Research* **1994**, *54* (14), 3889–3896.

(48) Cavalli, L. R.; Varella-Garcia, M.; Liang, B. C. Diminished Tumorigenic Phenotype after Depletion of Mitochondrial DNA. *Cell Growth Differ* **1997**, *8* (11), 1189–1198.

(49) Momcilovic, M.; McMickle, R.; Abt, E.; Seki, A.; Simko, S. A.; Magyar, C.; Stout, D. B.; Fishbein, M. C.; Walser, T. C.; Dubinett, S. M.; Shackelford, D. B. Heightening Energetic Stress Selectively Targets LKB1-Deficient Non–Small Cell Lung Cancers. *Cancer Research* **2015**, *75* (22), 4910–4922. https://doi.org/10.1158/0008-5472.CAN-15-0797.

(50) Shackelford, D. B.; Abt, E.; Gerken, L.; Vasquez, D. S.; Seki, A.; Leblanc, M.; Wei, L.; Fishbein, M. C.; Czernin, J.; Mischel, P. S.; Shaw, R. J. LKB1 Inactivation Dictates Therapeutic Response of Non-Small Cell Lung Cancer to the Metabolism Drug Phenformin. *Cancer Cell* **2013**, *23* (2), 143–158. https://doi.org/10.1016/j.ccr.2012.12.008.

(51) Birsoy, K.; Possemato, R.; Lorbeer, F. K.; Bayraktar, E. C.; Thiru, P.; Yucel, B.; Wang, T.; Chen, W. W.; Clish, C. B.; Sabatini, D. M. Metabolic Determinants of Cancer Cell Sensitivity to Glucose Limitation and Biguanides. *Nature* **2014**, *508* (7494), 108–112. https://doi.org/10.1038/nature13110.

(52) Waldmann, C. M.; Gomez, A.; Marchis, P.; Bailey, S. T.; Momcilovic, M.; Jones, A. E.; Shackelford, D. B.; Sadeghi, S. An Automated Multidose Synthesis of the Potentiometric PET Probe 4-[18F]Fluorobenzyl-Triphenylphosphonium ([18F]FBnTP). *Molecular imaging and biology : MIB : the official publication of the Academy of Molecular Imaging* **2018**, *20* (2), 205. https://doi.org/10.1007/s11307-017-1119-1.

(53) Momcilovic, M.; Bailey, S. T.; Lee, J. T.; Fishbein, M. C.; Braas, D.; Go, J.; Graeber, T. G.; Parlati, F.; Demo, S.; Li, R.; Walser, T. C.; Gricowski, M.; Shuman, R.; Ibarra, J.; Fridman, D.; Phelps, M. E.; Badran, K.; St. John, M.; Bernthal, N. M.; Federman, N.; Yanagawa, J.; Dubinett, S. M.; Sadeghi, S.; Christofk, H. R.; Shackelford, D. B. The GSK3 Signaling Axis

Regulates Adaptive Glutamine Metabolism in Lung Squamous Cell Carcinoma. *Cancer Cell* **2018**, *33* (5), 905-921.e5. https://doi.org/10.1016/j.ccell.2018.04.002.

(54) Wittig, I.; Braun, H.-P.; Schägger, H. Blue Native PAGE. *Nat Protoc* **2006**, *1* (1), 418–428. https://doi.org/10.1038/nprot.2006.62.

(55) Weinberg, F.; Hamanaka, R.; Wheaton, W. W.; Weinberg, S.; Joseph, J.; Lopez, M.; Kalyanaraman, B.; Mutlu, G. M.; Budinger, G. R. S.; Chandel, N. S. Mitochondrial Metabolism and ROS Generation Are Essential for Kras-Mediated Tumorigenicity. *Proceedings of the National Academy of Sciences* **2010**, *107* (19), 8788–8793. https://doi.org/10.1073/pnas.1003428107.

(56) Ji, H.; Ramsey, M. R.; Hayes, D. N.; Fan, C.; McNamara, K.; Kozlowski, P.; Torrice, C.; Wu, M. C.; Shimamura, T.; Perera, S. A.; Liang, M.-C.; Cai, D.; Naumov, G. N.; Bao, L.; Contreras, C. M.; Li, D.; Chen, L.; Krishnamurthy, J.; Koivunen, J.; Chirieac, L. R.; Padera, R. F.; Bronson, R. T.; Lindeman, N. I.; Christiani, D. C.; Lin, X.; Shapiro, G. I.; Jänne, P. A.; Johnson, B. E.; Meyerson, M.; Kwiatkowski, D. J.; Castrillon, D. H.; Bardeesy, N.; Sharpless, N. E.; Wong, K.-K. LKB1 Modulates Lung Cancer Differentiation and Metastasis. *Nature* **2007**, *448* (7155), 807–810. https://doi.org/10.1038/nature06030.

(57) Madar, I.; Ravert, H.; Nelkin, B.; Abro, M.; Pomper, M.; Dannals, R.; Frost, J. J. Characterization of Membrane Potential-Dependent Uptake of the Novel PET Tracer 18F-Fluorobenzyl Triphenylphosphonium Cation. *Eur J Nucl Med Mol Imaging* **2007**, *34* (12), 2057–2065. https://doi.org/10.1007/s00259-007-0500-8.

(58) Smith, R. A. J.; Hartley, R. C.; Murphy, M. P. Mitochondria-Targeted Small Molecule Therapeutics and Probes. *Antioxidants & Redox Signaling* **2011**, *15* (12), 3021–3038. https://doi.org/10.1089/ars.2011.3969.

(59) Kim, D.-Y.; Kim, H.-S.; Le, U. N.; Jiang, S. N.; Kim, H.-J.; Lee, K.-C.; Woo, S.-K.; Chung, J.; Kim, H.-S.; Bom, H.-S.; Yu, K.-H.; Min, J.-J. Evaluation of a Mitochondrial Voltage Sensor, (18F-Fluoropentyl)Triphenylphosphonium Cation, in a Rat Myocardial Infarction Model.

Journal of Nuclear Medicine **2012**, *53* (11), 1779–1785. https://doi.org/10.2967/jnumed.111.102657.

(60) Logan, A.; Pell, V. R.; Shaffer, K. J.; Evans, C.; Stanley, N. J.; Robb, E. L.; Prime, T. A.; Chouchani, E. T.; Cochemé, H. M.; Fearnley, I. M.; Vidoni, S.; James, A. M.; Porteous, C. M.; Partridge, L.; Krieg, T.; Smith, R. A. J.; Murphy, M. P. Assessing the Mitochondrial Membrane Potential in Cells and In Vivo Using Targeted Click Chemistry and Mass Spectrometry. *Cell Metab* **2016**, *23* (2), 379–385. https://doi.org/10.1016/j.cmet.2015.11.014.

(61) Dykens, J. A.; Jamieson, J.; Marroquin, L.; Nadanaciva, S.; Billis, P. A.; Will, Y. Biguanide-Induced Mitochondrial Dysfunction Yields Increased Lactate Production and Cytotoxicity of Aerobically-Poised HepG2 Cells and Human Hepatocytes in Vitro. *Toxicology and Applied Pharmacology* **2008**, *233* (2), 203–210. https://doi.org/10.1016/j.taap.2008.08.013.

(62) Li, F.; Han, X.; Li, F.; Wang, R.; Wang, H.; Gao, Y.; Wang, X.; Fang, Z.; Zhang, W.; Yao, S.; Tong, X.; Wang, Y.; Feng, Y.; Sun, Y.; Li, Y.; Wong, K.-K.; Zhai, Q.; Chen, H.; Ji, H. LKB1 Inactivation Elicits a Redox Imbalance to Modulate Non-Small Cell Lung Cancer Plasticity and Therapeutic Response. *Cancer Cell* **2015**, *27* (5), 698–711. https://doi.org/10.1016/j.ccell.2015.04.001.

(63) Giordano, S.; Lee, J.; Darley-Usmar, V. M.; Zhang, J. Distinct Effects of Rotenone, 1-Methyl-4-Phenylpyridinium and 6-Hydroxydopamine on Cellular Bioenergetics and Cell Death. *PLOS ONE* **2012**, *7* (9), e44610. https://doi.org/10.1371/journal.pone.0044610.

(64) Singer, T. P.; Ramsay, R. R. The Reaction Sites of Rotenone and Ubiquinone with Mitochondrial NADH Dehydrogenase. *Biochimica et Biophysica Acta (BBA) - Bioenergetics* **1994**, *1187* (2), 198–202. https://doi.org/10.1016/0005-2728(94)90110-4.

(65) Caboni, P.; Sherer, T. B.; Zhang, N.; Taylor, G.; Na, H. M.; Greenamyre, J. T.; Casida, J. E. Rotenone, Deguelin, Their Metabolites, and the Rat Model of Parkinson's Disease. *Chem. Res. Toxicol.* **2004**, *17* (11), 1540–1548. https://doi.org/10.1021/tx049867r.

(66) Bridges, H. R.; Jones, A. J. Y.; Pollak, M. N.; Hirst, J. Effects of Metformin and Other Biguanides on Oxidative Phosphorylation in Mitochondria. *Biochemical Journal* **2014**, *462* (3), 475–487. https://doi.org/10.1042/BJ20140620.

(67) OWEN, M. R.; DORAN, E.; HALESTRAP, A. P. Evidence That Metformin Exerts Its Anti-Diabetic Effects through Inhibition of Complex 1 of the Mitochondrial Respiratory Chain. *Biochemical Journal* **2000**, *348* (3), 607–614. https://doi.org/10.1042/bj3480607.

(68) Wheaton, W. W.; Weinberg, S. E.; Hamanaka, R. B.; Soberanes, S.; Sullivan, L. B.; Anso, E.; Glasauer, A.; Dufour, E.; Mutlu, G. M.; Budigner, G. S.; Chandel, N. S. Metformin Inhibits Mitochondrial Complex I of Cancer Cells to Reduce Tumorigenesis. *eLife* **2014**, *3*, e02242. https://doi.org/10.7554/eLife.02242.

(69) Sanchez-Rangel, E.; Inzucchi, S. E. Metformin: Clinical Use in Type 2 Diabetes. *Diabetologia* **2017**, *60* (9), 1586–1593. https://doi.org/10.1007/s00125-017-4336-x.

(70) Hensley, C. T.; Faubert, B.; Yuan, Q.; Lev-Cohain, N.; Jin, E.; Kim, J.; Jiang, L.; Ko, B.; Skelton, R.; Loudat, L.; Wodzak, M.; Klimko, C.; McMillan, E.; Butt, Y.; Ni, M.; Oliver, D.; Torrealba, J.; Malloy, C. R.; Kernstine, K.; Lenkinski, R. E.; DeBerardinis, R. J. Metabolic Heterogeneity in Human Lung Tumors. *Cell* **2016**, *164* (4), 681–694. https://doi.org/10.1016/j.cell.2015.12.034.

(71) de Bruin, E. C.; McGranahan, N.; Mitter, R.; Salm, M.; Wedge, D. C.; Yates, L.; Jamal-Hanjani, M.; Shafi, S.; Murugaesu, N.; Rowan, A. J.; Grönroos, E.; Muhammad, M. A.; Horswell, S.; Gerlinger, M.; Varela, I.; Jones, D.; Marshall, J.; Voet, T.; Van Loo, P.; Rassl, D. M.; Rintoul, R. C.; Janes, S. M.; Lee, S.-M.; Forster, M.; Ahmad, T.; Lawrence, D.; Falzon, M.; Capitanio, A.; Harkins, T. T.; Lee, C. C.; Tom, W.; Teefe, E.; Chen, S.-C.; Begum, S.; Rabinowitz, A.; Phillimore, B.; Spencer-Dene, B.; Stamp, G.; Szallasi, Z.; Matthews, N.; Stewart, A.; Campbell, P.; Swanton, C. Spatial and Temporal Diversity in Genomic Instability Processes Defines Lung Cancer Evolution. *Science* **2014**, *346* (6206), 251–256. https://doi.org/10.1126/science.1253462.

(72) Su, C.-Y.; Chang, Y.-C.; Yang, C.-J.; Huang, M.-S.; Hsiao, M. The Opposite Prognostic Effect of NDUFS1 and NDUFS8 in Lung Cancer Reflects the Oncojanus Role of Mitochondrial Complex I. *Sci Rep* **2016**, *6* (1), 31357. https://doi.org/10.1038/srep31357.

(73) Molina, J. R.; Sun, Y.; Protopopova, M.; Gera, S.; Bandi, M.; Bristow, C.; McAfoos, T.; Morlacchi, P.; Ackroyd, J.; Agip, A.-N. A.; Al-Atrash, G.; Asara, J.; Bardenhagen, J.; Carrillo, C. C.; Carroll, C.; Chang, E.; Ciurea, S.; Cross, J. B.; Czako, B.; Deem, A.; Daver, N.; de Groot, J. F.; Dong, J.-W.; Feng, N.; Gao, G.; Gay, J.; Do, M. G.; Greer, J.; Giuliani, V.; Han, J.; Han, L.; Henry, V. K.; Hirst, J.; Huang, S.; Jiang, Y.; Kang, Z.; Khor, T.; Konoplev, S.; Lin, Y.-H.; Liu, G.; Lodi, A.; Lofton, T.; Ma, H.; Mahendra, M.; Matre, P.; Mullinax, R.; Peoples, M.; Petrocchi, A.; Rodriguez-Canale, J.; Serreli, R.; Shi, T.; Smith, M.; Tabe, Y.; Theroff, J.; Tiziani, S.; Xu, Q.; Zhang, Q.; Muller, F.; DePinho, R. A.; Toniatti, C.; Draetta, G. F.; Heffernan, T. P.; Konopleva, M.; Jones, P.; Di Francesco, M. E.; Marszalek, J. R. An Inhibitor of Oxidative Phosphorylation Exploits Cancer Vulnerability. *Nat Med* **2018**, *24* (7), 1036–1046. https://doi.org/10.1038/s41591-018-0052-4.

(74) Murray, D.; McBride, W. H. Radioprotective Agents. In *Kirk-Othmer Encyclopedia of Chemical Technology*; John Wiley & Sons, Ltd, 2000. https://doi.org/10.1002/0471238961.1801040913211818.a01.

(75) Bond, V. P.; Fludner, T. M.; Archambeau, J. O. *Mammalian Radiation Lethality. A disturbance in cellular kinetics. by BOND, V.P., T.M. FLIEDNER & J.O. ARCHAMBEAU.: Lnbd. (1965) 0.* | *ANTIQUARIAT ERDLEN*. https://www.abebooks.com/Mammalian-Radiation-Lethality-disturbance-cellular-kinetics/16216004015/bd (accessed 2022-08-25).

(76) Kim, K.; Pollard, J. M.; Norris, A. J.; McDonald, J. T.; Sun, Y.; Micewicz, E.; Pettijohn, K.; Damoiseaux, R.; Iwamoto, K. S.; Sayre, J. W.; Price, B. D.; Gatti, R. A.; McBride, W. H. High-Throughput Screening Identifies Two Classes of Antibiotics as Radioprotectors: Tetracyclines and Fluoroquinolones. *Clin Cancer Res* **2009**, *15* (23), 7238–7245. https://doi.org/10.1158/1078-0432.CCR-09-1964.

(77) Burdelya, L. G.; Gleiberman, A. S.; Toshkov, I.; Aygun-Sunar, S.; Bapardekar, M.; Manderscheid-Kern, P.; Bellnier, D.; Krivokrysenko, V. I.; Feinstein, E.; Gudkov, A. V. Toll-like Receptor 5 Agonist Protects Mice from Dermatitis and Oral Mucositis Caused by Local Radiation: Implications for Head-and-Neck Cancer Radiotherapy. *Int J Radiat Oncol Biol Phys* **2012**, *83* (1), 228–234. https://doi.org/10.1016/j.ijrobp.2011.05.055.

(78) Medhora, M.; Gao, F.; Fish, B. L.; Jacobs, E. R.; Moulder, J. E.; Szabo, A. Dose-Modifying Factor for Captopril for Mitigation of Radiation Injury to Normal Lung. *J Radiat Res* **2012**, *53* (4), 633–640. https://doi.org/10.1093/jrr/rrs004.

(79) Himburg, H. A.; Yan, X.; Doan, P. L.; Quarmyne, M.; Micewicz, E.; McBride, W.; Chao, N. J.; Slamon, D. J.; Chute, J. P. Pleiotrophin Mediates Hematopoietic Regeneration via Activation of RAS. *J Clin Invest* **2014**, *124* (11), 4753–4758. https://doi.org/10.1172/JCI76838.

(80) Jiang, X.; Engelbach, J. A.; Yuan, L.; Cates, J.; Gao, F.; Drzymala, R. E.; Hallahan, D. E.; Rich, K. M.; Schmidt, R. E.; Ackerman, J. J. H.; Garbow, J. R. Anti-VEGF Antibodies Mitigate the Development of Radiation Necrosis in Mouse Brain. *Clin Cancer Res* **2014**, *20* (10), 2695–2702. https://doi.org/10.1158/1078-0432.CCR-13-1941.

(81) Cohen, E. P.; Fish, B. L.; Moulder, J. E. Clinically Relevant Doses of Enalapril Mitigate Multiple Organ Radiation Injury. *Radiat Res* **2016**, *185* (3), 313–318. https://doi.org/10.1667/RR4243.S1.

(82) Steinman, J.; Epperly, M.; Hou, W.; Willis, J.; Wang, H.; Fisher, R.; Liu, B.; Bahar, I.; McCaw, T.; Kagan, V.; Bayir, H.; Yu, J.; Wipf, P.; Li, S.; Huq, M. S.; Greenberger, J. S. Improved Total-Body Irradiation Survival by Delivery of Two Radiation Mitigators That Target Distinct Cell Death Pathways. *Radiat Res* **2018**, *189* (1), 68–83. https://doi.org/10.1667/RR14787.1.

(83) Quastler, H. Studies on Roentgen Death in Mice. *Am J Roentgenol Radium Ther* **1945**, *54*, 449–461.

(84) Quastler, H. Studies on Roentgen Death in Mice; Body Weight and Sensitivity. *Am J Roentgenol Radium Ther* **1945**, *54*, 457–461.

(85) Quastler, H. Studies on Roentgen Death in Mice; Survival Time and Dosage. *Am J Roentgenol Radium Ther* **1945**, *54*, 449–456.

(86) Austin, M. K.; Miller, M.; Quastler, H. Five- to Eight-Day Radiation Death in Mice. *Radiat Res* **1956**, *5* (3), 303–307.

(87) Sacher, G. A.; Grahn, D. SURVIVAL OF MICE UNDER DURATION-OF-LIFE EXPOSURE TO GAMMA RAYS. I. THE DOSAGE-SURVIVAL RELATION AND THE LETHALITY FUNCTION. *J Natl Cancer Inst* **1964**, *32*, 277–321.

(88) Schaue, D.; McBride, W. H. Are Animal Models a Necessity for Acute Radiation Syndrome Drug Discovery? *Expert Opin Drug Discov* **2019**, *14* (6), 511–515. https://doi.org/10.1080/17460441.2019.1591364.

(89) McBride, W. H.; Schaue, D. Radiation-Induced Tissue Damage and Response. *J Pathol* **2020**, *250* (5), 647–655. https://doi.org/10.1002/path.5389.

(90) Williams, J. P.; McBride, W. H. After the Bomb Drops: A New Look at Radiation-Induced Multiple Organ Dysfunction Syndrome (MODS). *Int J Radiat Biol* **2011**, *87* (8), 851–868. https://doi.org/10.3109/09553002.2011.560996.

(91) Micewicz, E. D.; Iwamoto, K. S.; Ratikan, J. A.; Nguyen, C.; Xie, M. W.; Cheng, G.; Boxx, G. M.; Deriu, E.; Damoiseaux, R. D.; Whitelegge, J. P.; Ruchala, P. P.; Avetisyan, R.; Jung, M. E.; Lawson, G.; Nemeth, E.; Ganz, T.; Sayre, J. W.; McBride, W. H.; Schaue, D. The Aftermath of Surviving Acute Radiation Hematopoietic Syndrome and Its Mitigation. *Radiat Res* **2019**, *191* (4), 323–334. https://doi.org/10.1667/RR15231.1.

(92) Singh, V. K.; Seed, T. M. Pharmacological Management of Ionizing Radiation Injuries: Current and Prospective Agents and Targeted Organ Systems. *Expert Opin Pharmacother* **2020**, *21* (3), 317–337. https://doi.org/10.1080/14656566.2019.1702968.

(93) Farese, A. M.; Bennett, A. W.; Gibbs, A. M.; Hankey, K. G.; Prado, K.; Jackson, W.; MacVittie, T. J. Efficacy of Neulasta or Neupogen on H-ARS and GI-ARS Mortality and Hematopoietic Recovery in Nonhuman Primates After 10-Gy Irradiation With 2.5% Bone Marrow Sparing. *Health Phys* **2019**, *116* (3), 339–353. https://doi.org/10.1097/HP.0000000000000878.

(94) van Os, R.; Robinson, S.; Sheridan, T.; Mauch, P. M. Granulocyte-Colony Stimulating Factor Impedes Recovery from Damage Caused by Cytotoxic Agents through Increased Differentiation at the Expense of Self-Renewal. *Stem Cells* **2000**, *18* (2), 120–127. https://doi.org/10.1634/stemcells.18-2-120.

(95) Li, C.; Lu, L.; Zhang, J.; Huang, S.; Xing, Y.; Zhao, M.; Zhou, D.; Li, D.; Meng, A. Granulocyte Colony-Stimulating Factor Exacerbates Hematopoietic Stem Cell Injury after Irradiation. *Cell Biosci* **2015**, *5*, 65. https://doi.org/10.1186/s13578-015-0057-3.

(96) Kim, K.; Damoiseaux, R.; Norris, A. J.; Rivina, L.; Bradley, K.; Jung, M. E.; Gatti, R. A.; Schiestl, R. H.; McBride, W. H. High Throughput Screening of Small Molecule Libraries for Modifiers of Radiation Responses. *Int J Radiat Biol* **2011**, *87* (8), 839–845. https://doi.org/10.3109/09553002.2011.560994.

(97) Lant, B.; Derry, W. B. High-Throughput RNAi Screening for Germline Apoptosis Genes in Caenorhabditis Elegans. *Cold Spring Harb Protoc* **2014**, *2014* (4), 428–434. https://doi.org/10.1101/pdb.prot080234.

(98) Contreras, J. I.; Robb, C. M.; King, H. M.; Baxter, J.; Crawford, A. J.; Kour, S.; Kizhake, S.; Sonawane, Y. A.; Rana, S.; Hollingsworth, M. A.; Luo, X.; Natarajan, A. Chemical Genetic Screens Identify Kinase Inhibitor Combinations That Target Anti-Apoptotic Proteins for Cancer Therapy. *ACS Chem Biol* **2018**, *13* (5), 1148–1152. https://doi.org/10.1021/acschembio.8b00077.

(99) Kim, K.; McBride, W. H. Modifying Radiation Damage. *Curr Drug Targets* **2010**, *11* (11), 1352–1365. https://doi.org/10.2174/1389450111009011352.

(100) Bhat, K.; Medina, P.; He, L.; Zhang, L.; Saki, M.; Ioannidis, A.; Nguyen, N. T.; Sodhi, S. S.; Sung, D.; Magyar, C. E.; Liau, L. M.; Kornblum, H. I.; Pajonk, F. 1-[(4-Nitrophenyl)Sulfonyl]-4-Phenylpiperazine Treatment after Brain Irradiation Preserves Cognitive Function in Mice. *Neuro Oncol* **2020**, *22* (10), 1484–1494. https://doi.org/10.1093/neuonc/noaa095.

(101) Duhachek-Muggy, S.; Bhat, K.; Medina, P.; Cheng, F.; He, L.; Alli, C.; Saki, M.; Muthukrishnan, S. D.; Ruffenach, G.; Eghbali, M.; Vlashi, E.; Pajonk, F. Radiation Mitigation of the Intestinal Acute Radiation Injury in Mice by 1-[(4-Nitrophenyl)Sulfonyl]-4-Phenylpiperazine. *Stem Cells Transl Med* **2020**, *9* (1), 106–119. https://doi.org/10.1002/sctm.19-0136.

(102) McBride, W. H.; Thacker, J. D.; Comora, S.; Economou, J.; Hogge, D.; Dougherty, G. J. IL-7 Gene Infection of a Murine Fibrosarcoma Fsa Enhances Tumor Immunity. *Proc. Am. Assoc. Cancer Res. Annu. Meet* **1992**, *33*, 334.

(103) Haribhai, D.; Williams, J. B.; Jia, S.; Nickerson, D.; Schmitt, E. G.; Edwards, B.; Ziegelbauer, J.; Yassai, M.; Li, S.-H.; Relland, L. M.; Wise, P. M.; Chen, A.; Zheng, Y.-Q.; Simpson, P. M.; Gorski, J.; Salzman, N. H.; Hessner, M. J.; Chatila, T. A.; Williams, C. B. A Requisite Role for Induced Regulatory T Cells in Tolerance Based on Expanding Antigen Receptor Diversity. *Immunity* **2011**, *35* (1), 109–122. https://doi.org/10.1016/j.immuni.2011.03.029.

(104) Laval, S.; Dayoub, W.; Favre-Reguillon, A.; Berthod, M.; Demonchaux, P.; Mignani, G.; Lemaire, M. A Mild and Efficient Method for the Reduction of Nitriles. *Tetrahedron Letters* **2009**, *50* (50), 7005–7007. https://doi.org/10.1016/j.tetlet.2009.09.164.

(105) Bhat, K.; Duhachek-Muggy, S.; Ramanathan, R.; Saki, M.; Alli, C.; Medina, P.; Damoiseaux, R.; Whitelegge, J.; McBride, W. H.; Schaue, D.; Vlashi, E.; Pajonk, F. 1-(4-Nitrobenzenesulfonyl)-4-Penylpiperazine Increases the Number of Peyer's Patch-Associated

Regenerating Crypts in the Small Intestines after Radiation Injury. *Radiother Oncol* **2019**, *132*, 8–15. https://doi.org/10.1016/j.radonc.2018.11.011.

(106) Gelderblom, H.; Verweij, J.; Nooter, K.; Sparreboom, A. Cremophor EL: The Drawbacks and Advantages of Vehicle Selection for Drug Formulation. *Eur J Cancer* **2001**, *37* (13), 1590–1598. https://doi.org/10.1016/s0959-8049(01)00171-x.

(107) Gomes, A. C.; Biswas, G.; Biswas, S.; Biswas, G. K.; Iitaka, Y.; Banerjee, A. Crystal Structure of N-(4-Nitrophenyl)-N-Phenylsulfonamide. *Journal of Crystallographic and Spectroscopic Research* **1993**, *23* (6), 513–517. https://doi.org/10.1007/BF01182529.

(108) Madsen, K.; Knudsen, L. B.; Agersoe, H.; Nielsen, P. F.; Thøgersen, H.; Wilken, M.; Johansen, N. L. Structure-Activity and Protraction Relationship of Long-Acting Glucagon-like Peptide-1 Derivatives: Importance of Fatty Acid Length, Polarity, and Bulkiness. *J Med Chem* **2007**, *50* (24), 6126–6132. https://doi.org/10.1021/jm070861j.

(109) Bellmann-Sickert, K.; Elling, C. E.; Madsen, A. N.; Little, P. B.; Lundgren, K.; Gerlach, L.-O.; Bergmann, R.; Holst, B.; Schwartz, T. W.; Beck-Sickinger, A. G. Long-Acting Lipidated Analogue of Human Pancreatic Polypeptide Is Slowly Released into Circulation. *J Med Chem* **2011**, *54* (8), 2658–2667. https://doi.org/10.1021/jm101357e.

(110) Wilson, B. R. SURVIVAL STUDIES OF WHOLE-BODY X-IRRADIATED GERMFREE (AXENIC) MICE. *Radiat Res* **1963**, *20*, 477–483.

(111) Matsuzawa, T. SURVIVAL TIME IN GERMFREE MICE AFTER LETHAL WHOLE BODY X-IRRADIATION. *Tohoku J Exp Med* **1965**, *85*, 257–263. https://doi.org/10.1620/tjem.85.257.

(112) Mason, K. A.; Withers, H. R.; McBride, W. H.; Davis, C. A.; Smathers, J. B. Comparison of the Gastrointestinal Syndrome after Total-Body or Total-Abdominal Irradiation. *Radiat Res* **1989**, *117* (3), 480–488.

(113) Hafer, K.; Rivina, Y.; Schiestl, R. H. Yeast DEL Assay Detects Protection against Radiation-Induced Cytotoxicity and Genotoxicity: Adaptation of a Microtiter Plate Version. *Radiat Res* **2010**, *174* (6), 719–726. https://doi.org/10.1667/RR2059.1.

(114) Bhanja, P.; Norris, A.; Gupta-Saraf, P.; Hoover, A.; Saha, S. BCN057 Induces Intestinal Stem Cell Repair and Mitigates Radiation-Induced Intestinal Injury. *Stem Cell Res Ther* **2018**, *9* (1), 26. https://doi.org/10.1186/s13287-017-0763-3.

(115) Hershman, J. M.; Okunyan, A.; Rivina, Y.; Cannon, S.; Hogen, V. Prevention of DNA Double-Strand Breaks Induced by Radioiodide-(131)I in FRTL-5 Thyroid Cells. *Endocrinology* **2011**, *152* (3), 1130–1135. https://doi.org/10.1210/en.2010-1163.

(116) Cejková, J.; Cejka, C.; Ardan, T.; Sirc, J.; Michálek, J.; Luyckx, J. Reduced UVB-Induced Corneal Damage Caused by Reactive Oxygen and Nitrogen Species and Decreased Changes in Corneal Optics after Trehalose Treatment. *Histol Histopathol* **2010**, *25* (11), 1403–1416. https://doi.org/10.14670/HH-25.1403.

(117) Cejková, J.; Cejka, C.; Luyckx, J. Trehalose Treatment Accelerates the Healing of UVB-Irradiated Corneas. Comparative Immunohistochemical Studies on Corneal Cryostat Sections and Corneal Impression Cytology. *Histol Histopathol* **2012**, *27* (8), 1029–1040. https://doi.org/10.14670/HH-27.1029.

(118) Emanuele, E.; Bertona, M.; Sanchis-Gomar, F.; Pareja-Galeano, H.; Lucia, A. Protective Effect of Trehalose-Loaded Liposomes against UVB-Induced Photodamage in Human Keratinocytes. *Biomed Rep* **2014**, *2* (5), 755–759. https://doi.org/10.3892/br.2014.310.

(119) Ledney, G. D.; Madonna, G. S.; Moore, M. M.; Elliott, T. B.; Brook, I. Synthetic Trehalose Dicorynomycolate and Antimicrobials Increase Survival from Sepsis in Mice Immunocompromised by Radiation and Trauma. *J Med* **1992**, *23* (3–4), 253–264.

(120) Yoshinaga, K.; Yoshioka, H.; Kurosaki, H.; Hirasawa, M.; Uritani, M.; Hasegawa, K. Protection by Trehalose of DNA from Radiation Damage. *Biosci Biotechnol Biochem* **1997**, *61* (1), 160–161. https://doi.org/10.1271/bbb.61.160.

(121) Webb, K. M.; DiRuggiero, J. Role of Mn2+ and Compatible Solutes in the Radiation Resistance of Thermophilic Bacteria and Archaea. *Archaea* **2012**, *2012*, 845756. https://doi.org/10.1155/2012/845756.

(122) Liu, T.; Zhu, L.; Zhang, Z.; Huang, H.; Zhang, Z.; Jiang, L. Protective Role of Trehalose during Radiation and Heavy Metal Stress in Aureobasidium Subglaciale F134. *Sci Rep* **2017**, *7* (1), 17586. https://doi.org/10.1038/s41598-017-15489-0.

(123) Paithankar, J. G.; Raghu, S. V.; Patil, R. K. Concomitant Changes in Radiation Resistance and Trehalose Levels during Life Stages of Drosophila Melanogaster Suggest Radio-Protective Function of Trehalose. *Int J Radiat Biol* **2018**, *94* (6), 576–589. https://doi.org/10.1080/09553002.2018.1460499.

(124) Elbein, A. D.; Pan, Y. T.; Pastuszak, I.; Carroll, D. New Insights on Trehalose: A Multifunctional Molecule. *Glycobiology* **2003**, *13* (4), 17R-27R. https://doi.org/10.1093/glycob/cwg047.

(125) Cejková, J.; Ardan, T.; Cejka, C.; Luyckx, J. Favorable Effects of Trehalose on the Development of UVB-Mediated Antioxidant/pro-Oxidant Imbalance in the Corneal Epithelium, Proinflammatory Cytokine and Matrix Metalloproteinase Induction, and Heat Shock Protein 70 Expression. *Graefes Arch Clin Exp Ophthalmol* **2011**, *249* (8), 1185–1194. https://doi.org/10.1007/s00417-011-1676-y.

(126) Higashiyama, T. Novel Functions and Applications of Trehalose. *Pure and Applied Chemistry* **2002**, *74* (7), 1263–1269. https://doi.org/10.1351/pac200274071263.

(127) Supuran, C. T. Special Issue: Sulfonamides. *Molecules* **2017**, *22* (10), E1642. https://doi.org/10.3390/molecules22101642.

(128) Perlovich, G. L.; Kazachenko, V. P.; Strakhova, N. N.; Raevsky, O. A. Impact of Sulfonamide Structure on Solubility and Transfer Processes in Biologically Relevant Solvents. *J. Chem. Eng. Data* **2014**, *59* (12), 4217–4226. https://doi.org/10.1021/je500918t.

(129) Hussaini, S. M. A. Therapeutic Significance of Quinolines: A Patent Review (2013-2015). *Expert Opin Ther Pat* **2016**, *26* (10), 1201–1221. https://doi.org/10.1080/13543776.2016.1216545.

(130) Na Nakorn, T.; Traver, D.; Weissman, I. L.; Akashi, K. Myeloerythroid-Restricted Progenitors Are Sufficient to Confer Radioprotection and Provide the Majority of Day 8 CFU-S. *J Clin Invest* **2002**, *109* (12), 1579–1585. https://doi.org/10.1172/JCI15272.

(131) Williams, G. T.; Smith, C. A.; Spooncer, E.; Dexter, T. M.; Taylor, D. R. Haemopoietic Colony Stimulating Factors Promote Cell Survival by Suppressing Apoptosis. *Nature* **1990**, *343* (6253), 76–79. https://doi.org/10.1038/343076a0.

(132) Yamaguchi, M.; Suzuki, M.; Funaba, M.; Chiba, A.; Kashiwakura, I. Mitigative Efficacy of the Clinical Dosage Administration of Granulocyte Colony-Stimulating Factor and Romiplostim in Mice with Severe Acute Radiation Syndrome. *Stem Cell Res Ther* **2020**, *11* (1), 339. https://doi.org/10.1186/s13287-020-01861-x.

(133) Hua, G.; Thin, T. H.; Feldman, R.; Haimovitz-Friedman, A.; Clevers, H.; Fuks, Z.; Kolesnick, R. Crypt Base Columnar Stem Cells in Small Intestines of Mice Are Radioresistant. *Gastroenterology* **2012**, *143* (5), 1266–1276. https://doi.org/10.1053/j.gastro.2012.07.106.

(134) Tian, H.; Biehs, B.; Warming, S.; Leong, K. G.; Rangell, L.; Klein, O. D.; de Sauvage, F. J. A Reserve Stem Cell Population in Small Intestine Renders Lgr5-Positive Cells Dispensable. *Nature* **2011**, *478* (7368), 255–259. https://doi.org/10.1038/nature10408.

(135) Yan, K. S.; Chia, L. A.; Li, X.; Ootani, A.; Su, J.; Lee, J. Y.; Su, N.; Luo, Y.; Heilshorn, S. C.; Amieva, M. R.; Sangiorgi, E.; Capecchi, M. R.; Kuo, C. J. The Intestinal Stem Cell Markers Bmi1 and Lgr5 Identify Two Functionally Distinct Populations. *Proc Natl Acad Sci U S A* **2012**, *109* (2), 466–471. https://doi.org/10.1073/pnas.1118857109.

(136) Tetteh, P. W.; Farin, H. F.; Clevers, H. Plasticity within Stem Cell Hierarchies in Mammalian Epithelia. *Trends Cell Biol* **2015**, *25* (2), 100–108. https://doi.org/10.1016/j.tcb.2014.09.003.

(137) Wabik, A.; Jones, P. H. Switching Roles: The Functional Plasticity of Adult Tissue Stem Cells. *EMBO J* **2015**, *34* (9), 1164–1179. https://doi.org/10.15252/embj.201490386.

(138) Beumer, J.; Clevers, H. Regulation and Plasticity of Intestinal Stem Cells during Homeostasis and Regeneration. *Development* **2016**, *143* (20), 3639–3649. https://doi.org/10.1242/dev.133132.

(139) Jones, J. C.; Dempsey, P. J. Enterocyte Progenitors Can Dedifferentiate to Replace Lost Lgr5+ Intestinal Stem Cells Revealing That Many Different Progenitor Populations Can Regain Stemness. *Stem Cell Investig* **2016**, *3*, 61. https://doi.org/10.21037/sci.2016.09.15.

(140) Gehart, H.; Clevers, H. Tales from the Crypt: New Insights into Intestinal Stem Cells. *Nat Rev Gastroenterol Hepatol* **2019**, *16* (1), 19–34. https://doi.org/10.1038/s41575-018-0081-y.

(141) Schaue, D.; McBride, W. H. Links between Innate Immunity and Normal Tissue Radiobiology. *Radiat Res* **2010**, *173* (4), 406–417. https://doi.org/10.1667/RR1931.1.

(142) Schaue, D.; Micewicz, E. D.; Ratikan, J. A.; Xie, M. W.; Cheng, G.; McBride, W. H. Radiation and Inflammation. *Semin Radiat Oncol* **2015**, *25* (1), 4–10. https://doi.org/10.1016/j.semradonc.2014.07.007.

(143) Maelfait, J.; Liverpool, L.; Rehwinkel, J. Nucleic Acid Sensors and Programmed Cell Death. *J Mol Biol* **2020**, *432* (2), 552–568. https://doi.org/10.1016/j.jmb.2019.11.016.

(144) Kim, J.-H.; Thimmulappa, R. K.; Kumar, V.; Cui, W.; Kumar, S.; Kombairaju, P.; Zhang, H.; Margolick, J.; Matsui, W.; Macvittie, T.; Malhotra, S. V.; Biswal, S. NRF2-Mediated Notch Pathway Activation Enhances Hematopoietic Reconstitution Following Myelosuppressive Radiation. *J Clin Invest* **2014**, *124* (2), 730–741. https://doi.org/10.1172/JCI70812.

(145) Schaue, D.; Xie, M. W.; Ratikan, J. A.; McBride, W. H. Regulatory T Cells in Radiotherapeutic Responses. *Front Oncol* **2012**, *2*, 90. https://doi.org/10.3389/fonc.2012.00090.

(146) Clevers, H. C. Organoids: Avatars for Personalized Medicine. *Keio J Med* **2019**, *68* (4), 95. https://doi.org/10.2302/kjm.68-006-ABST.

(147) Saha, S.; Aranda, E.; Hayakawa, Y.; Bhanja, P.; Atay, S.; Brodin, N. P.; Li, J.; Asfaha, S.; Liu, L.; Tailor, Y.; Zhang, J.; Godwin, A. K.; Tome, W. A.; Wang, T. C.; Guha, C.; Pollard, J.

W. Macrophage-Derived Extracellular Vesicle-Packaged WNTs Rescue Intestinal Stem Cells and Enhance Survival after Radiation Injury. *Nat Commun* **2016**, *7*, 13096. https://doi.org/10.1038/ncomms13096.

(148) Ouspenskaia, T.; Matos, I.; Mertz, A. F.; Fiore, V. F.; Fuchs, E. WNT-SHH Antagonism Specifies and Expands Stem Cells Prior to Niche Formation. *Cell* **2016**, *164* (1–2), 156–169. https://doi.org/10.1016/j.cell.2015.11.058.

(149) Singh, B. N.; Weaver, C. V.; Garry, M. G.; Garry, D. J. Hedgehog and Wnt Signaling Pathways Regulate Tail Regeneration. *Stem Cells Dev* **2018**, *27* (20), 1426–1437. https://doi.org/10.1089/scd.2018.0049.

(150) Cao, H.; Chen, X.; Hou, J.; Wang, C.; Xiang, Z.; Shen, Y.; Han, X. The Shh/Gli Signaling Cascade Regulates Myofibroblastic Activation of Lung-Resident Mesenchymal Stem Cells via the Modulation of Wnt10a Expression during Pulmonary Fibrogenesis. *Lab Invest* **2020**, *100* (3), 363–377. https://doi.org/10.1038/s41374-019-0316-8.

(151) Himburg, H. A.; Doan, P. L.; Quarmyne, M.; Yan, X.; Sasine, J.; Zhao, L.; Hancock, G. V.; Kan, J.; Pohl, K. A.; Tran, E.; Chao, N. J.; Harris, J. R.; Chute, J. P. Dickkopf-1 Promotes Hematopoietic Regeneration via Direct and Niche-Mediated Mechanisms. *Nat Med* **2017**, *23* (1), 91–99. https://doi.org/10.1038/nm.4251.

(152) Daniel, A. R.; Lee, C.-L.; Oh, P.; Luo, L.; Ma, Y.; Kirsch, D. G. Inhibiting Glycogen Synthase Kinase-3 Mitigates the Hematopoietic Acute Radiation Syndrome in a Sex- and Strain-Dependent Manner in Mice. *Health Phys* **2020**, *119* (3), 315–321. https://doi.org/10.1097/HP.0000000000001243.

(153) Luis, T. C.; Naber, B. A. E.; Roozen, P. P. C.; Brugman, M. H.; de Haas, E. F. E.; Ghazvini, M.; Fibbe, W. E.; van Dongen, J. J. M.; Fodde, R.; Staal, F. J. T. Canonical Wnt Signaling Regulates Hematopoiesis in a Dosage-Dependent Fashion. *Cell Stem Cell* **2011**, *9* (4), 345–356. https://doi.org/10.1016/j.stem.2011.07.017.

(154) Ma, J.; Wang, R.; Fang, X.; Sun, Z. β-Catenin/TCF-1 Pathway in T Cell Development and Differentiation. *J Neuroimmune Pharmacol* **2012**, *7* (4), 750–762. https://doi.org/10.1007/s11481-012-9367-y.

(155) Katoh, Y.; Katoh, M. Hedgehog Signaling Pathway and Gastrointestinal Stem Cell Signaling Network (Review). *Int J Mol Med* **2006**, *18* (6), 1019–1023.

(156) Amankulor, N. M.; Hambardzumyan, D.; Pyonteck, S. M.; Becher, O. J.; Joyce, J. A.; Holland, E. C. Sonic Hedgehog Pathway Activation Is Induced by Acute Brain Injury and Regulated by Injury-Related Inflammation. *J Neurosci* **2009**, *29* (33), 10299–10308. https://doi.org/10.1523/JNEUROSCI.2500-09.2009.

(157) Pitter, K. L.; Tamagno, I.; Feng, X.; Ghosal, K.; Amankulor, N.; Holland, E. C.; Hambardzumyan, D. The SHH/Gli Pathway Is Reactivated in Reactive Glia and Drives Proliferation in Response to Neurodegeneration-Induced Lesions. *Glia* **2014**, *62* (10), 1595–1607. https://doi.org/10.1002/glia.22702.

(158) Caradu, C.; Guy, A.; James, C.; Reynaud, A.; Gadeau, A.-P.; Renault, M.-A. Endogenous Sonic Hedgehog Limits Inflammation and Angiogenesis in the Ischaemic Skeletal Muscle of Mice. *Cardiovasc Res* **2018**, *114* (5), 759–770. https://doi.org/10.1093/cvr/cvy017.

(159) Guo, Y.; Shi, G.; Wan, H.; Zhou, M. Hedgehog Signaling Regulates the Expression Levels of Inflammatory Mediators in Cigarette-induced Airway Inflammation. *Mol Med Rep* **2018**, *17* (6), 8557–8563. https://doi.org/10.3892/mmr.2018.8861.

(160) Moparthi, L.; Koch, S. Wnt Signaling in Intestinal Inflammation. *Differentiation* **2019**, *108*, 24–32. https://doi.org/10.1016/j.diff.2019.01.002.

(161) Zhou, Y.; Jin, J.; Feng, M.; Zhu, D. Wnt Signaling in Inflammation in Tissue Repair and Regeneration. *Curr Protein Pept Sci* **2019**, *20* (8), 829–843. https://doi.org/10.2174/1389203720666190507094441.

(162) Omenetti, A.; Diehl, A. M. The Adventures of Sonic Hedgehog in Development and Repair. II. Sonic Hedgehog and Liver Development, Inflammation, and Cancer. *Am J Physiol*

Gastrointest Liver Physiol **2008**, *294* (3), G595-598. https://doi.org/10.1152/ajpgi.00543.2007.

(163) de la Roche, M.; Ritter, A. T.; Angus, K. L.; Dinsmore, C.; Earnshaw, C. H.; Reiter, J. F.; Griffiths, G. M. Hedgehog Signaling Controls T Cell Killing at the Immunological Synapse. *Science* **2013**, *342* (6163), 1247–1250. https://doi.org/10.1126/science.1244689.

(164) Braune, J.; Weyer, U.; Matz-Soja, M.; Hobusch, C.; Kern, M.; Kunath, A.; Klöting, N.; Kralisch, S.; Blüher, M.; Gebhardt, R.; Zavros, Y.; Bechmann, I.; Gericke, M. Hedgehog Signalling in Myeloid Cells Impacts on Body Weight, Adipose Tissue Inflammation and Glucose Metabolism. *Diabetologia* **2017**, *60* (5), 889–899. https://doi.org/10.1007/s00125-017-4223-5.

(165) Shen, X.; Peng, Y.; Li, H. The Injury-Related Activation of Hedgehog Signaling Pathway Modulates the Repair-Associated Inflammation in Liver Fibrosis. *Front Immunol* **2017**, *8*, 1450. https://doi.org/10.3389/fimmu.2017.01450.

(166) Razumilava, N.; Gumucio, D. L.; Samuelson, L. C.; Shah, Y. M.; Nusrat, A.; Merchant, J. L. Indian Hedgehog Suppresses Intestinal Inflammation. *Cell Mol Gastroenterol Hepatol* **2018**, *5* (1), 63–64. https://doi.org/10.1016/j.jcmgh.2017.10.003.

(167) Kornberg, M. D.; Bhargava, P.; Kim, P. M.; Putluri, V.; Snowman, A. M.; Putluri, N.; Calabresi, P. A.; Snyder, S. H. Dimethyl Fumarate Targets GAPDH and Aerobic Glycolysis to Modulate Immunity. *Science* **2018**, *360* (6387), 449–453. https://doi.org/10.1126/science.aan4665.

(168) Swed, A.; Eyal, S.; Madar, I.; Zohar-Kontante, H.; Weiss, L.; Hoffman, A. The Role of P-Glycoprotein in Intestinal Transport versus the BBB Transport of Tetraphenylphosphonium. *Mol. Pharmaceutics* **2009**, *6* (6), 1883–1890. https://doi.org/10.1021/mp900170y.

(169) Navarro, A.; Boveris, A. Brain Mitochondrial Dysfunction in Aging, Neurodegeneration, and Parkinson's Disease. *Front Aging Neurosci* **2010**, *2*, 34. https://doi.org/10.3389/fnagi.2010.00034.

(170) Uneyama, K. *Organofluorine Chemistry*; John Wiley & Sons, 2008.

(171) Bégué, J.-P.; Bonnet-Delpon, D. *Bioorganic and Medicinal Chemistry of Fluorine | Wiley*. Wiley.com. https://www.wiley.com/en-us/Bioorganic+and+Medicinal+Chemistry+of+Fluorine-p-9780470278307 (accessed 2022-08-08).

(172) O'Hagan, D. Fluorine in Health Care: Organofluorine Containing Blockbuster Drugs. *Journal of Fluorine Chemistry* **2010**, *131* (11), 1071–1081. https://doi.org/10.1016/j.jfluchem.2010.03.003.

(173) Purser, S.; Moore, P. R.; Swallow, S.; Gouverneur, V. Fluorine in Medicinal Chemistry. *Chem Soc Rev* **2008**, *37* (2), 320–330. https://doi.org/10.1039/b610213c.

(174) Appendix: Approved Active Pharmaceutical Ingredients Containing Fluorine. In *Fluorine in Medicinal Chemistry and Chemical Biology*; John Wiley & Sons, Ltd, 2009; pp 525–526. https://doi.org/10.1002/9781444312096.app1.

(175) Hiyama, T.; Yamamoto, H. Biologically Active Organofluorine Compounds. In *Organofluorine Compounds: Chemistry and Applications*; Hiyama, T., Yamamoto, H., Eds.; Springer: Berlin, Heidelberg, 2000; pp 137–182. https://doi.org/10.1007/978-3-662-04164-2_5.

(176) Villalba, G.; Ayres, R. U.; Schroder, H. Accounting for Fluorine: Production, Use, and Loss. *Journal of Industrial Ecology* **2007**, *11* (1), 85–101. https://doi.org/10.1162/jiec.2007.1075.

(177) *Electrophilic fluorination at saturated sites - Chemical Communications (RSC Publishing)*. https://pubs.rsc.org/en/content/articlelanding/2000/cc/b001624l (accessed 2022-08-08).

(178) Rozen, S. Elemental Fluorine: Not Only for Fluoroorganic Chemistry! *Acc. Chem. Res.* **1996**, *29* (5), 243–248. https://doi.org/10.1021/ar950106c.

(179) Ghatora, B. K.; Barton, S. J.; Foot, P. J. S.; Tate, P. M. The Effect of Direct Gas Fluorination on Medical Grade Poly(Methyl Methacrylate). *OJOPM* **2014**, *04* (04), 74–83. https://doi.org/10.4236/ojopm.2014.44010.

(180) Krasikova, R. PET Radiochemistry Automation: State of the Art and Future Trends in 18F-Nucleophilic Fluorination. *Current Organic Chemistry 17* (19), 2097–2107.

(181) Lee, E.; Kamlet, A. S.; Powers, D. C.; Neumann, C. N.; Boursalian, G. B.; Furuya, T.; Choi, D. C.; Hooker, J. M.; Ritter, T. A Fluoride-Derived Electrophilic Late-Stage Fluorination Reagent for PET Imaging. *Science* **2011**, *334* (6056), 639–642. https://doi.org/10.1126/science.1212625.

(182) Tredwell, M.; Gouverneur, V. 18F Labeling of Arenes. *Angew Chem Int Ed Engl* **2012**, *51* (46), 11426–11437. https://doi.org/10.1002/anie.201204687.

(183) Cole, E. L.; Stewart, M. N.; Littich, R.; Hoareau, R.; Scott, P. J. H. Radiosyntheses Using Fluorine-18: The Art and Science of Late Stage Fluorination. *Curr Top Med Chem* **2014**, *14* (7), 875–900.

(184) Fuchigami, T.; Shimojo, M.; Konno, A.; Nakagawa, K. Electrolytic Partial Fluorination of Organic Compounds. 1. Regioselective Anodic Monofluorination of Organosulfur Compounds. *J. Org. Chem.* **1990**, *55* (25), 6074–6075. https://doi.org/10.1021/jo00312a006.

(185) Baizer, M. M.; Lund, H. *Organic Electrochemistry: An Introduction and a Guide.*; M. Dekker: New York, 1983.

(186) Fuchigami, T.; Inagi, S. Selective Electrochemical Fluorination of Organic Molecules and Macromolecules in Ionic Liquids. *Chem Commun (Camb)* **2011**, *47* (37), 10211–10223. https://doi.org/10.1039/c1cc12414e.

(187) Prakash, G. K. S.; Olah, G. A. Synthetic Methods and Reactions. *Proc. Indian Acad. Sci. (Chem. Sci.)* **1988**, *100* (2–3), 143–185. https://doi.org/10.1007/BF02839446.

(188) Brigaud, T.; Laurent, A.; Laurent, E. OXIDATIVE FLUORINATION OF SULFIDES IN PRESENCE OF Et3N,3HF. *Phosphorus, Sulfur, and Silicon and the Related Elements* **1991**, *59* (1–4), 153–156. https://doi.org/10.1080/10426509108045712.

(189) Meurs, J. H. H.; Eilenberg, W. Oxidative Fluorination in Amine-Hf Mixturess. *Tetrahedron* **1991**, *47* (4), 705–714. https://doi.org/10.1016/S0040-4020(01)87060-5.

(190) Konno, A.; Nakagawa, K.; Fuchigami, T. New Mechanistic Aspects of Anodic Monofluorination of Halogenoalkyl and Alkyl Phenyl Sulphides. *J. Chem. Soc., Chem. Commun.* **1991**, No. 15, 1027–1029. https://doi.org/10.1039/C39910001027.

(191) Kim, D. W.; Jeong, H.-J.; Lim, S. T.; Sohn, M.-H. Recent Trends in the Nucleophilic [(18)F]-Radiolabeling Method with No-Carrier-Added [(18)F]Fluoride. *Nucl Med Mol Imaging* **2010**, *44* (1), 25–32. https://doi.org/10.1007/s13139-009-0008-1.

(192) He, Q.; Wang, Y.; Alfeazi, I.; Sadeghi, S. Electrochemical Nucleophilic Synthesis of Di-Tert-Butyl-(4-[18F]Fluoro-1,2-Phenylene)-Dicarbonate. *Appl Radiat Isot* **2014**, *92*, 52–57. https://doi.org/10.1016/j.apradiso.2014.06.013.

(193) Reischl, G.; Kienzle, G. J.; Machulla, H.-J. Electrochemical Radiofluorination: Labeling of Benzene with [18F]Fluoride by Nucleophilic Substitution. *Journal of Radioanalytical and Nuclear Chemistry* **2002**, *254* (2), 409–411. https://doi.org/10.1023/A:1021669126378.

(194) *Superacid Chemistry, 2nd Edition | Wiley*. Wiley.com. https://www.wiley.com/en-us/Superacid+Chemistry%2C+2nd+Edition-p-9780470421543 (accessed 2022-08-08).

(195) *Cyclotron Produced Radionuclides: Principles and Practice*. https://www.iaea.org/publications/7849/cyclotron-produced-radionuclides-principles-and-practice (accessed 2022-08-08).

(196) Campbell, M. G.; Mercier, J.; Genicot, C.; Gouverneur, V.; Hooker, J. M.; Ritter, T. Bridging the Gaps in 18F PET Tracer Development. *Nat Chem* **2016**, *9* (1), 1–3. https://doi.org/10.1038/nchem.2693.

(197) Tang, P.; Wang, W.; Ritter, T. Deoxyfluorination of Phenols. *J. Am. Chem. Soc.* **2011**, *133* (30), 11482–11484. https://doi.org/10.1021/ja2048072.

(198) Lewandowski, G.; Meissner, E.; Milchert, E. Special Applications of Fluorinated Organic Compounds. *J Hazard Mater* **2006**, *136* (3), 385–391. https://doi.org/10.1016/j.jhazmat.2006.04.017.

(199) Champagne, P. A.; Desroches, J.; Hamel, J.-D.; Vandamme, M.; Paquin, J.-F. Monofluorination of Organic Compounds: 10 Years of Innovation. *Chem Rev* **2015**, *115* (17), 9073–9174. https://doi.org/10.1021/cr500706a.

(200) Gillis, E. P.; Eastman, K. J.; Hill, M. D.; Donnelly, D. J.; Meanwell, N. A. Applications of Fluorine in Medicinal Chemistry. *J. Med. Chem.* **2015**, *58* (21), 8315–8359. https://doi.org/10.1021/acs.jmedchem.5b00258.

(201) Chambers, R. D.; Parsons, M.; Sandford, G.; Bowden, R. Electrophilic Fluorination at Saturated Sites. *Chem. Commun.* **2000**, No. 11, 959–960. https://doi.org/10.1039/B001624L.

(202) Kohlhepp, S. V.; Gulder, T. Hypervalent Iodine(III) Fluorinations of Alkenes and Diazo Compounds: New Opportunities in Fluorination Chemistry. *Chem. Soc. Rev.* **2016**, *45* (22), 6270–6288. https://doi.org/10.1039/C6CS00361C.

(203) Rotstein, B. H.; Stephenson, N. A.; Vasdev, N.; Liang, S. H. Spirocyclic Hypervalent Iodine(III)-Mediated Radiofluorination of Non-Activated and Hindered Aromatics. *Nat Commun* **2014**, *5* (1), 4365. https://doi.org/10.1038/ncomms5365.

(204) Ichiishi, N.; Brooks, A. F.; Topczewski, J. J.; Rodnick, M. E.; Sanford, M. S.; Scott, P. J. H. Copper-Catalyzed [18F]Fluorination of (Mesityl)(Aryl)Iodonium Salts. *Org Lett* **2014**, *16* (12), 3224–3227. https://doi.org/10.1021/ol501243g.

(205) Furuya, T.; Kamlet, A. S.; Ritter, T. Catalysis for Fluorination and Trifluoromethylation. *Nature* **2011**, *473* (7348), 470–477. https://doi.org/10.1038/nature10108.

(206) Preshlock, S.; Tredwell, M.; Gouverneur, V. (18)F-Labeling of Arenes and Heteroarenes for Applications in Positron Emission Tomography. *Chem Rev* **2016**, *116* (2), 719–766. https://doi.org/10.1021/acs.chemrev.5b00493.

(207) Wiebe, A.; Gieshoff, T.; Möhle, S.; Rodrigo, E.; Zirbes, M.; Waldvogel, S. R. Electrifying Organic Synthesis. *Angew Chem Int Ed Engl* **2018**, *57* (20), 5594–5619. https://doi.org/10.1002/anie.201711060.

(208) Möhle, S.; Zirbes, M.; Rodrigo, E.; Gieshoff, T.; Wiebe, A.; Waldvogel, S. R. Modern Electrochemical Aspects for the Synthesis of Value-Added Organic Products. *Angew Chem Int Ed Engl* **2018**, *57* (21), 6018–6041. https://doi.org/10.1002/anie.201712732.

(209) Sawamura, T.; Takahashi, K.; Inagi, S.; Fuchigami, T. Electrochemical Fluorination Using Alkali-Metal Fluorides. *Angewandte Chemie International Edition* **2012**, *51* (18), 4413–4416. https://doi.org/10.1002/anie.201200438.

(210) Lebedev, A.; Jiao, J.; Lee, J.; Yang, F.; Allison, N.; Herschman, H.; Sadeghi, S. Radiochemistry on Electrodes: Synthesis of an 18F-Labelled and in Vivo Stable COX-2 Inhibitor. *PLOS ONE* **2017**, *12* (5), e0176606. https://doi.org/10.1371/journal.pone.0176606.

(211) Yoshida, J.; Suga, S.; Suzuki, S.; Kinomura, N.; Yamamoto, A.; Fujiwara, K. Direct Oxidative Carbon−Carbon Bond Formation Using the “Cation Pool” Method. 1. Generation of Iminium Cation Pools and Their Reaction with Carbon Nucleophiles. *J. Am. Chem. Soc.* **1999**, *121* (41), 9546–9549. https://doi.org/10.1021/ja9920112.

(212) Fujie, S.; Matsumoto, K.; Suga, S.; Yoshida, J. Thiofluorination of Carbon–Carbon Multiple Bonds Using Electrochemically Generated ArS(ArSSAr) $^{+}$ BF_4^{-}. *Chem. Lett.* **2009**, *38* (12), 1186–1187. https://doi.org/10.1246/cl.2009.1186.

(213) Javed, M. R.; Chen, S.; Lei, J.; Collins, J.; Sergeev, M.; Kim, H.-K.; Kim, C.-J.; Dam, R. M. van; Keng, P. Y. High Yield and High Specific Activity Synthesis of [18F]Fallypride in a Batch Microfluidic Reactor for Micro-PET Imaging. *Chem. Commun.* **2014**, *50* (10), 1192–1194. https://doi.org/10.1039/C3CC47616B.

(214) Leroux, F.; Jeschke, P.; Schlosser, M. α-Fluorinated Ethers, Thioethers, and Amines: Anomerically Biased Species. *Chem. Rev.* **2005**, *105* (3), 827–856. https://doi.org/10.1021/cr040075b.

(215) Balandeh, M.; Waldmann, C.; Shirazi, D.; Gomez, A.; Rios, A.; Allison, N.; Khan, A.; Sadeghi, S. Electrochemical Fluorination and Radiofluorination of Methyl(Phenylthio)Acetate

Using Tetrabutylammonium Fluoride (TBAF). *J Electrochem Soc* **2017**, *164* (9), G99–G103. https://doi.org/10.1149/2.0941709jes.

(216) Chen, H.; Hu, Z.; Zhang, J.; Liang, G.; Xu, B. A Modified Fluoro-Pummerer Reaction with DAST and NIS for Synthesis of β-Amino-α-Fluoro-Sulfides from Corresponding β-Amino-Sulfides. *Tetrahedron* **2015**, *71* (14), 2089–2094. https://doi.org/10.1016/j.tet.2015.02.049.

(217) Waldmann, C. M.; Lebedev, A.; Allison, N.; Sadeghi, S. An Automated Synthesizer for Electrochemical 18F-Fluorination of Organic Compounds. *Appl Radiat Isot* **2017**, *127*, 245–252. https://doi.org/10.1016/j.apradiso.2017.06.028.

(218) Elsler, B.; Wiebe, A.; Schollmeyer, D.; Dyballa, K. M.; Franke, R.; Waldvogel, S. R. Source of Selectivity in Oxidative Cross-Coupling of Aryls by Solvent Effect of 1,1,1,3,3,3-Hexafluoropropan-2-Ol. *Chemistry – A European Journal* **2015**, *21* (35), 12321–12325. https://doi.org/10.1002/chem.201501604.

(219) Kirste, A.; Nieger, M.; Malkowsky, I. M.; Stecker, F.; Fischer, A.; Waldvogel, S. R. Ortho-Selective Phenol-Coupling Reaction by Anodic Treatment on Boron-Doped Diamond Electrode Using Fluorinated Alcohols. *Chemistry – A European Journal* **2009**, *15* (10), 2273–2277. https://doi.org/10.1002/chem.200802556.

(220) Waldvogel, S. R.; Lips, S.; Selt, M.; Riehl, B.; Kampf, C. J. Electrochemical Arylation Reaction. *Chem. Rev.* **2018**, *118* (14), 6706–6765. https://doi.org/10.1021/acs.chemrev.8b00233.

(221) Colomer, I.; Chamberlain, A. E. R.; Haughey, M. B.; Donohoe, T. J. Hexafluoroisopropanol as a Highly Versatile Solvent. *Nat Rev Chem* **2017**, *1* (11), 1–12. https://doi.org/10.1038/s41570-017-0088.

(222) Deng, X.; Rong, J.; Wang, L.; Vasdev, N.; Zhang, L.; Josephson, L.; Liang, S. H. Chemistry for Positron Emission Tomography: Recent Advances in 11C-, 18F-, 13N-, and 15O-Labeling Reactions. *Angewandte Chemie International Edition* **2019**, *58* (9), 2580–2605. https://doi.org/10.1002/anie.201805501.

(223) Glaudemans, A. W. J. M.; Enting, R. H.; Heesters, M. A. A. M.; Dierckx, R. A. J. O.; van Rheenen, R. W. J.; Walenkamp, A. M. E.; Slart, R. H. J. A. Value of 11C-Methionine PET in Imaging Brain Tumors and Metastases. *Eur J Nucl Med Mol Imaging* **2013**, *40* (4), 615–635. https://doi.org/10.1007/s00259-012-2295-5.

(224) Huang, T.; Tang, G.; Wang, H.; Nie, D.; Tang, X.; Liang, X.; Hu, K.; Yi, C.; Yao, B.; Tang, C. Synthesis and Preliminary Biological Evaluation of S-11C-Methyl-d-Cysteine as a New Amino Acid PET Tracer for Cancer Imaging. *Amino Acids* **2015**, *47* (4), 719–727. https://doi.org/10.1007/s00726-014-1899-4.

(225) Nuñez, R.; Macapinlac, H. A.; Yeung, H. W. D.; Akhurst, T.; Cai, S.; Osman, I.; Gonen, M.; Riedel, E.; Scher, H. I.; Larson, S. M. Combined 18F-FDG and 11C-Methionine PET Scans in Patients with Newly Progressive Metastatic Prostate Cancer. *J Nucl Med* **2002**, *43* (1), 46–55.

(226) Ilardi, E. A.; Vitaku, E.; Njardarson, J. T. Data-Mining for Sulfur and Fluorine: An Evaluation of Pharmaceuticals To Reveal Opportunities for Drug Design and Discovery. *J. Med. Chem.* **2014**, *57* (7), 2832–2842. https://doi.org/10.1021/jm401375q.

(227) Neal, T. R.; Apana, S.; Berridge, M. S. Improved Synthesis of [18F]Fluoromethyl Tosylate, a Convenient Reagent for Radiofluoromethylations. *Journal of Labelled Compounds and Radiopharmaceuticals* **2005**, *48* (8), 557–568. https://doi.org/10.1002/jlcr.949.

(228) Scott, K. A.; Njardarson, J. T. Analysis of US FDA-Approved Drugs Containing Sulfur Atoms. *Top Curr Chem (Z)* **2018**, *376* (1), 5. https://doi.org/10.1007/s41061-018-0184-5.

(229) Shinde, G. B.; Mahale, P. K.; Padaki, S. A.; Niphade, N. C.; Toche, R. B.; Mathad, V. T. An Efficient and Safe Process for the Preparation of Ticagrelor, a Platelet Aggregation Inhibitor via Resin-NO2 Catalyzed Formation of Triazole Ring. *SpringerPlus* **2015**, *4* (1), 493. https://doi.org/10.1186/s40064-015-1299-6.

(230) Albizati, K. F.; Babu, S.; Birchler, A.; Busse, J. K.; Fugett, M.; Grubbs, A.; Haddach, A.; Pagan, M.; Potts, B.; Remarchuk, T.; Rieger, D.; Rodriguez, R.; Shanley, J.; Szendroi, R.;

Tibbetts, T.; Whitten, K.; Borer, B. C. A Synthesis of the HIV-Protease Inhibitor Nelfinavir from d-Tartaric Acid. *Tetrahedron Letters* **2001**, *42* (37), 6481–6485. https://doi.org/10.1016/S0040-4039(01)01338-7.

(231) Meng, Q.; Zhao, T.; Kang, D.; Huang, B.; Zhan, P.; Liu, X. The Development of an Effective Synthetic Route of Lesinurad (RDEA594). *Chemistry Central Journal* **2017**, *11* (1), 86. https://doi.org/10.1186/s13065-017-0316-y.

(232) Fuchigami, T.; Tajima, T. Highly Selective Electrochemical Fluorination of Organic Compounds in Ionic Liquids. *Journal of Fluorine Chemistry* **2005**, *126* (2), 181–187. https://doi.org/10.1016/j.jfluchem.2004.11.003.

(233) Khan, Z. U. H.; Kong, D.; Chen, Y.; Muhammad, N.; Khan, A. U.; Khan, F. U.; Tahir, K.; Ahmad, A.; Wang, L.; Wan, P. Ionic Liquids Based Fluorination of Organic Compounds Using Electrochemical Method. *Journal of Industrial and Engineering Chemistry* **2015**, *31*, 26–38. https://doi.org/10.1016/j.jiec.2015.06.007.

(234) Noel, M.; Suryanarayanan, V.; Chellammal, S. A Review of Recent Developments in the Selective Electrochemical Fluorination of Organic Compounds. *Journal of Fluorine Chemistry* **1997**, *83* (1), 31–40. https://doi.org/10.1016/S0022-1139(96)03564-6.

(235) Dawood, K. M. Electrolytic Fluorination of Organic Compounds. *Tetrahedron* **2004**, *7* (60), 1435–1451.

(236) Fuchigami, T.; Shimojo, M.; Konno, A. Electrolytic Partial Fluorination of Organic Compounds. 17. Regiospecific Anodic Fluorination of Sulfides Bearing Electron-Withdrawing Substituents at the Position .Alpha. to the Sulfur Atom. *J. Org. Chem.* **1995**, *60* (11), 3459–3464. https://doi.org/10.1021/jo00116a037.

(237) Hugenberg, V.; Haufe, G. Fluoro-Pummerer Rearrangement and Analogous Reactions. *Journal of Fluorine Chemistry* **2012**, *143*, 238–262. https://doi.org/10.1016/j.jfluchem.2012.06.015.

(238) Bur, S. K.; Padwa, A. The Pummerer Reaction: Methodology and Strategy for the Synthesis of Heterocyclic Compounds. *Chem. Rev.* **2004**, *104* (5), 2401–2432. https://doi.org/10.1021/cr020090l.

(239) Wigman, B.; Lee, W.; Wei, W.; Houk, K. N.; Nelson, H. M. Electrochemical Fluorination of Vinyl Boronates through Donor-Stabilized Vinyl Carbocation Intermediates**. *Angewandte Chemie International Edition* **2022**, *61* (12), e202113972. https://doi.org/10.1002/anie.202113972.

(240) Fuchigami, T. Unique Solvent Effects on Selective Electrochemical Fluorination of Organic Compounds. *Journal of Fluorine Chemistry* **2007**, *128* (4), 311–316. https://doi.org/10.1016/j.jfluchem.2006.11.015.

(241) Hou, Y.; Fuchigami, T. Electrolytic Partial Fluorination of Organic Compounds XL. Solvent Effects on Anodic Fluorination of Heterocyclic Sulfides. *J. Electrochem. Soc.* **2000**, *147* (12), 4567. https://doi.org/10.1149/1.1394102.

(242) Jacobson, O.; Kiesewetter, D. O.; Chen, X. Fluorine-18 Radiochemistry, Labeling Strategies and Synthetic Routes. *Bioconjug Chem* **2015**, *26* (1), 1–18. https://doi.org/10.1021/bc500475e.

(243) Stang, P. J.; Anderson, A. G. Hammett and Taft Substituent Constants for the Mesylate, Tosylate, and Triflate Groups. *J. Org. Chem.* **1976**, *41* (5), 781–785. https://doi.org/10.1021/jo00867a007.

(244) Eberson, L.; Hartshorn, M. P.; Persson, O.; Radner, F. Making Radical Cations Live Longer. *Chem. Commun.* **1996**, No. 18, 2105–2112. https://doi.org/10.1039/CC9960002105.

(245) Eberson, L.; Hartshorn, M. P.; Persson, O. 1,1,1,3,3,3-Hexafluoropropan-2-Ol as a Solvent for the Generation of Highly Persistent Radical Cations. *J. Chem. Soc., Perkin Trans. 2* **1995**, No. 9, 1735–1744. https://doi.org/10.1039/P29950001735.

(246) Shuklov, I. A.; Dubrovina, N. V.; Börner, A. Fluorinated Alcohols as Solvents, Cosolvents and Additives in Homogeneous Catalysis. *Synthesis* **2007**, *2007* (19), 2925–2943. https://doi.org/10.1055/s-2007-983902.

(247) Shida, N.; Takenaka, H.; Gotou, A.; Isogai, T.; Yamauchi, A.; Kishikawa, Y.; Nagata, Y.; Tomita, I.; Fuchigami, T.; Inagi, S. Alkali Metal Fluorides in Fluorinated Alcohols: Fundamental Properties and Applications to Electrochemical Fluorination. *J. Org. Chem.* **2021**, *86* (22), 16128–16133. https://doi.org/10.1021/acs.joc.1c00692.

(248) Röckl, J. L.; Dörr, M.; Waldvogel, S. R. Electrosynthesis 2.0 in 1,1,1,3,3,3-Hexafluoroisopropanol/Amine Mixtures. *ChemElectroChem* **2020**, *7* (18), 3686–3694. https://doi.org/10.1002/celc.202000761.

(249) Collins, J.; Waldmann, C. M.; Drake, C.; Slavik, R.; Ha, N. S.; Sergeev, M.; Lazari, M.; Shen, B.; Chin, F. T.; Moore, M.; Sadeghi, S.; Phelps, M. E.; Murphy, J. M.; van Dam, R. M. Production of Diverse PET Probes with Limited Resources: 24 18F-Labeled Compounds Prepared with a Single Radiosynthesizer. *Proceedings of the National Academy of Sciences* **2017**, *114* (43), 11309–11314. https://doi.org/10.1073/pnas.1710466114.